

PREPARATION, CHEMICAL CONSTITUENTS AND ANTIMICROBIAL ACTIVITY OF PYROLIGNEOUS ACIDS FROM *SALIX PSAMMOPHILA* BRANCHES

JINGJING LI, XI MA, HAIYAN DUAN
NORTHWEST A&F UNIVERSITY
CHINA

(RECEIVED MAY 2021)

ABSTRACT

In order to improve the additional values of *Salix psammophila* bio-waste, pyroligneous acids (PAs) from *Salix psammophila* branches were extracted by the pyrolysis process at two temperature ranges: 90-380°C and 380-550°C. The chemical constituents and antimicrobial activities of PAs were investigated in detail. The GC-MS results showed that 34 compounds were identified from the two kinds of PAs. The main components were organic acids and ketones for PA at 90-380°C, while they were organic acids and phenols for PA at 380-550°C. The total content of acids and phenols was as high as 67.96% for PA at 380-550°C, which contributed to the strong antimicrobial activity. Two PAs both showed good antimicrobial activities for five pathogenic fungi and two pathogenic bacteria, especially against *Verticillium dahlia*. Compared with the antimicrobial activity of PA at 90-380°C, PA at 380-550°C showed greater antifungal activity but against *Fusarium oxysporum*.

KEYWORDS: *Salix psammophila*, pyroligneous acid, chemical constituents, antifungal activity, anti bacterial activity.

INTRODUCTION

Salix psammophila is a shrub mainly distributed in Northwest China and is endemic to the Kubuqi Desert and the Mu Us Desert. *S. psammophila* has extraordinary adaptation to abiotic stress, thus it is mainly planted to prevent wind erosion and control desertification (Hao et al. 2019). In order to maintain a benign ecological system, the stems of *S. psammophila* are required to flat stubble once every 3-5 years (Li et al. 2013, Zhou et al. 2017). Most of branch residues were discarded as waste or burnt as fuel. The burning of such biomass residue can lead to soil degradation by affecting the soil biota (Grewal et al. 2018). In addition, large number of particulates and trace gases released into the atmosphere can cause many environmental

problems. Therefore, it is of great significance to find an effective way to improve the additional values of this biomass residue. Until now, *S. psammophila* has been used as raw material for wood composite board, pulp and paper (Bao and Zhang 2012, Li et al. 2012, Xu et al. 2006, Ji et al. 2019). It is also a promising biomass feedstock for biofuels and bioenergy (Zhang et al. 2014). In addition, the branch residues can be converted into activated charcoal and pyroligneous acid (PA) by the pyrolysis process. Several researches concerning the activated charcoal from *S. psammophila* have been reported (Gong et al. 2018, Liu and Lang 2020, Liu et al. 2019). However, to the best of our knowledge, taking the *S. psammophila* branch residues as a bio-resource to make PA through pyrolysis, as well as for further development, has not yet been reported.

PA is an acidic, reddish-brown aqueous liquid resulted from the distillation of smoke in the anaerobic charcoal-making process (Mathew et al. 2015). The chemical compounds of PA belong to different classes of organic compounds, such as organic acids, phenols, ketones, aldehydes, alcohols, esters, in which the major ones are organic acids and phenols (Wei et al. 2010b). In China, PA has been used in medicine for more than 400 years. Currently, PA is mainly used as soil fertilizer, antimicrobial agents, sterilizing agent and flavor additive in food industry (Li and Wang 2014, Zhang et al. 2010, Pan et al. 2016). There are lots of studies showing that chemicals, yield, performance and applications of PA vary with the process conditions and raw materials (Ma et al. 2013, Wei et al. 2010a), so it is very necessary to investigate the chemical constituents and antimicrobial activities of PAs from *S. psammophila* branches.

In this paper, *S. psammophila* branches were used as raw material to produce PAs by the pyrolysis process at two temperature ranges: 90-380°C and 380-550°C. Antimicrobial activities of the PAs were evaluated, and the chemical constituents of PAs were analyzed by GC-MS in detail. The purpose of the study is to provide evidence for the development of a green antimicrobial agent from *S. psammophila* pyroligneous acid.

MATERIAL AND METHODS

S. psammophila branches were collected from the sandy land of Ordos city in Inner Mongolia, China. The materials were dried and cut into chips with an average size about 15 mm (diameter) × 100 mm (length).

Preparation and refinement of PAs from *S. psammophila* branches

A pyrolytic retort with dimension of 130 mm (diameter) × 270 mm (height) was used to make PA. About 600 g *S. psammophila* samples were loaded into the retort equipped with a water-cooling condenser. The retort was heated from room temperature to the target temperature with a rate of 1°C·min⁻¹ and maintained for 30 min to ensure completed pyrolysis. The condensed liquids were collected at two temperature ranges: 90-380°C and 380-550°C based on our preliminary test. We found that the color of pyroligneous acid (PA) at this two temperature ranges was different obviously. PA at 90-380°C was red brown, and PA at 380-550°C was black brown. The color of the former was slightly lighter than the latter, so we decided the two temperature range.

The collected raw PAs were stood for 3 months, and then the crude PA was divided into three distinct layers. The upper layer was thin oil, the middle layer was clear liquid, and the bottom layer was sticky wood tar with other substances. The middle layer was siphoned off and 5 wt% activated charcoal powders were added into. The mixture was stirred for 10 min, and then stood for 72 h. Refined PAs were labeled as E₁ for that collected at 90-380°C and E₂ at 380-550°C.

GC-MS test

About 50 ml refined PA was extracted with 15 ml ether for 6 times to remove the water in PA completely, and obtain the purified and concentrated PA, then the mixed solution was dried and distilled to remove ether. Concentrated PA was obtained and subjected to GC-MS test (TRACEGC-TRACEDSQ, Finnigan). DB-WAX capillary column with a size of 30.00 m × 0.25 mm × 0.25 μm was used to perform separation and N₂ was used as carrier gas with a constant flow rate of 1.0 mlmin⁻¹. The injection port temperature was set at 220°C and the injection volume was 1.00 μl. The column temperature was maintained at 40°C for 2 min, and then increased to 150°C at a rate of 4.0°Cmin⁻¹ for 3 min, finally increased to 240°C at a rate of 6.0°Cmin⁻¹ for 8 min. Split injection was conducted at a split rate of 80 : 1.

Mass spectroscopic conditions were set as follows, electron energy: 70 eV, ion source temperature: 280°C, mass scanning range: 35-400 amu·s⁻¹. Compounds were identified by comparison of the retention time and mass spectra with library data of mass spectra (NIST). The corresponding peak areas were used to determine the relative content of compounds.

Antimicrobial activity

The antifungal effects of PAs from *S. psammophila* branches were investigated on five pathogenic fungi, such as *Verticillium dahlia*, *Fusarium oxysporum*, *Fusarium equiseti*, *Alternaria solani* and *Fusarium graminearum*. The pathogenic fungi were cultured on potato dextrose agar (PDA) medium. The antibacterial effects of PAs were investigated on two pathogenic bacteria, including *Escherichia coli* and *Staphylococcus aureus*. The pathogenic bacteria were cultured on beef extract peptone agar (BPA) medium.

The Oxford cup method was adopted to investigate the antimicrobial activities of PAs from *S. psammophila* branches (Wang et al. 2017). The refined PAs were diluted 10 times and 100 times with sterile water, respectively. About 20 ml sterile PDA or BPA medium was heated until completely melted and then poured into a culture dish. Bacterium or fungus was dissolved in sterile physiological saline to form mixed suspension with the microbial content of 10⁶-10⁷ CFU·ml⁻¹. Then about 0.1 ml mixed suspension was inoculated on the cured BPA (PDA) medium uniformly. Two Oxford cups were placed within equal distance in each medium culture dish. About 0.25 ml refined PA suspension of different concentration was injected into the Oxford cups. Finally, the culture dishes were placed into a conditioning chamber at a temperature of 28°C for 3 days. The antimicrobial activity was represented by the inhibition zone diameter, which was measured via the cross intersect method with a vernier caliper.

RESULTS AND DISCUSSION

GC-MS analysis

The chemical constituents of PAs from *S. psammophila* branches at different pyrolysis temperature ranges were analyzed by GC-MS and listed in Tab. 1. A total of 34 compounds were identified from the PAs of *S. psammophila* branches. For E₁, 33 compounds were identified, accounting for 97% of the total amount of chemicals, and for E₂, 31 compounds were identified, representing 91% of the total amount. The chemical composition of the two kinds of PAs was very similar to each other with 30 identical compounds, except for different content. Organic acids were the dominant component of the two PAs, accounting for 36.63% and 41.86% for E₁ and E₂, resp. Among three organic acids (acetic acid, propionic acid and butanoic acid), the content of acetic acids was the highest, accounting for 79.12% and 91.76% of the total acids for E₁ and E₂. Ketones were the second highest compound for E₁, representing 29.85% of the total amount, while for E₂, phenols were the second highest constituent, representing 26.1% of the total amount. The different results indicate that the dominant components of PA from *S. psammophila* branches are organic acids and ketones at relatively low temperature stage, but organic acids and phenols at relatively high temperature stage. In addition, three unique compounds could be identified from E₁, including 1,6-dehydrated pyranoglucose, 1,2,3-trimethoxy-5-methyl-benzene and oligogalactose trisaccharide. Only one unique compound could be identified from E₂, which is furfuryl alcohol with the content of 3.37%. All above results suggest that collection of PAs at different temperature ranges is an effective way to pre-fractionate chemicals in PAs. Different products could be achieved based on the different thermal degradation characteristics for chemical constituents (cellulose, hemicellulose, and lignin) (Bradbury et al. 1979, Ben et al. 2013, Zhai et al. 2015, Nakamura et al. 2007). As we know, the pyrolysis of hemicelluloses mainly happened at 220-315°C, and that of cellulose mainly happened at 315-400°C. Cellulose and hemicellulose were thermally degraded into ketones, alcohols, furan and pyran derivatives. However, lignin was more difficult to decompose in a wide temperature range (from 160°C to 900°C), and mainly converted into phenol, guaiacol, syringol, pyrocatechol, and their derivatives (Que et al. 2019).

Tab.1: The chemical composition of PAs from *S. psammophila* branches.

Chemicals	Name	Molecular formula	PA content (%)	
			E ₁	E ₂
Organic acids	Acetic acid	C ₂ H ₄ O ₂	28.98	38.41
	Propionic acid	C ₃ H ₆ O ₂	5.04	1.80
	Butanoic acid	C ₄ H ₈ O ₂	2.61	1.65
	Total content		36.63	41.86
	1-Hydroxy-2-acetone	C ₃ H ₆ O ₂	18.42	0.92
	2-Hydroxy-3-methyl-2-cyclopenten-1-one	C ₆ H ₈ O ₂	3.84	2.27
	2(5H)-Furanone	C ₄ H ₄ O ₂	3.49	2.93
	1-Acetoxy-2-acetone	C ₅ H ₈ O ₃	2.22	1.51
Ketones	2-Methyl-2-cyclopenten-1-one	C ₆ H ₈ O	0.54	0.74
	1-Hydroxy-2-butanone	C ₄ H ₈ O ₂	0.33	0.83
	2, 4-Dimethyl-1, 3-cyclopentone	C ₇ H ₁₀ O ₂	0.39	0.13

	2-Methyl-3-hydroxy-4-pyranone	C ₆ H ₆ O ₃	0.36	0.28
	2, 3-Pentanedione	C ₅ H ₈ O ₂	0.21	0.55
	2, 5-Hexanedione	C ₆ H ₁₀ O ₂	0.05	0.17
	Total content		29.85	10.33
	Furfural	C ₅ H ₄ O ₂	8.85	6.87
	5-Methyl furfural	C ₆ H ₆ O ₂	1.93	2.95
Aldehydes	Butanedial	C ₄ H ₆ O ₂	0.36	1.00
	Glutaraldehyde	C ₅ H ₈ O ₂	0.20	0.15
	Total content		11.34	10.97
	Phenol	C ₆ H ₆ O	5.06	4.74
	1, 2-Benzenediol	C ₆ H ₆ O ₂	3.10	12.09
	3-methoxy-1, 2-Benzenediol	C ₇ H ₈ O ₃	0.73	2.49
	2-Methoxyphenol	C ₇ H ₈ O ₂	0.76	2.81
Phenols	4-Methyl-1, 2-benzenediol	C ₇ H ₈ O ₂	0.45	3.04
	2, 6-Dimethoxy-4-methylphenol	C ₉ H ₁₂ O ₃	0.37	0.61
	2-Methoxy-4-methylphenol	C ₈ H ₁₀ O ₂	0.22	0.32
	Total content		10.69	26.1
	Propionic acid vinyl ester	C ₅ H ₈ O ₂	1.25	0.33
Esters	Butyrolactone	C ₄ H ₆ O ₂	0.87	2.35
	4-Oxo-methyl pentanoic acid	C ₆ H ₁₀ O ₃	0.54	3.37
	Total content		2.66	6.05
	Butyric anhydride	C ₈ H ₁₄ O ₃	2.54	0.33
	Tetrahydro-2-furancarboxyl chloride	C ₅ H ₇ ClO ₂	0.97	0.45
	2, 5- Dimethoxy tetrahydrofuran	C ₆ H ₁₂ O ₃	0.39	0.54
Others	1, 6- Dehydrated pyranoglucose	C ₆ H ₁₀ O ₅	3.55	-
	1, 2, 3-Trimethoxy-5-methyl-benzene	C ₁₀ H ₁₄ O ₃	0.84	-
	Oligogalactose trisaccharide	C ₁₈ H ₃₂ O ₁₆	0.54	-
	Furfuryl alcohol	C ₅ H ₆ O ₂	-	3.37

Antifungal activity

The antifungal activities of PAs extracted at two temperature ranges are shown in Tab. 2 and Fig. 1. Both two kinds of PAs exhibited antifungal activities against five pathogenic fungi when the PA samples were diluted 10 times. The inhibition zone diameters were distributed in the range of 13 mm and 45 mm, indicating that PAs from *S. psammophila* branches possessed a broad antifungal spectrum against different pathogenic fungi. Most notably, PAs had excellent antifungal performance against *Verticillium dahlia* with the inhibition zone diameter of 42.5 mm for E₁, and 44.6 mm for E₂. After the PAs were diluted 100 times, they still had good antifungal activities with the inhibition zone diameter of 12.5 mm for E₁, and 21.5 mm for E₂. It suggested that PA originated from *S. psammophila* branches had the potential to be a low-cost and environmental friendly antifungal agent for preventing attack by *Verticillium dahlia*. As shown in Tab. 2, it could be seen that E₁ had better antifungal performance against *Fusarium oxysporum* and *Fusarium equiseti* as compared to the other two fungi. However, E₂ had better antifungal performance against *F. equiseti* and *F. graminearum* than the other two fungi. In general, E₂ showed high antifungal effect as compared to E₁ with the exception of against *F. oxysporum*. The reason for high antifungal activity of PA produced at high temperature might be the high total amount of phenols and acids. The total content of phenols and acids for E₂ was 67.96%, while the corresponding data was 47.59% for E₁. Compared to other raw materials in Tab. 3, the total

content of phenols and acids for E₂ extracted from *S. psammophila* branches was much higher than that from some common forestry residues (Lu et al. 2017), such as China fir, pine nut shell, bamboo, and so on. Many papers reported that the components of phenol and acid contributed to the increase in controlling the growth of fungal. This might be due to the inhibition of enzymatic activity by the compounds of phenol and acid in wood vinegar (Oramahi et al. 2018). In addition, from the results, it could be seen the antifungal effect of PA was affected seriously by the process conditions, such as the final temperature and heating rate (Choi et al. 2015, Wu et al. 2015). PAs with complex compositions at different temperature ranges selectively changed the permeability of cell membrane, inhibited the division speed of fungus or the synthesis of protein, which could result in the metabolism disorder, thus showing the inhibitory effect (Walsh et al. 2003).

Tab. 2: The inhibition zone diameter of PAs from *S. psammophila* branches with different concentration against pathogenic fungi.

Fungi	The inhibition zone diameter (mm)			
	E ₁		E ₂	
	10 times	100 times	10 times	100 times
<i>Verticillium dahlia</i>	42.5	12.5	44.6	21.5
<i>Fusarium oxysporum</i>	16.2	8.0	13.5	8.0
<i>Fusarium equiseti</i>	15.5	8.0	19.8	8.0
<i>Alternaria solani</i>	13.3	8.0	14.6	8.0
<i>Fusarium graminearum</i>	14.8	8.0	16.1	8.0

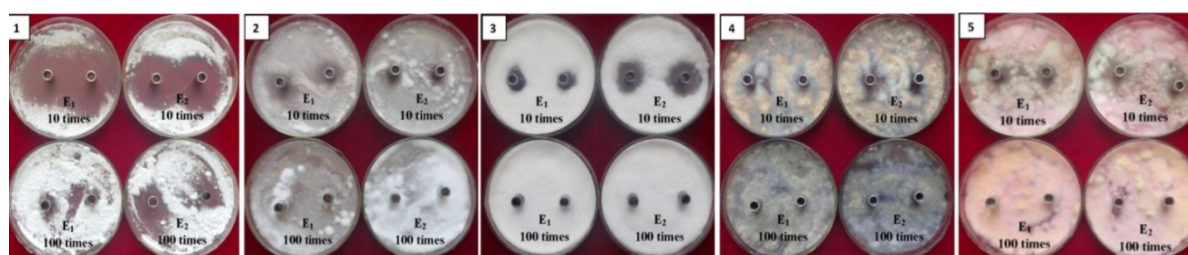


Fig. 1: The antifungal activity of PAs from *S. psammophila* branches with different concentration against pathogenic fungi: 1) *Verticillium dahlia*, 2) *Fusarium oxysporum*, 3) *Fusarium equiseti*, 4) *Alternaria solani*, 5) *Fusarium graminearum*.

Tab. 3: The chemical compositions of pyroligneous acids from different materials (Lu et al. 2017).

Materials	Phenols content (%)	Acids content (%)	Total content of phenols and acids (%)
China fir	17.62	9.97	27.59
Apple wood	13.44	52.73	66.17
Pear wood	13.23	53.09	66.32
Pine nut shell	53.88	3.78	57.66
Walnut shell	43.18	37.52	80.70
Apricot shell	42.83	23.00	65.83
Bamboo	23.29	33.04	56.33
Rice straw	9.37	38.02	47.39
Corn stalk	6.09	35.71	41.80

Antibacterial activity

The antibacterial activities of PAs produced at different temperature ranges on two kinds of bacteria including *Escherichia coli* and *Staphylococcus aureus* are shown in Tab. 3 and Fig. 2. PAs extracted at low and high temperature ranges both showed antibacterial activities for the two bacteria when they were diluted 10 times. However, the antibacterial activities were relatively weak when the PAs were diluted 100 times. Furthermore, E₂ had better antibacterial effect than E₁ against *E. coli*. While for *S. aureus*, E₁ had better antibacterial effect than E₂. It indicated that the antibacterial activity was not only determined by the chemical constituents of PAs, but also by the characteristic of the tested bacteria. Therefore, the optimum pyrolysis temperature range of PAs should be selected based on the characteristic of bacteria (Hou et al. 2018). Furthermore, it could be found that the antibacterial activity (the inhibition zone diameter range: 20-22 mm) was greater than the antifungal activity (the inhibition zone diameter range: 13-19 mm) but against the fungus *Verticillium dahlia*. The antibacterial mechanism of PAs was unclear until now. Some research reported that the pH value of PAs (2.20-3.01) was much lower than the optimal value of the bacteria growth (7.0), leading to the inhibition of bacterial growth (Oramahi and Yoshimura 2013). But some insisted that the phenolic compounds, such as phenol, cresols, were directly responsible for the antibacterial activity of PAs (Loo et al. 2007, Baimark and Niamsa 2009).

Tab. 4: The inhibition zone diameter of PAs from *S. psammophila* branches with different concentration against pathogenic bacteria.

Bacteria	The inhibition zone diameter (mm)			
	E ₁		E ₂	
	10 times	100 times	10 times	100 times
<i>Escherichia coli</i>	20.8	8.0	22.0	8.0
<i>Staphylococcus aureus</i>	21.6	8.0	20.5	8.0

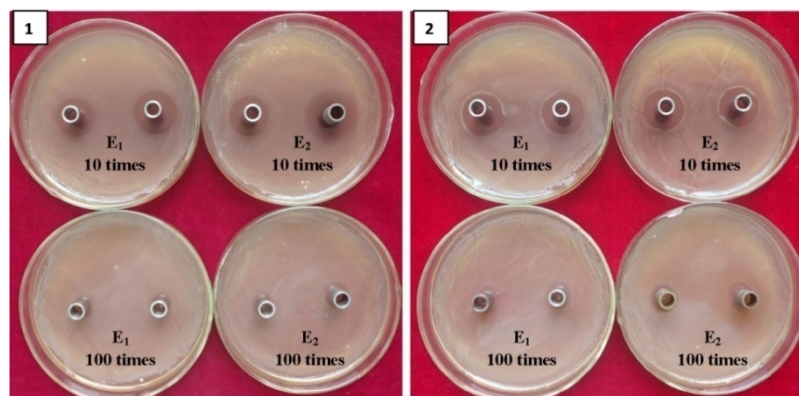


Fig. 2: The antibacterial activity of PAs from *S. psammophila* branches with different concentration against pathogenic bacteria: 1) *E. coli*, 2) *S. aureus*.

CONCLUSIONS

Pyrolygneous acids were prepared from *S. psammophila* branches by the pyrolysis process at two temperature ranges, and the chemical constituents and antimicrobial activities were investigated in detail: 1) 34 compounds were identified from the pyrolygneous acids of *S. psammophila* branches. The main components were organic acids and ketones for E₁, and organic acids and phenols for E₂. The total content of acids and phenols for E₂ was as high as 67.96%, which was much higher than that of PAs from some common biomass waste. 2) PAs extracted at two temperature ranges both showed good antimicrobial activities for the five pathogenic fungi and two pathogenic bacteria, indicating PAs from *S. psammophila* had a broad antimicrobial spectrum. It was worth noting that PAs had excellent antifungal performance against *Verticillium dahlia* with the inhibition zone diameter of 42.5 mm for E₁, and 44.6 mm for E₂. Except for the *Verticillium dahlia*, the antibacterial activity was superior to the antifungal activity. 3) In general, E₂ showed better antifungal activity compared to E₁ but against *Fusarium oxysporum*. Therefore, PA at high temperature range had a high potential to be an antifungal agent. However, for bacteria, E₂ had better antibacterial activity against *Escherichia coli* than E₁, and E₁ had better antibacterial activity against *Staphylococcus aureus* than E₂.

ACKNOWLEDGEMENTS

The authors are grateful for the support of Natural Science Foundation of Shaanxi Province in China (grant number: 2019JQ-331) and the Open Fund of Jiangsu Key Laboratory of Biomass Energy and Materials in China (grant number: JSBEM201910).

REFERENCES

1. Baimark, Y., Niamsa, N., 2009: Study on wood vinegars for use as coagulating and antifungal agents on the production of natural rubber sheets. *Biomass & Bioenergy* 33(6-7): 994-998.
2. Bao, Y., Zhang, G., 2012: Study of adsorption characteristics of methylene blue onto activated carbon made by *Salix psammophila*. *Energy Procedia* 16: 1141-1146.
3. Ben, H., Mu, W., Deng, Y., Ragauskas, A.J., 2013: Production of renewable gasoline from aqueous phase hydrogenation of lignin pyrolysis oil. *Fuel* 103: 1148-1153.
4. Bradbury, A.G.W., Sakai, Y., Shafizadeh, F., 1979: A kinetic model for pyrolysis of cellulose. *Journal of Analytical and Applied Pyrolysis* 23: 3271-3280.
5. Choi, G.G., Oh, S.J., Lee, S.J., Kim, J.S., 2015: Production of bio-based phenolic resin and activated carbon from bio-oil and biochar derived from fast pyrolysis of palm kernel shells. *Bioresource Technology* 178: 99-107.
6. Gong, J., Shao, T., Wang, K., 2018: Synergetic effect and product characteristics of coal and *Salix psammophila* co-pyrolysis. *Bioresources* 13(2): 2846-2860.

7. Grewal, A., Abbey, L., Gunupuru, L.R., 2018: Production, prospects and potential application of pyroligneous acid in agriculture. *Journal of Analytical and Applied Pyrolysis* 135: 152-159.
8. Hao, L., Zhang, G., Lu, D., Hu, J., Jia, H., 2019: Analysis of the genetic diversity and population structure of *Salix psammophila* based on phenotypic traits and simple sequence repeat markers. *Peer Journal* 7: 1-20.
9. Hou, X., Qiu, L., Luo, S., Kang, K., Zhu, M., Yao, Y., 2018: Chemical constituents and antimicrobial activity of wood vinegars at different pyrolysis temperature ranges obtained from *Eucommia ulmoides* Olivers branches. *RSC Advances* 8(71): 40941-40949.
10. Ji, Y., Lin, Q., Huang, Y., Rao, F., Yu, W., 2019: High-performance wood composites from desert shrub *Salix psammophila*. *Green Materials* 7(4): 177-184.
11. Li, C., Yang, X., Zhang, Z., Zhou, D., Zhang, L., Zhang, S., Chen, J., 2013: Hydrothermal liquefaction of desert shrub *Salix psammophila* to high value-added chemicals and hydrochar with recycled processing water. *Bioresources* 8(2): 2981-2997.
12. Li, Y.B., Yang, G.H., Chen, J.C., 2012: Effects of pretreatment by xylanase on properties of *Salix psammophila* kraft pulp. *Advanced Materials Research* 610-613: 3505-3510.
13. Li, Z.H., Wang, X.D., 2014: Effect of wood vinegar on soil properties and plant growth. *Plant Nutrition and Fertilizer Science* 20(2): 510-516.
14. Liu, W., Lang, Z., 2020: The structure and self-regeneration performance of *Salix psammophila*-activated carbon modified by Ag and N co-doped TiO₂. *RSC Advances* 10(7): 3844-3852.
15. Liu, X., Wan, Y., Liu, P., Zhao, L., Zou, W., 2019: Optimization of sulfamethazine sodium adsorption onto activated carbon-based *Salix psammophila*: investigation of adsorption behavior and mechanism. *Journal of Dispersion Science and Technology* 40(4): 507-518.
16. Loo, A.Y., Jain, K., Darah, I., 2007: Antioxidant and radical scavenging activities of the pyroligneous acid from a mangrove plant, *Rhizophora apiculata*. *Food Chemistry* 104(1): 300-307.
17. Lu, X., Jiang, J., Sun, K., Sun, Y., 2017: Review on preparation and application of wood vinegar. *Chemistry and Industry of Forest Products* 37(3): 21-30.
18. Ma, C., Song, K., Yu, J., Yang, L., Zhao, C., Wang, W., Zu, G., Zu, Y., 2013: Pyrolysis process and antioxidant activity of pyroligneous acid from *Rosmarinus officinalis* leaves. *Journal of Analytical and Applied Pyrolysis* 104: 38-47.
19. Mathew, S., Zakaria, Z.A., Musa, N.F., 2015: Antioxidant property and chemical profile of pyroligneous acid from pineapple plant waste biomass. *Process Biochemistry* 50(11): 1985-1992.
20. Nakamura, T., Kawamoto, H., Saka, S., 2007: Condensation reactions of some lignin related compounds at relatively low pyrolysis temperature. *Journal of Wood Chemistry and Technology* 27(2): 121-133.
21. Oramahi, H.A., Yoshimura, T., 2013: Antifungal and antitermitic activities of wood vinegar from *Vitex pubescens* Vahl. *Journal of Wood Science* 59(4): 344-350.
22. Oramahi, H.A., Yoshimura, T., Diba, F., Setyawati, D., 2018: Antifungal and antitermitic activities of wood vinegar from oil palm trunk. *Journal of Wood Science* 64(3): 311-317.

23. Pan, J., Xiao, H., Cheng, W., Wang, L., Lu, W., 2016: Effect of wood vinegar on soil nutrient, tomato yield and quality. *Soils and Fertilizers Sciences in China* 2 (61-64): 77.
24. Que, H., Dong, Y.G., Guo, H.Q., Lu, X.Y., Zhu, X.J., Zhang, Y.M., Gu, X.L., 2019: Pyrolytic kinetics of steam exploded lignin by Tg/Dtg analysis. *Wood Research* 64(5): 871-878.
25. Walsh, S.E., Maillard, J.Y., Russell, A.D., Catrenich, C.E., Charbonneau D.L., Bartolo, R.G., 2003: Activity and mechanisms of action of selected biocidal agents on Gram-positive and -negative bacteria. *Journal of Applied Microbiology* 94(2): 240-247.
26. Wang, Z.D., Zheng, L.C., Li, C.C., Wu, S.H., Xiao, Y.N., 2017: Preparation and antimicrobial activity of sulfopropyl chitosan in an ionic liquid aqueous solution. *Journal of Applied Polymer Science* 134(26): 1-8.
27. Wei, Q., Ma, X., Dong, J., 2010a: Preparation, chemical constituents and antimicrobial activity of pyroligneous acids from walnut tree branches. *Journal of Analytical and Applied Pyrolysis* 87: 24-28.
28. Wei, Q., Ma, X., Zhao, Z., Zhang, S., Liu, S., 2010b: Antioxidant activities and chemical profiles of pyroligneous acids from walnut shell. *Journal of Analytical and Applied Pyrolysis* 88(2): 149-154.
29. Wu, Q., Zhang, S., Hou, B., Zheng, H., Deng, W., Liu, D., Tang, W., 2015: Study on the preparation of wood vinegar from biomass residues by carbonization process. *Bioresource Technology* 179: 98-103.
30. Xu, F., Geng, Z.C., Lu, Q., Sun, R.C., 2006: *Salix psammophila* pulp obtained by alkaline hydrogen peroxide process. *Cellulose Chemistry and Technology* 40(1-2): 93-107.
31. Zhai, M.Z., Shi, G.Z., Wang, Y., Ragauskas, A.J., 2015: Chemical compositions and biological activities of pyroligneous acids from walnut shell. *Bioresources* 10(1): 1715-1729.
32. Zhang, L., Dong, L., Wang, J., Zuo, Q., Xiao Q., 2010: Influence of wood vinegar as leaves fertilizer on growth and quality of tomato. *Beijing Agriculture* 30: 58-62.
33. Zhang, X.F., Wang, K.B., Yan, X.L., Zhao, Y.B., Guo, X.M., 2014: Alcoholysis of *Salix psammophila* liquefaction. *Science & Technology Review* 32(31): 37-40.
34. Zhou, X.W., Wang, Y.R., Wang, L., Lv, J.X., Zhao, R.J., Yao, L.H., Chen, Z.J., 2017: Cell wall structure and mechanical properties of *Salix psammophila*. *Wood Research* 62(1): 1-12.

JINGJING LI, XI MA, HAIYAN DUAN*
NORTHWEST A&F UNIVERSITY
COLLEGE OF FORESTRY
NO.3 TAICHENG ROAD, YANGLING, SHAANXI, CHINA, 712100
YANGLING, CHINA

*Corresponding author: hyd0355@163.com

ANALYTICAL STUDY ON AXIAL AND ECCENTRIC COMPRESSIVE BEHAVIOR OF POPLAR COLUMN STRENGTHENED BY BFRP

FENGXIA HAN, QING LIU, XIN GUO, MENG ZHANG, XIA HAN
XINJIANG UNIVERSITY
CHINA

(RECEIVED JULY 2021)

ABSTRACT

In this work, the compression behaviour of the Xinjiang poplar column was reinforced by basalt fibre reinforced polymer (BFRP) strips with different reinforced configurations, and the numerical simulations were performed on the axial and eccentric compressions of poplar columns unreinforced and reinforced with BFRP to assess the effect of the bearing capacity and deformation of the columns. The results show that the use of BFRP to reinforce the Xinjiang poplar column effectively improves its axial compressive bearing capacity (axial compression) and bending bearing capacity (eccentric compression), and at the same time, the bearing capacity and stiffness of the columns strengthened by BFRP increased with the bonding area of BFRP.

KEYWORDS: Xinjiang poplar, timber column, BFRP, numerical simulations, compression behavior.

INTRODUCTION

Columns are often used as pressure-bearing members in timber structures, and the Xinjiang poplar in China is also one of the component materials as timber structural members (Hao 2004 and Lü 2001). The poplars growing in Xinjiang are called Xinjiang poplar, which the scientific name is *Populus bolleana* Lauche. The poplars are widely distributed in Xinjiang of China, especially in the south of Xinjiang and Ili River Valley. The poplar has the characteristics of easy reproduction, fast-growing, drought and frost tolerance, little knots, being easy to dry at room temperature (Zeng 2002, Yang 2005, Shu 2005). However, poplar is an anisotropic material (Shen 2013), which has defects, such as natural cracks, and low strength requiring the reinforcement of the Xinjiang poplar members. As a kind of reinforcement material, basalt fiber reinforced polymer (BFRP) composites have the advantages of high strength, lightweight, erosion resistance, corrosion resistance, and convenient construction. Its advantages help to compensate for the deficiencies of the Xinjiang poplar members. Therefore, BFRP is a composite

material suitable for timber structures reinforcement (Sha and Zhu 2012, Chun and Pan 2011, Chen 1995).

Scholars have presented numerous studies on the reinforcement of timber structures. Zhu and Xu (2009), Xu and Zhu (2007) and Zhou et al. (2009) found that the use of carbon fiber reinforced polymer composites to reinforce locally damaged timber columns can restore the compressive bearing capacity and ductility of the columns. Through experimental research on timber columns strengthened with fiber-reinforced polymer composites, some authors (Johns and Lacroix 2000, Shao et al. 2012, Khelifa et al. 2016) found that the bearing capacity and ductility of the strengthened timber columns were improved to a certain extent. Based on experimental results on timber columns, Khelifa et al. (2015), Sotayo et al. (2016), Zeng et al. (2016) used the timber constitutive model which is based on the elastic theory of small deformation and found that the numerical simulation results are consistent with the experimental results.

The present study on wood structures mainly focuses on strengthening the timber structural members of columns or beams strengthened with fiber cloth based on pine and cedar raw materials by experimental research. The experimental research and numerical simulation analysis of Xinjiang poplar are still relatively limited. Therefore, based on an experiment, numerical simulation is used for finite element analysis to refine and study the mechanical properties of BFRP-strengthened Xinjiang poplar columns.

MATERIAL AND METHODS

Materials

The *Populus bolleana* Lauche material of timber specimens was from Turpan, Xinjiang China. According to GB/T1931 (2009) and GB/T1928 (2009), the moisture content of the sample cut from poplar was tested. The size of the sample was 20 × 20 × 20 mm and continuously dried for 8 hours in a drying oven at 103 ± 2°C. The test result of the poplar moisture content is 10%.

According to GB/T1938 (2009) and GB/T1933 (2009), the density and the tensile and compressive strength tests along the grain of the poplar were obtained as the main mechanical properties. Tab. 1 lists the main properties of the poplar with 10% moisture content.

Tab. 1: Main mechanical characteristics of Xinjiang poplar.

Moisture content (%)	Density (g cm ⁻³)	Tensile strength along grain (MPa)	Compressive strength along grain (MPa)
10.0	4.725	114.4	36.5

The structural adhesive (YZJ-CD), which had a weight ratio of 3:1, was produced by Wuhan Changjiang Reinforcement Technology Co., Ltd in China. The YZJ-CD had a tensile strength of 53.9 MPa, a high elastic modulus of 2885.1 GPa, the axial compression strength of 101.7 MPa, and an elongation of 3.0%. The main performance parameters of the structural adhesive are shown in Tab. 2.

Tab. 2: Properties of structural adhesive.

Tensile strength (MPa)	Modulus of elasticity (GPa)	Axial compression strength (MPa)	Elongation at break (%)
53.9	2885.1	101.7	3.0

The BFRP was acquired from Xinjiang Tuoxin Basalt Fiber Products Co., Ltd in China. The BFRP composite material had a surface density of 360 gm^{-2} , a single fiber diameter of $13 \text{ }\mu\text{m}$, and a thickness of 0.138 mm . The tensile strength, modulus of elasticity, and elongation of the BFRP were 2100 MPa , 105 GPa , and 2.6% , resp. The main mechanical property parameters of BFRP are shown in Tab. 3.

Tab. 3: Mechanical property indexes of BFRP.

Surface density (gm^{-2})	Single fiber diameter (μm)	Tensile strength (MPa)	Modulus of elasticity (GPa)	Elongation rate (%)	Thickness (mm)
360	13	2100	105	2.6	0.138

Specimens preparation

Based on the codes of design standard for timber structures (GB50005, 2017) and standard for test methods of timber structures (GB/T50329, 2012), the dimensions of the timber columns were $100 \times 100 \times 1200 \text{ mm}$ for axial and eccentric compression. The initial eccentricity is defined as the distance between the center of the cross-section of the compression column and the point of the external force. 14 axial compression and eccentric compression members were tested respectively. The specific parameters of the specimens are shown in Tab. 4.

Tab. 4: Parameters of Xinjiang poplar long column specimens.

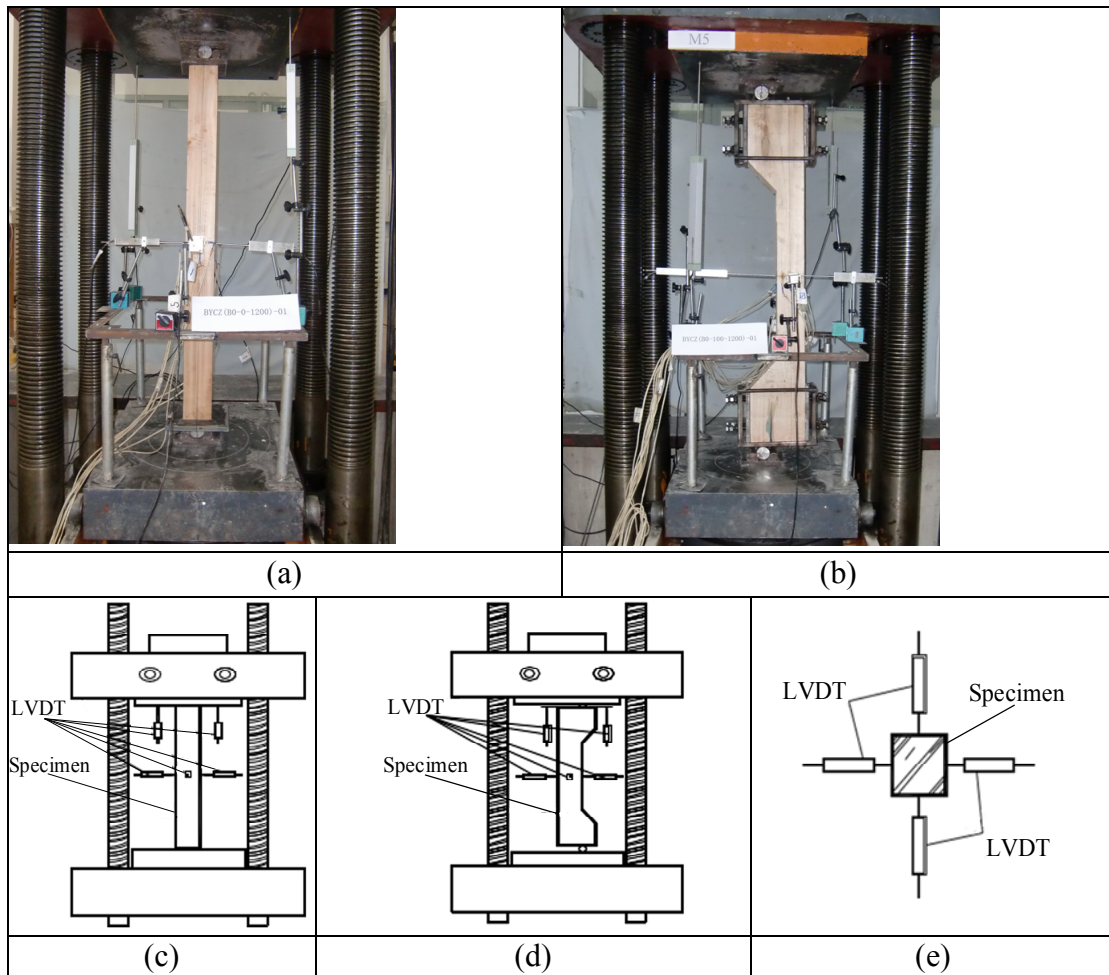
Specimen type	Specimen number	Number	Reinforcement method	Reinforced with BFRP layers	Section size	Initial eccentricity (mm)
Axial compression	DBZ	3	Unreinforced	0	$100 \times 100 \times 1200$	0
	BJ1	3	BFRP strips with saping	1	$100 \times 100 \times 1200$	
	BJ2	3	BFRP strips with saping	2	$100 \times 100 \times 1200$	
	BM1	3	Fully reinforced by BFRP	1	$100 \times 100 \times 1200$	
	BM2	3	Fully reinforced by BFRP	2	$100 \times 100 \times 1200$	
Eccentric compressive	DBZ	3	Unreinforced	0	$100 \times 100 \times 1200$	100
	BJ1	3	BFRP strips with saping	1	$100 \times 100 \times 1200$	
	BJ2	3	BFRP strips with saping	2	$100 \times 100 \times 1200$	
	BM1	3	Fully reinforced by BFRP	1	$100 \times 100 \times 1200$	
	BM2	3	Fully reinforced by BFRP	2	$100 \times 100 \times 1200$	

DBZ - an unreinforced column; in BJn/BMn, J - column reinforced by BFRP strips with 50 mm spacing, M - fully reinforced by BFRP, n - the number of layers about BFRP.

Measurement and loading procedure

In the specimens loading process, the static load method was adopted. In the preloading stage, the load was between 0% and 10% of the ultimate load, each load level was 5 kN, and the load holding time was 3 min. When the load was between 10 - 80% of the ultimate load, 10 kN was applied in each load stage, and the load holding time was 3 min. When the load reached 80% of the ultimate load, 4 kN was applied to each stage, also with 3 min of loading duration. When the load limit was reached, the displacement control of the loading method was adopted in the test. The running speed of the experimental machine was controlled at 1.00 mm s^{-1} .

Four linear voltage displacement transducers (LVDTs) (type: YDH-100) were individually arranged in the front, back, left, and right directions of the middle of the specimen to measure the lateral displacement of the specimens. Two LVDTs were arranged vertically to measure the vertical displacement of the specimens. The detailed layout of LVDT is shown in Figs. 1a-e. The detailed layout of strain gauges on each surface of the specimen was shown in Figs. 1f-j.



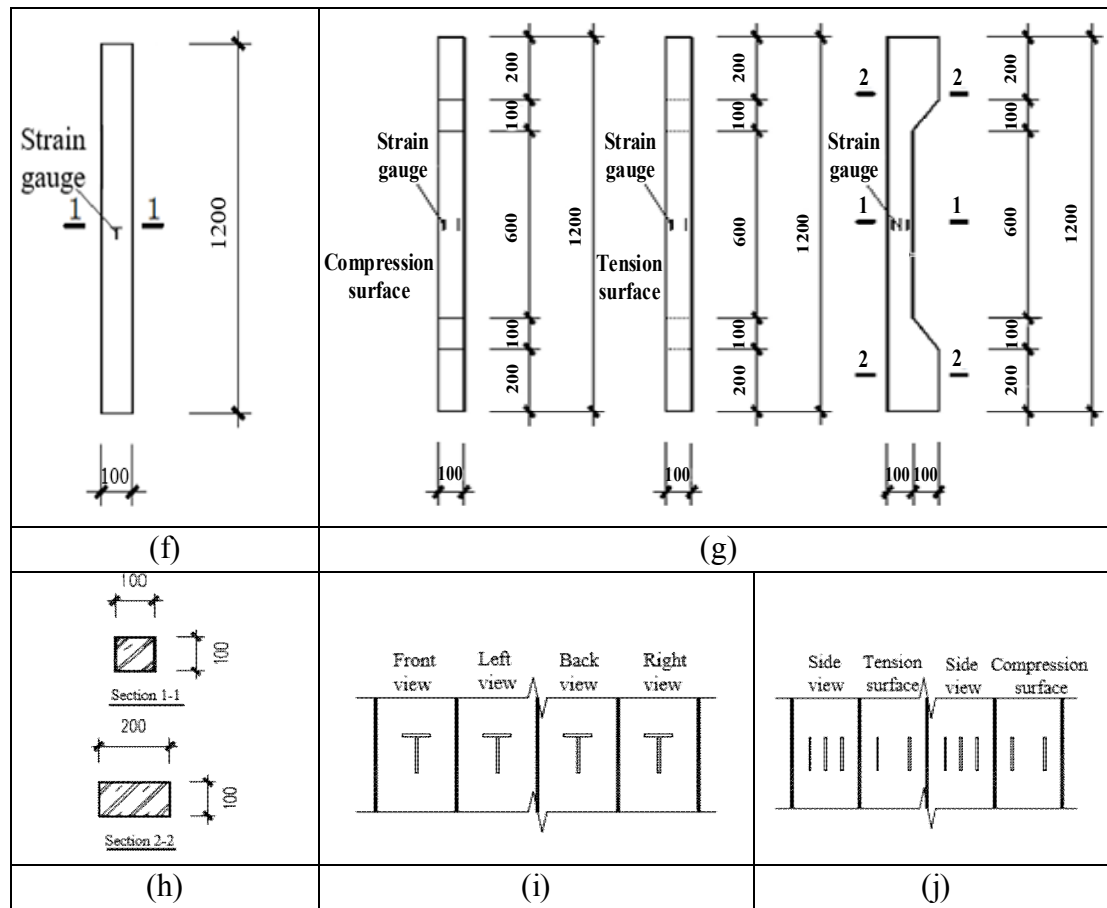


Fig. 1: Layout of measuring points: (a) LVDT arrangement of axial compressive specimen, (b) LVDT arrangement of eccentric compressive specimen, (c) Layout of the axial compressive experiment, (d) Layout of the eccentric compressive experiment, (e) Horizontal layout of LVDT, (f) Paste position and size of strain gauge of axial compressive specimen, (g) Paste position and size of strain gauge of the eccentric compressive specimen, (h) Section size of the specimen, (i) Detailed drawing of strain gauge of the axial compressive specimen, (j) Detailed drawing of strain gauge of the eccentric compressive specimen.

RESULTS AND DISCUSSION

Fracture characteristics

The failure modes of the square timber columns under axial compression are shown in Fig. 2a. The failure modes of the columns are bending failure and the degree of bending failure is different. The distance from the top, middle, and bottom of the damaged timber columns was 300 mm (DBZ), 50 mm (BJn), and 160 mm (BMn) resp. According to observation, it can be found that the failure process of the square timber columns under axial compression was as follows: (1) The unreinforced column was basically in the elastic stage when the load was 0-100 kN and the reinforced column was 0-150 kN, exhibiting no fold or other abnormal phenomena in the specimens; (2) With the increase of the load, the middle of the unreinforced timber column height was bent, and the timber fiber in the compression zone was crushed, while most of the poplar columns strengthened with the BFRP interval paste were damaged in places without fiber cloth;

increasing folds appeared in the middle of the fully pasted timber columns, and most of the experienced bending failure; (3) When the timber columns reached the limit, a fracture appeared at the middle part of the timber column with a sudden sharp “crack” sound. The average ultimate load of the unreinforced timber columns was 126.33 kN. The average ultimate load of the timber columns strengthened by the BFRP interval pastes fiber cloth with 1, and 2 layers and the fully pasted BFRP fiber cloth with 1, and 2 layers and were 160.50 kN, 195.33 kN, 186.50 kN, and 242.00 kN, respectively. Also, It can be seen from Fig. 2a that the bending failure in the middle of the poplar column is a typical failure mode.

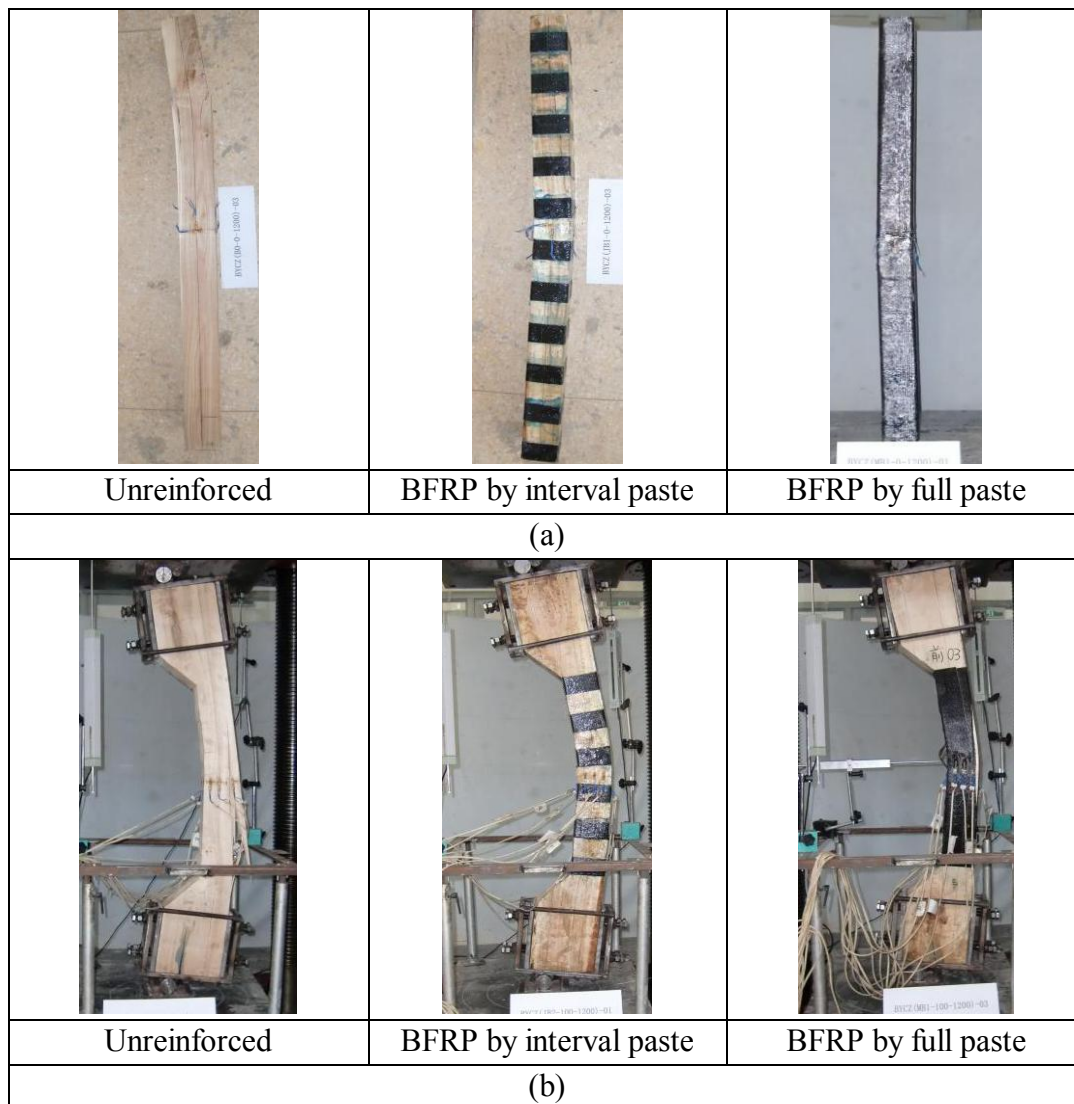


Fig. 2: Typical failure characteristics of columns: (a) axial compressive, (b) eccentric compressive.

The failure mode of the square timber columns under eccentric compression is shown in Fig. 2b. The failure modes of all the columns are bending failure and the phenomenon is very obvious. The damage location was approximately in the middle of the specimen. Its characteristics are mainly described as follows: (1) at the beginning of the experiment loading, the load was small, and the horizontal and vertical deformation of the specimen was very small.

At this time, the confined force of the basalt fiber cloth was not produced, and the stress and strain of the specimens were the same as those of the unreinforced column; (2) compression cracks first appeared in the middle of the compression surface of the unreinforced specimen with the increase of the load, and the compression area gradually increased with the load. Fig. 2b shows that the ultimate failure of the specimen was caused by the tensile fracture of the timber fiber in the tensile zone, and the cracks at the fracture exhibited a zigzag distribution; (3) Fig. 2b indicates that the failure locations in the specimens strengthened by BFRP interval paste were mostly in the unreinforced area, and timber fiber crushing developed into shear failure with a “crackling” sound, displaying a certain suddenness; (4) most of the specimens strengthened by BFRP by fully pasting showed a slow development rate of longitudinal flexural deformation, and the fiber cloth was sheared due to the shear failure of the timber fiber in the compression section.

Load-strain response

The load-strain curves of the Xinjiang poplar column specimens strengthened by BFRP are shown in Fig. 3. The load-strain curves of the square columns under axial and eccentric compressions have the same trend, which can be divided into two stages: the elastic and plastic stages. The strain in the elastic stage increased linearly with the load. When the yield load of the specimens was reached, the inflection point of the curve appeared (not obvious, but the slope of the curve decreased gradually), and the strain increased rapidly, but continued to increase linearly until the ultimate load of each specimen was reached. In addition, the comparison of the load-strain curves of the axial and eccentric compression specimens indicates that the strain values of the eccentric columns were significantly greater than those of the axial columns at the same load. However, the ultimate load of the eccentric columns was significantly lower than that of the axial columns, such as the BM2 specimen. The results show that fiber cloth can react against the lateral deformation of timber columns. Also, under the same load and reinforcement method, the strain of the axial compressive column was less than that of the eccentric compressive column, the strain of both axial and eccentric compression specimens increased with the increase of BFRP cloth reinforced lays at the same load.

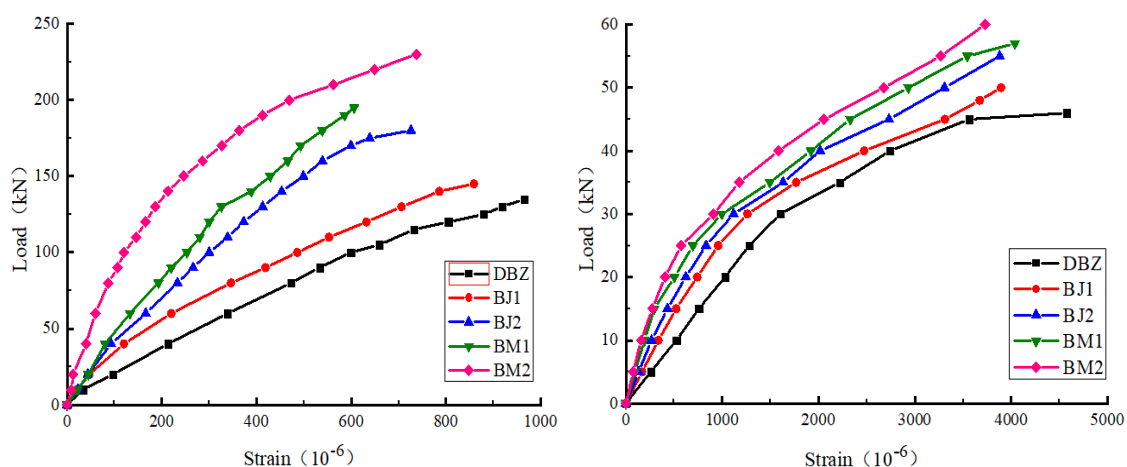


Fig. 3: Load-strain curves: (a) axial compressive, (b) eccentric compressive.

The load-displacement curves of the Xinjiang poplar column specimens are shown in Fig. 4. As can be seen that the load-displacement curve trends of the specimens are the same and can be divided into two stages: the elastic and plastic stages. The displacement in the elastic stage increases linearly with the load.

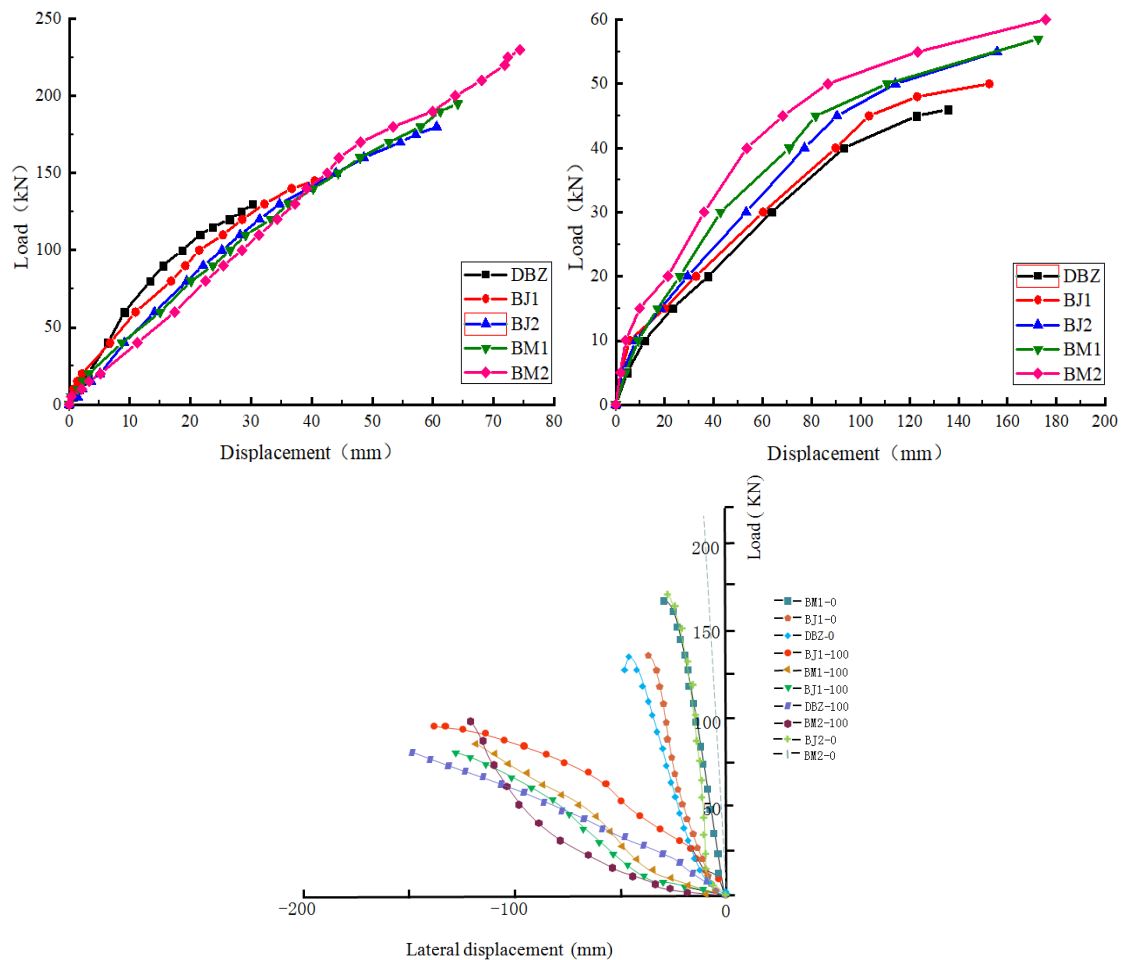


Fig. 4: Load-displacement curves: (a) axial compressive, (b) eccentric compressive, (c) load-lateral displacement curves.

When the yield load of each specimen was reached, an inflection point appeared on the curve. In both axial and eccentric compression columns, the ultimate displacement of the BM2 specimens, which were reinforced with BFRP cloth, reached the maximum value. When the same load and reinforcement method, the displacement of the axial compression column was generally less than that of the eccentric compression column, indicating that the longitudinal deformation capacity of the eccentric column was lower than that of the axial compressive column due to the joint action of the axial force and the bending moment. When the same displacement and reinforcement method, the load of the axial compression column was much higher than that of the eccentric compression column, indicating that the bearing capacity of the eccentric columns was lower than that of the axial columns. The load-lateral displacement curves of the Xinjiang poplar column specimens are shown in Fig. 4c. The lateral displacement of the axial compression columns decrease with the increase of the number of BFRP paste layers,

which demonstrated hoop effects with fiber sheets on the lateral displacement for the specimens. Compared with the unreinforced eccentric compression columns, the lateral displacement of the reinforced eccentric compression columns was decreased and the magnitude of lateral displacement reduction varies with the number of fiber bonded layers. Compared with the axial compression columns, the hoop effect with fiber sheets for the eccentric compression columns is not significant.

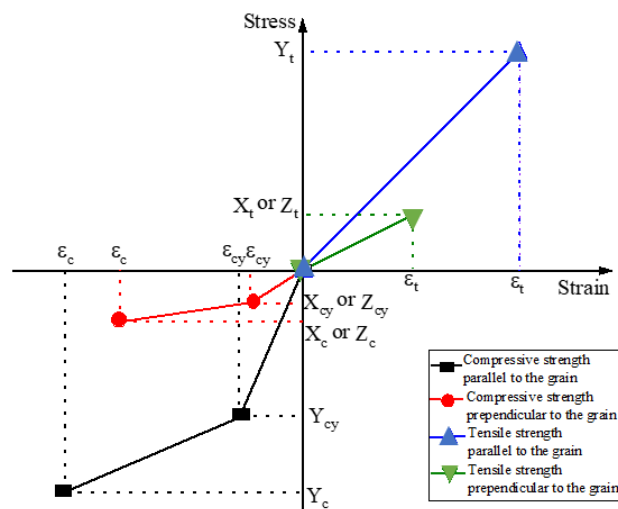
Finite element analysis (FEA)

Considering the defects of wood material, the data obtained from the above experiments are quite discrete. To solve this problem, numerical simulation (Hu and Li 2015, Wang 2007) can be used to establish models to simulate the experiment, which is convenient for optimization and accurate for simulating the mechanical properties of structural members.

Stress-strain of materials

Material model of unreinforced Xinjiang poplar

Xinjiang poplar is a kind of heterogeneous and orthotropic material whose constitutive curves can be divided into different stress-strain curves, such as longitudinal tension and compression parallel to the grain, radial tension and compression perpendicular to the grain, and tangential tension and compression, as shown in Fig. 5.



Note: Y_c and Y_{cy} are compressive strength and yield strength parallel to the grain respectively; X_c and Z_c are compressive strength perpendicular to the grain in radial and tangential direction respectively; X_{cy} and Z_{cy} are the yield compressive strength perpendicular to the grain in radial and tangential direction respectively; Y_t is the tensile strength parallel to the grain; X_t and Z_t are the tensile strength perpendicular to the grain in radial and tangential direction; ϵ_c and ϵ_{cy} are compression strain and ultimate strain of timber; ϵ_t is tension strain of timber.

Fig. 5: Stress-strain curves of Xinjiang poplar.

Wood is a complex anisotropic material (Jeong 2016). In this paper, the orthotropic constitutive relation of the Xinjiang poplar is simplified as transversely isotropic. In the general finite element analysis software ANSYS, the characteristics of the model are as follows:

1) The constitutive relation is orthotropic in the elastic stage and isotropic in the radial and tangential direction, and thus simplified to transverse isotropic. The constitutive relation of poplar in the elastic stage by using the tensor method and the elastic parameters are shown in Tab. 5. 2) The generalized HILL yield criterion (Chen et al. 2013), which is an anisotropic model for different yield strength in three orthogonal directions of the material, is adopted in the plastic stage. The generalized HILL yield criterion not only considers the difference in yield strength in the three orthogonal directions of the material but also the different yield strengths in the tensile and compressive states. This characteristic is similar to the properties of wood. Thus, the criteria are used as the strength criterion in the plastic stage of Xinjiang poplar. The plastic parameters are shown in Tab. 6. Four independent of each other in three directions of Xinjiang poplar material. The tensile and compressive strength along the grain is different, the tensile and compressive strength perpendicular to the grain is different in the radial direction and the strength perpendicular to the grain is equal to the radial and tangential direction.

Tab. 5: Elastic constitutive parameters of Xinjiang poplar.

EX (MPa)	EY (MPa)	EZ (MPa)	PRXY	PRYZ	PRXZ	GXY (MPa)	GYZ (MPa)	GXZ (MPa)
900	12600	900	0.12	0.47	0.43	915	732	915

Tab. 6: Plastic constitutive parameters of Xinjiang poplar.

Direction	X	Y	Z
Tensile yield stress (MPa)	2.6	81.2	2.6
Tensile tangent modulus (MPa)	0	0	0
Compression yield stress (MPa)	2.6551	25.4	2.6551
Compression tangent modulus (MPa)	0	3200	0
Shear yield stress (MPa)	5	5	5
Shear tangent modulus (MPa)	0	0	0

Model of Xinjiang poplar reinforced with BFRP

The tensile strength of the BFRP fiber cloth was used in the tests to produce lateral restraint on the timber column. During the experiment, the BFRP fiber cloth was completely in the elastic stage. Therefore, the constitutive model of the Xinjiang poplar column can be obtained by superimposing the elastic constitutive relation of the BFRP and that of the unreinforced Xinjiang poplar column. The BFRP fiber cloth was bonded to the timber column by a structural adhesive. Given the very small thickness of the structural adhesive layer, the influence of the adhesive layer is ignored in this model.

Element applied

The Solid45 element in Fig. 6a is applied to the orthotropic materials in ANSYS and wood is a typical orthotropic material. Thus, the element is used for the wood column. The element was used to construct a three-dimensional solid structure. The element is defined by eight nodes, and each node has three degrees of freedom to translate in the X, Y, and Z directions to match the orthotropic properties of the wood material.

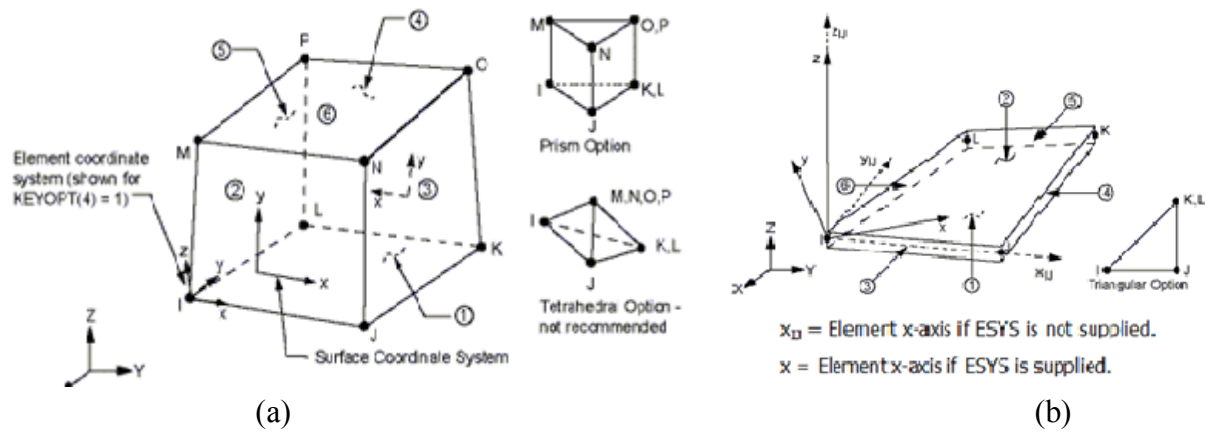


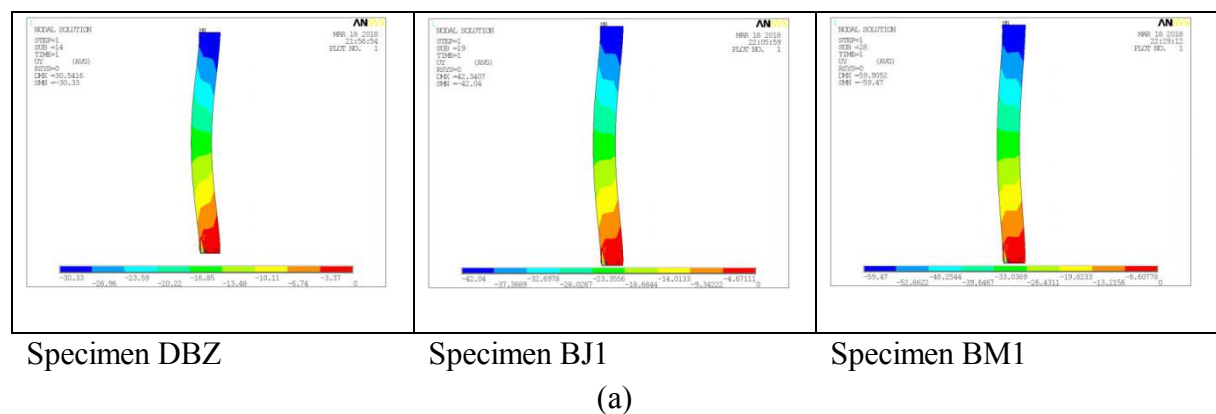
Fig. 6: Details of finite elements: (a) Solid45, (b) SHELL41.

The SHELL41 element in Fig. 6b was applied to mesh the BFRP fiber cloth. The element has large deformation and stress stiffening characteristics. The element is defined by four nodes and each node has three degrees of freedom to translate in the X, Y, and Z directions. The BFRP can be modeled with the SHELL41 element considering the variable thickness and strain strength of the BFRP cloth.

The geometric model meshed with a size of 25 mm of hexahedral mapping, which can satisfy the convergence and accuracy of the modeling results. Boundary and loading conditions were applied to the tested timber column, in which the two ends of the column are the hinged supports, model by restraining the essential nodes to stand for the simply-supported situation.

Comparison of experimental and FEA results

When calculating the models, the initial defect (initial bending) is considered. In this study, the initial defect is set as 1/1000 of the specimen length (i.e. 1.2 mm). The finite element results are shown in Fig. 7, 8, and 9.



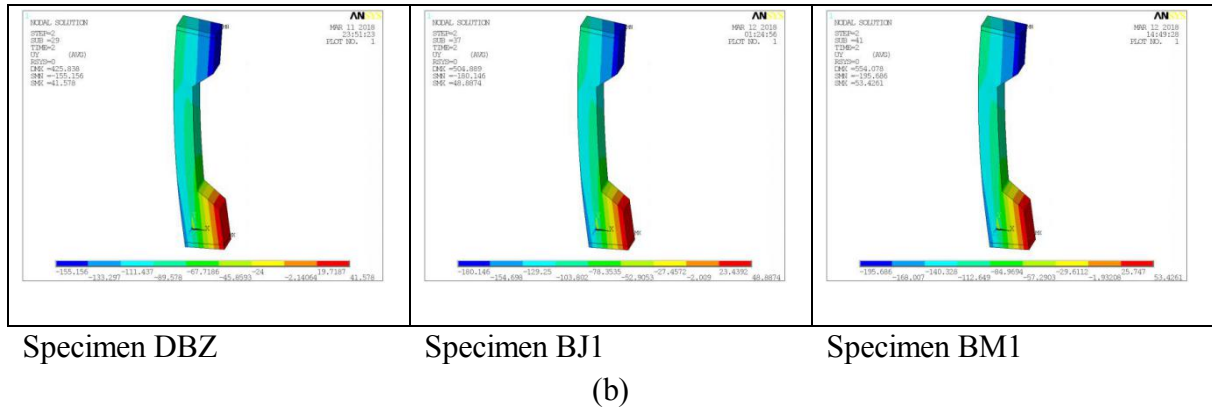


Fig. 7: Displacement nephogram of specimens: (a) axial compressive long columns, (b) eccentric compressive long columns.

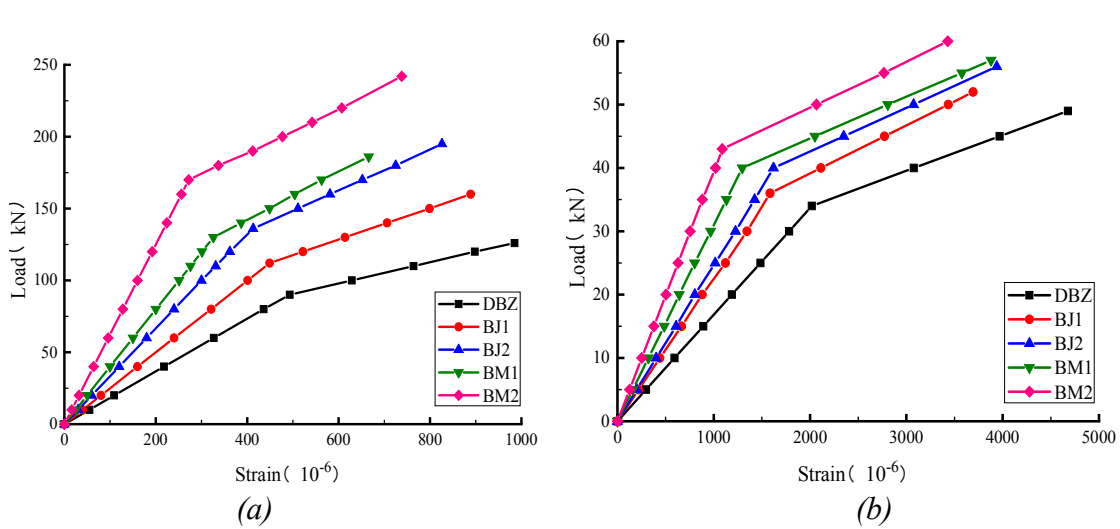


Fig. 8: Load-strain curves of the model columns: (a) axial compressive square columns, (b) eccentric compressive square columns.

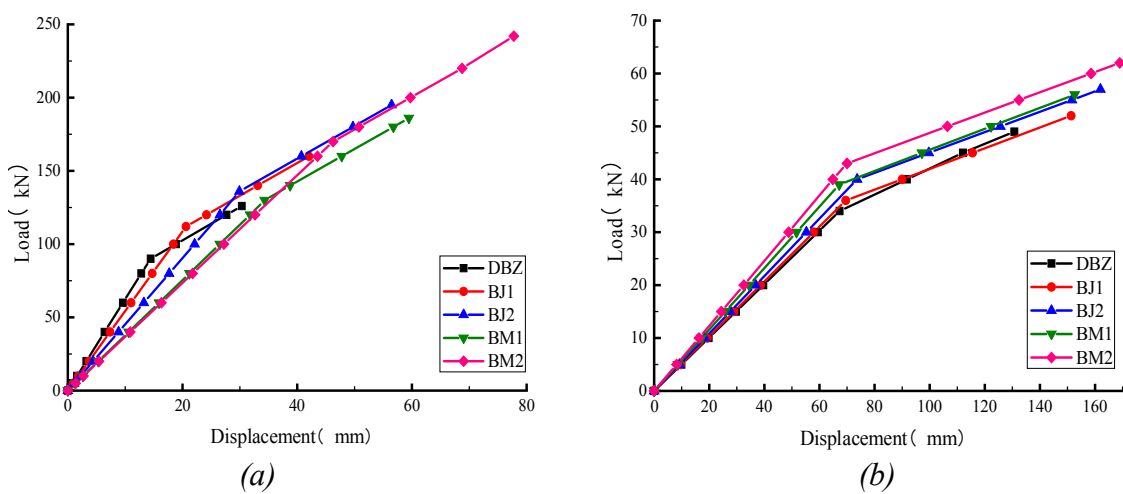


Fig. 9: Load-displacement curves of the model columns: (a) axial compressive square columns, (b) eccentric compressive square columns.

The comparison of the tests and numerical simulation results indicates the following: (1) According to the comparison between Figs. 2 and 7, the typical longitudinal bending failure is dominant in the timber column under axial compression, and the timber fiber on the compression side is crushed; the failure mode of the timber column under eccentric compression is mainly longitudinal bending. (2) The comparisons between Figs. 3, 4, 8 and 9 indicate the following: 1) For the timber column, the load-strain curve of each specimen is the same, which can be divided into two stages: the elastic and plastic stages. The displacement of the specimen in the elastic stage increases slowly and evenly with the increasing load. When the yield load is reached, the displacement increases rapidly until the ultimate load of each specimen is reached; 2) When the BFRP cloth is used to reinforce the timber columns with one layer or two layers of interval and one layer or two layers of full paste, the yield load of the columns under axial compression is increased by 22.2% or 51.1%, and 44.4% or 88.9%, respectively, and the ultimate load increases by 27.0% or 54.8% and 47.6% or 92.1%, respectively; 3) When the BFRP cloth is used to reinforce the columns with one or two layers of interval and one or two layers of full paste, the yield load of the eccentric compression columns increases by 5.9% or 17.6% and 14.7% or 23.5%, and the ultimate load of the eccentric compression columns increases by 6.1% or 16.3% and 14.3% or 22.4%, respectively.

The modulus of elasticity of each specimen is calculated according to the load-strain curves at the elastic stage and used as the index in the stiffness analysis (Tab. 7). The stiffness of the Xinjiang poplar columns strengthened by BFRP improved in different degrees compared with the unreinforced columns. The increased range for the axial compression long columns is 35.2%-96.4%, and 9.1%-67.4% for the eccentric compression long columns.

Tab. 7: Percentage of stiffness improvement.

Type	Number	Modulus of elasticity (MPa)	Percentage increase in stiffness compared to unreinforced (%)
Axial compression	DBZ	5097	-
	BJ1	6891	35.2
	BJ2	8122	59.3
	BM1	7891	54.8
	BM2	10011	96.4
Eccentric compression	DBZ	2083	-
	BJ1	2272	9.1
	BJ2	2487	19.4
	BM1	2815	35.1
	BM2	3486	67.4

CONCLUSIONS

In this study, the material model of the Xinjiang poplar was established by ANSYS, and the numerical model of the Xinjiang poplar square and eccentric long columns strengthened by BFRP was established. The load-strain, and load-displacement curves and the bearing capacity with the corresponding experiment results of each specimen were analyzed and compared. The main conclusions are as follows: (1) The experimental and numerical simulation results indicate that when the long square columns are reinforced with the same reinforcement method, their

bearing capacity and deformation capacity under axial compression is significantly better than those under eccentric compression. (2) The bearing capacity and stiffness of the columns strengthened by BFRP increased with the BFRP bonding area. The bearing capacity and stiffness from low to high follows the order unreinforced, 1 layer BFRP by interval paste, 2 layers BFRP by interval paste, 1 layer BFRP by full paste, and 2 layers BFRP by full paste.

ACKNOWLEDGMENTS

This study was conducted with the support of Natural Science Foundation Youth Regional Fund (51708479) and Xinjiang Uygur Autonomous Region (2019D01C028). The authors declare that they have no competing interests.

REFERENCES

1. Chen, L., Wen, W.D., Cui, H.T., 2013: Generalization of Hill's yield criterion to tension-compression asymmetry materials. *Science China Technological Sciences* 56(1): 89-97.
2. Chun, Q., Pan, J.W., 2011: Experimental study on mechanical properties of timber columns strengthened with CFRP/AFRP hybrid FRP sheets under axial compression. *Journal of Building Materials (in Chinese)* 14: 427-431.
3. Chen, Y.S., 1995: Maintenance guide of ancient buildings and wooden relics: Protection of timber structures in ancient buildings. China Forestry Press (in Chinese). Beijing, 180 pp.
4. GB/T1931, 2009: Methods for determination of wood moisture content.
5. GB/T1928, 2009: General test methods for wood physics and mechanics.
6. GB/T1933, 2009: Method for determination of the density of wood.
7. GB/T 1938, 2009: Method of testing in tensile strength parallel to grain of wood.
8. GB50005, 2017: Design standard for timber structures.
9. GB/T50329, 2012: Standard for test methods of timber structures.
10. Hao, C.R., 2004: Looking at the prospects of Chinese wood structure building from the development of Chinese and western wood structure buildings. Master's Thesis. Tsinghua University.
11. Johns, K.C., Lacroix, S., 2000: Composites reinforcement of timber in bending. *Canadian Journal of Civil Engineering* 27: 899-906.
12. Jeong, G.Y., Park, M.J., 2016: Evaluate orthotropic properties of wood using digital image correlation. *Construction and Building Materials* 113: 864-9.
13. Khelifa, M., Celzard, A., Oudjene, M., Ruelle, J., 2016: Experimental and numerical analysis of CFRP strengthened finger-jointed timber beams. *International Journal of Adhesion and Adhesions* 68: 283-297.
14. Khelifa, M., Lahouar, M.A., Celzard, A., 2015: Flexural strengthening of finger-jointed Spruce timber beams with CFRP. *Journal of Adhesion Science and Technology* 29: 2104-2116.

15. Lü, J., 2001: Studies on adaptability of *Populus bolleana* and other poplar trees in northwest Shanxi Province. *Journal of Forestry Research*12(1): 31-34.
16. Shen, G.L., 2013: *Mechanics of Composite Materials*. Tsinghua University Press (in Chinese), Beijing, 343 pp.
17. Shao, J.S., Xue, W.C., Liu, W.Q., Jiang, J.Q., Jiang, T., 2012: Calculation of axial compressive behavior of timber column laterally strengthened with FRP. *China Civil Engineering Journal* 45(8): 48-54.
18. Sha, Z., Zhu, X.D., 2012: Literature review of the research on wood structure strengthened by FRP. *Forest engineering (in Chinese)* 28: 57-61.
19. Shu, Q.L., Chen, C.Y., Zhang, H., Sun, Q., Zhang, X., 2005: Investigation of the species, occurrence character and control measures of poplar diseases in Anhui province. *Journal of Anhui agricultural sciences (in Chinese)*33(7) : 1193-1195.
20. Sotayo, A., Green, S., Turvey, G., 2016: Experimental and finite element (FE) modelling of timber fencing for benchmarking novel composite fencing. *Composite Structures* 158: 44-55.
21. Wang, X.M., 2007: *Numerical analysis of ANSYS engineering structure*. China Communications Press (in Chinese). Beijing, 554 pp.
22. Xu, Q.F., Zhu, L., 2007: An experimental study on partially-damaged wood columns re-paired and strengthened with CFRP. *China Civil Engineering Journal (in Chinese)* 8: 41-46.
23. Yang, Z.J., 2005: Wood structure-green energy-saving building structure. *Building Energy Conservation* 33(3): 50-52.
24. Zeng, D.P., 2002: Research status and control of poplar disease in China forest pests. *Forest Pest and Disease (in Chinese)* 21(1): 20-26.
25. Zhou, Q., Yan, W.M., Li, Z.B., Ji, J.B., 2009: Study on strengthening methods of timber structures of ancient buildings. *Earthquake Resistant Engineering and Retrofitting (in Chinese)* 31(01): 84-90.
26. Zhu, L., Xu, Q.F., 2009: Experimental research on short cracked timber columns strengthened with CFRP. *Building structure (in Chinese)* 11: 101-103.
27. Zeng, D., Zhou, X.Y., Cao, L., 2016: Research on the mechanical properties of larch glulam columns under axial compression. *Industrial Construction (in Chinese)* 46: 63-67, 71.

FENGXIA HAN*, QING LIU*, XIN GUO, MENG ZHANG, XIA HAN
XINJIANG UNIVERSITY
SCHOOL OF ARCHITECTURAL AND CIVIL ENGINEERING
XINJIANG, 830047
CHINA

*Corresponding authors: csjjj02@sina.com and liuqing2666@163.com

EFFECT OF SMOOTHING IN CALENDER AND HOT STAMPING MACHINE ON THE PROPERTIES OF COATED PAPERBOARDS FOR PRINTED ELECTRONICS

JURAJ GIGAC, MÁRIA FIŠEROVÁ
PULP AND PAPER RESEARCH INSTITUTE
SLOVAK REPUBLIC

(RECEIVED JULY 2021)

ABSTRACT

The methods of coated paperboards smoothing with a hot stamping machine using a smooth metal die and a conventional calender were compared. The printing roughness required for printing electrical and electronic components was achieved by both smoothing methods. The printing roughness of the coated paperboards decreased after hot stamping by 18 to 42% and after calendering by 22 to 41% depending on the grade of coated paperboard. The stiffness of coated paperboards decreased after hot stamping by only 4 to 21%, while by up to 38 to 51% after calendering. The ratio of specific stiffness and printing roughness of coated paperboards after hot stamping ranged from 2.5 to 8.1 $\text{mN}\cdot\mu\text{m}^{-2}$ and after calendering from 2.0 to 6.7 $\text{mN}\cdot\mu\text{m}^{-2}$. The stiffness of the coated paperboards decreased less after hot stamping, and that only in the printed electronics area, while after calendering the stiffness decreased significantly more in the whole profile. It can be assumed that packaging made from coated paperboards smoothed by hot stamping will have a lower weight and thus lower costs than packaging from calendered coated paperboards.

KEYWORDS: Coated paperboard, calendering, hot stamping, printing roughness, stiffness, surface free energy.

INTRODUCTION

Packaging is a big part of everyday life of people all around the world. According to a market survey carried out by Smithers Pira, in the next decade, the global packaging market will grow by almost 3% annually and will exceed \$1.2 trillion by 2030. The global packaging market has increased by 6.8% over the past 5 years. In addition, one of Unesco's Sustainable Development Goals for 2030 is the significant reduction of single-use plastics. Currently, trends such as

e-commerce and the digitization of packaging are emerging as the big challengers over the next 10 years; and while these trends are not new, the COVID-19 pandemic has accelerated their adoption. The market for paper packaging is seen as ready for the use of digital printing technology (<https://www.elempaque.com/temas/The-packaging-and-conversion-industry-in-2030-challenges-and-opportunities>).

Paperboards are currently one of the most commonly used packaging materials. Paperboards are layered products, which are made from primary or recycled fibres. Paperboards from primary fibres use different types of pulps in different parts of the layered structure. Outer layer consists of bleached chemical pulps and the middle ply consist of any type of mechanical pulp like TMP or CTMP, so that the final product has the necessary stiffness and bulk. Paperboards made from recycled fibres use deinked pulps from different types of waste paper in different part of the layered structure. Higher quality types of recycled fibres form the top layers, while the middle layers are made of lower quality recycled fibres. Stiffness of paperboards is important, because it correlates well with stacking strength of the final package, their purity is also important. Typical tests include internal bonding strength Scott Bond and surface strength IGT (Kiviranta 2000, Häggblom-Ahnger and Komulainen 2003).

Printed electronics has a great potential to offer biodegradable and recyclable solutions, which is a way forward to minimize the electronic waste caused by the ever-increasing number of disposable electronic devices (Tan et al. 2016, Zeng et al. 2017). Printed electronics are manufactured in a process of registering thin functional material (ink) layer combinations on a low-cost substrate that may be recycled and/or naturally degraded in the environment. Manufacture of electrical and electronic components by conventional and the state-of-the-art printing methods makes it possible to reduce the amount of waste materials as well as the fact that it is not necessary to use etching and masking (Maddipatla et al. 2020). Correspondingly, the manufacturing process is composed of three complementary stages: material selection, printing and post-printing (Wiklund et al. 2021).

Recently, the popularity of radio frequency identification has increased significantly, especially in connection with the printing of antennas on paper labels. Low-cost and recyclable paper substrates are being considered for various novel, value-added printed applications. This opens up the possibility of using RFID tags, for example, as part of packaging and other applications, for which the device has short life expectancy and is ultimately disposed. Literature on this subject has shown that manufacturing of RFID tags is not limited to a specific printing technology and gravure, screen, flexographic, inkjet, thermal-transfer and hot stamping printing technologies have been effectively used (Salmerón et al. 2014, Fernández-Salmerón et al. 2015, Voigt et al. 2010, Kavčič et al. 2014, Bollström 2013, Xiao et al. 2018, Gigac et al. 2021a,b, Lyashenko et al. 2012).

Hot stamping is the process of using heat and pressure to apply metallic ribbon or holograms to materials such as papers, paperboard, laminated board, plastics and corrugated board. A stamping ribbon includes a carrier film, a release layer, a layer of vacuum deposited metal such as aluminum or gold, silver, copper and chromium (Kipphan 2001), and a layer of heat activated adhesive. The layers are activated by heat and pressure by a die which causes the layers to

delaminate from the carrier film and adhere to a surface of a substrate in a predetermined electrically conductive pattern (Agca and Tasdemir 2016).

Different printed electronic devices require different substrate properties such as flexibility, high light transmittance, low surface roughness, light weight, low thermal expansion, stiffness, heat resistance, low cost and low thickness (Suganuma 2014). The print quality is affected by the surface roughness and porosity of the substrate (Morfa et al. 2016, Agate et al. 2018, Bollström et al. 2014).

The paper substrates have a rougher surface compared to the plastic film. The irregular surfaces and structural properties of conventional paper substrates allow their use only for electronic components with lower resolution requirements or printing quality. The surface of paper substrates can be modified by coating and smoothing. The smoothness of the surface depends on composition of coatings, the amount and layers of the coating, and the final surface finish. Depending on the composition of the coatings, properties such as smoothness, porosity, permeability and surface energy as well as optical properties (brightness and opacity) can be varied. The properties of the paper substrate can be adjusted to achieve also simultaneously functional properties such as water, oil and grease resistance, low vapor and gas permeability and flame retardation.

Coated paper substrates do not have a sufficient surface smoothness for good quality printed electronics, so it is necessary to reduce surface roughness and tighten the holes, which is conventionally achieved by calendering (Gullichsen and Paulapuro 1999). Surface smoothness of the paper substrate is achieved by exposing the fibre structure of the paper substrate to high pressure and temperature by heating the hard calender rolls and by pressing the rolls against one another such that a high nip pressure is obtained in the nip between the rolls. Due to these forces the fibres forming the web reach their glass transition temperature, and the deformation caused by the nip load is permanent. The gliding of the web surface against the roll surfaces may also give rise to alterations in fibre shape, thus enhancing the smoothing effect.

The longer nip dwell time and the reduction of the nip load during calendering can essentially reduce the structural changes in the paper web so that it is possible to reach a good surface quality at the same time. Long nip calendering resulted in a better volume and improved flexural resistance together with good surface properties compared with the common hard nip or soft nip calendering (Leinonen et al. 2001). The calender, which is also called a shoe calender, uses the same shoe roller technology as the press section of the paper machine. The long nip is formed between a heated hard roller and a soft belt of the shoe roller. The nip dwell time is not determined by the nip load when using a long nip calender but the needed dwell time is reached by the choice of a suitable shoe rail length.

Hot stamping (without ribbon) with smooth die can be used for smoothing surface of paper substrates before printing of electrical and electronics components. The smoothing effect of paper substrates depends on input parameters of hot stamping such as pressure time, pressure, temperature and surface roughness of the die.

The aim of the study of smoothing methods was to improve the printing roughness of coated paperboards to the level required for printed electronics and to compare hot stamping and calendering methods.

MATERIAL AND METHODS

Materials

Coated paperboard A is a single-sided white light folding boxboard (FBB2), which contains chemical thermo-mechanical pulp while the top layer consists of chemical pulp and the bottom side has a hint of yellow. *Coated paperboard B* is a single-sided coated white lined chipboard (WLC2) made from recycled fibres, the top layer is white, the inner layer and the bottom side are both gray. Its bulk was $1.43 \text{ cm}^3 \cdot \text{g}^{-1}$.

Coated paperboards C, D, E are single-sided coated white lined chipboards (WLC3) made from recycled fibres, the top layer is white, the inner layer and the bottom side are both gray. Their bulk were $1.12\text{-}1.29 \text{ cm}^3 \cdot \text{g}^{-1}$.

Methods

Calendering

The smoothing in the two-roll calender FUS 80 (Kleinewefers GmbH, Germany) was performed by one or two coated paperboard passes between a paper and a metal roller with a temperature of 80°C , a surface roughness R_a of $0.5 \mu\text{m}$ and a dwell time in pressure zone of 0.12 s at a pressure of 52 MPa . The coated side was in contact with the heated metal roller (Gigac et al. 2021a,b).

Hot stamping

The smoothing of coated paperboard in the HX-358 stamping machine (Ruian Hongxing Machinery Co., Ltd., China) was performed with a metal die with dimensions ($l \times w \times h$) $110 \times 70 \times 10 \text{ mm}$, surface roughness R_a $0.7 \mu\text{m}$, temperature 95°C and a dwell time 3 s at a pressure of 2.6 MPa .

Stiffness

Stiffness is defined as the paperboard's resistance to bending caused by a given applied force. Stiffness was determined as bending resistance (mN) by the two-point method, at a 15° bending angle, 38 mm wide strip, 10 mm distance of clamp and blade distance according to the standard ISO 2493-1 method on L&W Bending tester, app. 16 0, type 10-1 (Lorentzen & Wettre GmbH, Germany). The ratio of specific stiffness and printing roughness values ($\text{mN} \cdot \mu\text{m}^{-2}$), determined 48 hours after smoothing, was used to compare the effect of smoothing methods on the properties of coated paperboard. The specific stiffness ($\text{mN} \cdot \mu\text{m}^{-1}$) was calculated from the ratio of bending resistance and a thickness of coated paperboard.

Printing roughness

Printing roughness PPS (Parker Print-Surf) was calculated from the measured values of the average surface roughness OVS (Optical Variability of Surface) using the Eq. 1:

$$\text{PPS} = 0.103 \text{ OVS} + 0.192 \quad (1)$$

The surface roughness OVS of coated paperboards was evaluated by the photoclinometric method as optical variability of surface (Kasajová and Gigac 2013). Photoclinometry in the visible range of electromagnetic radiation is a promising method that may be used for on-line measurement of paper roughness. It describes the process of transformation of a 2D surface image into a map of various height levels. Incident light creates shadows (different gray levels). Paper is an anisotropic material, therefore it is necessary to obtain surface images from at least two directions: machine direction (MD) and cross direction (CD). The paperboards surface was scanned using charge-coupled device (CCD) Nikon Coolpix E4500 camera (Nikon Corporation, Japan) by inclined illumination at 10° from MD and CD. Optical variability of surface was calculated from image analysis using the program ImageJ.

Surface free energy

Initial and dynamic contact angle (CA), surface tension (γ) of liquids, as well as surface free energy (SFE) of coated paperboards were measured using the OCA 35 optical tensiometer (Dataphysics Instruments GmbH, Germany). Contact angle was measured by sessile drop method. Wetting time was recorded by a CCD camera at the sequence 20 frames s⁻¹ from the first contact of the liquid drop with the paperboards surface from 0.05 to 5 s. Contact angle was calculated as the average of 10 parallel measurements (Gigac et al. 2014a,b). Three testing liquids (diiodomethane, ethylene glycol, thiodiglycol) with different surface tensions were used to determine SFE of paperboards. SFE (ISO 19403-2: 2017), as well as its dispersive and polar components (ISO 19403-5: 2017), was calculated by the OWRK (Owens-Wendt-Rabel and Kaelble) method using values of initial CA.

RESULTS AND DISCUSSION

Printing, converting and finishing processes are used to increase the added value and improve the overall quality of paperboards packaging, which depend on the properties of the paperboards, in particular basis weight, thickness, stiffness, printing roughness and free surface energy.

Characteristics of coated paperboards

Coated paperboards A, B, C, D and E were selected to study the effects of smoothing with a calender and stamping machine. The basis weight of the coated paperboards ranged from 179 to 352 g m⁻², the thickness from 201 to 455 μ m and the bulk from 1.12 to 1.68 cm³ g⁻¹ (Tab. 1).

Besides basis weight and thickness, stiffness is especially important when choosing the right paperboard grade for packaging applications. Because paperboard is an anisotropic material, which means that the properties have a direction caused by the alignment of fibres in the machine direction (MD), it was necessary to make measurements of stiffness both in this direction and in the cross direction (CD).

The stiffness of coated paperboards in the MD direction ranged from 779 to 4510 mN and in the CD direction from 375 to 1937 mN (Tab. 1). As a result of this directional effect, the stiffness was approximately 55% higher in the MD direction than in the CD direction. From the stiffness

values in the MD and CD directions, the arithmetic mean stiffness value was calculated, which ranged from 577 to 3224 mN for the tested coated paperboards. Higher stiffness values were obtained for coated paperboards E and A with greater thickness (455 and 402 μm). In addition to thickness, the modulus of elasticity in the outer layers also affects the stiffness of the coated paperboard. Thickness affects stiffness more significantly as compared to modulus of elasticity.

Tab. 1: Properties of coated paperboards.

Sample	Grade	Basis weight	Thickness	Stiffness			Side	Printing roughness PPS	Surface energy		
				MD	CD	Average			SFE	SE disp	SE polar
		g m^{-2}	μm	mN	mN	mN	μm	mJ m^{-2}	mJ m^{-2}	mJ m^{-2}	
A	FBB2	239	402	2815	1665	2240	top	0.80	20.40	20.06	0.34
							bottom	4.80	27.39	27.20	0.19
B	WLC2	252	361	2238	1016	1627	top	1.17	37.21	36.40	0.80
							bottom	4.15	29.21	29.11	0.10
C	WLC3	179	201	779	375	577	top	1.21	28.62	28.50	0.12
							bottom	3.80	33.89	30.17	3.72
D	WLC3	228	264	1325	630	978	top	1.28	37.18	36.50	0.68
							bottom	4.05	34.12	32.10	2.02
E	WLC3	352	455	4510	1937	3224	top	1.63	36.33	35.85	0.48
							bottom	4.15	65.97	63.51	2.46

Long fibres from chemical pulp make it possible to have a good bonding and hence a high modulus of elasticity, and are most efficiently utilised in the outer plies of the paperboard. The type of fibre also influences thickness, for example mechanical fibre creates higher bulk when used in the centre plies. The various layers of fibres have to be well bonded together for optimum utilisation of the fibre characteristics.

Printing roughness and surface energy of paper substrates are important in terms of print quality. Each paper has a unique structure in terms of surface roughness, porosity, and surface energy that are the result of manufacturing technology (Gigac et al. 2014a). In Tab. 1, the printing roughness of the coated paperboards are presented, which range from 0.80 to 1.63 μm on the top side and from 3.80 to 4.80 μm on the bottom side. The coated paperboard A had the lowest printing roughness on the top side of 0.80 μm , while the coated paperboard C had the lowest printing roughness on the bottom side of 3.80 μm .

The surface properties of printing substrates and inks determine the success of all printing processes, whether they are conventional or digital printing technologies, because wetting and spreading of printing inks on the surface and good adhesion of the printed layer are determined by these properties. The free surface energy of substrates and inks determines their cohesive and adhesive energy. The difference between the adhesive and cohesive energies is expressed by the Harkinson spreading coefficient, which determines whether (or not) the ink wets the surface of the substrate (Kaplanová et al. 2009). Low surface dispersive energy of papers negatively influences wetting and spreading inkjet inks on surface, print density and colour gamut (Gigac et al. 2014b). Techniques such as corona, UV ozone, sintering, plasma, and laser treatments are employed to modify the surface energy of the substrates (Ali et al. 2018, Gerhard et al. 2012). In printed electronics, it is always desirable to have the surface energy of the substrate at least

above 7-10 mJ·m⁻² compared to surface tension of the ink to get good wetting and adhesion characteristics (Turkani et al. 2018).

While variations in printed layers are relevant for graphic papers only if they can be perceived by the human eye, for printed electronics papers, detailed reproduction of structural elements is essential for the reproducibility and reliability of electrical properties of the printed layers (Fugmann et al. 2006).

Surface free energy, dispersive and polar component of surface energy of coated paperboards are given in Tab. 1. The surface free energy (SFE) of the coated paperboards ranged from 20.4 to 37.2 mJ·m⁻² for the top side and from 27.4 to 66.0 mJ·m⁻² for the bottom side. The coated paperboards B and D had the highest surface free energy of the top side, while the coated paperboard E had the highest surface free energy of the bottom side. The dispersive component of surface energy of the coated paperboards ranged from 20.1 to 36.5 mJ·m⁻² for the top side and from 27.2 to 63.5 mJ·m⁻² for the bottom side. The coated paperboard D had the highest dispersive component of surface energy of the top side, while the coated paperboard E had the highest dispersive component of surface energy of the bottom side. The polar components of the surface energy of the coated paperboards ranged from 0.13 to 0.80 mJ·m⁻² for the top side and from 0.10 to 3.72 mJ·m⁻² for the bottom side (Tab. 1). The coated paperboard B had the highest polar component of surface energy of the top side, while the coated paperboard E had the highest polar component of surface energy of the bottom side.

The effect of calendering and hot stamping on coated paperboards properties

The quality of printed electrical and electronic components is affected mostly by printing roughness of the paper substrate. Smoothing the coated paperboard in a calender commonly used in the paper industry to reduce printing roughness was compared with smoothing in a stamping machine.

Changes in printing roughness, thickness and stiffness of coated paperboards (Tab. 1) after smoothing by calendering (C1 or C2) and hot stamping (HS) methods are shown in Figs. 1-5. Procedures C1 or C2 indicate 1 or 2 passes of coated paperboard in a nip between calender rollers. There are three graphs in each figure. The graphical representation of the relationship between print roughness and thickness is located at the top left of each figure, the relationship between average stiffness and thickness at the top right, and the relationship between printing roughness and average stiffness in the center at the bottom. The measurements of the evaluated properties in Figs. 1-5 were performed 2 and 24 hours after smoothing.

Coated paperboard A with a thickness of 402 µm, an average stiffness of 2025 mN and a printing roughness of 0.80 µm was smoothed in a calender using procedures C1 and C2 and in a hot stamping machine HS (Fig. 1). After smoothing in a calender by the C2 procedure, the original coated paperboard A thickness was reduced to 268 µm, the average stiffness to 1125 mN and the printing roughness to 0.63 µm. After hot stamping, the thickness of the original coated paperboard A was reduced to 297 µm, the average stiffness to 1535 mN and the printing roughness to 0.64 µm. A comparison of the properties after 24 hours shows that after calendering the thickness decreased by 34%, the average stiffness decreased by 44% and the

printing roughness by 22% and after hot stamping the thickness decreased by 26%, the average stiffness decreased by 24% and the printing roughness by 21%.

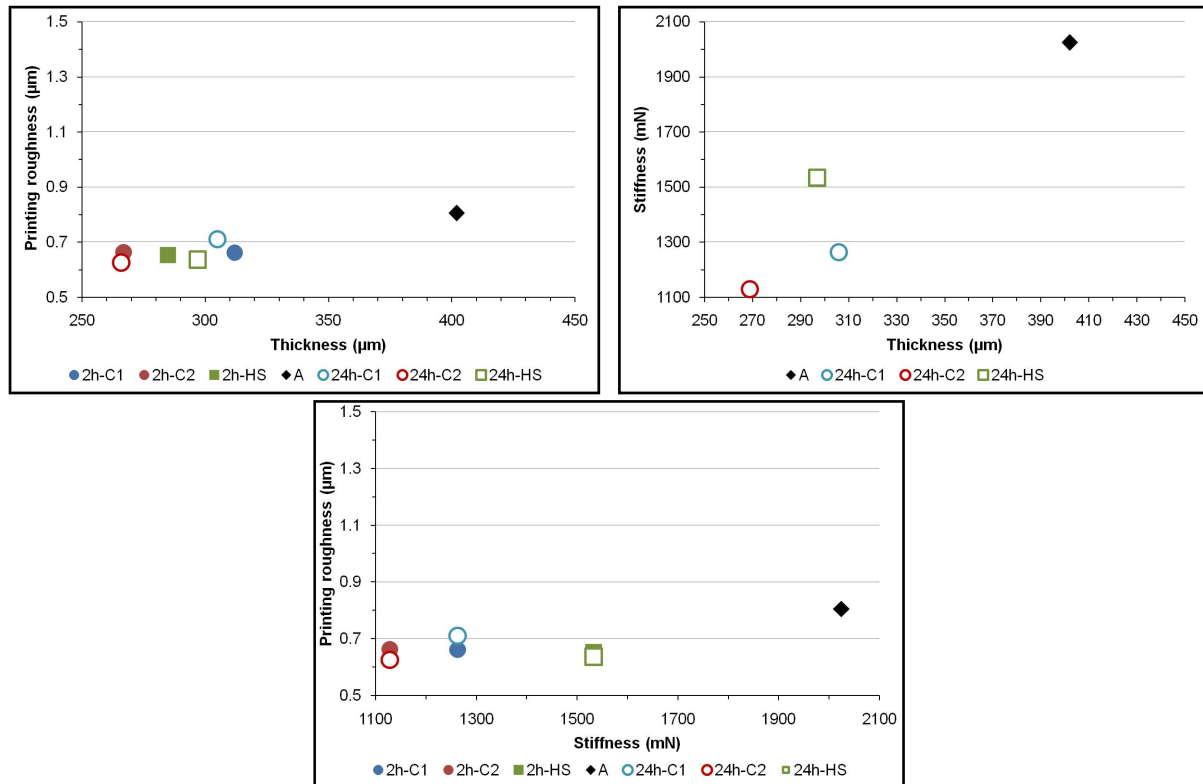


Fig. 1: The effect of smoothing by calendering and hot stamping on the relationships between thickness, printing roughness and stiffness of coated paperboard A.

Coated paperboard B with a thickness of 356 μm, an average stiffness of 1595 mN and a printing roughness of 1.17 μm was smoothed in a calender using procedures C1 and C2 and in a hot stamping machine HS (Fig. 2). After smoothing in a calender by the C2 procedure, the thickness of the original coated paperboard B was reduced to 241 μm, the average stiffness to 775 mN and the printing roughness to 0.85 μm. After hot stamping, the thickness of the original coated paperboard B decreased to 306 μm, the average stiffness to 1260 mN and the printing roughness to 0.94 μm. A comparison of the properties after 24 hours shows that after calendering the thickness decreased by 33%, the average stiffness decreased by 51% and the printing roughness by 28% and after hot stamping the thickness decreased by 14%, the average stiffness decreased by 21% and the printing roughness by 18%.

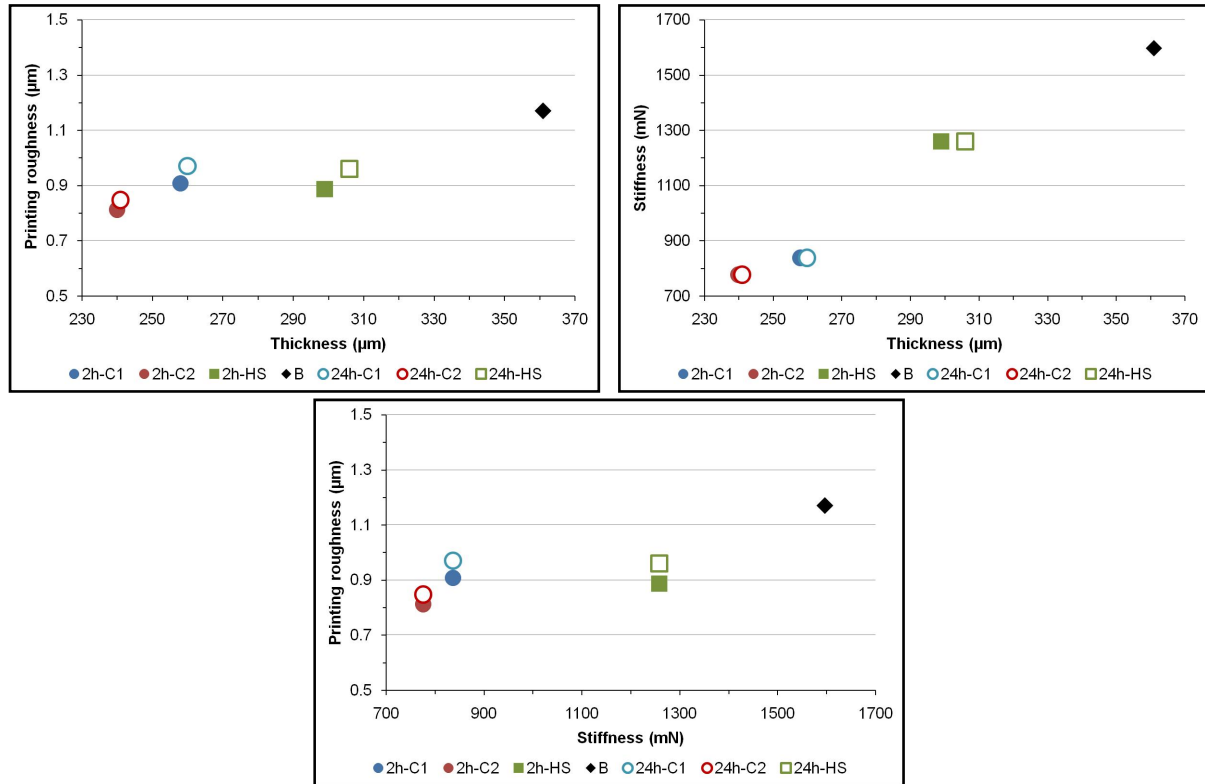
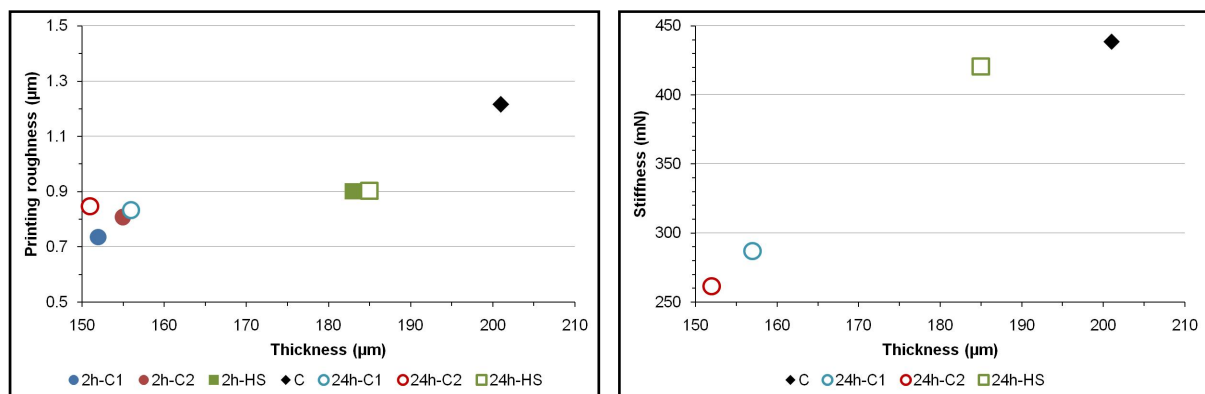


Fig. 2: The effect of smoothing by calendering and hot stamping on the relationships between thickness, printing roughness and stiffness of coated paperboard B.

Coated paperboard C with a thickness of 201 μm, an average stiffness of 440 mN and a printing roughness of 1.21 μm was smoothed in a calender using procedures C1 and C2 and in a hot stamping machine HS (Fig. 3). After smoothing in a calender by the C2 procedure, the thickness of the original coated paperboard C was reduced to 151 μm, the average stiffness to 260 mN and the printing roughness to 0.85 μm. After hot stamping, the thickness of the original coated paperboard C was reduced to 183 μm, the average stiffness to 420 mN and the printing roughness to 0.90 μm. It follows that after calendering, the thickness decreased by 25%, the average stiffness decreased by 40% and the printing roughness by 30%, and after hot stamping, the thickness decreased by 8%, the stiffness decreased by 4% and the printing roughness by 26%.



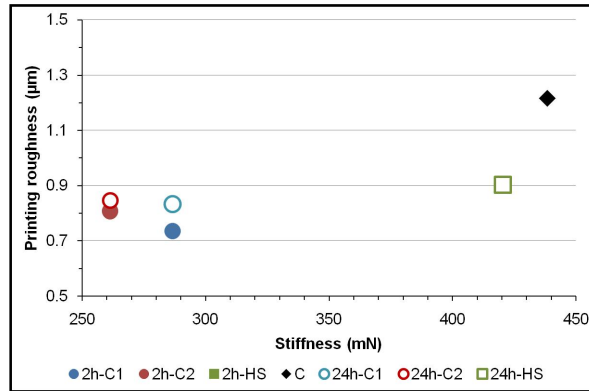


Fig. 3: The effect of smoothing by calendering and hot stamping on the relationships between thickness, printing roughness and stiffness of coated paperboard C.

Coated paperboard D with a thickness of 264 µm, an average stiffness of 835 mN and a printing roughness of 1.28 µm was smoothed in a calender using procedures C1 and C2 and in a hot machine HS (Fig. 4). After smoothing in a calender by the C2 procedure, the thickness was reduced to 191 µm, the average stiffness to 515 mN and the printing roughness to 0.84 µm. After hot stamping, the thickness of the original coated paperboard D was reduced to 240 µm, the average stiffness to 795 mN and the printing roughness to 0.75 µm. It follows that after calendering, the thickness decreased by 28%, the average stiffness decreased by 38% and the printing roughness by 35%, and after hot stamping the thickness decreased by 9%, the average stiffness decreased by 5% and the printing roughness by 42%.

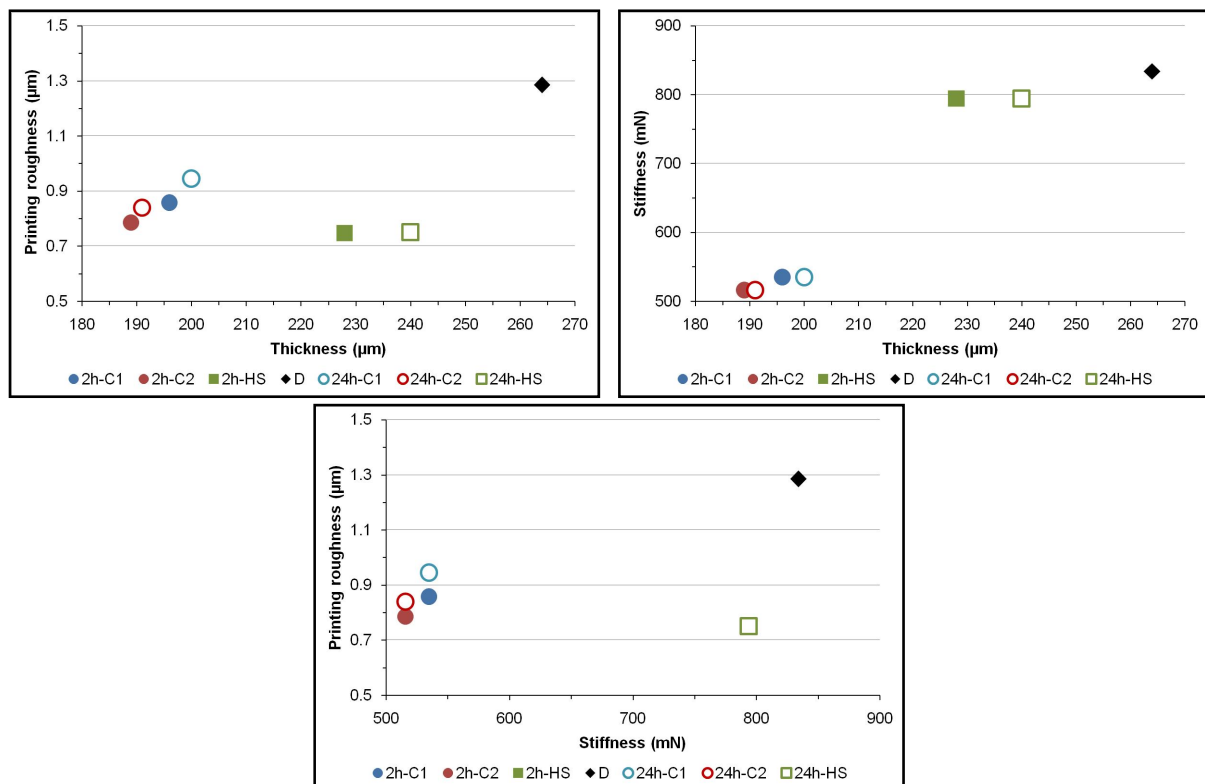


Fig. 4: The effect of smoothing by calendering and hot stamping on the relationships between thickness, printing roughness and stiffness of coated paperboard D.

Coated paperboard E with a thickness of 455 μm , an average stiffness of 3130 mN and a printing roughness of 1.63 μm was smoothed in a calender using procedures C1 and C2 and in a hot stamping machine HS (Fig. 5). After smoothing in a calender by the C2 procedure, the thickness of the original coated paperboard E was reduced to 336 μm , the average stiffness to 1805 mN and the printing roughness to 0.83 μm . After hot stamping, the thickness of the original coated paperboard E decreased to 407 μm , the average stiffness to 2825 mN and the printing roughness to 1.02 μm . It follows that after calendering, the thickness decreased by 26%, the average stiffness decreased by 42% and the printing roughness by 41%, and after hot stamping, the thickness decreased by 11%, the average stiffness decreased by 10% and the printing roughness by 28%.

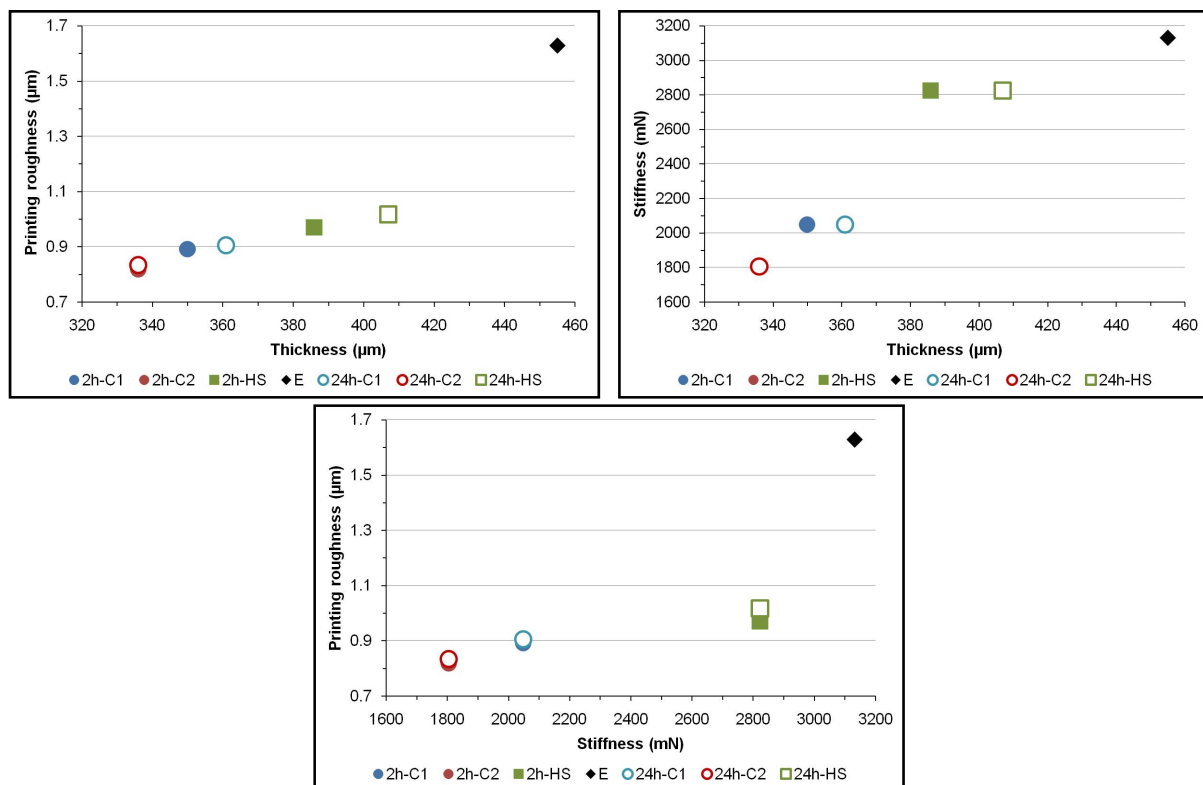


Fig. 5: The effect of smoothing by calendering and hot stamping on the relationships between thickness, printing roughness and stiffness of coated paperboard E.

Calendering of the original coated paperboards A, B, C, D and E was carried out at a temperature of 80°C and a dwell time in the pressure zone of 0.12 s at a pressure of 52 MPa, while the smoothing with a hot stamping machine took place at a temperature of 95°C and a dwell time in the pressure zone of 3 s at a pressure of 2.6 MPa. For comparison of the effect of both smoothing methods, carried out under different conditions, on the properties of the original coated paperboards, the specific stiffness per unit printing roughness parameter was used, calculated from the ratio of specific stiffness and printing roughness from values determined 48 hours after smoothing. A comparison of the procedures of smoothing C1 and C2 in the calender and in the hot stamping machine HS on the ratio of specific stiffness and printing roughness of original coated paperboards is shown in Fig. 6. Smoothing in the calender using the

C1 procedure did not significantly increase the ratio of specific stiffness and printing roughness, therefore the original coated paperboards were smoothed two times in the calender under the same conditions (C2 procedure). The hot stamping method reduces the printing roughness of the original coated paperboards while achieving a higher thickness and stiffness compared to the calendering method. For this reason, the highest values of the ratio of specific stiffness and printing roughness were achieved with smoothing with a hot stamping method of the original coated paperboards.

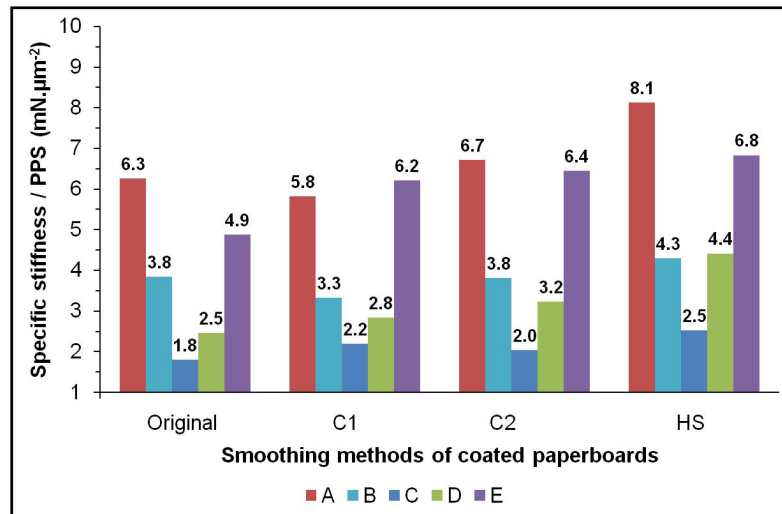


Fig. 6: The effect of smoothing methods of the original coated paperboards on the ratio of specific stiffness and printing roughness.

For the converter or end user, stiffness is a critical parameter which has a significant influence on conversion and packaging line efficiency. The maximum stiffness has to be achieved at the lowest possible grammage and thereby cost, whilst maintaining a consistent and uniform level.

When smoothing in a hot stamping machine, the thickness and stiffness of the coated paperboards were reduced only in place of a smooth metal die, while after smoothing with a calender in the whole profile. From the above it can be concluded that it will be possible to produce lighter packaging from coated cardboard smoothed by hot stamping.

CONCLUSIONS

The printing roughness of the coated paperboards to the level required for the printing of electrical and electronic components was achieved by smoothing in a calender and in a hot stamping machine. The advantage of the hot stamping machine compared to the calender was to achieve a higher stiffness of the smoothed coated paperboards with the same printing roughness.

Calendering reduces stiffness in the whole profile of the coated paperboards, while the hot stamping machine smoothed only a certain area, which is needed for printing electrical and electronic components. From the above it can be concluded that the coated paperboards smoothed by hot stamping have the same stiffness at a lower basis weight than those calendered.

Therefore, it will be possible to produce a packaging with a lower weight from coated paperboards smoothed by hot stamping.

In addition, calendering causes a reduction of the friction coefficient in the whole profile of the coated paperboards, which is often the cause of deteriorated stackability of packaging.

Direct printing of electrical and electronic components on coated paperboards smoothed by hot stamping can be an interesting alternative to the technology of gluing smart labels to packaging.

ACKNOWLEDGEMENTS

This work was supported by Slovak Research and Development Agency under contract No. APVV-19-0029.

REFERENCES

1. Agate, S., Joyce, M., Lucia, L., Pal, L., 2018: Cellulose and nanocellulose-based flexible-hybrid printed electronics and conductive composites. A review. *Carbohydrate Polymers* 198: 249-260.
2. Agca, M.A., Tasdemir, M., 2016: Investigation of hot stamping parameters in up/down machining on ABS materials under quality purposes of different stamping processes. *ICAMS 2016 – 6th International Conference on Advanced Materials and Systems*. Vol. 1.
3. Ali, S., Maddipatla, D., Narakathu, B.B., Chlaihawi, A.A., Emamian, S., Janabi, F., Bazuin, B.J., Atashbar, M.Z., 2018: Flexible capacitive pressure sensor based on pdms substrate and Ga-In liquid metal. *IEEE Sensors Journals* 19: 97-104.
4. Bollström, R., 2013: Paper for printed electronics and functionality. Ph.D. Thesis, Abo Akademi University, Turku, Finland, 100 pp.
5. Bollström, R., Pettersson, F., Dolietis, P., Preston, J., Österbacka, R., Toivakka, M., 2014: Impact of humidity on functionality of on-paper printed electronics. *Nanotechnology* 25(9): 094003.
6. Fernández-Salmerón, J., Rivadeneyra, A., Martínez-Martí, F., Capitán-Vallvey, L.F., Palma, A.J., Carvajal, M.A., 2015: Passive UHF RFID tag with multiple sensing capabilities. *Sensors* 15(10): 26769-26782.
7. Fugmann, U., Kempa, H., Preissler, K., Bartzsch, M., Zillger, T., Fischer, T., Schmidt, G., Brandt, N., Hahn, U., Huebler, A.C., 2006: Printed electronics is leaving the laboratory. *MST News* (2): 13-16.
8. Gerhard, C., Roux, S., Brückner, S., Wieneke, S., Viol, W., 2012: Low-temperature atmospheric pressure argon plasma treatment and hybrid laser-plasma ablation of barite crown and heavy flint glass. *Applied Optics* 51: 3847-3852.
9. Gigac, J., Kasajová, M., Stankovská, M., 2014a: The influence of paper surface energy on multicolor offset print mottling. *Tappi Journal* 13(2): 55-64.
10. Gigac, J., Stankovská, M., Letko, M., Opálená, E., 2014b: Effect of base paper properties on inkjet print quality. *Wood Research* 59(4): 717-730.

11. Gigac, J., Fišerová, M., Hegyi, S., 2021a: Comparison of thermal transfer and inkjet Printing of UHF RFID tag antennas on paper substrate. *Wood Research* 66(1): 71-84.
12. Gigac, J., Fišerová, M., Kováč, M., Hegyi, S., 2021b: Passive UHF RFID tags with thermal-transfer-printed antennas. *Materials and Technology* 55(2): 277-282.
13. Gullichsen, J., Paulapuro, H., 1999: Papermaking science and technology, Papermaking Part 3, Finishing. Book 10, Chapter 1, Eds. Juha Ehrola, Ari Hernesniemi, Harri Kuosa, Markku Kyytsönen, Pekka Linnonmaa, Tapio Maenpaa, Reijo Pietikainen, Rob Stapels, Mikko Tani and Hannu Vuorikari, (book 10), Published by Fapet Oy, Helsinki, Finland. Pp 14-140.
14. Häggblom-Ahnger, U., Komulainen, P., 2003. Paperin ja Kartongin Valmistus, Helsinki: Opetushallitus. Pp 1-279.
15. Kaplanová, M., Srový, T., Držková, M., Hejduk, J., Svoboda, J., Holická, H., Dohnal, M., Vališ, J., Veselý, M., Otáhalová, L., Panák, O., 2009: Polygrafické materiály (Polygraphic materials) (in Slovak). In: Pp 123-174, *Moderní polygrafie. Svaz polygrafických podnikatelů*.
16. Kasajová, M., Gigac J., 2013: Comparison of print mottle and surface topography testing methods. *Nordic Pulp Paper Research Journal* 28(3): 443–449.
17. Kavčič, U., Pivar, M., Dokič, M., Svetec, D.G., Pavlovič, L., Muck, T., 2014: UHF RFID tags with printed antennas on recycled papers and cardboards. *Materials and Technology* 48(2): 261-267.
18. Kipphan, H., 2001: Technologies and production methods. In: *Handbook of print media*. Springer. Pp 4-1173. DOI:10.1007/978-3-540-29900-4 (eBook).
19. Kiviranta, A., 2000: Paperboard Grades. *Paper and Board Grades*. Helsinki, Finland: Fapet Oy. Pp 55-75.
20. Leinonen, H., Lares, M., Tani, M., 2001: Long nip calendaring. Quality and productivity. *Wochenblatt für Papierfabrikation* 129(20): 1320-1324.
21. Lyashenko, A., Salun, L., Dörsam, E., 2012: Hot stamping technology for functional printing. *Advances in Printing and Media Technology*. In: *Proceedings of the 39th International Research Conference of iarigai Ljubljana, Slovenia, September 2012, Vol. XXXIX: 64-74*.
22. Maddipatla, D., Narakathu, B.B., Atashbar, M., 2020: Recent Progress in Manufacturing Techniques of Printed and Flexible Sensors. A Review. *Biosensors* 10(12): 199-222.
23. Morfa, A., Rödlmeier, T., Jürgensen, N., Stolz, S., Hernandez-Sosa, G., 2016: Comparison of biodegradable substrates for printed organic electronic devices. *Cellulose* 23(6): 3809–3817.
24. Salmerón, J.F., Molina-Lopez, F., Briand, D.; Ruan, J.J., Rivadeneyra, A., Carvajal, M.A., Capitán-Vallvey, L.F., de Rooij, N.F., Palma, A.J., 2014: Properties and printability of inkjet and screen-printed silver patterns for RFID antennas. *Journal of Electronic Materials* 43: 604-617.
25. Suganuma, K., 2014: Introduction to printed electronics. Springer Science & Business Media: Berlin/Heidelberg, Germany, 74: 1-124.

26. Tan, M.J., Owh, C., Chee, P.L., Kyaw, A.K.K., Kai, D., Loh, X.J., 2016: Biodegradable electronics: Cornerstone for sustainable electronics and transient applications. *Journal of Materials Chemistry C*(4): 5531-5558.
27. Turkani, V.S., Maddipatla, D., Narakathu, B.B., Bazuin, B.J., Atashbar, M.Z., 2018: A carbon nanotube based NTC thermistor using additive print manufacturing processes. *Sensors and Actuators A: Physical* 279: 1–9.
28. Voigt, M.M., Guite, A., Chung, D.Y., Khan, R.U.A., Campbell, A.J., Bradley, D.D.C., Meng, F., Steinke, J.H.G., Tierney, S., McCulloch, I., Penxten, H., Lutsen, L., Douheret, O., Manca, J., Brockmann, U., Sönnichsen, K., Hülsenberg, D., Bock, W., Barron, C., Blanckaert, N., Springer, S., Grupp, J., Mosley, A., 2010: Polymer field-effect transistors fabricated by the sequential gravure printing of polythiophene, two insulator layers, and a metal ink gate. *Advanced Functional Materials* 20(2): 239-246.
29. Wiklund, J., Karakoç, A., Palko, T., Yiğitler, H., Ruttik, K., Jäntti, R., Paltakari, J., 2021: A review on printed electronics: Fabrication methods, inks, substrates, applications and environmental impacts. *Journal of Manufacturing and Materials Processing* 53: 89-124.
30. Xiao, G., Zhang, Z., Fukutani, H., Tao, Y., Lang, S., 2018: Improving the Q -factor of printed HF RFID loop antennas on flexible substrates by condensing the microstructures of conductors. *IEEE Journal of Radio Frequency Identification*.
31. Zeng, X., Yang, C., Chiang, J.F., Li, J., 2017: Innovating e-waste management: From macroscopic to microscopic scales. *Science of the Total Environment* 575: 1-5.

JURAJ GIGAC*, MÁRIA FIŠEROVÁ
PULP AND PAPER RESEARCH INSTITUTE
DÚBRAVSKÁ CESTA 14
841 04 BRATISLAVA
SLOVAK REPUBLIC

*Corresponding author: gigac@vupc.sk

EFFECT OF OPEN-HOLES ON MECHANICAL PROPERTIES OF WOOD COMPOSITE MATERIALS

SIMONA GAURONSKAITĖ, VAIDA DOBILAITĖ, MILDA JUCIENĖ
KAUNAS UNIVERSITY OF TECHNOLOGY
LITHUANIA

DARIUS ALBREKTAS
KAUNAS UNIVERSITY OF APPLIED SCIENCES
LITHUANIA

(RECEIVED MAY 2021)

ABSTRACT

A few variations of open-holes in wood-based pieces, particle board and plywood were modeled in this article. The modulus of elasticity and the coefficient of damping for these pieces were determined using static and dynamic methods and the effect of holes of different quantity and size on mechanical properties were evaluated. As regards to wood particle boards, it was found that the modulus of elasticity decreased to 10% after drilling holes, and the coefficient of damping increased to 13%. With regard to plywood pieces these changes were up to 14.5% and up to 21.5%, respectively.

KEYWORDS: Wood particle board, plywood, open-hole, modulus of elasticity, coefficient of damping, mechanical properties.

INTRODUCTION

Pieces of furniture, construction and other structures made of wood and wood-based materials are joined together using a variety of universal or special fittings and for this purpose, in many cases, various holes, open-holes, and notches are drilled in the pieces. Most of pieces are various bending, tensile, compressive and other mechanical load-carrying structures. Wooden buildings have heavy-duty beams that require holes to be drilled to allow plumbing, electrical wiring and other technical units to pass through. Making any open-holes in a wood element causes change in concentration of tensile and compressive stresses around the open-hole, which

can lead to deterioration in the mechanical properties of the pieces and various defects that impair their properties.

Research of laminated veneer lumber beams have shown that cutting a sufficiently large open-hole (the ratio of the hole diameter to the beam width is 0.4, 0.5 and 0.6) in the beam reduces its strength by 30-52% (Ardalany et al. 2013), and even by 50-69% (Zhang et al. 2018).

In order to reduce such a significant loss of strength properties, as well as to stop or prevent the formation or spread of cracks at the open-hole, various methods of beam reinforcement around the open-hole are used, such as the use of nailed or glued plywood sheets, steel panels, threaded rods and glue-in bolts. The scientific works analyze the efficiency of these methods depending on the shape of the open-hole dimensions, parameters of reinforcement method and other structural features (Aldalany et al. 2013, Zhang et al. 2018, Aldalany et al. 2012, Aicher 2011, Tu et al. 2016, Danzer et al. 2016, Aicher and Höfflin 2008).

Research showed that deterioration of mechanical properties of the specimens is relevant not only in the case of a large diameter open-hole. It was found that open-holes Ø13, Ø16 and Ø20 mm lead to reduction of bending strength by 5 -17% fir specimens, and by 13 - 23% (Chen et al. 2019) for Douglas fir wood specimens. The research of wood particle board, particle board, oriented strandboard and plywood boards has shown, that the values of bending test properties decrease due to occurrence of open-holes (Yerlikaya and Karaman 2020). However, there are few works concerning research of the effect of smaller diameter open-holes on the change in mechanical properties of wood pieces.

It is important to note that the universal mechanical testing machine and standard test methodologies were used (Chen et al. 2019, Yerlikaya and Karaman 2020) to investigate the effect of open-holes on the mechanical properties of wood pieces. Specimens of Japanese cedar and Japanese cypress wood were examined using ultrasonic waves (Mori et al. 2016). After drilling open-holes in the specimens, MOE and MOR of the specimens were found to decrease. The obtained results revealed that such a non-contact and non-destructive method is suitable for evaluation of mechanical properties of wood elements with open-holes.

An analysis of literature review showed that there is a lack of studies regarding changes in mechanical properties of wood used in the furniture industry after drilling holes, because in this area, e.g. the structural solutions used in furniture frames manufacturing (shape and dimensions of the open-hole, location in the element, ratio of dimensions of the open-hole/piece, etc.) are very different from those relevant in construction or other areas. In addition, it is important to analyze suitability of non-destructive methods for determination of mechanical properties of wood pieces with open-holes.

The objective of the thesis is to determine the effect of size and location of open-holes on the mechanical properties of wood composite materials.

MATERIAL AND METHODS

Pieces made of glued plywood and wood particle board were used for the research. The research involved a multipurpose plywood intended for application in closed, dry rooms, flat sheets, without finishing coat. Particle boards are a multipurpose, three-layer board with a

density of 640 - 655 kg m⁻³ and a humidity of 9.8 – 10.7%. Plywood 690 - 710 kg m⁻³ and 9.8 - 10.4%, resp. The research involved 50 particle boards and 50 plywood specimens with dimensions of 500 x 100 x 15 mm. The moisture content of the specimens was determined according to the EN 13183-2 standard using a Gann Hydromette moisture meter. The density was determined according to the EN 323 standard, the specimens were weighed using an electronic scale to the nearest 0.01 g and measured with a caliper (length – to the nearest 0.05 mm, thickness and width – to the nearest 0.02 mm). The dynamic modulus of elasticity, the coefficient of damping of the specimens were determined using the original methodology and equipment (Fig. 1) (Albrektas and Vobolis 2003, Timoshenko et al. 1985). The studies were performed at a frequency of 20-2000 Hz.

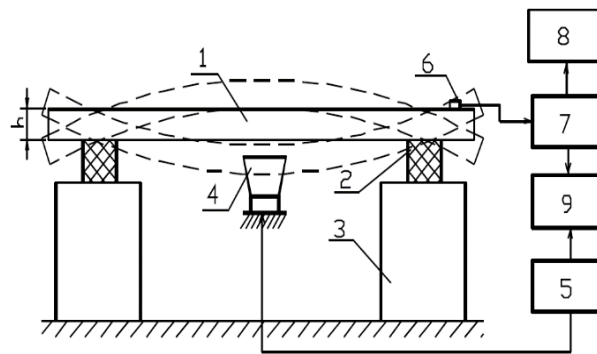


Fig. 1. The scheme of the test stand: 1 – specimen; 2 – vibration damping material (foam rubber); 3 – massive supports; 4 – loudspeaker; 5 – vibration generator; 6 – sensor; 7 – measuring instrument; 8 – oscilloscope; 9 – phase meter.

A beam-shaped body, which vibrates at a resonance (natural) frequency, depending on its anchorage, curves to a corresponding shape (mode), which in many cases is close to the mode of a theoretical isotropic beam. The *MOE* was calculated based on Eq. 1, the viscous properties (coefficient of damping) of studied specimens were evaluated based on Eq. 2:

$$E = \frac{f_{rez}^2 4\pi^2 \rho s l^4}{IA^2} \quad (1)$$

where: E – modulus of elasticity, f_{rez} – frequency of transverse vibrations, ρ – density of wood, s – cross-sectional area, l – specimens length, I – cross-sectional moment of inertia, A – method of fastening represented by a coefficient.

$$tg\delta \approx \frac{\Delta f}{f_{rez}} \quad (2)$$

where: f_{rez} – frequency of transverse vibrations, Δf – frequency bandwidth when amplitude of vibrations decreases by 0.7 times.

The static modulus of elasticity was determined in accordance to the EN 310 standard. Bending test was performed using a universal testing machine BTI-FB 050 TN (Zwick). Prior to

testing, specimens were conditioned for 14 days at $(20 \pm 2)^\circ\text{C}$ and $(55 \pm 5)\%$ relative humidity. The conditioned plywood and wood particle board specimens were randomly segregated into five subgroups, BI, BII, BIII, BIV, BV, and PI, PII, PIII, PIV, PV, resp. Subsequently, the dynamic modulus of elasticity and coefficient of damping of all specimens were determined using the original methodology. Open-holes were then drilled in the specimens of subgroups II to V. Schemes of these specimens are shown in Fig. 2.

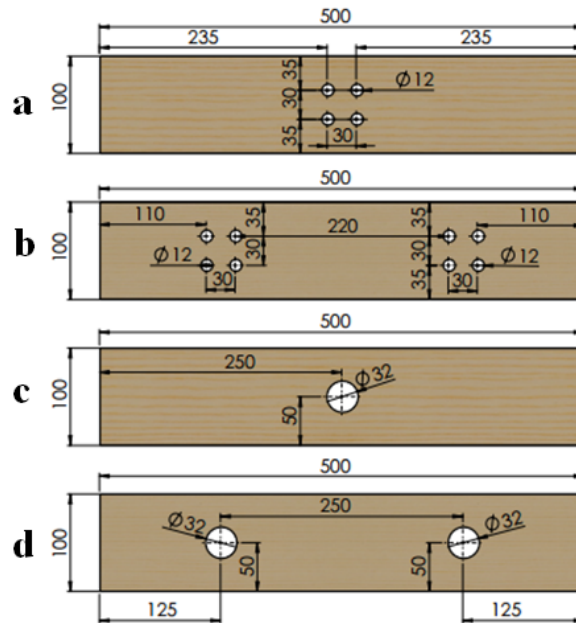


Fig. 2: Specimen drilling schemes: specimen group a – II, b – III, c – IV, d – V.

After drilling, the static, dynamic modulus of elasticity and the coefficient of damping of the specimens of subgroups II - V were determined repeatedly. Fig. 3 shows the position of the specimens of subgroups II - V during bending when the center of the specimen placed on two supports is under load.

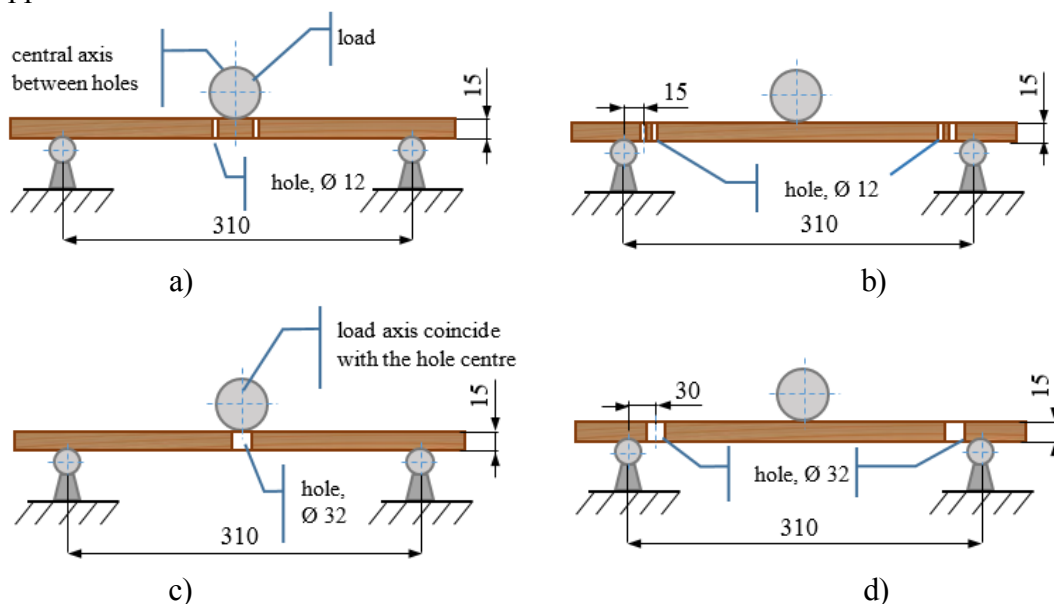


Fig. 3: Location of open-hole-support/load: group of specimens a) II, b) III, c) IV, and d) V.

All obtained values of static and dynamic modulus of elasticity and the coefficient of damping were statistically processed. The highest variance of values of the static modulus of elasticity was found in the group of wood particle board specimens B1 and is equal to 11%, and the lowest was found in the group of plywood PI specimens and is up to 6%.

RESULTS AND DISCUSSION

Open-holes of various sizes and shapes are drilled in wood and wood-based products and structures, and are usually intended for passage or fastening various communications. These holes are made in other ways as well, but they are usually drilled (Jaiprakash et al. 2020). For pieces used in the production of cabinet furniture, open-holes are made for fixing other pieces or fittings. An open-hole or notch can also serve as a design feature that gives furniture exclusivity. These areas are often damaged during use.

Average values of the dynamic and static modulus of elasticity and the coefficient of damping for groups of particle board specimens are given in Tabs. 1 and 2, resp. It is evident that the average dynamic modulus of elasticity of subgroups of wood particle board specimens varied between 3030 and 3230 MPa. This corresponds to the known values of the modulus of elasticity of wood particle board. In all cases, the modulus of elasticity decreased after drilling open-holes in the specimens. Regarding average values of the subgroups, this change ranged from 6.5 to 9.5%, and for the individual specimens the modulus of elasticity decreased to 14%. It has been found that the static modulus of elasticity of wood particle board was about 2840 MPa. The values obtained correspond to the values found by other authors (Wood Handbook 2010, Kord et al. 2016, Astari et al. 2018). The average static modulus of elasticity of groups of the board specimens with drilled open-holes was in the range of 2150 - 2640 MPa. That holes degrade the mechanical properties of wooden structures has been found and in other works (Chen et al. 2021). In addition, wood and wood-based products have a high dispersion of mechanical properties (Nowak et al. 2021).

Tab. 1: Values of dynamic (dMOE) and static (MOE) modulus of elasticity for wood particle board specimens.

Subgroup	B1	BII		BIII		BIV		BV	
Open-hole	-	-	+	-	+	-	+	-	+
dMOE (MPa)	3105	3231	3026	3144	2953	3092	2822	3021	2745
MOE (MPa)	2837	-	2540	-	2638	-	2154	-	2379

The obtained static modulus of elasticity of the specimens was about 8.5% lower than the dynamic one. Analogous results were obtained in other works (Albrektas and Navickas 2017, Divos and Tanaka 2005, Chauhan and Sethy 2016, Nowak et al. 2021). The average static modulus of elasticity of groups of the board specimens with drilled open-holes was in the range of 2150 - 2640 MPa. Regarding open-holes drilled at the ends of the specimens their static modulus of elasticity was 11 – 13% lower than the dynamic one and close to the difference between the static and dynamic modulus of elasticity of the co-examined specimens. This can be explained by the fact that by defining the dynamic modulus of elasticity, the average mechanical

property of the whole specimen material is determined. Determination of the static modulus of elasticity by loading the specimen at three points results in creation of a concentrated load. When the specimen is subjected to a concentrated load at the point of defect (open-hole), its resistance obtained, as well as its modulus of elasticity, is much lower.

Tab. 2: Values of coefficients of damping for particle board specimens.

Subgroup	BI	BII		BIII		BIV		BV	
Open-hole	-	-	+	-	+	-	+	-	+
Coefficient of damping (r.u.)	0,022	0.024	0.026	0.023	0.026	0.020	0.023	0.022	0.025

Drilled open-holes also caused a change in the coefficient of damping of the specimens. It is apparent that the average coefficient of damping of subgroups of wood particle board specimens varied from 0.022 to 0.024 r.u. In all cases, the coefficient of damping increased after drilling open-holes in the specimens. Taking into account the average values of subgroups, this change ranged from 7.7 to 13.0%, and the coefficient of damping for individual specimens increased up to 20%. The average value of the coefficient of damping increased the most in group IV specimens. In other works has also found that coefficient of damping increases with decreasing MOE (Brémaud et al. 2009, Albrektas and Vobolis 2004).

The average values of the dynamic and static modulus of elasticity and the coefficient of damping for groups of plywood specimens are given in Tabs. 3 and 4, resp.

Tab. 3: Values of dynamic (dMOE) and static (MOE) modulus of elasticity for plywood specimens.

Subgroup	PI	PII		PIII		PIV		PV	
Open-hole	-	-	+	-	+	-	+	-	+
dMOE (MPa)	10470	10970	10056	9710	9055	10048	8790	10916	9695
MOE (MPa)	9695	-	8367	-	8245	-	6973	-	8636

As is obvious, the average dynamic modulus of elasticity of the subgroups of plywood specimens varied in the range of 9700 - 11000 MPa. This corresponds to known values of the modulus of elasticity of plywood (Forest Products Laboratory 2010). In all cases, the dynamic modulus of elasticity decreased after drilling open-holes in the specimens. Taking into account the average values of subgroups this change ranged from 7 to 14%, and for individual specimens the modulus of elasticity decreased up to 17%. The static modulus of elasticity was found to be about 7.5% lower than the dynamic one (Albrektas and Navickas 2017, Shan-ging and Feng 2007, Divos and Tanaka 2005, Nzokou et al. 2006, Zalcmans et al. 2018). When the open-holes in the specimens are drilled at the ends, the average static modulus of elasticity of their groups is 9 - 11% lower than that of the dynamic modulus of elasticity. For groups where open-holes were drilled in the center of the specimens, the average static modulus of elasticity was 17–21% lower than the dynamic one. This can be explained analogously, as in the case of wood particle board - the dynamic modulus of elasticity shows the average mechanical properties of the specimen material. Under static concentrated load, the loaded point of the specimen is characterized.

Tab. 4: Values of coefficients of damping for plywood samples.

Subgroup	PI	PII		PIII		PIV		PV	
Open-hole	-	-	+	-	+	-	+	-	+
Coefficient of damping (r.u.)	0.012	0.012	0.013	0.012	0.014	0.011	0.014	0.011	0.013

Apparently, the average values of the coefficient of damping of subgroups of plywood specimens varied from 0.011 to 0.012 r.u. In all cases, drilling open-holes in the specimens resulted in an increase in the coefficient of damping. Taking into account the average values of subgroups, this change ranged from 8 to 21%, and for individual specimens the coefficient of damping increased to 25%. The most significant increase of the coefficient of damping was observed in group IV specimens. As for the failure mode of specimens (failure mode), it can be said that due to the structure of the material it was observed only in plywood specimens; for wood particle board specimens consisting of wood particles that are glued together, separations occurred in the inner layers of the board under load, however no failure line, cracking, bursting or other structural damage became apparent. For plywood specimens during breakage cracks appeared in the inner layers of the plywood (typical case); in some cases, the separation of the glued layers became apparent (Fig. 4), failure line is visible in the outer layer, resulting in reduced bending strength of the specimen. During bending, the upper surface layer of the specimen is compressed and the lower one is subject to tension. When the force exceeds wood tensile strength limit values, the fiber ruptures. The specimen deforms due to internal cracks either in the layers of wood (plywood) (probably they are less plastic) or between the layers (probably due to poor adhesion). The location of open-hole did not affect failure mode of the specimen; failure always appeared at the point of load.



Fig. 4: Failure mode for wood particle board specimens: a) top view, b) side view.

Apparently, the values obtained correspond to the known values of the modulus of elasticity and the coefficient of damping of these materials. It is obvious that due to the structure of the composite materials the plywood has a much higher modulus of elasticity than the wood particle board. On average, this difference is equal to 3.42 times for the static modulus of elasticity and about 3.37 times for the dynamic one. The coefficients of damping varied less (about 1.8 times). The drilled open-holes changed the mechanical properties of the specimens – the modulus of

elasticity of all specimens decreased, while the coefficient of damping increased. In all cases, the mechanical properties of the specimens were mostly changed due to a large open-hole drilled in the center of the specimen (group IV). Regarding the wood particle board, a similar modulus of elasticity was caused by two open-holes of the same diameter drilled at the ends of the sample (group V).

CONCLUSIONS

(1) Open-holes (holes) change the mechanical properties of the specimens - the modulus of elasticity (static and dynamic) decreases, and the coefficient of damping increases. (2) The large diameter open-hole drilled in the center of the specimen mainly determines the mechanical properties of the specimen – the modulus of elasticity mostly decreases, and the coefficient of damping mostly increases (up to 15% and up to 21% for the groups of specimens tested, respectively). Open-holes located at the ends of the specimen or the one smaller in diameter have less effect on the change in mechanical properties (up to 14% and up to 15% for the groups of specimens tested, respective). (3) Open-holes at different locations and with different diameters have a different effect on changes in the static and dynamic modulus of elasticity – the dynamic modulus of elasticity characterizes the average properties of the specimen material, while the static modulus characterizes properties at the specific location. Depending on the location and diameter of the open-holes, the difference between static and dynamic modulus of elasticity can vary from 7 to 21%. (4) The location of the open-hole did not affect the failure mode of the specimen; in all cases the failure appeared at the point of load. When the load is applied perpendicular to the open-hole, no cracks appear at its edges which would spread deep into the specimen.

REFERENCES

1. Aicher, S., 2011: Glulam beams with internally and externally reinforced holes - tests, detailing and design. Conference: CIB Working Commission W18 - Timber Structures, Meeting 44, Alghero, Italy August: 474 pp.
2. Aicher, S., Höfflin, L., 2008: Fracture behaviour and design of glulam beams with round holes. 10th World Conference on Timber Engineering, Miyazaki, Japan 2-5 June: 132-139.
3. Albrektas, D., Navickas, P., 2017: An evaluation of modulus of elasticity, dimensional stability and bonding strength of bonded heat - treated wood. *Drvna Industrija* 68(2): 137-144.
4. Albrektas, D., Vobolis, J., 2003: Investigation of mechanical parameters and defects of solid wood glued panels. *Materials Science* 9(4): 368-373.
5. Albrektas, D., Vobolis, J., 2004: Modeling and study of glued wood panel. *Materials Science* 10(4): 370-373.
6. Ardalany, M., Fragiaco, M., Carradine, D., Moss, P., 2013: Experimental behavior of laminated veneer lumber (LVL) joists with holes and different methods of reinforcement. *Engineering Structures* 56: 2154–2164.

7. Ardalany, M., Fragiaco, M., Moss, P., Buchanan, A., 2012: Design of reinforcement around holes in laminated veneer lumber (LVL) beams. WCTE World Conference on Timber Engineering Auckland New Zealand 15 – 19 July: 6-17.
8. Astari, L., Prasetyo, K.W., Suryanegara, L., 2018: Properties of particleboard made from wood waste with various size. IOP Conf. Series: Earth and Environmental Science 166: 1-7.
9. Brémaud, I., Minato, K., Thibaut, B. 2009: Mechanical damping of wood as related to species classification. A preliminary survey. 6th Plant Biomechanics Conference PBM09: 536-542.
10. Chauhan, S., Sethy, A., 2016: Differences in dynamic modulus of elasticity determined by three vibration methods and their relationship with static modulus of elasticity. Maderas. Ciencia y tecnología 18(2).
11. Chen, D., Zhang, W., Wu, Y., Jin, Z., Zhang, Q., 2019: Investigation on the mechanical properties of open-hole spruce and Douglas fir. Wood Research 64(1): 155-164
12. Chen, G., Tan, Ch., Yang, W., Wu, J., Zhou, T., Jiang, H., Zhang, Y., 2021: Wood I-joists with web holes and flange notches: A literature review. Journal of Building Engineering 38.
13. Danzer, M., Dietsch, P., Winter, S., 2016: Reinforcement of round holes in glulam beams arranged eccentrically or in groups. Conference: WCTE World Conference on Timber Engineering 2016 Vienna, Austria: 9 pp.
14. Divos, F., Tanaka, T., 2005: Relation between static and dynamic modulus of elasticity of wood. Acta Silvatica & Lignaria Hungarica 1: 105-110.
15. Forest Products Laboratory, 2010: Wood handbook. Wood as an engineering material. General Technical Report FPL-GTR-190. Madison, WI: U.S. Department of Agriculture, Forest Service, 508 pp.
16. Jaiprakash, M., Nagamadhu, M., Karthikeyan, K., Kiran, Mudabbir Shariff, G.C., Kumarb, M., 2020: Effect of drilling parameters on Neem wood veneer epoxy composites using grey relational analysis. Materials Today: Proceedings 24(4): 2163-2173.
17. Kord, B., Zare, H., Hosseinzadeh, A., 2016: Evaluation of the mechanical and physical properties of particleboard manufactured from canola (*Brassica napus*) straws. Maderas. Ciencia y tecnología 18(1): 9-18.
18. Mori, M., Hasegawa, M., Yoo, J., Kang, S., Matsumura, J., 2016: Nondestructive evaluation of bending strength of wood with artificial holes by employing air-coupled ultrasonics. Construction and Building Materials 110(1): 24–31.
19. Nowak, T., Patalas, F., Karolak, A., 2021: Estimating mechanical properties of wood in existing structures - selected aspects. Materials 14: 1-26.
20. Nzokou, P., Freed, J., Kamden, D.P., 2006: Relationship between non destructive and static modulus of elasticity of commercial wood plastic composites. Holz als Rohund Werkstoff 64(2): 90-93.
21. Shan-qing, L., Feng, F., 2007: Comparative study on three dynamic modulus of elasticity and static modulus of elasticity for Lodgepole pine lumber. Journal of Forestry Research 18(4): 309-312.
22. Timoshenko, S.P., Young, D.H., Weaver, W.Jr., 1985: Vibration problems in engineering. Moscow, Mashinostroenie, 472 pp.

23. Tu, W., Que, Z., Chen, Y., Huang, H., Li, H., Wu, M., 2016: Failure mechanism analysis of laminated veneer lumber (LVL) joists with holes and plywood reinforcement methods. 3rd International Conference on Materials Science and Mechanical Engineering, September 29-30, Windsor, UK. Pp 46-49.
24. Wood Handbook 2010: Wood as an engineering material. General Technical Report FPL-GTR-190, Madison, 509 pp.
25. Yerlikaya, N.C., Karaman, A., 2020: Effect of the fabric reinforcement of structural holes in wood based panels. Wood Research 65(3): 485-496.
26. Zalcmanis, A., Zudrags, K., Japiņš, G., 2018: Birch plywood sample tension and bending property investigation and validation in Solidworks environment. Research for rural development 1: 103-110.
27. Zhang, X., Que, Y., Wang, X., Li, Z., Zhang, L., Han, C., Que, Z., Komatsu, K., 2018: Experimental behavior of laminated veneer lumber with round holes, with and without reinforcement. Bioresources 13(4): 8899-8910.

SIMONA GAURONSKAITĖ
KAUNAS UNIVERSITY OF TECHNOLOGY
FACULTY OF MECHANICAL ENGINEERING AND DESIGN
STUDENTU ST. 56
LT – 51424 KAUNAS
LITHUANIA

VAIDA DOBILAITĖ, MILDA JUCIENĖ*
KAUNAS UNIVERSITY OF TECHNOLOGY
INSTITUTE OF ARCHITECTURE AND CONSTRUCTION
TUNELIO ST. 60
LT – 44405 KAUNAS
LITHUANIA

*Corresponding author: milda.juciene@ktu.lt

DARIUS ALBREKTAS
KAUNAS UNIVERSITY OF APPLIED SCIENCES
FACULTY OF TECHNOLOGIES
PRAMONĖS PR. 20
LT – 50468 KAUNAS
LITHUANIA

EFFECTS OF MODIFICATION WITH MELAMINE–UREA–FORMALDEHYDE RESIN ON THE PROPERTIES OF UREA PRETREATED EUCALYPTUS

YINLUAN QIN^{1,2}, LONGHAI CHEN²

¹GUANGXI ECO-ENGINEERING VOCATIONAL AND TECHNICAL COLLEGE

²BEIJING FORESTRY UNIVERSITY

CHINA

(RECEIVED JUNE 2021)

ABSTRACT

Eucalyptus urophylla was treated with melamine-urea-formaldehyde resin (MUF) after pretreatment with urea solution. The properties of the wood were then determined. The weight percent gain (WPG) and, antiswelling efficiencies (ASE) of the wood treated with urea+MUF were 14% and, 45% higher than those of untreated wood, respectively. The water absorption (WA) of the wood treated with urea+MUF was decreased approximately 50% lower than that of the untreated wood. However, the mechanical properties of the wood treated with urea+MUF were weakened due to the destruction of the structure of wood. An X-ray photoelectron spectroscopy (XPS) analysis revealed that the atomic concentration ratio of O/C was increased. The ratio of C1 was decreased as the lignin and extractives contents were decreased, while the ratios of C2 and C3 were increased. The urea solution pretreatment was conducive to the impregnation of wood functional modifiers.

KEY WORDS: Urea, pretreatment, melamine–urea–formaldehyde, wood properties.

INTRODUCTION

Plantation fast growing eucalyptus was introduced to locals worldwide because of the growing rapidity and short rotation (5-7 years). As of 2009, there were 95 countries with planted eucalyptus, with an eucalyptus area of 20.07 million hm² (Chen et al. 2018b). Eucalyptus is mainly used for particleboard, medium density fiberboard, wood pulp, and export wood chips in China (Chen et al. 2019, Tao and Chen 2016). The wood of eucalyptus is suitable for furniture and floor material because of its fineness, high hardness and beautiful tread patterns. However, the disadvantage of large growth stress, enrichment extractives, and poor permeability have led to dimensional instability and limited structural timber of eucalyptus (Lu et al. 2017, Zhou et al.

2019). Permeability is a physical property of porous materials (Chaiyo and Rattanadecho 2013), which reflects the porous structure and its interconnectivity. It may also provide useful information for practical wood applications, such as the optimization of impregnation with fluids to achieve protection against biological deteriorating agents and fire. Owing to the high porous structure variability between and within species, the permeability of species is crucial for wood modification and protection.

The permeability of wood is affected by wood species, fluids, infiltration processes, etc. Among them, the pore size, size and number of pore membranes, gum in the cell cavity, etc. were main factors affecting the permeability (Li et al. 2011, Lv et al. 2019). For eucalyptus, the main factors affecting the permeability are the extracts contained in wood and tylosis in the conduit (Silva et al. 2010). It is very challenging to effectively improve the permeability for the functional improvement of eucalyptus and utilization of high value-added solid wood. Detailed studies have been carried out on methods to improve the wood permeability (Comstock 1970, Esmailpour et al. 2019, Nicholasd 1977, Torgovnikov and Vinden 2009). Yang (2004) treated *Larix gmelinii* with different microwave powers and times, and reported that the microwave treatment destroyed the weak position on the cell wall and formed a fluid channel, which improved the permeability of *Larix gmelinii* without changing the mechanical properties of wood. Lv (2000) used alcohol to replace the water in the heartwood and sapwood of *Picea jezoensis* Carr. var. *microsperma*, and green wood of *Abies nephrolepis* to maintain with green wood for the pores state, while dissolving a part of the extract. As a result, the average permeability of the replacement wood was 101.5 times that of the ordinary air-dry material.

Since the 1990s, microwave, steam, and blasting technologies have been used to treat eucalyptus. Its microstructure and permeability have been studied (Li et al. 2007, Lv et al. 2001, Wang et al. 2013, Zhang and Cai 2008, Zhou et al. 2009). Owing to the evaporation of moisture or increase in air pressure inside the wood, which affected the weak parts such as the pore membrane, the microstructure of the wood was destroyed and eventually, the permeability was improved. Microwave, steam, and other technologies have improved the permeability of wood, but are complex and costly. To simplify the process and reduce costs, based on previous studies, the author (Qin et al. 2020) used urea solution to treat wood. The gas permeability of eucalyptus was increased by 40%, while the liquid permeability was increased by 180%. This provides a new method for a functional improvement of wood.

Based on the previous research, this study used melamine-urea-formaldehyde resin to modify eucalyptus, which was pretreated with urea solution to determine the properties of the modified wood, and investigated the effect of the urea solution pretreatment on wood functional improvement.

MATERIAL AND METHODS

Materials

After air drying, eucalyptus (*Eucalyptus urophylla*) was cut according to the required specifications, and the defects were removed. Wood was extracted using a benzene-ethanol mixed solution (2 : 1). 300 × 20 × 20 mm, seven pieces in one group, a total of three groups; 20 ×

20 × 20 mm, five pieces in one group, a total of four groups; 30 × 20 × 20 mm, seven pieces in one group, a total of three groups), and then placed in oven and dried to a constant weight at 103 ± 2°C. The size and weight of the sample were then recorded. Ethanol, benzene, and NaOH were purchased from Beijing Chemical Plant. Urea, formaldehyde and melamine were purchased from Xilong Science Co., Ltd.

Preparation of the MUF resin

Melamine, 37% formaldehyde, and urea solution (with the same amount of urea), were placed in four-round bottom flask. The mixture was adjusted to pH of 7.0 - 8.0 by adding 40% NaOH solution (the pH value was maintained throughout the reaction). The mixture was then heated to 75°C, maintained for 10 min. The temperature was then decreased to 50°C and maintained for 30 min to obtain the MUF resin. The final molar ratio of MUF (formaldehyde to urea and melamine) was 0.8. The viscosity and solid content of the MUF resin were 6.58 mPa.s and 42.6%, respectively (measured according to GB/T 14074, 2006).

Pretreatment and modification of test pieces

Samples (apart from the untreated sample) were placed in 20% urea solution and soaked for 36 h. Some of them were removed, and placed in a MUF solution (concentration of 30%). The impregnate MUF samples were then exposed to atmospheric pressure for 3 h after application of vacuum for 30 min (-0.095 MPa). Then, the solution on the surface of all samples was removed. All samples were placed in an oven to dry to a constant weight their weights were the measured.

Scanning electron microscopy (SEM) observation

Treated and untreated samples were adhered to double-sided tapes and then sputter-coated with a gold layer. SEM images were recorded using a ZeissEVO18SEM analyzer (Germany) with an acceleration voltage of 10-15 kV.

Physical property tests

The weight percent gain (WPG) was calculated for the treated samples by:

$$\text{WPG} = (W_1 - W_0) / W_0 \times 100 \quad (1)$$

where: W_0 and W_1 are represent the weights of the untreated and impregnated MUF wood specimens, respectively, after oven drying to achieve constant weight.

The treated and untreated specimens were placed into beakers (filled with water), subjected to vacuum for 30 min (-0.095 MPa), and then exposed to atmospheric pressure for 12 h. The weights and sizes of the samples were measured. The water absorption rate (WA) and anti-swelling efficiencies (ASE) of the samples during water absorption were calculated by the volumetric change:

$$\text{WA} = (M_2 - M_0) / M_0 \times 100 \quad (2)$$

where: M_0 is the oven dried weight of the sample and M_2 is the weight of the sample after water absorption:

$$ASE = (S_u - S_t) / S_u \times 100 \quad (3)$$

where: S_u represents the volumetric swelling of the untreated wood samples and S_t represents the volumetric swelling of the treated samples.

The volume change rate (S) is the percentage of sample volume change upon immersion in water,

$$S = (V_2 - V_0) / V_0 \times 100 \quad (4)$$

where: V_0 represents the oven dried volume before impregnation (cm^3) and V_2 represents the volume after immersion in water (cm^3).

The following equation was used to determine the volume bulking coefficient (B) (oven dried) owing to sample modification:

$$B = (V_1 - V_0) / V_0 \times 100 \quad (5)$$

where: V_1 represents the oven dried volume after impregnation (cm^3).

X-ray photoelectron spectroscopy (XPS) tests

Treated and untreated wood pieces were cut with a blade along the tangential direction of the sample, (size $10 \times 10 \times 2$ mm, longitudinal \times tangential \times radial). The energy of the wood surface was measured using photoelectron spectroscopy with a monochromatic Al target, full spectral step of 1 eV, energy of 160, narrow spectral step of 0.1 eV, energy of 40, and beam size of 300×700 μm .

Mechanical property tests

The bending properties (MOR) and compression strength (CS) were determined according to the Chinese standards GB/T 1936.1 (2009) and GB/T 1935 (2009). The lengths, widths, thicknesses (± 0.02 mm), and weights (± 0.01 g) of the samples were measured.

RESULTS AND DISCUSSION

Physical properties

The properties of wood are showed in Tab. 1. Compared to the MUF treated wood, the WPG of the MUF modified wood with the urea pretreatment was increased by 14%. After the pretreated with urea solution (pH = 7.2), the lignin, pectin, wax lipids and other substances

inside the wood reacted with urea or were dissolved, and the amide bonds of some protein molecules in the nitrogen containing compound were hydrolyzed (Chen et al. 2018a, Chen 2019), resulting in an increased internal porosity and significantly improved wood permeability (Qin et al. 2020). More MUF entered into the interior of wood, and thus the WPG of urea+MUF treated wood was higher than that of MUF treated samples. Urea removes a part of the lignin and extracts of wood to improve its permeability. Water and small urea molecules can enter into the cellulose noncrystalline area and swell the cellulose, resulting in higher WPG. The treatment agent entering the interior of the wood cell wall changed the wood volume, which led to gain *B* of the wood.

Tab. 1: Properties of the wood samples treated with different methods.

Treatment method	WPG (%)	WA (%)	S (%)	ASE (%)	B (%)
untreated	-	78.35 (27.00)	12.89 (3.56)	-	-
urea+MUF	8.31 (1.34)	40.20 (19.00)	7.26 (1.34)	43.70 (21.99)	6.65 (1.23)
urea	9.45 (2.50)	41.02 (15.78)	7.16 (2.37)	44.46 (18.38)	6.72 (0.77)
MUF	7.29 (6.56)	45.54 (14.42)	12.06 (4.56)	30.94 (17.55)	3.99 (1.50)

Note: The numbers in parentheses are standard deviations.

The WA and *S* values of treated samples were significantly reduced. Compared to the untreated wood, the WA of urea+MUF treated wood was decreased by approximately 50%. The hydroxyl groups on lignin easily form hydrogen bonds with water molecules. When urea-pretreated wood, lignin, hemicellulose, and extract were dissolved. The hydroxyl groups that would be combined with water were reduced, which reduced the WA of wood. The reduction in WA promoted an improvement in the dimensional stability of the wood and decrease in the volume expansion of water absorption. Owing to the dissolution of lignin, the wood shrinks (Dong 2018). These interaction of the two factors reduce the volume expansion of the urea-treatment wood.

Microstructure

The microstructures of wood samples treated by different methods are shown in Figs. 1 and 2. After the urea pretreatment, the porous structure of wood was not changed, but the cell wall became smoother and the pore membrane was damaged. There was a separation between the cell walls (Dong 2018). The lignin content in the intercellular layers was high. After the urea pretreatment, the horizontal penetration of the wood was increased, because the lignin was broke down, resulting in cell gaps and cracks in the pores of the wood cell wall, which was conducive to resin-impregnation. In addition, after the pretreatment with urea solution, a fraction of hemicellulose was dissolved, leading to the formation of many micropores on the wood cells. These micropores are conducive to the increase in the permeability of wood and penetration and diffusion of modifiers. Previous studies confirmed the improvement in wood permeability by urea treatment (Qin et al. 2020). The MUF resin deposited in the cell cavity basically disappeared after the pretreatment with urea, which indicates that, after the pretreatment with urea, the resin entered the cell wall, causing expansion of cell wall (swelling rate of 6.65%), and significantly improved the dimensional stability of wood. This is consistent with the above results.

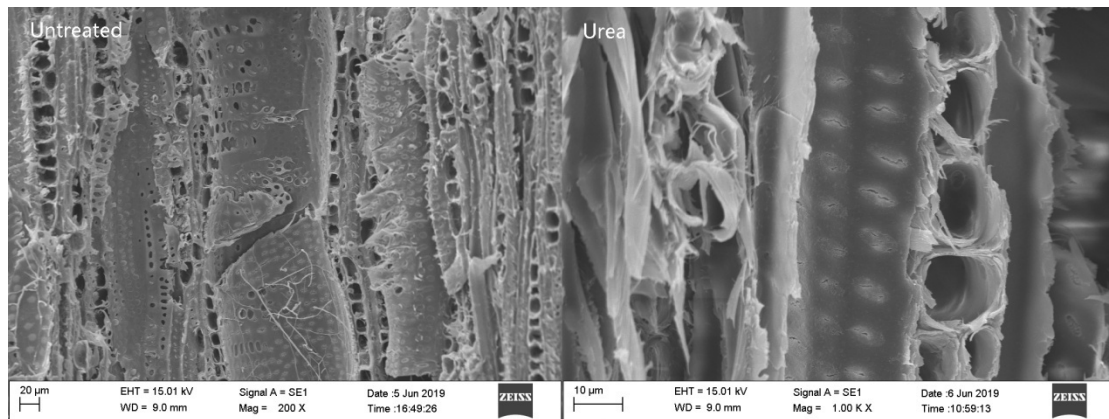


Fig. 1: Microstructures of untreated and 20% urea solution treated wood samples.

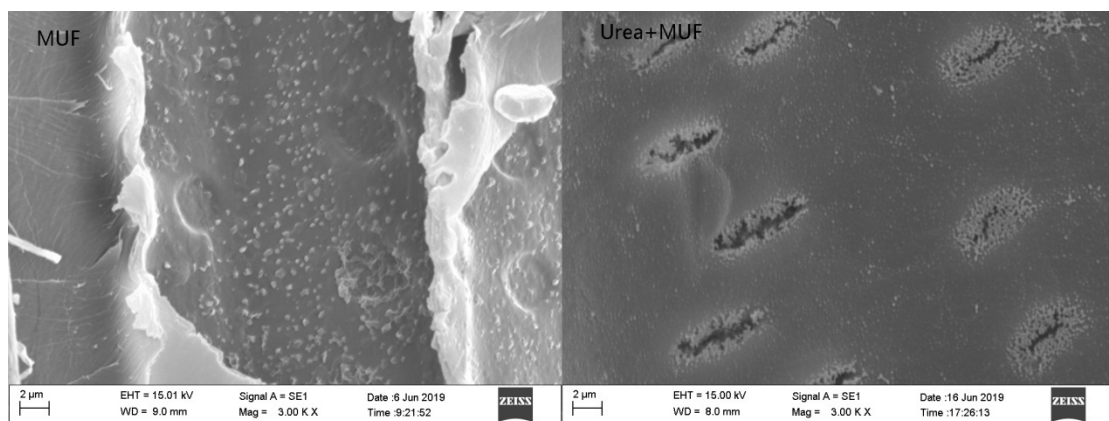


Fig. 2: Microstructures of MUF and urea+MUF treated wood samples.

Mechanical properties

The mechanical properties of wood are shown in Tab. 2. Compared to the untreated wood, the MOR and CS of urea+MUF treated wood were decreased by 7% and 8%, respectively, while the MOR and CS of MUF-treated wood was increased by 12% and 22%, respectively. The urea pretreatment had an adverse effect on the mechanical properties of wood.

Wood is mainly composed of cellulose, lignin, and hemicellulose. Cellulose is the main determinant of the strength and stiffness of the wood. Lignin has a supporting role in the hardness and toughness of the wood. After the impregnation with urea solution, the acids, lignin and other substances in the wood were partially dissolved. The urea solution infiltrated and swelled the cellulose, broke the bond between cellulose and hemicellulose, and destroyed the structure of the wood cell wall (Figs. 1 and 2), making wood prone to slack (Chen et al. 2018a). Many nanoscale pores were formed in the wood cell wall (Li et al. 2016), which were conducive to the impregnation of resin, while weakening the mechanical properties of wood. The resin was impregnated into the wood to form a polymer, which would crosslink with the hydroxyl groups of the wood at high temperatures, and enhanced the resistance of the wood to external forces. Therefore, the reductions in the MOR and CS of urea+MUF treated wood were due to the combined effect of the above factors.

Tab. 2: Properties of wood treated by different methods (moisture content 5.35 - 8.70%).

Approach	WPG (%)	MOR (MPa)	CS (MPa)
untreated		102.53 (25.03)	49.79 (3.97)
urea+MUF	4.00 (2.50)	94.99 (35.80)	46.43 (12.93)
MUF	1.63 (1.14)	114.91 (42.38)	60.73 (6.55)
urea	4.53 (2.13)	89.46 (20.08)	40.27 (4.19)

Note: The numbers in parentheses are standard deviations.

XPS analysis

Various properties of polymer materials are closely related to their surface compositions. Wood is a complex material composed mainly of lignin, cellulose, and hemicellulose. In addition to these polymer components, wood may contain large amounts of extractives.

XPS was used to analyze the surface chemical elements of eucalyptus. The contents of the elements on the surface of the wood sample are shown in Tab. 3. The XPS spectra of wood are shown in Fig. 3. All wood samples had strong peaks near 285 and 535 eV, which are the absorption peaks of C and O atoms, respectively. The main elements of eucalyptus were C, O, and small amount of N. The contents of these elements changed largely upon the treatments with different reagents. After MUF treatment, the content of C was decreased, while that of O and concentration ratio of O/C were increased. The O/C ratio from 0.26 increased to 0.46 for untreated wood. Tserki et al. (2005) reported that the O/C ratio closed to 0.35 can be explained by the removal of waxy substances on the surface of wood, and large exposure of hemicellulose and cellulose on the wood surface. The proportion of oxygen atoms on the surface increased, i.e., the lignin and extracts on the surface were reduced. However, when the urea solution was used to treat wood, the content of O decreased sharply. This indicates that the amounts of OH, C=O, and -COOH on the wood surface decreased (Wang et al. 2009). After urea+MUF treatment, the O/C ratio was close to 0.35. The urea+MUF treated wood was largely affected by urea, but the OH contents of the MUF and, urea+MUF treated wood samples were higher than that of urea treated samples. Thus, the WA after urea treatment was smaller than those after the MUF and urea+MUF treatments.

Tab. 3: Elemental composition on the surface of wood.

Approach	WPG (%)	Element (%)			
		C	O	N	O/C
untreated wood	-	79.11	20.63	0.26	0.26
MUF	7.29	60.29	27.76	11.94	0.46
urea + MUF	8.31	73.49	24.29	2.22	0.33
urea	9.45	79.91	1.16	18.90	0.24

The intensity of the N1s peak in the spectrum of the treated wood at 399.88 eV was increased. This indicated that N elements was introduced on the surface of the treated wood. The change in the peak intensities of C, O, and N showed that the wood surface had obvious chemical changes. However, the urea+MUF treated wood was affected by urea and the O atom content was lower than that of the MUF treated wood.

An XPS peak fitting diagram after C 1s peaking on the sample surface is shown in Fig. 4.

After the Gaussian fitting of the untreated wood C 1s spectrum, three C1, C2 and C3 peaks were obtained. This indicates three states of carbon on the wood surface. ① The carbon atom C1 (-C-C, C-H), which is only combined with C or H atoms, mainly originates from the carbon connected to the lignin, hemicellulose, and C-C groups in the extract (such as fatty acids and hydrogen groups in lignin and extracts). ② C2 was only bound to a single non-carbonyl oxygen, which is correspond to the O-CH group of lignin and C-O-C bond of wood extracts and polysaccharides. There is more C2 in cellulose and hemicellulose than in lignin, which is considered to be derived mainly from cellulose. ③ C3 is bound to the carbonyl group or two non-carbonyl oxygen atoms, which are considered to originate from the O-C-O structure and carbonyl group in the cellulose and hemicellulose molecules (C=O) (Inari et al. 2006, Sinn et al. 2001, Stark and Matuan 2007). The C 1s spectrum of the modified wood was also fitted with three peaks. This indicates that the type of carbon after treatment was not change. Tab. 4 shows that, after the MUF treatment, the proportion of C1 decreased, which was reflected in the spectrum as the height of the C1 peak became smaller and the peak area decreased, corresponding to the reduction of lignin and carbon in the extract connected to the carbon (C-C) group (Qin et al. 2019). However, the C1 ratio of urea treated wood was decreased slightly. The extracts and lignin reductions of the urea treated wood were confirmed by the previous analysis.

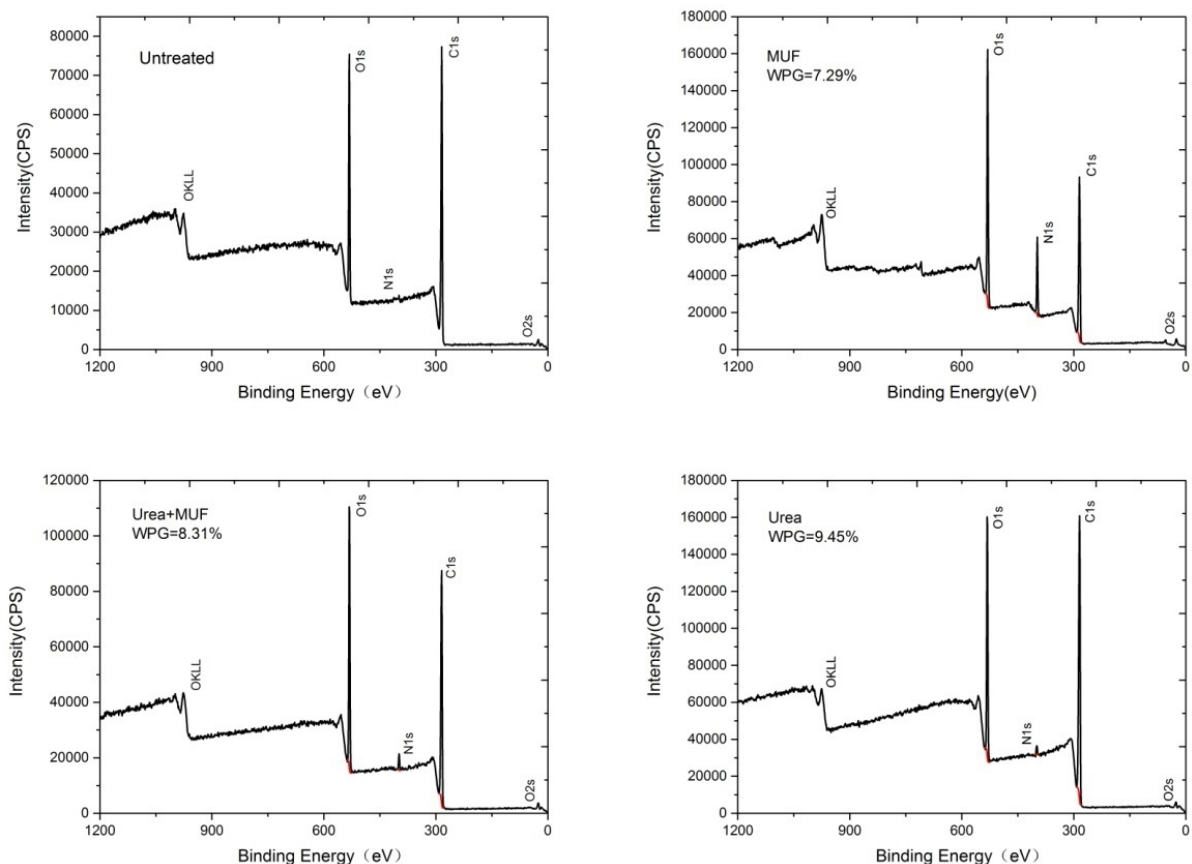


Fig. 3: Survey XPS of the treated and untreated eucalyptus wood.

After the treatment, the proportion of C2 varies largely due to the difference in treatment reagent and WPG. Because cellulose contributes more to C2, the change in C2 content indicated changed in the cellulose content on the wood surface. In the MUF impregnated wood, cellulose, and hemicellulose participated in the resin curing process, forming an ether bond, which resulted in a decrease C2 content. After the urea treatment, the wood surface C2 content increased by 20% compared to that of the untreated wood. The urea can decompose a part of the lignin, resulting in an increase in the cellulose and hemicellulose contents of the wood. The urea +MUF treated material was affected by urea, which increased the C2 content. The C3 contents of MUF and urea treated wood samples exhibited the opposite behavior, which may be caused by the different effects of MUF and urea on the chemical composition of the wood.

According to the above analysis, the changes in C1, C2, and C3 indicated that the MUF resin and urea caused chemical changes in the wood. A large number of -O-C=O bonds appeared in the wood after MUF treatment. The -O-C=O ratio was reduced after the urea treatment. This indicated that the cellulose and hemicellulose contents in the wood surface were reduced. The urea partially degraded wood cellulose and hemicellulose, which coincided with the wood damage (Fig. 1). In addition, the MUF would generate an -O-C=O bond after the reaction with the wood hydroxyl group. As a result, the contents of other C1 and C2 structures in the wood were relatively reduced.

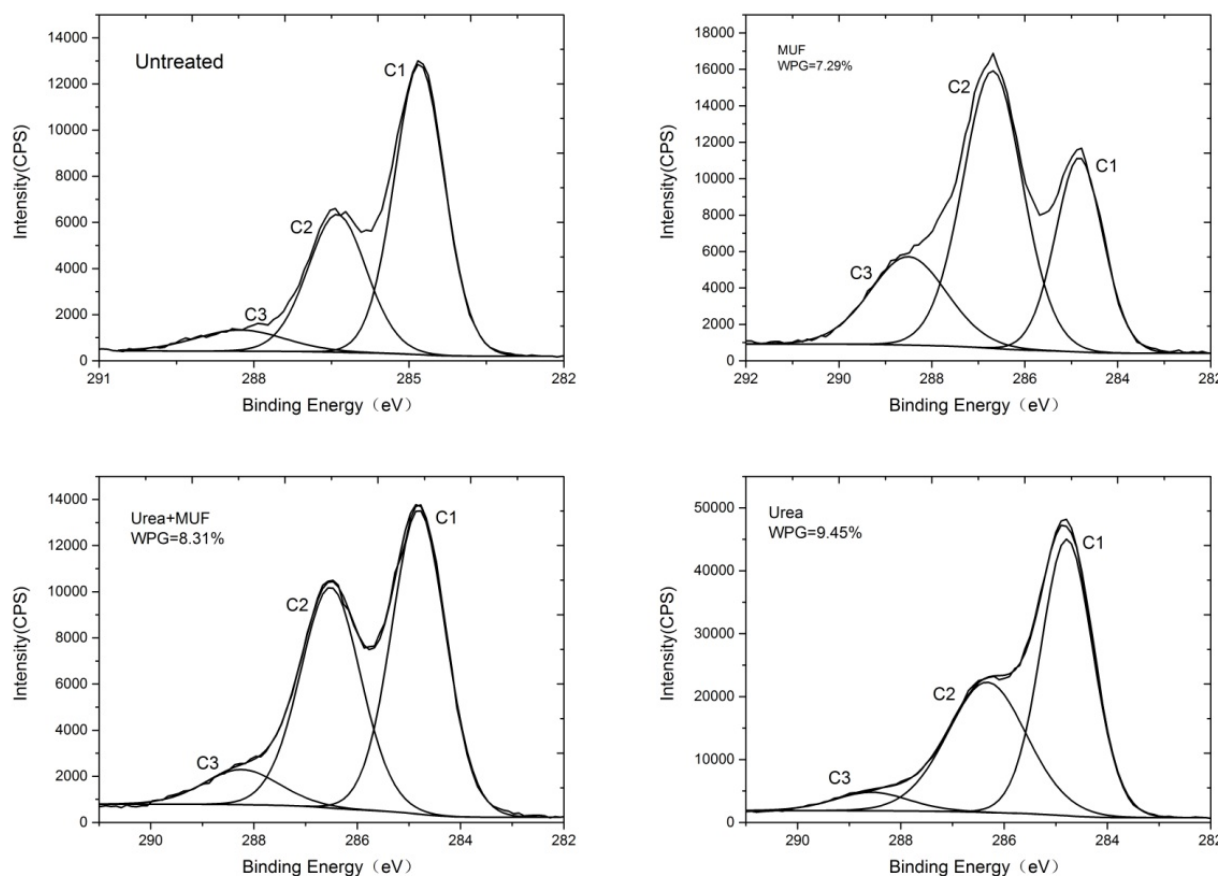


Fig. 4: XPS C 1s of eucalyptus treated and untreated wood surfaces.

Tab. 4: Elemental composition on the surface of eucalyptus.

Approach	WPG (%)	Fit peak area ratio		
		C1 (%)	C2 (%)	C3 (%)
untreated	-	59.40	32.95	7.65
MUF	7.29	50.80	28.41	20.79
urea + MUF	8.31	50.68	41.16	8.15
urea	9.45	55.17	39.54	5.28

CONCLUSION

The weakly alkaline urea improved the wood permeability by dissolving extracts and wood constituents in the wood structure and swollen cell walls. Compared to the MUF treatment of wood, the WPG of the urea+MUF treated wood was increased by 14%. The ASE was increased from 30% to 43.7%. The WA of the wood was reduced by approximately 50% compared to that of untreated wood. However, the mechanical properties of the urea+MUF treated wood were weakened owing to the destruction of the wood structure.

The XPS analysis revealed that the MUF and urea+MUF treatments caused obvious chemical changes on the wood surface. The C content decreased, while the O contents and ratio of O to C (O/C) increased. The proportion of C1 on the wood surface was reduced, mainly due to the reduced contents of lignin and extracts. The urea+MUF treated wood was affected by the urea-dissolved lignin, which led to an increase in the C2 content. The ratios of C3 of the MUF and urea+MUF treated wood samples were increased. This corresponded to the acetal structure in the wood cellulose and hemicellulose molecules. The contents of retinyl in lignin molecules were increased and decreased, respectively.

ACKNOWLEDGEMENT

This work was supported by Guangxi colleges and universities the Young Teachers' Basic Ability Improvement Project under the grant (KY2021KY1225).

REFERENCES

1. Chaiyo, K., Rattanadecho, P., 2013: Numerical analysis of heat–mass transport and pressure build-up in 1D unsaturated porous medium subjected to a combined microwave and vacuum system. *Drying Technology* 31: 684-697.
2. Chen, S.Y., Xue, Z.H., Liu, J.W., Zhao, K.Y., Bao, X.X., 2018a: Effect of alkali treatment on relaxation properties of wood. *Journal of Northwest Forestry University* 33(2): 193-197.
3. Chen, S.X., Zheng, J.Q., Liu, X.F., 2018b: Hundred-year histories and prospect of eucalyptus cultivation technology development in China. *World Forestry Research* 31(2): 7-12.
4. Chen, X., 2019: Study on the improvement of dyeing properties of Chinese fir wood by sodium hydroxide-freeze-thaw cycles pretreatment. Vol. Master's. Fujian Agriculture and Forestry University Fuzhou. Pp 17-18.
5. Chen, Y.P., Lv, J.X., Chen, Z.L., 2019: Status of development and wood utilization of

- eucalyptus plantation in China. *China Wood-Based Panels* 12: 6-9.
6. Comstock, G.L., 1970: Directional permeability of softwoods. *Wood and Fiber Science* 1: 283-289.
 7. Dong, Y.M., 2018: Performance and enhancement mechanism of cell wall modification of fast-growing poplar wood. Vol. Ph.D. Beijing Forestry University, Beijing. Pp: 53-54.
 8. Esmailpour, A., Taghiyari, H.R., Golchin, M., Avramidis, S., 2019: On the fluid permeability of heat-treated paulownia wood. *International Wood Products Journal* 10: 55-63.
 9. GB/T 14074, 2006: Testing methods for wood adhesive and their resins.
 10. GB/T 1936.1, 2009: Method of testing of bending strength of wood.
 11. GB/T 1935, 2009: Methods of testing of compressive strength parallel to grain of wood.
 12. Inari, G.N., Petrissans, M., Lambert, J., Ehrhardt, J.J., G´erardin, P., 2006: XPS characterization of wood chemical composition after heat-treatment. *Surface and Interface Analysis* 38(10): 1336-1342.
 13. Li, X.J., Fu, F., Zhou, Y.D., Chen, Z.L., 2007: Advance in the research of wood microwave modification. *Material Reports* 21(11): 295-298.
 14. Li, Y., Fu, Q., Yu, S., Yan, M., Berglund, L., 2016: Optically transparent wood from a nanoporous cellulosic template: Combining Functional and Structural Performance. *Biomacromolecules* 17(4): 1358-1364.
 15. Li, Y.F., Liu, Y.X., Wang, F.H., Gang, G.J., 2011: Controlling factors of wood permeability and its improving measures. *Scientia Silvae Sinicae* 47(5): 131-139.
 16. Lu, C.X., Jiang, T., Liu, Y., Guo, D.Q., Ren, S.Q., Deng, Z.Y., 2017: Research progresses of influencing factors and improvement methods of *Eucalyptus robusta* impregnated modification. *Journal of Southwest Forestry University* 37(5): 214-220.
 17. Lv, C., Zhan, T.Y., Wang, X., Zhang, Y.L., 2019: Research on water diffusion characteristics in wood. *World Forestry Research* 32(6): 43-48.
 18. Lv, J.X., Bao, F.C.H., Jiang, X.M., Zhao, Y.K., 2000: Studies on the effect of three different treatments on wood permeability. *Scientia Silvae Sinicae* 36(4): 67-76.
 19. Lv, Y.X., Xue, Z.H., Xue, L.Z., 2001: Observing ex microcosmic structure of microwave modified wood. *Inner Mongolia Forestry Science & Technology* 4: 31-33.
 20. Nicholasd, D.D., 1977: Chemical methods of improving the permeability of wood. *ACS Symposium Series American Chemical Society* 43: 33-46.
 21. Qin, Y.X., Dong, Y.M., Li, J.Z., 2019: Effect of modification with melamine urea formaldehyde resin on the properties of eucalyptus and poplar. *Journal of Wood Chemistry and Technology* 39(5): 360-371.
 22. Qin, Y.X., Lu, C.X., Li, J.Z., Mo, Y.Y., 2020: Study on different treatment methods for improving permeability of eucalyptus. *China Forest Products Industry* 57(04): 10-13, 24.
 23. Silva, M.R.D., Machado, G.D.O., Deiner, J., Juniora, C.C., 2010: Permeability measurements of Brazilian eucalyptus. *Materials Research* 13(3): 281-286.
 24. Sinn, G., Reiterer, A., Stanzl-Tschegg, S.E., 2001: Surface analysis of different wood species using X-ray photoelectron spectroscopy (XPS). *Journal of Materials Science* 36(19): 4673-4680.
 25. Stark, N.M., Matuan, L.M., 2007: Characterization of weathered wood plastic composite

- surfaces using FTIR spectroscopy, contact angle, and XPS. *Polymer Degradation and Stability* 92: 1883-1890.
26. Tao, L., Chen, N., 2016: Analysis of the current status and prospect of eucalyptus forest in short rotation. *South China Agriculture* 10(3): 92-93.
 27. Torgovnikov, G., Vinden, P., 2009: High-intensity microwave wood modification for increasing permeability. *Forest Products Journal* 59(4): 84-92.
 28. Tserki, V., Zafeiropoulos, N.E., Simon, F., Panayiotou, C., 2005: A study of the effect of acetylation and propionylation surface treatments on natural fibres. *Composites Part A: Applied Science and Manufacturing* 36(8): 1110-1118.
 29. Wang, X.Q., Ren, H.Q., Zhao, R.J., Cheng, Q., Chen, Y.P., 2009: FTIR and XPS spectroscopic studies of photodegradation of Moso bamboo (*Phyllostachys pubescens* Mazel). *Spectroscopy and Spectral Analysis* 7: 138-141.
 30. Wang, X.M., He, Q., Zhao, X.L., 2013: Study on drying and collapse properties of eucalypts plantation. *Journal of Inner Mongolia Agricultural University* 1: 123-127.
 31. Yang, L., 2004: Modification on the permeability of larch wood by microwave. Vol. Master's Northeast Forestry University, Harbin. Pp 21-24.
 32. Zhang, Y.L., Cai, L.P., 2008: Impact of heating speed on permeability of sub-alpine fir. *Wood Science and Technology* 42(3): 241-250.
 33. Zhou, Y.D., Fu, F., Li, X.J., Jiang, X.M., Chen, Z.L., 2009: Effects of microwave treatment on residue growth stress and microstructure of *Eucalyptus urophylla*. *Journal of Beijing Forestry University* 2: 146-150.
 34. Zhou, Y., Li, P., Zuo, Y.F., Yuan, G.M., Li, X.J., Wu, Y.Q., 2019: Research progress and development trend of inorganic reinforced wood. *Material Reports* 33(17): 2289-2296.

YINLUAN QIN*

¹GUANGXI ECO-ENGINEERING VOCATIONAL AND TECHNICAL COLLEGE
JUNWU ROAD 168
LIUZHOU, CHINA

²BEIJING FORESTRY UNIVERSITY
MOE ENGINEERING RESEARCH CENTRE OF FORESTRY BIOMASS MATERIALS
AND BIOENERGY
QINGHUA EAST ROAD 35
BEIJING, CHINA

LONGHAI CHEN
GUANGXI ECO-ENGINEERING VOCATIONAL AND TECHNICAL COLLEGE
JUNWU ROAD 168
LIUZHOU, CHINA

*Corresponding author: 310227543@qq.com

INFLUENCE OF SIZE EFFECT ON THE BEARING CAPACITY OF THE AXIALLY COMPRESSED COMPONENTS OF CORN STRAW INTEGRATED MATERIAL AND ITS CALCULATION METHOD

XUE FENG, BOXIN WANG
JILIN UNIVERSITY
CHINA

YONGMEI QIAN, WEI TIAN
JILIN JIANZHU UNIVERSITY
CHINA

(RECEIVED MAY 2021)

ABSTRACT

Our paper proposed a new type of environmentally friendly biomass material, corn straw integrated material (CSIM). In this paper, the ultimate bearing capacity of the axially compressed components under parallel, vertical and combined texture-integrated methods are compared and analyzed through the experimental research. The influence of size effect on the bearing capacity of the axially compressed components of the CSIM is determined, and the calculation method of the bearing capacity of the axially compressed components under vertical texture-integrated method is proposed. Results showed that the slenderness ratio of 35 was the dividing point between the strength and instability failures of the CSIM axially compressed component, and the calculated value of the revised bearing capacity calculation method agreed with the test value. The result is very close to the American National design specification for wood construction (ANSI/AF&PA NDS, 2005).

KEYWORDS: Corn straw integrated material, size effect, cross-section aspect ratio, slenderness ratio, axial compression.

INTRODUCTION

In the past, traditional biomass building materials rely on wood. However, excessive deforestation, lack of forest resources, and characteristics of flammable, perishable, and insect-eaten wood severely restrict the application and development of biomass building materials (Lazar and Chithra 2020). The corn straw integrated material (CSIM) is a new type of

biomass high-strength composite material produced through a series of processes, such as reorganization and integration of corn straw fiber raw materials. According to the different horizontal and vertical textures, the corn straw restructured plank can be made into parallel, vertical, and combined texture-integrated materials. The corn straw restructured plank has excellent characteristics, such as high strength, high hardness, insect resistance, moisture resistance, corrosion resistance, high fire resistance, and good compression mechanical properties (Qian et al. 2019a).

Straws as a building material first appeared in the 19th century when the residents of Nebraska, USA used straw bricks made of straw stalks to build brick walls to support their roofs (Kammoun and Trabelsi 2020). At the beginning of the 20th century, the United Kingdom, Poland, and other countries mastered the production technology of straw wood-based panels (Marques et al. 2020, Owodunni et al. 2020). At present, straw wood-based panel processing plants led by the United States have spread in more than 20 countries around the world (Mehrashadi et al. 2019), and the development and utilization of straw materials are well developed. The research of stem-based biomass building materials in China particularly in the research of stem-based and straw panels began in the 1980s (Tu 2004, Liuzzi et al. 2020, Aladejana et al. 2020, Koh and Kraniotis 2020, Chinh et al. 2020). In 2006, the first continuous production line of straw plank established by China Yantai Wanhua Group was officially put into production (Liu et al. 2019), which put the research on straw building materials go further.

In recent years, integrated wood (Wechsler and Hiziroglu 2007, Leggate et al. 2020), integrated bamboo (Li et al. 2019, Wei et al. 2020), and straw-based integrated wood (Soroshian et al. 2004) have received increasing research and applications, thereby promoting the development of biomass building materials. At present, domestic and foreign straw-based biomass building materials are mostly made of wood-based panels, bamboo-wood (metal/concrete) composite materials, and reinforced cement-based materials (Zhao et al. 2019, Hu et al. 2020, Sun et al. 2020). The stem-based panel is a man-made synthetic plank made by hot pressing and other processes after the stalk is processed into particles. The stem-based panel cannot be used as a building structural material during use and is mostly used in carriage floor and as furniture material and decoration (Yang et al. 2020, Qian et al. 2019b, Wang et al. 2019, Qi et al. 2019, Titirla et al. 2020, Xie et al. 2020). According to the preliminary experimental research of the research group, it is different from the processing technology and application scope of the stem-based panel's materials currently on the market. The integrated material processed and produced from corn straw intact fiber makes up for the shortcomings of existing materials and can be used in traditional home decoration and as building structural materials.

Therefore, this paper adopts the CSIM as a new type of biomass building structural material and studies the equal-scale axially compressed components of the CSIM by using three integration methods (i.e. parallel, vertical, and combined texture-integrated). By comparing the ultimate bearing capacity of the axially compressed components with different size parameters, the influence of factors, such as cross-section aspect and slenderness ratios, on the bearing capacity of axially compressed components is analyzed. The theoretical value of the bearing capacity in the specification is compared with the experimental value, and the calculation method of the bearing capacity of the axially compressed component with

the vertical texture-integrated is proposed. The calculation method provides theoretical support for the application of CSIM in building structures and promotes the effective use of corn straws as agricultural waste and environmental protection in the building materials industry.

MATERIAL AND METHODS

Corn straw integrated material (CSIM) is composed of corn straw restructured planks, which are processed and produced by sizing and pressing with a factory cold press. Corn straw recombination material, is a new type of high-strength composite material that is formed by layer-by-layer overlaying and sizing and pressing of corn straw fibers (Qian et al. 2019a,b, Tian et al. 2020), as shown in Fig. 1.

According to the different transverse and longitudinal textures of the cross-section of the recombination material, recombination material were cut into planks along the X- and Y-directions to obtain the parallel texture plank and the vertical texture plank of the corn straw recombination material. The planks with different textures were sized, pressed and integrated to obtain the corn straw parallel texture, vertical texture or combined texture components.

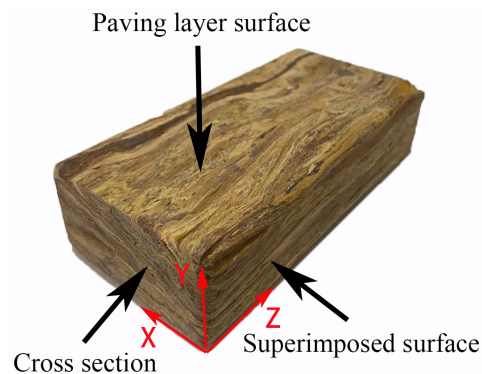


Fig. 1: Corn straw recombination material.

Considering that different integration methods have different mechanical properties, the axial compression test was carried out on the components of three integration methods to study the influence of different size parameters on the bearing capacity of the axial compression components of the CSIM.

In this paper, the JAY-10000KN microcomputer-controlled electrohydraulic servo pressure testing machine was used to carry out the uniform speed loading test. Test was terminated when the test specimen failed. The axially compressed components of the CSIM were divided into three groups, i.e., P, V, and C, which represented parallel, vertical, and combined texture-integrated methods, respectively. The components had cross-sectional dimensions of 150×150 mm and 150×180 mm and heights of 1000 mm and 1800 mm. The thickness of the integrated plank was 30 mm, and a total of 12 integrated material axial compression column components were designed. The calculation of Slenderness ratio λ refers to the American *National design specification for wood construction* (ANSI/AF&PA NDS, 2005).

The physical specimens are shown in Fig. 2. The arrangement of measuring points is shown in Fig. 3, and the specific design parameters of the component are presented in Tab. 1.



Fig. 2: CSIM specimens.

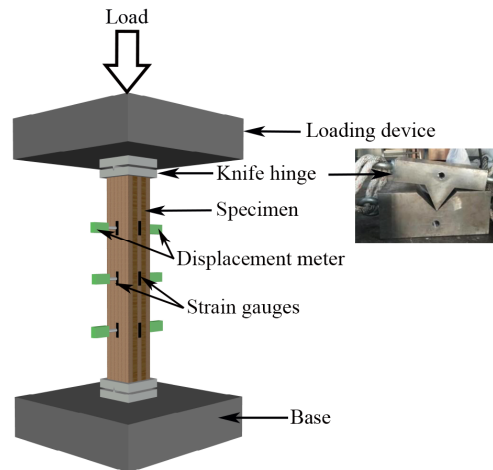


Fig. 3: Location of measuring points.

Tab. 1: Design parameters of the CSIM.

Integrated texture	Specimen number	Number	Sectional dimension, b_{\max} (mm) \times b_{\min} (mm)	Height (mm)	Cross-section aspect ratio, b_{\max}/b_{\min}	Slenderness ratio, λ
Parallel texture integration	P-1	1	150 \times 150	1000	1.0	23.09
	P-2	1	150 \times 150	1800	1.0	41.57
	P-3	1	150 \times 180	1000	1.2	19.24
	P-4	1	150 \times 180	1800	1.2	34.64
Vertical texture integration	V-1	1	150 \times 150	1000	1.0	23.09
	V-2	1	150 \times 150	1800	1.0	41.57
	V-3	1	150 \times 180	1000	1.2	19.24
	V-4	1	150 \times 180	1800	1.2	34.64
Combined texture integration	C-1	1	150 \times 150	1000	1.0	23.09
	C-2	1	150 \times 150	1800	1.0	41.57
	C-3	1	150 \times 180	1000	1.2	19.24
	C-4	1	150 \times 180	1800	1.2	34.64

RESULTS AND DISCUSSION

The failure traits of the CSIM are strength and instability failures. The strength failure is divided into split and end partial pressure failures. The instability failure is an overall buckling failure, and the failure mode of the CSIM is similar to that of steel–wood (bamboo) composites under axial compression (Razavian et al. 2020, Zhang et al. 2020). All components are divided into four groups. Group 1 contains P-1, V-1, and C-1. Group 2 includes P-2, V-2, and C-2. Group 3 includes P-3, V-3, and C-3. Group 4 contains P-4, V-4, and C-4. The following is an analysis of the effect of size parameters on the bearing capacity of the axially compressed components of CSIM under different integration methods through the cross-sectional aspect and slenderness ratios, and proposes the calculation method for the bearing capacity of vertical texture-integrated axial compression components.

Plotted the midpoint cross-sectional stress–strain relationship curve of all components of the CSIM, as shown in Fig. 4.

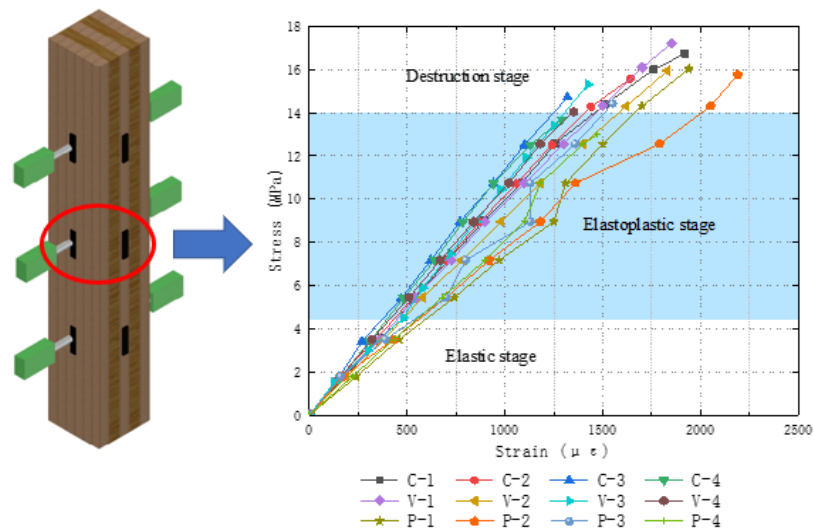


Fig. 4: Stress–strain curve of all components.

Research results show that the strain increases with stress during the whole loading process of axially compressed components. In the initial stage of test loading, the strain of the component increases linearly with stress. In the elastic stage, the slope of the stress–strain curve is basically the same, and the developed stress–strain relationship that the component under axial compression is regular. When the test enters the late stage of elastoplasticity, the slope of the stress–strain curve of each specimen gradually slows down. In the whole process, no evident yield platform and a descending section for each integrated axial compression component are observed. When the bearing capacity reaches the ultimate load, the material suddenly fails without evident plastic deformation. When the test force is relieved, the axial deformation of each component is generally restored to a straight state, indicating that although the axial compression component of the CSIM has a certain elastoplasticity when broken, CSIM is generally brittle. Under the condition of same section size, a high slenderness ratio of the

component results in low stress. At the same column height, a small section size of the component increases the stress.

Influence of cross-section aspect ratio on the bearing capacity

Among the three components under different integration methods, components with different cross-sectional aspect ratios and same integration method and height are selected for comparison. Figs. 5a-c are the load–axial displacement comparison curves of groups 1 and 3 under parallel, vertical, and combined texture-integrated methods. Figs. 5d-f are the load–axial displacement comparison curves of groups 2 and 4 under parallel, vertical, and combined texture-integrated methods.

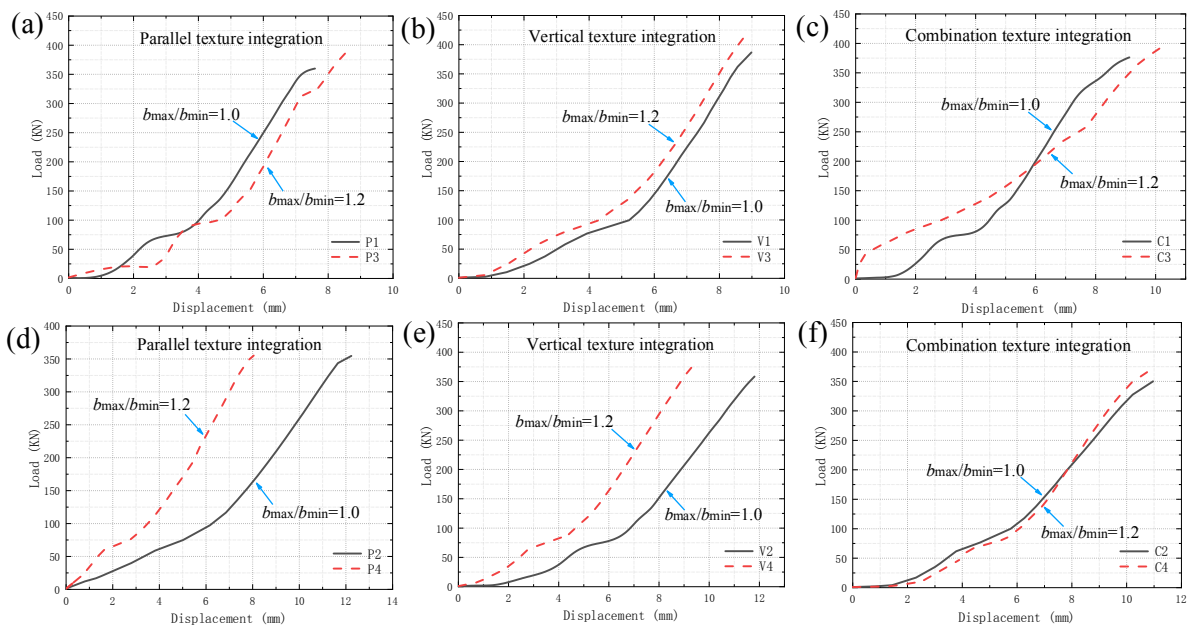


Fig. 5: Load–axial displacement curves of components with different cross-section aspect ratios. Groups 1 and 3 under parallel (a), vertical (b), and combined (c) texture-integrated methods. Groups 2 and 4 under parallel (d), vertical (e), and combined (f) texture-integrated methods.

Fig. 5 shows that with increasing cross-section aspect ratio, increased ultimate load of the component and decreased axial displacement are observed. Compared with those of components under parallel and combined texture-integrated methods, the curve growth trend of components under the vertical texture-integrated is more regular under the same load. In the whole process of loading, the components exhibit mechanical properties, and a large cross-section aspect ratio results in strong ultimate load-carrying capacity. The large cross-section aspect ratio of the individual components under the parallel texture-integrated results in low ultimate load-bearing capacity. This phenomenon occurred when the parallel texture-integrated plank is subjected to axial pressure, the cracks generated follow the longitudinal texture of the component, and the internal bonding capacity of the material is weakened. When the crack develops to a certain extent, the component loses its load-bearing

capacity and reaches destruction, and the vertical texture-integrated plank limits the development of the crack under the action of the axial pressure, thereby improving the load-bearing capacity of the component.

Influence of slenderness ratio on the bearing capacity

The components with different slenderness ratios under the three integration methods are compared. Figs. 6a-c plot the load–axial displacement comparison curves of the components with different slenderness ratios under the parallel, vertical, and combined texture-integrated methods, resp.

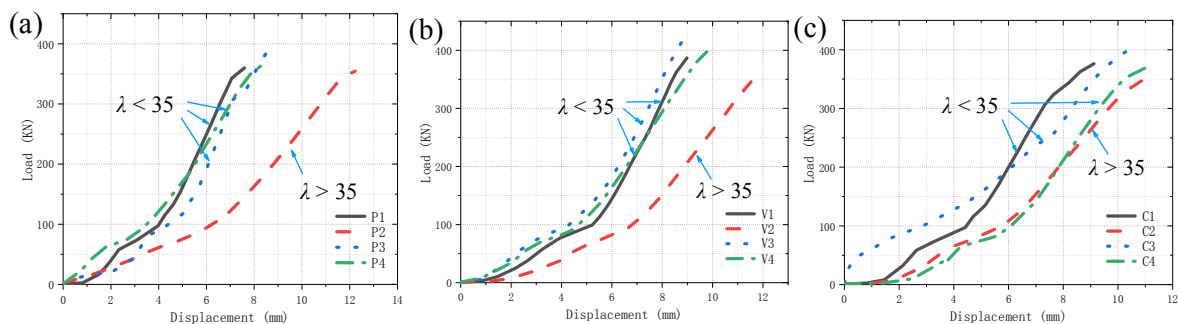


Fig. 6: Load–axial displacement curves of components with different slenderness ratios under parallel (a), vertical (b), and combined (c) texture-integrated methods.

Fig. 6 shows that as the slenderness ratio increases, the bearing capacity of the axially compressed components of each integration method is significantly reduced. From the perspective of the trend of displacement with load, a high slenderness ratio of the component results in high displacement change. Under the same load, the displacement of the component under the parallel texture-integrated is the largest followed by that under the combined texture-integrated. The component under the vertical texture-integrated has the smallest displacement. The load–displacement relationship increases linearly during the entire process from the beginning of loading to the ultimate load. The load–axial displacement curve shows that the axial displacement value of the component with $\lambda > 35$ is greater than that of the component with $\lambda < 35$. The curve trend of the vertical texture-integrated component is regular, and the load change under the axial pressure has good reliability and predictability. When the component is subjected to axial pressure, a small slenderness ratio results in strong bearing capacity.

The ultimate load–slenderness ratio comparison curve of different integration methods is drawn and shown in Fig. 7. The above data show that among the three integration methods of the CSIM, the vertical texture-integrated provides the highest ultimate bearing capacity followed by the combined and parallel texture-integrated methods. The trend of the ultimate load–slenderness ratio curve of the three integrated axially compressed components is the same. With increasing slenderness ratio, the ultimate load of the axially compressed components of each integration method gradually decreases. Given that the *Technical code of glued laminated timber structures* (GBT50708, 2012) and the *National design specification for wood*

construction (ANSI/AF&PA NDS, 2005) require that the slenderness ratio for solid columns shall not exceed 50, when the slenderness ratio is higher than 40, the bearing capacity of the component decreases remarkable. Combined with the test results in this paper, the study shows that when $\lambda > 35$, the ultimate bearing capacity of the axially compressed components under various integration methods of CSIM is significantly reduced, and the axial displacement is significantly increased. It indicates that this is the dividing point between the strength failure and the instability failure of the axially compressed component. When $\lambda < 35$, the component has strength failure. When $35 < \lambda < 40$, the component has strength and instability failures, and when $\lambda > 40$, the component has the instability failure.

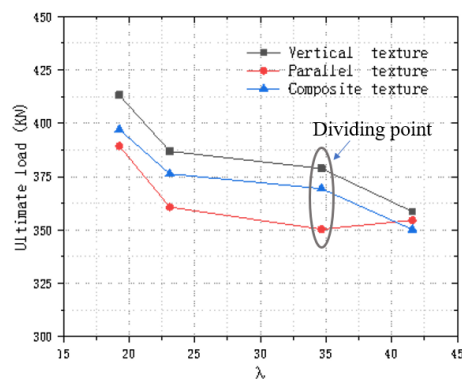


Fig. 7: Load–slenderness ratio comparison curve of components under different integration methods.

In summary, the cross-sectional aspect and slenderness ratios as different size parameters of the components have a higher effect on the compressive bearing capacity of the CSIM. The cross-sectional aspect ratio determines the bearing capacity of the component, and the slenderness ratio determines the difference in the failure traits of the component. However, increasing the cross-section aspect ratio reduces the slenderness ratio of the component, affects the damage traits of the component, and increases the engineering cost. Therefore, the rationality of the cross-section aspect and the slenderness ratios should be fully considered in the component design.

Calculation method of the bearing capacity of the axially compressed component under the vertical texture-integrated

Based on the above research, under the action of axial compression, the vertical texture-integrated method has the highest bearing capacity among the three integration methods of CSIM. This finding shows that when using an axially compressed component, the optimal integration method is the vertical texture-integrated method. The calculation method of the bearing capacity of the axially compressed component under the vertical texture-integrated is analyzed below. The bearing capacity test results of axially compressed components with different slenderness ratios are compared with that in the American *National design specification for wood construction* (ANSI/AF&PA NDS, 2005). The slenderness ratio–ultimate load comparison curve of the axially compressed components under the vertical

texture-integrated is shown in Fig. 8. Figs. 11a,b show specimens with sectional dimensions of 150×150 mm and 150×180 mm.

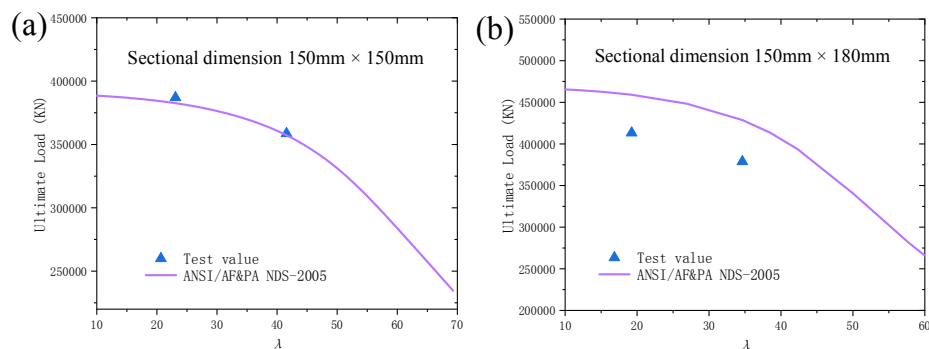


Fig. 8: Load–slenderness ratio comparison curve of the axially compressed component under the vertical texture-integrated. Sectional dimensions 150×150 mm (a), 150×180 mm (b).

Fig. 8a shows that for components with equal cross-section sides, test results are close to the calculated results of the American *National design specification for wood construction*. This finding shows that the American *National design specification for wood construction* applies to the calculation of the ultimate bearing capacity of the vertical texture-integrated axial compression component of the CSIM. For components with unequal cross-section side lengths, the actual test results are quite different from the specification calculated values, and the effective side lengths (b_c) in the specification should be introduced to modify the formula (Fig. 8b). The calculation formula of the vertical texture-integrated axial compression bearing capacity of CSIM is established:

$$N = \varphi b_c^2 f_c \quad (1)$$

where: N - axial compression design value for the vertical texture-integrated material (N), φ - stability coefficient, b_c - effective side lengths (mm), f_c - compressive strength design value parallel to the grain of vertical texture-integrated material ($\text{N}\cdot\text{mm}^{-2}$), $f_c = 17.32$ MPa.

The CSIM, a reorganized integrated material, is different from wood in terms of specifications, and the calculated area of the cross-section of the compression component is different from that of ordinary wood. Therefore, when calculating the bearing capacity of axially compressed components, b_c is introduced in this article to correct the calculated area of the axial compression component cross-section in the calculation formula of bearing capacity. The calculation coefficient of the support condition in the original b_c calculation formula is removed to avoid repeated calculations, and the calculation is adjusted to the formula:

$$b_c = b_{\min} + 0.15(b_{\max} - b_{\min})(b_{\min} / b_{\max}) \quad (2)$$

where: b_{\max} - maximum dimension for that face of the column (mm), and b_{\min} - minimum dimension for that face of the column (mm).

The stability coefficient (φ) in Eq. 1 is calculated in accordance with φ of axially compressed components in the American National design specification for wood construction:

$$\varphi = \frac{1 + (f_{cE} / f_c)}{2c} - \sqrt{\left[\frac{1 + (f_{cE} / f_c)}{2c} \right]^2 - \frac{f_{cE} / f_c}{c}} \quad (3)$$

where:

$$f_{cE} = \frac{0.822 E_{\min}'}{(l_0 / b_c)^2} \quad (4)$$

and

$$E_{\min}' = E[1 - 1.645 COV_E](1.05)/1.66 \quad (5)$$

where: f_{cE} - critical buckling strength design value for compressive parallel to grain ($\text{N}\cdot\text{mm}^{-2}$), $c = 0.9$ for bending coefficient for glued laminated timber, E_{\min}' - reference and adjusted moduli of elasticity for stability calculations ($\text{N}\cdot\text{mm}^{-2}$), l_0 - effective length (mm), E - elastic modulus ($\text{N}\cdot\text{mm}^{-2}$), $E = 11053 \text{ MPa}$, $COV_E = 0.1$ for the coefficient of variation of elastic modulus.

The calculation curves of the bearing capacity before and after correction with the test values are compared. Figs. 9a,b plot the slenderness ratio–ultimate load comparison curves of the test value, specification value, and the value calculated using the modified formula of the specimen with the cross-section size of $150 \times 150 \text{ mm}$ and $150 \times 180 \text{ mm}$.

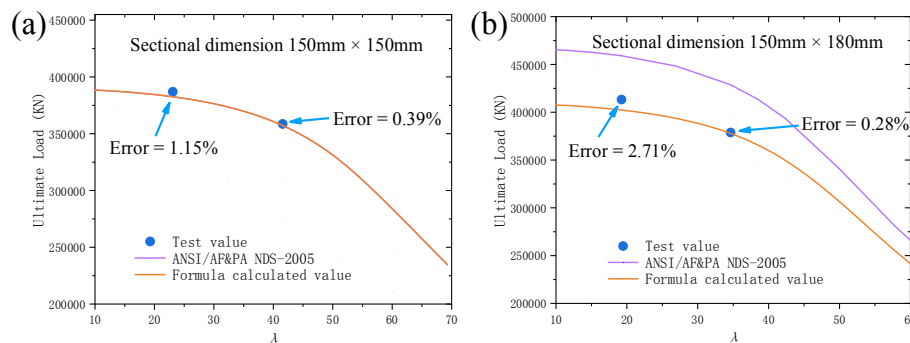


Fig. 9: Load–slenderness ratio comparison curve of the axially compressed component under the vertical texture-integrated: Sectional dimension $150 \times 150 \text{ mm}$ (a), Sectional dimensions $150 \times 180 \text{ mm}$ (b).

Figs. 9a,b show that the average error between the value calculated using the modified formula and the measured ultimate load in the test is 1.13%. The data are in good agreement, indicating that this calculation method can effectively predict the ultimate bearing capacity of vertical texture-integrated axial compression components. The above calculation method can be used as a theoretical basis for the study of the ultimate bearing capacity of the axial compressed components of CSIM under the vertical texture-integrated.

CONCLUSIONS

This paper studies the influence of size effect on the bearing capacity of the axially compressed components of CSIM and provides a reference for the promotion and design of new biomass building structural materials. The following conclusions can be drawn from this study: (1) On the basis of the calculation method of the bearing capacity of axially compressed components in the American National design specification for wood construction, b_c is introduced and modified to improve the formula. A calculation method for the axial compression bearing capacity of the component of the CSIM under the vertical texture-integrated is proposed. The theoretical calculation value obtained by this calculation method agrees with the experimental value, which can effectively predict the ultimate bearing capacity of the axially compressed component under the vertical texture-integrated. (2) The failure traits of the axially compressed components of the CSIM are divided into strength and instability failures. $\lambda = 35$ is the cutoff point between the strength and instability failures of the axially compressed components. When $\lambda < 35$, the component has strength failure, when $35 < \lambda < 40$, the component has strength and instability failures, and when $\lambda > 40$, the component has instability failure. (3) For the axially compressed components of CSIM, a large slenderness ratio results in small bearing capacity under the condition of the same cross-sectional aspect ratio. At the same column height, as the cross-sectional aspect ratio increases, decreased slenderness ratio, increased bearing capacity, and increased damage phenomenon are observed. (4) From the perspective of integrated texture, the parallel texture-integrated plank reduces the bearing capacity of the component when subjected to axial pressure, whereas the vertical texture-integrated plank can improve the overall strength of the component, and the vertical texture-integrated provides higher material stability after failure than the two other integration method.

ACKNOWLEDGMENTS

This research work was financially supported by the Key Science and Technology Projects in Jilin Province, China (Grant No. 20180201066SF). The authors have no conflict of interest to declare.

REFERENCES

1. Aladejana, J.T., Wu, Z., Fan, M., Xie, Y., 2020: Key advances in development of straw fibre bio-composite boards: An overview. *Materials Research Express* 7(1): 1-19.
2. Chinh Van, N., Mangat, P.S., 2020: Properties of rice straw reinforced alkali activated cementitious composites. *Construction and Building Materials* 261(2): 120536.
3. Hu, Q., Gao, Y., Meng, X., Diao, Y., 2020: Axial compression of steel-timber composite column consisting of H-shaped steel and glulam. *Engineering Structures* 216: 110561.
4. Kammoun, Z., Trabelsi, A., 2020: A high-strength lightweight concrete mace using straw. *Magazine of Concrete Research* 72(9): 460-470.

5. Koh, C.H., Kraniotis, D., 2020: A review of material properties and performance of straw bale as building material. *Construction and Building Materials* 259: 120385.
6. Lazar, N., Chithra, K., 2020: A comprehensive literature review on development of building sustainability assessment systems. *Journal of Building Engineering* 32: 101450.
7. Leggate, W., McGavin, R.L., Miao, C., Outhwaite, A., Chandra, K., Dorries, J., Kumar, C., Knackstedt, M., 2020: The influence of mechanical surface preparation methods on southern pine and spotted gum wood properties: Wettability and Permeability. *Bioresources* 15(4): 8554-8576.
8. Li, H.T., Liu, R., Lorenzo, R., Wu, G., Wang, L.B., 2019: Eccentric compression properties of laminated bamboo columns with different slenderness ratios. *Proceedings of the Institution of Civil Engineers: Structures and Buildings* 172(5): 314-326.
9. Liu, H.G., Luo, B., Shen, S.J., Li, L., 2019: Review of research and development of straw building materials. *Forestry Machinery & Woodworking Equipment* 47(05): 4-12.
10. Liuzzi, S., Rubino, C., Martellotta, F., Stefanizzi, P., Casavola, C., Pappaletta, G., 2020: Characterization of biomass-based materials for building applications: The case of straw and olive tree waste. *Industrial Crops and Products* 147: 112229.
11. Marques, B., Tadeu, A., Almeida, J., Antonio, J., de Brito, J., 2020: Characterisation of sustainable building walls made from rice straw bales. *Journal of Building Engineering* 28: 101041.
12. Mehrmashadi, J., Chen, Z.G., Zhao, J.M., Bobaru, F., 2019: A stochastically homogenized peridynamic model for intraply fracture in fiber-reinforced composites. *Composites Science and Technology* 182: 107770.
13. Owodunni, A.A., Lamaming, J., Hashim, R., Taiwo, O.F.A., Hussin, M.H., Mohamad Kassim, M.H., Bustami, Y., Sulaiman, O., Amini, M.H.M., Hiziroglu, S., 2020: Adhesive application on particleboard from natural fibers: A review. *Polymer Composites* 41(11): 4448-4460.
14. Qi, Y., Xie, L., Bai, Y., Liu, W., Fang, H., 2019: Axial compression behaviours of pultruded GFRP-Wood Composite Columns. *Sensors* 19(4): 755.
15. Qian, Y.M., Feng, X., Tian, W., Liu, Z.P., 2019a: Experimental research on compressive performance parameters of new type corn straw. *Industrial Construction* 49(08): 163-166.
16. Qian, Y.M., Feng, X., Tian, W., 2019b: Preliminary study on mechanical properties of corn straw recombinant glulam. *Building Structure* 49(S1): 273-275.
17. Razavian, L., Naghipour, M., Shariati, M., Safa, M., 2020: Experimental study of the behavior of composite timber columns confined with hollow rectangular steel sections under compression. *Structural engineering and mechanics* 74(1): 145-156.
18. Soroushian, P., Aouadi, F., Chowdhury, H., Nossoni, A., Sarwar, G., 2004: Cement-bonded straw board subjected to accelerated processing. *Cement & Concrete Composites* 26(7): 797-802.
19. Sun, X., He, M., Li, Z., 2020: Novel engineered wood and bamboo composites for structural applications: State-of-art of manufacturing technology and mechanical performance evaluation. *Construction & Building Materials* 249: 118751.

20. Titirla, M.D., Ferrier, E., Michel, L., 2020: On the mechanical behaviour of innovative moment connections between composite floor panels and glulam columns. *International Journal of Architectural Heritage* 15(2): 321-333.
21. Tian, W., Wang, Y.M., Qian, Y.M., Wang, R.Z., 2020: Finite element modeling and analysis of tensile strength of novel corn stalk recombinant glulam component. *Dynamic Systems and Applications* 29(6): 20202969.
22. Tu, P.T., 2004: Building board produced by agricultural residues and its development status. *Brick-Tile* 12: 30-36.
23. Wang, J., Duan, S., He, J., Wang, Z., 2019: Experimental analysis of eccentric compression performance of larch wood-steel composite columns. *Advances in Civil Engineering* 2019: 1-17.
24. Wechsler, A., Hiziroglu, S., 2007: Some of the properties of wood-plastic composites. *Building and Environment* 42(7): 2637-2644.
25. Wei, Y., Zhou, M., Zhao, K., Zhao, K., Li, G., 2020: Stress-strain relationship model of glulam bamboo under axial loading. *Advanced Composites Letters* 29.10.1177/2633366X20958726.
26. Xie, Z., Hu, X., Du, H., Zhang, X., 2020: Vibration behavior of timber-concrete composite floors under human-induced excitation. *Journal of Building Engineering* 32: 101744.
27. Yang, R., Li, H., Lorenzo, R., Ashraf, M., Sun, Y., Yuan, Q., 2020: Mechanical behaviour of steel timber composite shear connections. *Construction and Building Materials* 258: 119605.
28. Zhang, X.B., Jiang, Z.H., Fei, B.H., Fang, C.H., Liu, H.R., 2020: Experimental performance of threaded steel glued into laminated bamboo. *Construction and building materials* 249: 118780.
29. Zhao, W., Yang, B., Zhou, J., 2019: Axial compressive creep behaviour of a square steel tube/bamboo plywood composite column with binding bars. *Wood Research* 64(2): 223-235.

XUE FENG, BOXIN WANG
JILIN UNIVERSITY
COLLEGE OF CONSTRUCTION ENGINEERING
CHANGCHUN, JILIN 130021
CHINA

YONGMEI QIAN*, WEI TIAN
JILIN JIANZHU UNIVERSITY
CHANGCHUN, JILIN 130118
CHINA

*Corresponding author: qianyongmei@jlju.edu.cn

WOOD CHEMICAL COMPONENTS AND DECAY RESISTANCE OF FOUR COMMON MONGOLIAN SOFTWOODS

MURZABYEK SARKHAD^{1,2,3}, FUTOSHI ISHIGURI¹, IKUMI NEZU^{1,2},
BAYASAA TUMENJARGAL³, BAYARTSETSEG BAASAN³, GANBAATAR
CHULTEM³, JYUNICHI OHSHIMA¹, NAOTO HABU¹, SHINSO YOKOTA¹

¹ UTSUNOMIYA UNIVERSITY, JAPAN

² TOKYO UNIVERSITY OF AGRICULTURE & TECHNOLOGY, JAPAN

³ MONGOLIAN UNIVERSITY OF SCIENCE & TECHNOLOGY, MONGOLIA

(RECEIVED JULY 2021)

ABSTRACT

To utilize wood resources in Mongolia, amounts of wood chemical components (hot-water extracts, 1% NaOH extracts, ethanol-toluene extracts, holocellulose, α -, β -, and γ -cellulose, Klason lignin, and ash) were determined in four common Mongolian softwoods, *Pinus sylvestris*, *Pinus sibirica*, *Picea obovata*, and *Larix sibirica*. In addition, decay resistance of heartwood was evaluated against a white-rot fungus *Trametes versicolor*, and a brown-rot fungus *Formitopsis palustris*. Among the four species, heartwood of *Larix sibirica* was chemically characterized by higher amounts of hot-water and 1% NaOH extracts, and lower amounts of holocellulose and Klason lignin. These characteristics may be related to the presence of arabinogalactan which is easily extracted with cold water. Mean mass loss in each softwood ranged from 6.9% to 28.1% in white-rot fungus, and from 24.8% to 48.3% in brown-rot fungus. Among four species, *Pinus sibirica* showed the highest decay resistance against both fungi. By the linear mixed-effects model analysis, negative relationships were found between mass loss and amounts of extracts in heartwood, suggesting that heartwood having larger amounts of extracts showed higher natural decay durability.

KEYWORDS: *Pinus sylvestris*, *Pinus sibirica*, *Picea obovata*, *Larix sibirica*, *Trametes versicolor*, *Formitopsis palustris*, extractives.

INTRODUCTION

Forests of Mongolia are mainly found in the northern parts and west parts of the country (FAO 2020). Almost all forests are natural forests and approximately 80% in stock volume of the forests is occupied by *Larix sibirica* (Ministry of Nature, Environment and Tourism 2019). The

nearly 15% of remaining stock volume is composed of *Pinus sylvestris*, *Pinus sibirica*, *Picea obovata* and others (Ministry of Nature, Environment and Tourism 2019). Thus, these four softwood species are considered as common forestry coniferous species in Mongolia.

Recently, we investigated properties of Mongolian wood (Ayush et al. 2019, Tumenjargal et al. 2019, 2020a,b,c, Erdene-Ochir et al. 2020). In our previous reports, we examined dimension lumber quality of the four common Mongolian softwoods (Sarkhad et al. 2020). We found that bending properties of dimension lumber were almost similar with those in similar species in Japan, US and other countries (Sarkhad et al. 2020). Thus, high quality solid wood can be produced from Mongolian softwoods. On the other hand, natural decay resistance of wood is one of the important factors to utilize the wood resources as solid wood production, especially for construction lumber. However, there is currently no information regarding the natural decay resistance of these four common Mongolian softwoods, with the exception of *Larix sibirica* (Ishiguri et al. 2018).

It is known that natural decay resistance of wood is closely related to the extractive contents (Srinivasan et al. 1999, Taylor et al. 2002, Windeisen et al. 2002, Venäläinen et al. 2003, 2006, Archer and Lebow 2010, Jebrane et al. 2014, Takashima et al. 2015, Belt et al. 2017). Venäläinen et al. (2006) reported that significant negative correlations were found between mass loss of wood by three brown-rot fungi (*Coniophora puteana*, *Poria placenta* and *Gloeophyllum trabeum*) and amounts of extractives such as total phenolics, taxifolin, total flavonoids, and water-soluble extractives in *Larix sibirica* wood. Unfortunately, information about the amounts of wood chemical components including extractives is still limited for all four common Mongolian softwoods except for *L. sibirica* (Ishiguri et al. 2018). Thus, wood chemical components, especially for extractives, should be clarified in relation to natural decay resistance of wood in common conifers grown in Mongolia.

This is the first report dealing with amounts of wood chemical components and decay resistance of four common Mongolian softwoods. We determined amounts of wood chemical components (hot-water extracts, 1% NaOH extracts, ethanol-toluene extracts, holocellulose, α -cellulose, β -cellulose, γ -cellulose, Klason lignin and ash). In addition, decay resistance of heartwood was investigated against a white-rot fungus, *Trametes versicolor*, and a brown-rot fungus, *Formitopsis palustris*. Based on the results, relationships between mass loss and amounts of extractives were discussed.

MATERIALS AND METHODS

Materials

P. sylvestris, *P. sibirica*, *P. obovata*, and *L. sibirica* trees were harvested from natural forests located in Mandal, Selenge, Mongolia (Tab. 1). The samples used in the present study were the same as the samples used in the previous study (Sarkhad et al. 2020). Five trees in each species were harvested. The logs with 50 cm lengths were collected from 0.8 to 1.3 m above the ground. The logs were sawn into radial boards (bark to bark with the pith, 30 mm in thickness) and were subsequently air-dried. A board from a tree of *P. obovata* had partial decay in heartwood. Thus, heartwood samples were collected from the boards of 19 trees. By using these

air-dried boards, heartwood and sapwood wood meal (42 to 80 mesh) and small wood blocks of heartwood (10 x 20 x 20 mm, L x R x T) were prepared for determining the wood chemical components and performing the decay test, respectively.

Tab. 1: Information of sampling sites and sample trees (Sarkhad et al. 2020).

Information		<i>Pinus sylvestris</i>	<i>Pinus sibirica</i>	<i>Picea obovata</i>	<i>Larix sibirica</i>
Sampling site	Latitude	48°49'N	48°41'N	48°41'N	48°41'N
	Longitude	106°53'E	106°38'E	106°38'E	106°38'E
Sample	<i>n</i>	5	5	5	5
	D (cm)	27.1 (2.2)	26.5 (1.3)	27.9 (2.2)	25.6 (1.6)
	TH (m)	16.2 (2.2)	11.9 (1.5)	14.3 (2.3)	15.3 (1.3)
	ARN	72 (3)	62 (4)	60 (6)	50 (9)

Note: *n*- number of sample trees; *D*- stem diameter at 1.3 m above the ground; TH- tree height; ARN- annual ring number at 1.3 m above the ground. Values in parenthesis are standard deviation. Number of heartwood samples in *P. obovata* was four due to partial decay of heartwood.

Wood chemical components

The following wood chemical components were determined: hot-water extracts, 1% NaOH extracts, ethanol-toluene extracts, holocellulose, α -cellulose, β -cellulose, γ -cellulose, Klason lignin, and ash. These chemical components were quantified according to the method described by Kuroda (2000).

Decay resistance

The decay test was conducted according to the Japan Industrial Standard (JIS) K1571: 2010 and Takashima et al. (2015). A white-rot fungus, *Trametes versicolor* (FFPRI 1030), and a brown-rot fungus, *Formitopsis palustris* (FFPRI 0507), were used as the fungal materials. The heartwood samples were weighed after oven-drying at 60°C for 48 hours, and then sterilized with propylene oxide for 2 days. Three sterilized heartwood samples were placed on the surface of the fungal mat which was spread out on the medium (4% glucose, 0.3% peptone, 1.5% malt extracts, and 2.0% agar) in plastic bottles (9.5 cm in diameter and 850 mL in volume). Three bottles were prepared in each tree and fungus. The fungi with heartwood specimens were cultured at 26 ± 2°C and 70% relative humidity for 12 weeks. After 12 weeks of incubation, mycelium was carefully removed from the heartwood specimens using small brush or tweezers. Heartwood specimens were weighed after oven-drying at 60°C for 48 hours. To compare the degree of decay, sapwood samples of *Cryptomeria japonica* were also tested using the same method.

Statistical analysis

Statistical analysis was conducted by R software (R Core Team 2020). For the wood chemical components, mean values and standard deviations in each species were calculated from the data collected from each tree and wood type (heartwood or sapwood). Mean values of mass loss after the decay test in a tree were calculated by averaging the mass loss data of nine heartwood specimens from three plastic bottles for a species. The mean, standard deviation, and minimum and maximum values in each species were calculated by using the mean value for

a tree. The Tukey HSD test (5% level) was applied for detecting the differences of mass loss among species. To evaluate the relationships between mass loss and amounts of extracts in sound wood, the following linear mixed-effects model with species as random intercept was developed by using lmer function in lme4 package (Bates et al. 2015):

$$y_{ij} = \beta_0 x_{ij} + \beta_1 + u_{1j} + e_{ij} \quad (1)$$

where: y_{ij} is the measured value for the i^{th} individual tree of the j^{th} species; x_{ij} is the i^{th} individual tree of the j^{th} species, β_0 and β_1 are the fixed effects parameters, u_{1j} is the random effect of β_1 at the species levels, and e_{ij} is residual. Correlations of determination (R^2) were calculated for each linear mixed-effects model by using the rsq.lmm function in the rsq package (Zhang 2020).

RESULTS AND DISCUSSION

Wood chemical components

Tab. 2 shows amounts of wood chemical components in four common Mongolian softwoods. *L. sibirica* heartwood showed higher amounts of hot-water and 1% NaOH extracts and lower amounts of holocellulose, α -cellulose and Klason lignin as compared to the three other species. With the exception of *L. sibirica*, amounts of wood chemical components in heartwood were similar to those in sapwood. The heartwood of *L. sibirica* contained a large amount of arabinogalactan, which is easily extracted with hot or cold water (Côté et al. 1966, Venäläinen et al. 2006). Higher amounts of arabinogalactan in heartwood may potentially result in lower amounts of polysaccharides and Klason lignin.

Tab. 2: Amounts of wood chemical components in four Mongolian softwoods.

Species	Wood type	Extracts (%)			HC (%)	Cellulose (%)			KL (%)	Ash (%)
		Hot water	1% NaOH	ET		α	β	γ		
<i>Pinus sylvestris</i>	HW	5.6	17.4	5.8	81.5	50.3	1.9	28.7	27.8	0.3
		(1.7)	(2.4)	(3.3)	(2.1)	(2.0)	(0.4)	(1.3)	(1.9)	(0.1)
	SW	3.6	16.1	4.1	79.3	50.6	3.0	25.7	28.1	0.4
		(0.5)	(0.9)	(0.7)	(1.0)	(1.8)	(0.7)	(1.4)	(2.7)	(0.2)
<i>Pinus sibirica</i>	HW	9.3	21.2	7.0	76.7	46.0	1.9	28.8	28.1	0.3
		(1.1)	(2.0)	(1.3)	(2.9)	(2.3)	(0.5)	(0.9)	(1.7)	(0.1)
	SW	5.9	17.8	5.4	76.6	46.9	2.8	26.9	30.0	0.4
		(0.3)	(1.1)	(0.7)	(3.0)	(3.6)	(1.0)	(1.4)	(3.2)	(0.0)
<i>Picea obovata</i>	HW	3.2	13.3	2.8	79.0	49.0	3.3	26.7	28.0	0.4
		(1.0)	(0.8)	(1.0)	(0.9)	(0.9)	(0.9)	(1.3)	(0.8)	(0.1)
	SW	3.5	13.9	2.9	77.9	48.7	2.9	26.3	29.0	0.3
		(0.7)	(0.3)	(0.7)	(3.0)	(2.5)	(0.8)	(0.7)	(0.8)	(0.1)
<i>Larix sibirica</i>	HW	18.9	27.4	5.4	62.6	38.2	2.3	22.2	23.6	0.4
		(4.0)	(5.2)	(1.9)	(5.5)	(5.5)	(0.5)	(2.5)	(2.1)	(0.1)
	SW	4.9	14.3	6.3	78.6	50.8	2.4	25.4	27.1	0.3
		(1.1)	(1.8)	(4.3)	(2.7)	(3.9)	(0.5)	(3.4)	(0.6)	(0.1)

Note: ET- ethanol-toluene; HC- holocellulose; KL- Klason lignin; HW- heartwood; SW- sapwood. Values in parenthesis indicate standard deviations. Number of sample trees $n = 5$ except for α -, β -, and γ -cellulose in heartwood of *P. sylvestris* ($n = 4$) and heartwood of *P. obovata* ($n = 4$).

Amounts of wood chemical components of Japanese softwoods similar to Mongolian softwood species used in the present study are shown in Tab. 3. Compared to Japanese species, Mongolian softwoods showed relatively higher amounts of holocellulose and α -cellulose, although amounts of other wood chemical components were similar.

Tab. 3: Amounts of wood chemical components in Japanese softwoods (Yonezawa et al. 1973).

Species	Extracts (%)		Holocellulose (%)	α -cellulose (%)	Klason lignin (%)	Ash (%)
	Hot water	Ethanol-benzene				
<i>Pinus densiflora</i>	3.3	2.7	71.1	46.5	26.0	0.33
<i>Pinus densiflora</i>	3.9	4.1	65.8	43.6	26.1	0.22
<i>Pinus densiflora</i>	5.7	2.9	65.2	43.6	27.9	0.22
<i>Pinus thunbergia</i>	3.0	3.3	62.9	44.0	25.8	0.21
<i>Pinus pentaphylla</i>	3.2	8.1	68.4	44.5	27.1	0.27
<i>Picea jezoensis</i>	3.6	1.3	71.0	47.3	28.4	0.20
<i>Picea glehnii</i>	3.6	2.0	73.5	49.9	27.8	0.20
<i>Picea hondoensis</i>	3.3	2.2	64.4	41.9	28.8	0.15
<i>Larix kaempferi</i>	9.5	3.2	68.5	47.8	28.0	0.34

Note: Wood chemical components, except for holocellulose and α -cellulose, were determined by method described in JIS. Holocellulose was determined by the Wise method.

Decay resistance

Tab. 4 shows the mass loss of heartwood in four Mongolian common softwoods by *T. versicolor* and *F. palustris*. The mean mass loss ranged from 6.9% to 28.1% in *T. versicolor* and from 24.8% to 48.3% in *F. palustris*. In all four species, mass loss by *F. palustris* was higher than by *T. versicolor*. In general, most brown-rot fungi affect conifers, while white-rot fungi occur more frequently on hardwoods (Schmidt 2006). Our results were similar to those of the previous report (Schmidt 2006).

Among four species, *P. sibirica* heartwood showed the highest decay resistance against both *T. versicolor* and *F. palustris*, whereas mass loss in *P. obovata* showed the highest values (Tab. 4). In Japanese softwoods, a similar tendency was also found: *P. pentaphylla* (five-needle pine, similar to *P. sibirica*) showed relatively higher decay resistance, and mean values of *Picea* species (*P. jezoensis*, *P. glehnii*, and *P. hondoensis*) showed the lowest resistance.

Tab. 4: Mass loss (%) of heartwood specimens by *T. versicolor* and *F. palustris*.

Fungus	Statistics	<i>P. sylvestris</i>	<i>P. sibirica</i>	<i>P. obovata</i>	<i>L. sibirica</i>	Control
<i>T. versicolor</i>	<i>n</i>	5	5	4	5	1
	Mean	14.1 ^{ab}	6.9 ^b	28.1 ^a	23.4 ^a	34.3
	SD	4.6	1.7	16.3	7.6	5.4
	Min	9.2	5.0	11.2	15.5	-
	Max	19.7	9.6	43.6	32.1	-
<i>F. palustris</i>	<i>n</i>	5	5	4	5	1
	Mean	44.5 ^a	24.8 ^b	48.3 ^a	30.5 ^b	51.4
	SD	10.6	7.2	7.3	8.7	6.9
	Min	29.3	16.7	42.5	19.3	-
	Max	55.3	34.6	59.0	41.5	-

Note: *n*- number of sample trees (one tree has nine specimens). Control was sapwood of *C. japonica*. The same alphabet letters after mean values indicate no significances among species at 5% level in the Tukey HSD test.

Fig. 1 shows relative mass loss against the mass loss of sapwood of *Cryptomeria japonica*. Fig. 1 also included the relative mass loss for Japanese softwoods calculated from the data listed in Tab. 5. Compared to the Japanese two-needle *Pinus* spp., *P. sylvestris* showed a similar ratio in *T. versicolor* but a relatively higher ratio in *F. palustris*. In *P. sibirica*, the ratio in *T. versicolor* was lower than that of *P. pentaphylla*, whereas the ratio was higher in *F. palustris*. *P. obovata* showed a lower ratio compared to the Japanese *Picea* spp. in both fungi. *L. sibirica* showed a higher ratio in *T. versicolor* and a lower ratio in *F. palustris* as compared to *L. kaempferi*. It is concluded that higher decay resistance was found in *P. sibirica* against *T. versicolor*, *P. obovata* to both fungi, and *L. sibirica* to *F. palustris* compared to similar Japanese softwoods.

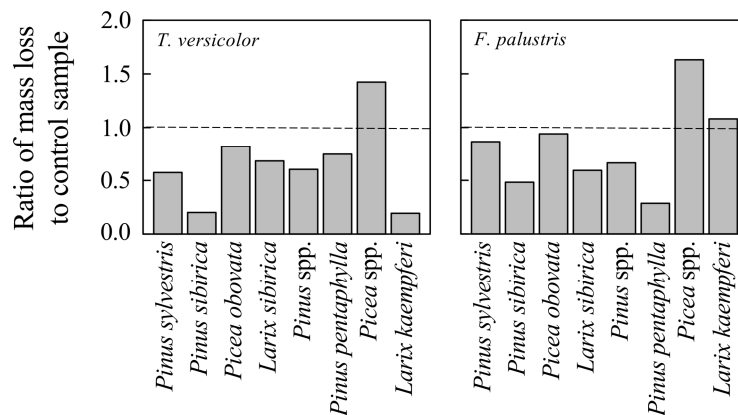


Fig. 1: Mass loss ratio of Mongolian species and Japanese softwoods against mass loss of sapwood in *Cryptomeria japonica*. Data of four Mongolian species are listed in Tab. 3. Data of *Pinus* spp. (two-needle pine), *P. pentaphylla*, *Picea* spp., *L. kaempferi* are listed in Tab. 5.

Tab. 5: Mass loss (%) of heartwood in Japanese softwoods by *T. versicolor* and *F. palustris* (Wood Technology and Wood Utilization Division 1982).

Species	<i>T. versicolor</i>	<i>F. palustris</i>
<i>Pinus densiflora</i>	7.0	8.0
<i>Pinus densiflora</i>	2.5	1.2
<i>Pinus densiflora</i>	3.6	13.1
<i>Pinus thunbergia</i>	5.4	3.2
<i>Pinus</i> (two-needle pine, mean)	4.4	7.4
<i>Pinus pentaphylla</i>	2.3	2.0
<i>Picea jezoensis</i>	11.7	20.1
<i>Picea glehnii</i>	13.9	17.5
<i>Picea hondoensis</i>	5.3	17.2
<i>Picea</i> spp. (mean)	10.3	18.3
<i>Larix kaempferi</i>	1.4	12.1
<i>Cryptomeria japonica</i> (SW)	10.8	11.9
<i>Cryptomeria japonica</i> (SW)	6.4	6.2
<i>Cryptomeria japonica</i> (SW)	4.5	15.5
<i>Cryptomeria</i> (SW, mean)	7.2	11.2

Note: Decay test was conducted according to JIS Z2119 (sample size = 20 x 20 x 20; incubation period 60 days). Two-needle pine, *Picea* spp., and *Cryptomeria* was calculated from averaging the two *Pinus* species (*P. densiflora* and *P. thunbergia*), three *Picea* species (*P. jezoensis*, *P. glehnii*, and *P. hondoensis*), and three *Cryptomeria japonica*, resp. SW- sapwood.

Amounts of extracts are closely related to the natural decay resistance of wood (Taylor et al. 2002, Windeisen et al. 2002, Venäläinen et al. 2003, 2006, Archer and Lebow 2010, Takashima et al. 2015). The heartwood of many tree species exhibits some degree of resistance to attack by decay fungi and insects, and this natural durability can be attributed to a combination of toxic extractives present in the wood as well as low inherent permeability (Archer and Lebow 2010).

Relationships between mass loss and amounts of extracts in normal wood are shown in Fig. 2.

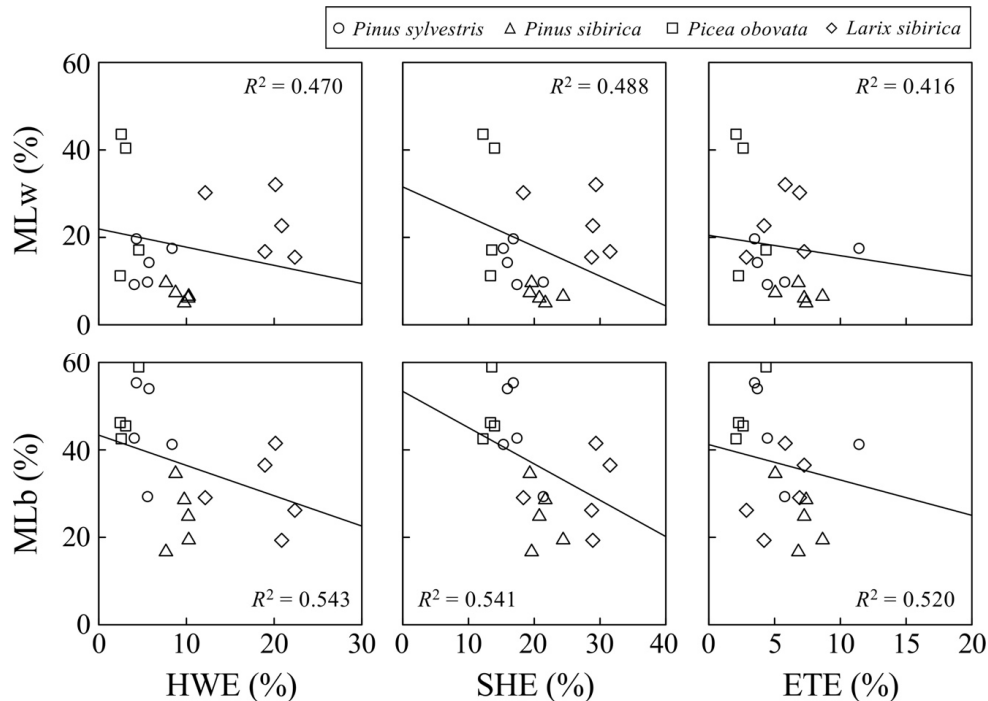


Fig. 2: Relationships between amounts of extracts in heartwood of sound wood and mass loss of heartwood specimens by *T. versicolor* and *F. palustris* ($n = 19$, HWE- hot-water extracts; SHE- 1% sodium hydride (NaOH) extracts; ETE- ethanol-toluene extracts; MLw- mass loss by *T. versicolor*; MLb- mass loss by *F. palustris*). Regression lines indicate linear mixed-effects models with species as random intercepts. R^2 is correlation coefficient of the linear mixed-effects model.

By the linear mixed-effects model, mass loss by both fungi was negatively correlated with amounts of extracts, suggesting that wood with larger amounts of extracts has a strong decay resistance. Specifically regarding mass loss by *F. palustris*, correlations of determination showed higher values, indicating that the relationships between mass loss and amounts of extracts in *F. palustris* is stronger than those in *T. versicolor*. In regards to *P. sibirica*, mass loss was significantly lower among four species, and amounts of extracts in heartwood showed relatively higher values. Thus, heartwood of *P. sibirica* may include some extractives with antifungal activities. Further research is needed to clarify the natural decay ability in *P. sibirica* growing in Mongolia.

CONCLUSIONS

In the present study, amounts of wood chemical components and decay resistance of wood against a white-rot fungus, *Trametes versicolor*, and a brown-rot fungus, *Formitopsis palustris*, were determined for four common Mongolian softwoods, *Pinus sylvestris*, *Pinus sibirica*, *Picea obovata*, and *Larix sibirica*. Compared to Japanese species, Mongolian softwoods showed relatively higher amounts of holocellulose and α -cellulose, although amounts of other wood chemical components were similar. In addition, heartwood of *Larix sibirica* was characterized by higher extracts and lower holocellulose and Klason lignin due to the presence of arabinogalactan. The highest decay resistance of heartwood was found in *Pinus sibirica* for both fungi. Negative correlations were obtained between mass loss and amounts of extracts by linear mixed-effects models, suggesting that heartwood having larger amounts of extracts showed higher natural decay durability.

ACKNOWLEDGEMENTS

The authors would like to thank Ms. Togtokhbayar Erdene-Ochir, Ms. Yui Kobayashi, and Mr. Tappei Takashima for their assistance in the experiments. This research was financially supported in part by the Higher Engineering Education Development Project, implemented by the Ministry of Education, Culture, Science, and Sports, Mongolia.

REFERENCES

1. Archer, K., Lebow, S., 2010: Wood preservation. In: Primary wood processing: principles and practice (2nd edition) (ed. Walker JCF). Pp. 297-338, Springer, Dordrecht.
2. Ayush, T., Jigjiv, A., Baasan, B., Pertiwi, Y.A.B., Ishiguri, F., Yokota, S., 2019: Drying performance of a direct-fired kiln developed in Mongolia. *Wood Research* 64: 177-184.
3. Bates, D., Mächler, M., Bolker, B.M., Walker, S.C., 2015: Fitting linear mixed-effects models using lme4. *Journal of Statistical Software* 67: 1-48.
4. Belt, T., Hänninen, T., Rautkari, L., 2017: Antioxidant activity of Scots pine heartwood and knot extractives and implications for resistance to brown rot. *Holzforschung* 71: 527-534.
5. Côté, Jr, W.A., Day, A.C., Simson, B.W., Timell, T.E., 1996: Studies on larch arabinogalactan (I): the distribution of arabinogalactan in larch wood. *Holzforschung* 20: 178-192.
6. Erdene-Ochir, T., Ishiguri, F., Nezu, I., Tumenjargal, B., Baasan, B., Chultem, G., Ohshima, J., Yokota, S., 2020: Utilization potential of naturally regenerated Mongolian *Betula platyphylla* wood based on growth characteristics and wood properties. *Silva Fennica* 54: 10284.
7. Ishiguri, F., Tumenjargal, B., Baasan, B., Jigjiv, A., Pertiwi, Y.A.B., Aiso-Sanada, H., Takashima, Y., Iki, T., Ohshima, J., Iizuka, K., Yokota, S., 2018: Wood properties of *Larix sibirica* naturally grown in Tosontsesngel, Mongolia. *International Wood Products Journal* 9: 127-133.

8. JIS K1571, 2010: Wood preservatives-performance requirements and their test methods for determining effectiveness.
9. Jebrane, M., Pockrandt, M., Terziev, N., 2014. Natural durability of selected larch and Scots pine heartwoods in laboratory and field tests. *International Biodeterioration and Biodegradation* 91: 88-96.
10. Kuroda, K., 2000: III. Chemistry, 1. Wood analysis, (2) Main components. In: *Manual for wood science experiments* (ed. Japan Wood Research Society). Pp 92-97, Buneido, Tokyo.
11. Sarkhad, M., Ishiguri, F., Nezu, I., Tumenjargal, B., Takahashi, Y., Baasan, B., Chultem, G., Ohshima, J., Yokota, S., 2020: Preliminary evaluation for quality of dimension lumber in four common softwoods in Mongolia. *Journal of Wood Science* 66: 72.
12. Schmidt, O., 2006: *Wood and tree fungi: biology, damage, protection, and use*. Springer, Berlin, Heidelberg, 348 pp.
13. Srinivasan, U., Ung, T., Taylor, A., Cooper, P.A., 1999: Natural durability and waterborne preservative treatability of tamarack. *Forest Products Journal* 49(1): 82-87.
14. Takashima, Y., Tamura, A., Noseda, N., Tanabe, J., Makino, K., Ishiguri, F., Habu, N., Iizuka, K., Yokota, S., 2015: Diversities of decay resistance and *n*-hexane-extractable contents in seven half-sib families from plus trees in todomatsu (*Abies sachalinensis*). *Journal of Wood Science* 61: 192-198.
15. Tumenjargal, B., Ishiguri, F., Aiso-Sanada, H., Takahashi, Y., Nezu, I., Baasan, B., Chultem, G., Ohshima, J., Yokota, S., 2019: Geographical variations of lumber quality of *Larix sibirica* naturally grown in five different provenances of Mongolia. *Journal of Wood Science* 65: 43.
16. Tumenjargal, B., Ishiguri, F., Aiso, H., Takahashi, Y., Nezu, I., Takashima, Y., Baasan, B., Chultem, G., Ohshima, J., Yokota, S., 2020a: Physical and mechanical properties of wood and their geographic variations in *Larix sibirica* trees naturally grown in Mongolia. *Scientific Reports* 10: 12936.
17. Tumenjargal, B., Ishiguri, F., Takahashi, Y., Nezu, I., Baasan, B., Chultem, G., Aiso-Sanada, H., Ohshima, J., Yokota, S., 2020b: Bending properties of dimension lumber produced from Siberian larch (*Larix sibirica*) in Mongolia. *Journal of Wood Science* 66: 17.
18. Tumenjargal, B., Ishiguri, F., Takahashi, Y., Nezu, I., Baasan, B., Chultem, G., Aiso-Sanada, H., Ohshima, J., Yokota, S., 2020c: Predicting the bending properties of *Larix sibirica* lumber using nondestructive-testing methods. *International Wood Products Journal* 11: 115-121.
19. Taylor, A.M., Gartner, B.L., Morrell, J.J., 2002: Heartwood formation and natural durability. *Wood and Fiber Science* 34: 587-611.
20. Venäläinen, M., Harju, A.M., Kainulainen, P., Viitanen, H., Nikulainen, H., 2003: Variation in the decay resistance and its relationship with other wood characteristics in old Scots pines. *Annals of Forest Science* 60: 409-417.
21. Venäläinen, M., Harju, A.M., Terziev, N., Laakso, T., Saranpää, P., 2006: Decay resistance, extractive content, and water sorption capacity of Siberian larch (*Larix sibirica* Lebed.) heartwood timber. *Holzforschung* 60: 99-103.

22. Windeisen, E., Wegener, G., Lesnino, G., Schumacher, P., 2002: Investigation of the correlation between extractives content and natural durability in 20 cultivated larch trees. *Holz als Roh- und Werkstoff* 60: 373-374.
23. Wood Technology and Wood Utilization Division, 1982: Properties of the important Japanese woods: table of the properties of woods. *Bulletin of the Forestry and Forest Products Research Institute* 319: 85-126.
24. Yonezawa, Y., Kayama, T., Kikuchi, F., Usami, K., Takano, I., Ogino, T., Honda, O., 1973: The properties of the important Japanese woods: chemical analysis, kraft pulping and papermaking characteristics of the important Japanese woods. *Bulletin of the Government Forestry Experiment Station* 253: 55-99.
25. Zhang, D., 2020: Coefficient of determination for mixed-effects models. Technical Report, Department of Statistics, Purdue University 20(01): 1-20.

MURZABYEK SARKHAD, FUTOSHI ISHIGURI*, IKUMI NEZU, JYUNICHI OHSHIMA,
NAOTO HABU, SHINSO YOKOTA
UTSUNOMIYA UNIVERSITY
SCHOOL OF AGRICULTURE
UTSUNOMIYA 321-8505
JAPAN

* Corresponding author: ishiguri@cc.utsunomiya-u.ac.jp

MURZABYEK SARKHAD, IKUMI NEZU
TOKYO UNIVERSITY OF AGRICULTURE & TECHNOLOGY
UNITED GRADUATE SCHOOL OF AGRICULTURAL SCIENCE
FUCHU TOKYO 183-8509
JAPAN

MURZABYEK SARKHAD, BAYASAA TUMENJARGAL
MONGOLIAN UNIVERSITY OF SCIENCE & TECHNOLOGY
TRAINING & RESEARCH INSTITUTE OF FORESTRY & WOOD INDUSTRY
ULAANBAATAR 15172
MONGOLIA

BAYARTSETSEG BAASAN, GANBAATAR CHULTEM
MONGOLIAN UNIVERSITY OF SCIENCE & TECHNOLOGY
SCHOOL OF INDUSTRIAL TECHNOLOGY
ULAANBAATAR 14191
MONGOLIA

CHEMICAL CONSTITUENTS OF THE STEM IN *DALBERGIA SISSOO*

MENGXUE LI, LEI SHI, FUXIAN XIA, JIANG DENG, HUIJIAN LIAO, TING DU,
BINGYI WANG
CHINESE ACADEMY OF FORESTRY
CHINA

(RECEIVED JUNE 2021)

ABSTRACT

The chemical constituents of ethyl acetate extracts from heartwood and sapwood of different ages of *Dalbergia sissoo* were studied by gas chromatography-mass spectrometry. The results showed that the chemical composition of wood heartwood and sapwood is significantly different. In the vertical direction, the type of the ethyl acetate extract from *Dalbergia sissoo* tends to decrease from the base to the upper portion; in the horizontal direction, the type of extract gradually decreases from the center to the periphery. And it showed an increasing trend with the age of the trees. The experiment also revealed that there were significant differences in chemical components between heartwood and sapwood. We speculated that the main chemical component trimethoxyresveratrol of heartwood extract may be related to the formation of heartwood, and the specific correlation needs to be further verified.

KEYWORDS: Chemical compound, *Dalbergia sissoo*, sapwood, heartwood, gas chromatography-mass spectrometry, ethyl acetate extract, trimethoxyresveratrol.

INTRODUCTION

Dalbergia sissoo is one of the most important precious woods in agroforestry production, especially heartwood, excellent in durability and processing properties, and resistant to insects. *Dalbergia sissoo* Roxb. commonly known as Sissoo or Shisham, is an evergreen or deciduous medium tree with small canopy, widely distributed throughout the Indian subcontinent (Sultana et al. 2015), as well as Nepal, Pakistan, Bangladesh. Countries, Brazil, Madagascar and other countries, and it has been introduced to Yunnan, China since 1999 (Pande and Singh 2005, Shi et al. 2011). Due to its interlaced texture, fine and beautiful structure, anti-termite, outstanding abrasion resistance, hard and not easy to crack, the heartwood of the *Dalbergia sissoo* is suitable for engraving, finishing, decorating and furniture and so on (Khan and Faruque 2010, Al-Snafi 2017). In terms of various aspects of use and processing performance, the heartwood of

Dalbergia sissoo is obviously superior to sapwood, and sapwood is difficult to put into use in most cases, resulting in greatly reduced wood utilization. In addition, the formation of the heartwood is special slow, it can't be promoted artificially, and the output of the heartwood is not well controlled (Hirano et al. 2001). Therefore, the quality and output of the heartwood of *Dalbergia sissoo* is our ultimate goal, but we have not yet fully understood the process of heartwood formation.

The essential difference between heartwood and sapwood is that they have different composition components, and the difference in structure and composition between heartwood and sapwood makes it very different in terms of application range, economic value and comprehensive benefits (Kumar et al. 2005, Zhang et al. 2020). At present, systematic research on its chemical composition is rare (Inyang et al. 2014, Javaid et al. 2015), so we need to studies the chemical composition in the stem of *Dalbergia sissoo* cultivated systematically, in order to provide certain basic data for the development and utilization of *Dalbergia sissoo*. Therefore, the study of the difference between the composition of heartwood and sapwood, as well as the spatial and temporal distribution of matter in the heartwood and sapwood, will greatly help reveal the cause and mechanism of the formation of the heartwood, and is conducive to artificially promote the formation of heartwood to achieve the full use of wood.

In this paper, the type and content of ethyl acetate extract of sapwood and heartwood were measured by measuring the formation of heartwood, and the content and distribution of the extract were analyzed. On the one hand, it lays a foundation for the research on the quality of *Dalbergia sissoo* heartwood and sapwood. On the other hand, it helps to understand the formation process of the heartwood in the stem of *Dalbergia sissoo*, which provides a scientific basis for the excellent breeding of *Dalbergia sissoo*.

MATERIAL AND METHODS

Materials

The test material was collected from the Yuanjiang Test Base of the Resource Insect Institute of the Chinese Academy of Forestry. The plantation in the test station management level was consistent, the plant growth condition was robust. Four tree strains of different ages and the same growth state were selected in the experimental plots. After the sample wood was selected, it was numbered Ds.1 – Ds.4 (3, 7, 12 and 18 years) according to the age of the trees. According to the height of each tree, about 10 cm from the ground was regarded as the base of the trunk, the middle of the trunk was the middle, and the upper 10 cm below the crown was regarded as the upper part of the trunk. The base was marked on the trunk for felling. After the felling, a disc of about 5 cm thick was cut in the middle and upper part of the base of the sample trunk, and the tree number and the position of the disc relative to the trunk were marked.

Sample preparation

Before the formal sampling, we did a preliminary experiment to determine whether to take multiple directions in the horizontal direction or single-direction sampling. We cut a part of

the tree with the heartwood in the upper and lower sections in advance, sampled in the three directions of the upper section of the sample, and sampled in the corresponding direction in the lower section.

According to the cross-sectional state of the test material, the upper, middle and base portions were divided into two parts (heartwood and sapwood), and each part took 2 samples of similar size (Fig. 1), and took a sample in the transition zone between heartwood and sapwood. The samples were cut into particles as small as possible, and then directly immersed in a glass test tube containing ethyl acetate, which was placed in a fume hood with a test tube rack. There was no significant environmental change and pollution during extraction, and shaken periodically for 5 days. 2 mL supernatant and 0.45 μm microporous membrane were used in the injection bottle. The supernatant in the sample bottle was taken for GC-MS analysis.



Fig. 1: A cross section of the base of a 15-year-old Dalbergia sissoo stem, indicating the difference in color between the heartwood and the sapwood of the wood.

Gas chromatography–mass spectrometry (GC–MS) analysis

GC–MS analyses were performed using a Shimadzu Gas Chromatograph QP2010 Ultra equipped with Autosampler AOC-20i, Ion source: electronic impact High-performance Quadrupole Mass Filter. Separation of compounds was carried out in a DB-5J&W capillary column (30×0.25 mm inner diameter, $0.25 \mu\text{m}$ film thickness) using helium as the carrier gas ($35 \text{ cm}\cdot\text{s}^{-1}$). The chromatographic conditions were as follows: start time at 6.5 min; initial temperature 90°C for 4 min; temperature rate, $16^\circ\text{C}\cdot\text{min}^{-1}$ up to 180°C , followed by temperature rate $6^\circ\text{C}\cdot\text{min}^{-1}$ up to 250°C ; followed by temperature rate, $3^\circ\text{C}\cdot\text{min}^{-1}$ up to 300°C which was maintained for 5 min; injector temperature 320°C ; transfer-line temperature, 300°C ; split ratio 1:50. The mass spectrometer was operated in the electron impact (EI) mode with energy of 70 eV, and data were collected at a rate of $1 \text{ scan}\cdot\text{s}^{-1}$ over a range of $33\text{--}750 \text{ m}\cdot\text{z}^{-1}$. The ion source was kept at 250°C . The total ion flow chart of ethyl acetate extract was obtained, and the peak of the extract was deleted from the total ion flow chart of ethyl acetate. Then the GC-MS total ion graph was integrated and the peak area (A) of the relative peak area (A) was more than 1% was selected and the similarity ratio of the peak of the satisfied conditions was compared with the system. From total ion chromatogram, the peaks were identified by

comparing their mass spectra with the mass spectral libraries (NIST 14 Mass Spectral and Wiley Registry TM of Mass Spectral Data), with MS spectra and MS fragmentation pattern published in the literature, by comparing the retention times and mass spectra data of the standard compounds injected in the same chromatographic conditions. The chemical constituents of ethyl acetate extract from *Dalbergia sissoo* were obtained ultimately.

RESULTS AND DISCUSSION

Ethyl acetate extract of *Dalbergia sissoo* and its position

The results of preliminary experiments showed that there was no difference in extracts between samples in the same height horizontal direction, so the sampling method in the experiment did not take parallel samples of the samples in the horizontal direction of the same height. It can be seen that the heartwood and sapwood of *Dalbergia sissoo* are distinct in color and can be easily distinguished (Fig. 1). By observing the gas chromatogram of each sample, we found that the mass spectrums of the heartwood sample were approximately the same, and the sapwood was approximately the same (Fig. 2). We list the state of the wood of the cross section of the four sample trees (the presence or absence of the heartwood) as Tab. 1. Totally, there are 11 substances in the extract from the heartwood, and the other 6 from the sapwood. The substances are numbered in Tab. 2.

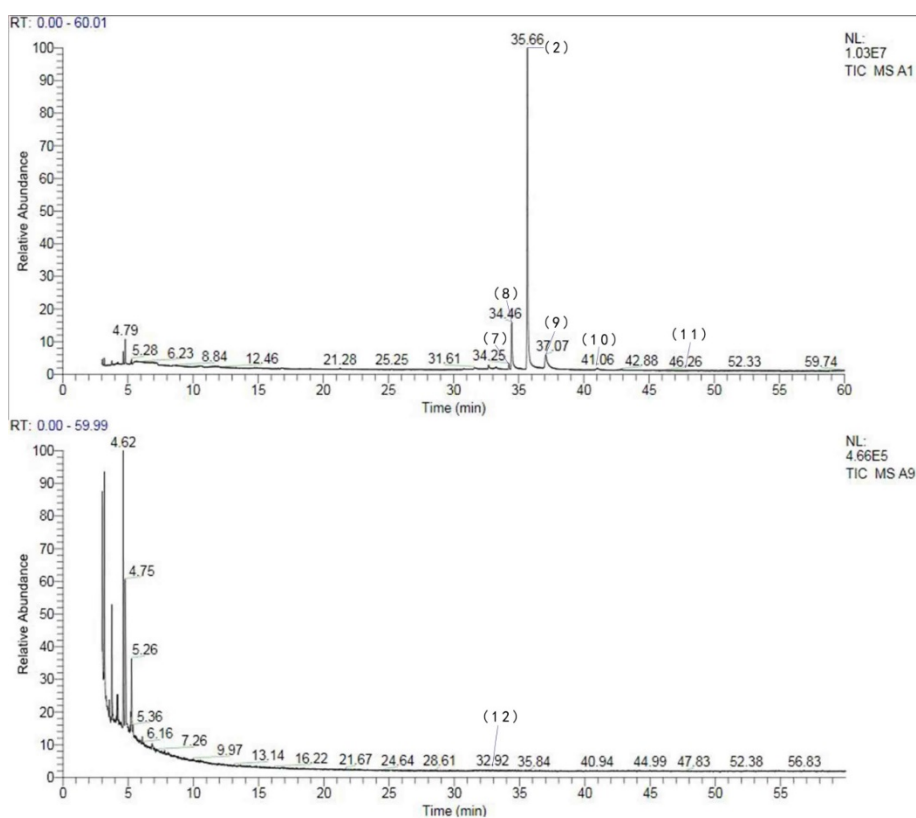


Fig. 2: Gas chromatographic mass spectrum of ethyl acetate extract of heartwood (upper) and sapwood (lower) of *Ds.4*

Tab. 1: The presence or absence of heartwood of four sample trees.

Samples	Top	Middle	Base
Ds.1	no	no	no
Ds.2	no	no	have
Ds.3	have	have	have
Ds.4	have	have	have

Tab. 2: Ethyl acetate extract of *Dalbergia sissoo*.

Position	Serial number (SN)	Molecular formula	Identified compounds
Heartwood	1	C ₁₆ H ₁₄ O ₃	Xyloltenin;
	2	C ₁₇ H ₁₈ O ₃	Trismethoxyresveratrol;
	3	C ₁₄ H ₁₂ N ₂ O ₃	1,9-Dimethoxyphenazine 5-oxide;
	4	C ₁₂ H ₁₆ N ₆ O ₆	N-2,4-Dnp-L-arginine;
	5	C ₁₈ H ₂₀ O ₃	Allogibberic acid;
	6	C ₁₄ H ₁₂ N ₂ OS	Phenol, 4-methyl-2-[5-(2-thienyl)pyrazol-3-yl]-;
	7	C ₁₈ H ₂₀ O ₃	Dibenz[a,c]cyclohexane, 2,4,7-trimethoxy- ;
	8	C ₁₆ H ₁₆ O ₂	Benzene, 1,3-dimethoxy-5-[(1E)-2-phenylethenyl]-;
	9	C ₂₅ H ₂₇ NO ₃	α -Phenyldihydrothebaine;
	10	C ₁₆ H ₁₄ O ₃	Benzoic acid, 4-[2-(3-methoxyphenyl)-1-ethylenyl]; 3,4-Dimethoxy-benzoic acid
Sapwood	11	C ₂₃ H ₂₂ N ₂ O ₃	(1-biphenyl-4-yl-ethylidene)-hydrazide;
	12	C ₁₆ H ₁₂ O ₄	7-hydroxy-3-(4-methoxyphenyl)-2H-chromen-2-one;
	13	C ₁₈ H ₂₂ O ₂	Estra-4,9,11-trien-3-one, 17- β -hydroxy- ;
	14	C ₂₀ H ₂₅ NO ₃ S	Androst-4-en-9-methylthio-11-ol-3,17-dione;
	15	C ₁₅ H ₁₂ N ₂ O ₃	1,4-diamino-2-methoxyanthracene-9,10-dione;
	16	C ₁₆ H ₁₂ O ₄	2,3-dimethoxyanthracene-9,10-dione;
	17	C ₃₀ H ₅₀ O	α -amyrin;

* The substances in the table are all compounds with a content greater than 1% after GC-MS analysis of the ethyl acetate extract from the trunk.

Temporal and spatial distribution of various chemical components in stem

First, for samples with heartwood from the inside to the outside in the cross section of the wood, the type of the extract gradually decreases from the base to the upper part (Tab. 3). The columns in the table represent the compounds extracted from the corresponding position by the trunk, while the rows represent the serial number of the tree and the position of the sample inside and outside the cross section of the vertical position of the trunk. The percentages in the table show the relative amounts of various substances. The component content of a substance is the average taken from multiple samples. 100% indicates that only one compound of the samples in this position has a peak area of more than 1%.

As can be seen from the Tab. 3, from the ethyl acetate extracted material of the sample from the Ds.4, that there are seven kinds of extracts at the base. And two compounds are extracted in the middle. Similarly, only two compounds were detected in the upper part. The GC-MS of ethyl acetate extract of Ds.3 wood has detected seven chemical constituents at the base. Only two substances were detected in the middle. In the upper part, two compounds were detected. In the samples of Ds.2, five extracts were extracted at the base, and one was detected in the middle and upper samples.

Tab. 3: The position of the extract in the sample tree and its relative percentage.

SN	Percentage content (%)																					
	Ds.1		Ds.2				Ds.3				Ds.4											
	Mid		Top	Mid	Base		Top		Mid	Base		Top		Mid		Base						
HP	In	Out	Out	Out	Ins	Out	In	Out	In	Out	In	Out	In	Tra	Out	In	Tra	Out	In	Tran	Out	
1					82.6															81.5		
2					7.83		100		100		90.16		100	100		100	100		9.32	95.84		
3																				4.93		
4																				2.29		
5																					2.22	
6																					1.31	
7											2.08											
8					2.74						1.45											
9					2.26						2.51											
10											1.74											
11											1.86											
12			100			100							100		100		100					100
13				100						100												
14								100														
15	100																					
16		47.2																				
17		43.6																				

*In - inside, Out - outside, Tran - transition, SN - serial number of the sample tree, VP - vertical position, HP - horizontal position.

Secondly, for samples with heartwood from the cross section of the wood, the type of the extract is reduced from the inside to the outside part (Tab. 3). Among the multiple samples of Ds.4 wood, there were four kinds of substances extracted by ethyl acetate in the center part of the heartwood, and there are three compounds detected from the transition zone, only one compound was obtained in the outer part of the sapwood. In the samples taken from Ds.3 wood, six compounds were detected in the ethyl acetate extract at the center of the heartwood, and three substances were get from the outside of the sapwood. The GC-MS of ethyl acetate extract of Ds.2 wood has detected four compounds in the heartwood, and only two compound in the sapwood.

Obviously, the chemical constituents of ethyl acetate extracted from *Dalbergia sissoo* wood are gradually increasing with the increase of tree age. A total of three chemical components were detected in the extract of ethyl acetate from wood of Ds.1, six compounds were got in the Ds.2, nine compounds were detected in the Ds.3, and seven chemical components were detected in the Ds.4.

Referring to the gas chromatogram of the ethyl acetate extract of sapwood and heartwood (Fig. 2), it is clear that the sapwood has a small number of species and relatively lower content of components; while in the heartwood, there are more species and obvious main substance with high content.

Discussion

First of all, in appearance, there is no heartwood in young wood. With the growth of tree age, heartwood begins to form at the base of wood. The color and anatomical structure of heartwood and sapwood are significantly different, and their chemical composition is also greatly different. We speculate that some extracts may have an impact on the color of wood, and the specific substance or substances need to be verified. Then, in connection with the extractives of different ages and parts of trees and their spatial variation, we believe that trismethoxyresveratrol may be related to the formation of heartwood. First, the trismethoxyresveratrol is only present in the ethyl acetate extract of the heartwood sample in the middle position. In addition, compared with the extracts of samples, trismethoxyresveratrol only exists in Ds.2, Ds.3 and Ds.4 (Tab. 3), and they differ from the Ds.1 in: There is a clear color difference between the interior and exterior of the wood cross section, and the interior is darker. Furthermore, in the Ds.2 sample, only the cross section of the base has a color difference, and only the trismethoxyresveratrol is detected in the extract of the base, but not in the middle and the upper parts. Combined with the peak area of the total ion current map, which is its relative percentage in the heartwood, we consider the material to be a characteristic substance of the heartwood.

The heartwood is the central part of the tree that does not contain living cells, and the storage material in the trees has been eliminated or converted into extracts of the heartwood (Anatomists 1964, Taylor et al. 2002). The formation mechanism of wood is very complicated, and many changes are closely combined and occur instantaneously (Jaemo et al. 2004, Gowariker et al. 2008), so it is difficult to conduct in-depth systematic research on its occurrence process. This experiment attempts to link the extracts from sapwood and heartwood through secondary metabolic pathways in plants, which is of great significance for explaining the process and mechanism of heartwood formation or sapwood conversion into heartwood. At present, there are two hypotheses about the formation mechanism of heartwood: The first hypothesis is that heartwood is the site where trees accumulate toxic secondary metabolites. The second hypothesis is that the formation of heartwood is the result of the unique physiological functions of parenchyma cells in the transition zone (Fengel 1970, Hugentobler 1965, Stewart 1966, Hillis 1971, Bamber 1976, Cui et al. 2016).

When a normal growing tree reaches a certain age, it will form a heartwood inside the xylem. The trees continue to grow, except for the addition of new sapwood on the periphery, while the heartwood gradually extends outward (Bamber and Humphreys 1965, Spicer 2016). *Catalpa bignoniodes* and *Crytomeria japonica* form heartwood at very young ages, while *Pinus ponderosa* and *Nyssa sylvatica* begin to grow in centuries (Yang and Hazenberg 1991, Yang et al. 1994, Harrington and Warren 2011). According to the investigation, it was found that the heartwood of *Dalbergia fragrans* began to form 6-7 a (Cui et al. 2016). In our study, by observing the formation of heartwood of four trees of different ages, we believe that the time required for the formation of heartwood in *Dalbergia sissoo* was 3-7 years.

After research, growth regulators, fungal infections, exogenous gases and water and fertilizer management, thinning tending, pruning and cutting, cutting and stripping bark and other tending measures can affect the formation of the heartwood (Hillis 1999, Kuroda et al. 2009, Tanabe et al. 2019, Nagai and Utsumi 2012, Basu 2014, Cui et al. 2020).

CONCLUSIONS

The number of ethyl acetate extract from the stem of the *Dalbergia sissoo* showed an increasing trend with the age of the trees; as for space, from the base to the upper part, from the center of the tree to the periphery, the trend was decreasing. The chemical composition of wood heartwood and sapwood is significantly different, therefore, we believe that the formation of heartwood is inseparable from its chemical composition. It is speculated that the heartwood of *Dalbergia sissoo* is formed for about 3-7 years. In addition, we found that the main component of the heartwood extract is trimethoxyresveratrol, which could be a derivative of plant phenylalanine metabolism. And other ingredients such as Xyloltenin may have a potential link to the intermediate coumaric acid. By analyzing the chemical constituents extracted from the wood, it may have a positive effect on guiding the regulation, material metabolism, sampling and research methods in the process of heartwood formation.

ACKNOWLEDGMENTS

The research was Supported by National Key R&D Program of China (2016YFD0600600504), Forestry Science and Technology Extension project in Yunnan (2018ts06) and Training project of scientific and technological innovation talents in Yunnan (2018HB096). Thanks to all the authors who contributed to this article, and to the Key Laboratory of Research Institute of resource insects, Chinese Academy of Forestry for providing experimental instruments and reagents.

REFERENCES

1. Al-Snafi, A.E., 2017: Chemical constituents and pharmacological effects of *Dalbergia sissoo* - A review. IOSR Journal of Pharmacy (IOSRPHR) 4(01): 67-73.
2. Anatomists I., 1964: Multilingual glossary of terms used in wood anatomy. Verlagsanstalt Buchdruckerei Konkordia. Pp: 32-43.
3. Bamber, R., Humphreys, F., 1965: Variations in sapwood starch levels in some Australian forest species. Australian Forestry 29(1): 15-23.
4. Bamber, R.K., 1976: Heartwood, its function and formation. Wood Science and Technology 10: 1-8.
5. Basu, J.P., 2014: Agroforestry, climate change mitigation and livelihood security in India. New Zealand Journal of Forestry Science 44(Suppl 1)S11: 1-10.
6. Cui, Z.Y., Xu, D.P., Yang, Z.J., Zhang, N.N., Liu, X.J., Hong, Z., 2016: A review of mechanism and artificial promotion of heartwood formation. World Forestry Research 29(6): 33-37.
7. Cui, Z., Li, X., Xu, D., Yang, Z., 2020: Changes in non-structural carbohydrates. Wood properties and essential oil during chemically-induced heartwood formation in *Dalbergia odorifera*. Frontiers in Plant Science 11: 1161.

8. Fengel, D., 1970: Ultrastructural changes during aging of wood cells. *Wood Science and Technology* 4(3): 176–188.
9. Gowariker, V., Krishnamurthy, V.N., Gowariker, S., Dhanorkar, M., Paranjape, K., 2008: The fertilizer encyclopedia. John Wiley & Sons, Inc. USA, pp 465-540.
10. Harrington, C.A., Warren, D., 2011: Stand development following precommercial thinning and fertilization treatments in a western red cedar (*Thuja plicata*) dominated forest. *Canadian Journal of Forest Research* 41(1): 151-164.
11. Hillis, W.E., 1971: Distribution, properties and formation of some wood extractives. *Wood Science and Technology* 5(4): 272-289.
12. Hillis, W.E., 1999: The formation of heartwood and its extractives. In: Romeo J.T. (eds) *Phytochemicals in Human Health Protection, Nutrition, and Plant Defense. Recent Advances in Phytochemistry (Proceedings of the Phytochemical Society of North America)*, vol 33. Springer, Boston, MA. Pp: 215-253.
13. Hirano, Y., Kondo, R., Sakai, K., 2001: Compounds inhibitory to rat liver 5 α -reductase from tropical commercial wood species: resveratrol trimers from melapi (*Shorea* sp.) heartwood. *Journal of Wood Science* 47: 308–312.
14. Hugentobler, U.H., 1965: Cytology of heartwood formation. *Vierteljahrsschrift der Naturforschenden Gesellschaft in Zurich* 110(2): 321-342.
15. Inyang, A.F., Tchanque-Fossuo, C.N., Merati, M., Radzolsky, E.R., Buchman, S.R., 2014: Microdensitometric and microarchitectural alterations in irradiated mandibular fracture repair. *The Journal of Craniofacial Surgery* 25(6): 2022-2026.
16. Jaemo, Y.D., Pascal, K., Daniel, E.K., Kyung-Hwan, H., 2004: Seasonal changes in gene expression at the sapwood—heartwood transition zone of black locust (*Robinia pseudoacacia*) revealed by cDNA microarray analysis. *Tree Physiology* 24(4): 461–474.
17. Javaid, M.K., Kyer, C., Mitchell, P.J., Chana, J., Moss, C., Edwards, M.H., Mclellan, A.R., Stenmark, J., Pierroz, D.D., Schneider, M.C., Kanis, J.A., Akesson, K., Cooper, C., Group IOFFW, Exco, 2015: Effective secondary fracture prevention: Implementation of a global benchmarking of clinical quality using the IOF capture the fracture (R) Best Practice Framework tool. *Osteoporosis International* 26(11): 2573-2578.
18. Khan, M., Faruque, O., 2010: Allometric relationships for predicting the stem volume in a *Dalbergia sissoo* Roxb. plantation in Bangladesh. *iforest-Biogeosciences and Forestry* 3(6): 153-158.
19. Kumar, R., Sharma, K.R., Gupta, L.M., 2005: Variation in physico-chemical characteristics of wood of candidate plus trees of Shisham (*Dalbergia sissoo* Roxb.). *The Indian Forester* 131(8): 1012-1023.
20. Kuroda, K., Yamashita, K., Fujiwara, T., 2009: Cellular level observation of water loss and the refilling of tracheids in the xylem of *Cryptomeria japonica* during heartwood formation. *Trees* 23(6): 1163.
21. Nagai, S., Utsumi, Y., 2012: The function of intercellular spaces along the ray parenchyma in sapwood, intermediate wood, and heartwood of *Cryptomeria japonica* (Cupressaceae). *American Journal of Botany* 99(9): 1553-1561.

22. Pande, P.K., Singh, M., 2005: Inter-clonal, intra-clonal, and single tree variations of wood anatomical properties and specific gravity of clonal ramets of *Dalbergia sissoo* Roxb. *Wood Science and Technology* 39(5): 351-366.
23. Shi, L., Sun, Q.F., Deng, J., 2011: Primary study on the wood anatomical and physical-mechanical properties of introduced *Dalbergia sissoo*. *Advanced Materials Research* 179–180: 1446–1452.
24. Spicer, R., 2016: Variation in angiosperm wood structure and its physiological and evolutionary significance. In: Groover A., Cronk Q. (eds) *Comparative and Evolutionary Genomics of Angiosperm Trees. Plant Genetics and Genomics: Crops and Models*, vol 21. Springer, Cham. Pp: 26-40.
25. Stewart, C.M., 1966: Excretion and heartwood formation in living trees. *Science* 153(3740): 1068-1074.
26. Sultana, S., Asif, H.M., Naveed, Akhtar, N., 2015: *Dalbergia sissoo* Roxb: monograph. *International Journal of Pharmacognosy* 2(9): 440-43.
27. Tanabe, J., Takashima, Y., Ishiguri, F., Sanpe, H., Ohshima, J., Lizuka, K., Yokota, S., 2019: Differences in β -thujaplicin content of wood between plantation- and naturally grown *Thujopsis dolabrata* var. *hondae* (hinokiasunaro) trees in Shimokita Peninsula, Aomori, Japan. *Journal of Wood Science* 65: 56.
28. Taylor, A.M., Gartner, B.L., Morrell, J.J., 2002: Heartwood formation and natural durability-a review. *Wood and Fiber Science* 34(4): 587-611.
29. Yang, K.C., Hazenberg, G., 1991: Relationship between tree age and sapwood / heartwood width in *Populus tremuloides* Michx. *Wood and Fiber Science* 23(2): 247-252.
30. Yang, K.C., Chen, Y.S., Chiu, C., Hazenberg, G., 1994: Formation and vertical distribution of sapwood and heartwood in *Cryptomeria japonica* D. Don. *Trees* 9: 35-40.
31. Zhang, H., Tu, K., Hou, Q., Lin, H., Li, Q., 2020: The physiological and biochemical mechanisms of *Cinnamomum camphora* xylem extracts inhibit wood-decay fungi. *Wood Research* 65(4): 531-542.

MENGXUE LI, FUXIAN XIA, JIANG DENG, HUAJIAN LIAO, TING DU, LEI SHI*,
BINGYI WANG*
CHINESE ACADEMY OF FORESTRY
RESEARCH INSTITUTE OF RESOURCE INSECTS
650224 YUNNAN
CHINA

*Corresponding authors: leishi@139.com and wbykm@aliyun.com

EXTRACTIVE CONTENTS OF THE JUVENILE STEMWOOD AND BARK OF TEAK

FAIS RAHMAN, GANIS LUKMANDARU
UNIVERSITAS GADJAH MADA
INDONESIA

(RECEIVED JULY 2021)

ABSTRACT

Teak wood is used at the juvenile stage due to short-rotation, therefore, this study aims to describe the extractive content of stem, bark, branch, and twig parts of the wood as value-added chemicals from secondary metabolites. Moreover, the main stems comprise of sapwood, heartwood, and bark while the branch and twig are made of sapwood together with bark. In this study, the sample trees were 6 and 8 years old with three replications from clonal superior teak wood and were extracted using *n*-hexane, methanol, and hot water as the solvents. The average of *n*-hexane, methanol, hot water, and total extractives ranged from 0.49 to 2.77%, 2.27 to 17.76%, 0.65 to 7.47%, and 5.96 to 25.40%, respectively. Furthermore, the total phenolic content from soluble *n*-hexane and methanol extracts ranged from 162.16 to 295.24 mg GAE/g, while the total soluble polysaccharides ranged from 166.28 to 423.97 mg GluE/g. The results showed that the 8-year-samples had higher values in methanol extractive content (MEC) and lower in hot-water extractive content (HWEC) than the 6-year-old trees. In addition, the bark together with sapwood in branch and twig parts had higher concentrations of MEC and total extractive content (TEC) compared to the main stems. For radial direction, MEC, HWEC, and TEC levels were greater in bark than in other parts. The branch and twig parts also had higher phenolic concentrations compared to the main stem at the base part. Meanwhile, the sapwood at the branch and twig parts have higher total soluble polysaccharide concentration compared to the main stem.

KEYWORDS: *Tectona grandis*, quinones, fast-growing, soluble polysaccharide, bark, teak.

INTRODUCTION

In Indonesia, teak wood is one of the most important timber sources for construction, sawn wood, furniture, and others. Moreover, the use of young trees as wood from the community

forest for multi-purpose products has increased in the past decade. These trees are managed in the community forest as a short rotation for approximately less than 20 years or juvenile stage. To meet the demand of wooden industries, superior teak wood from clonal breeding with a faster growth rate are introduced in the community forests and Perhutani (own-state forest enterprise) plantations.

Harvesting the trees generates large amounts of biomass residues such as leaves, barks, branches, twigs, and stumps which are left in the field or burned for energy production. Although branch and twig of teak wood have been used for furniture parts, its potential application to value-added products has not been adequately studied. Meanwhile, bark wastage is a major problem in the timber industry which contributes a great amount of biomass as a source of value-added chemicals from secondary metabolites. The extractive composition of teak wood is known, while there is little information about the bark. Moreover, the bark contains phenolic compounds such as stilbenes, lignans, flavonoids, and tannins (Fengel and Wegener 1984, Drozd and Pyrzynska 2018) that are valuable sources of antioxidants and health care industries.

The necessity of maximizing the use of the remaining scarce resource leads to the complete utilization of trees which has increased the interest in the basic properties of tree parts other than the main stem. Several studies on the chemical analysis of teak wood have focused on the bole wood (Windeisen et al. 2003, Lukmandaru and Takahashi 2008, Niamke et al. 2018) while studies on stem, branch, and twigs are limited. The phenolic compounds from the quinone group of teak wood have attracted much attention among secondary metabolites because they exhibit an array of biological activities and relate to natural durability, dimensional stability, and color (Haupt et al. 2003, Neamatallah et al. 2005, Thulasidas, and Bhat 2007, Niamke et al. 2012, Lukmandaru, and Takahashi 2008, Li et al. 2018). Furthermore, its insoluble polysaccharide or non-structural carbohydrate has also attracted interest due to the association between heartwood formation and natural durability (Niamke et al. 2011).

This study aims to describe the extractive content of stem, bark, and twig parts of juvenile teak wood which are sources of potential biochemicals. Since different positions and ages of the individuals affect extractive contents in teak wood (Lukmandaru and Takahashi 2009, Rizanti et al. 2018), two ages and tree positions with various parts were included to cover a large variety of the potential sources of different extractive content. The results of this study are expected to provide a basis for future applications.

MATERIALS AND METHODS

Samples preparation

The trees were 6 and 8 years old (14 to 18 cm DBH) from a clonal superior teak wood (Jati Unggul Nusantara) in Gunungkidul Regency, while three trees were sawn from each age for replication. Meanwhile, the discs were sawn (5 cm in thickness) at the base (0.5 m above the ground), top (4.5 m above the ground), branch, and twigs (Fig. 1) for each tree. The branch (diameter of 2.5 to 5.5 cm) was defined as the first ramification from main the stem and twig (diameter of 1.0 to 2.2 cm) was the second. Also, the proportion of the heartwood at the base and top part were 26 to 56% and 9 to 32%, respectively. For radial direction, the discs from

the trunk were divided into sapwood, heartwood, and bark, while the branches and twigs were divided into sapwood and bark parts. Each part was converted into a wood meal in 40 to 60 mesh size.

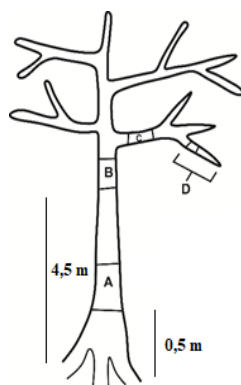


Fig. 1: The scheme of teak trees sampling, A - base stem, B - top stem, C - branch, D - twig.

Extraction

The wood meal (5 g) was extracted using *n*-hexane, methanol, and hot water. Meanwhile, the extraction with *n*-hexane and methanol solvents was carried out in a soxhlet apparatus for 6 hours. The solvent was later evaporated using a rotary evaporator and the extract was dried in an oven for 1 hour (100°C). Furthermore, the hot-water extraction was conducted in a water bath by reflux for 3 hours (100°C) and the extract was obtained after filtering and evaporating the water. This extractive content was measured using an oven-dry wood meal, while the total extractive content (TEC) was calculated by determining the sum of all extractive contents.

Total phenolic content

Total phenolic content (TPC) was determined using the Folin-Ciocalteu method (Singleton et al. 1999) with slight modifications. The extracts (*n*-hexane and methanol) were dissolved in methanol (1 mg ml⁻¹) and 2.5 ml diluted (10 times) Folin-Ciocalteu reagent (Merck, Germany) was added. This mixture was maintained for 2 min and 2 ml Na₂CO₃ (7.5%) was added. After 30 min at room temperature, the mixture was placed in the equipment and was followed by the sample absorbance which reads 765 nm (Spectrophotometer UV-Vis Optima Nano 3000 SP). The results were expressed as gallic acid equivalents based on dry extract (mg GAE/g). Furthermore, the calibration curve was determined using gallic acid at 0.125, 0.0625, 0.03125, 0.015625, and 0.0078125 mg ml⁻¹ concentrations ($y = 0.1064x - 0.0056$, $R^2 = 0.9954$). The TPC was calculated as the mean \pm standard deviation of three replications for each sample. The combined total phenolic content (CTPC) was calculated as the sum of all TPC contents.

Total soluble polysaccharide

The total soluble polysaccharides (TSP) contents were determined using the phenol-sulfuric acid method (DuBois et al. 1956). The amount of 1 ml of hot-water extract (1 mg ml⁻¹ in water) was mixed with 1 ml of phenol (5%) and 5 ml of concentrated sulfuric acid (98%). This mixture was allowed to stand for 20 min at room temperature, while the sample's absorbance was measured at 490 nm wavelength. Furthermore, the TSP value was calculated from the

calibration curve using glucose at 0.250, 0.125, 0.0625, 0.03125, and 0.015625 mg·ml⁻¹ concentration ($y = 0.1264x - 0.0076$, $R^2 = 0.9939$). The results were expressed as glucose equivalent based on dry extract (mg GluE/g) from the three replications.

Statistical analysis

Statistical analysis was carried out with Microsoft excel 2010 on Windows and the results were expressed as means \pm standard deviation.

RESULTS AND DISCUSSION

Extractive content

The extractive content of samples using three different solvents is shown in Figs. 1-4. The average of *n*-hexane, methanol, hot water, and total extractives ranged from 0.49 to 2.77%, 2.27 to 17.76%, 0.65 to 7.47%, and 5.96 to 25.40%, respectively. Similarly, the number of extractives is lower than the TEC of the teak from the forest in India (Thulasidas and Bhat 2007), farmlands, and Perhutani plantations except for the sapwood parts (Lukmandaru and Takahashi 2008). Furthermore, the TEC levels were higher compared to the teak wood from 10 and 40-year-old trees in Indonesia (Rizanti et al. 2018). The average total extractives of teak bark (50 to 60 years) were 10.7% which corresponds to polar extractives with water-soluble extract as the major fraction (Baptista et al. 2013). That result was lower compared to this experiment at the same part (12-24%).

The non-polar solvent dissolved quinone compounds in teak wood (Windeisen et al. 2003, Lukmandaru and Takahashi 2009). Meanwhile, there was no consistent trend for *n*-hexane extractive content (NHEC) and TEC levels between the 6 and 8 years old samples. It is assumed that TEC between these years is in a narrow range compared to other earlier studies on teak wood (Haupt et al. 2003, Lukmandaru and Takahashi 2008, Rizanti et al. 2018). Generally, the 8-year-old sample had higher values in methanol extractive content (MEC) and lower in hot-water extractive content (HWEC) than the 6-year-old. Based on extract weight (Fig. 5), the differences between 6 and 8-year-old samples were the percentage of MEC and HWEC fractions, especially in bark and in sapwood at the base part. Their MEC values were not greater than 50% and had a higher portion of HWEC when compared with the 8-year-old samples and vice versa. Furthermore, phenolic compounds such as tannins, flavonoids, and stilbenes are soluble in methanol (Sjöström 1993), while the bark contains excess polyphenols (Drozd and Pырzynska 2018). The higher MEC levels in the stem indicated a heartwood formation which is characterized by polyphenols increase in heartwood and decrease sugars in sapwood (Hillis 1987, Niamke et al. 2011).

A previous work showed that the variation among different parts of the tree indicated that the stem base had the highest extractive concentration (Caron et al. 2013). Meanwhile, some systematic differences were observed in line with the vertical direction or stem part. The results showed that sapwood at the main stem had higher levels than sapwood at branch and twigs for NHEC, while the base part had a higher level of NHEC than other parts. When compared to the bark in the main stems, the branch and twig showed higher concentrations in MEC, HWEC, and

TEC. Furthermore, TEC in the sapwood of branch and twig has also higher values than the sapwood in the main stem. This is due to a large number of living cells related to the cambial part and is active in the metabolism processes of the stem (Yeh et al. 2006). Moreover, the amount of extractive is relatively high in certain parts such as bark, heartwood, root, wounded tissue, branches, and twigs (Hillis 1987).

NHEC in sapwood tends to decrease in values than other parts in the radial direction. Meanwhile, heartwood contained higher amounts than sapwood in main stems for NHEC, MEC, and TEC. The huge differences in MEC between sapwood and heartwood were observed at the base part of 6-year-old samples. Furthermore, the bark had higher amounts than other parts in MEC, HWEC, and TEC. Based on extract weight, MEC was the major fraction in all parts except bark and sapwood in the main stem of the 6-year-old trees. These comparatively high values were due to the presence of parenchyma cells in the bark as storage tissues (Sjöström 1993).

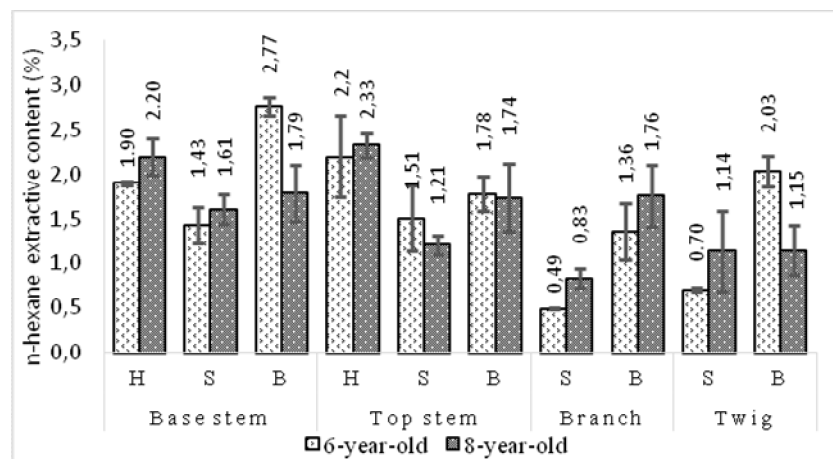


Fig. 1: The hexane extractive content (% based on oven-dry wood) from *T. grandis* (means of three trees) with error bar standard deviation. H- heartwood, S- sapwood and B-bark.

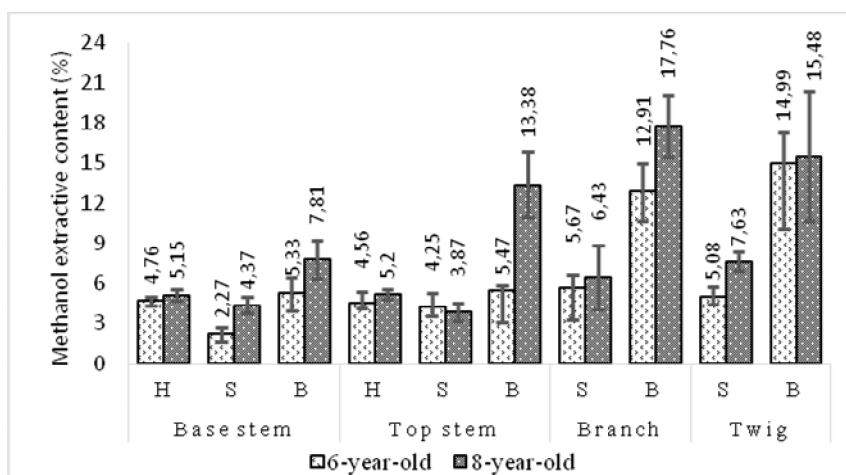


Fig. 2: The methanol extractive content (% based on oven-dry wood) from *T. grandis* (means of three trees) with error bar standard deviation. H- heartwood, S- sapwood and B-bark.

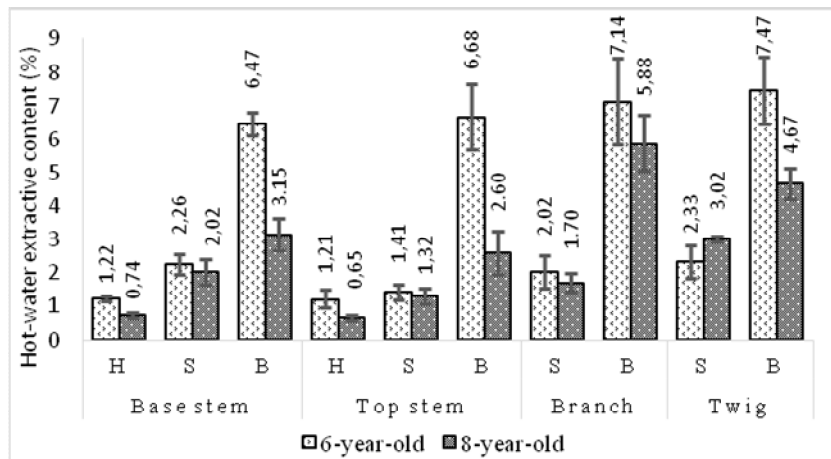


Fig. 3: The hot-water extractive content (% based on oven-dry wood) from *T. grandis* (means of three trees) with error bar standard deviation. H- heartwood, S- sapwood and B-bark.

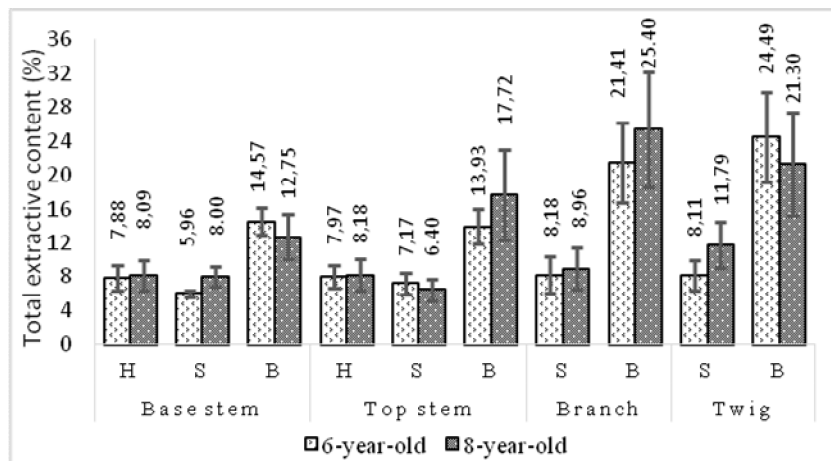


Fig. 4: The total extractive content (% based on oven-dry wood) from *T. grandis* (means of three trees) with error bar standard deviation. H- heartwood, S- sapwood and B-bark.

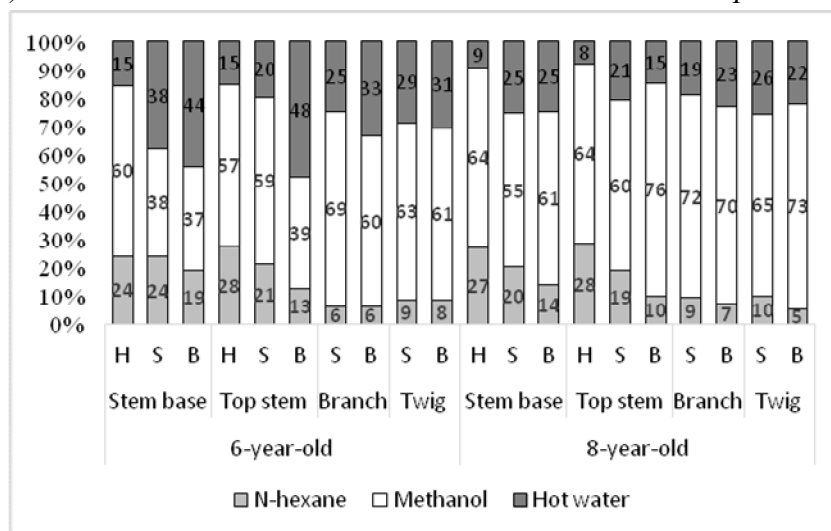


Fig. 5: The composition of extractive based on extract weight (n-hexane, methanol, and hot water) from *T. grandis* (means of three trees). H- heartwood, S- sapwood and B-bark.

Total phenolic contents

The total phenolic contents were measured from *n*-hexane and methanol soluble extracts. Meanwhile, the methanol total phenolic contents (MTPC) (ranged from 149.68 to 261.90 mg GAE/g) had higher values compared to the *n*-hexane total phenolic contents (HTPC) (ranged from 10.87 to 47.51 mg GAE/g). This low level of HTPC was due to the presence of more non-phenolic components by less polar solvent. The largest amount of HTPC in all radial parts, age groups, and part of the tree were in the sapwood branch of the 8-year-old trees (47.51 mg GAE/g) and the lowest was in the bark of the top stem of 6-year-old. (10.87 mg GAE/g) (Tab. 2). Furthermore, the HTPC of the bark showed higher levels in 8-year-old samples than 6-year-old. However, the reverse pattern was observed in the sapwood at the main stem parts, while it gives higher values of HTPC than its bark at the branch and twigs parts.

The combined total phenolic content (CTPC) ranged from 162.16 to 295.24 mg GAE/g (Tab. 2). These results were higher than a previous study conducted by Villagomez (2005), which showed that the same parts of pines ranged from 1.8 to 98.2 mg GAE/g. However, these values were considerably lower in the same parts compared to previous studies on the bark of *Swietenia macrophylla* (Masendra et al. 2021) and stem as well as the bark of *Eucalyptus pellita* (Arisandi et al. 2019).

The phenolic content in plants changes gradually in the tissues and is distinguished based on growth rate as due to tree age (Lattanzio et al. 2008). Meanwhile, the MTPC and CTPC had a similar pattern due to the high proportion of MPTC. This showed that the tissues of the base part have lower concentrations in MPTC and CPTC compared to the branch and twig parts. Furthermore, there was no systematic pattern in tree age and radial direction for MTPC and CTPC values. A previous study showed that the heartwood contains more phenolic compounds than sapwood (Hillis 1987, Fengel and Wegener 1984). This is caused by the wood region which has a smaller dimension of juvenile wood than the mature (Zobel and Buijtenen 1989). Meanwhile, the positive trend of CTPC levels with tree age (Ayton et al. 2007, Aregay et al. 2021) was not clearly shown in this study. The increase in phenolic compounds in older trees is affected by mineral nutrient imbalance and water stress due to a reduction in xylem and wounded tissue efficiency (Aregay et al. 2021).

Meanwhile, the high value of CTPC is due to the function of the bark for protecting from fungal attack and resistance against pathogens (Withouck et al. 2019, Sakai 2001). Furthermore, there were no striking differences in the CTPC levels of the barks and woods. This finding is different from other species such as *Picea abies* (Neiva et al. 2018) and Belgian apple (Withouck et al. 2019). It is noticed that the highest values were measured in the bark at the twig part while the lowest was in the sapwood at the base part. This shows that phenolic compounds are transported from source cells to other tissues and are usually accumulated in sub-epidermal cells of leaves and shoots (Lattanzio et al. 2008).

Phenolic compounds are the most common secondary metabolites in plants that are known to have some important roles. The quinones from teak wood have been detected and related to their natural durability in sapwood and heartwood regions (Windeisen et al. 2003, Lukmandaru and Takahashi 2009, Niamke et al. 2011, 2012). Therefore, the phenolics in sapwood including in the branch and twig parts might be the precursor for toxic components in the heartwood.

Although antibacterial activity has been observed from a teak bark quinone (Neamatallah et al. 2005), the phenolics in the bark are less investigated. The high content of phenolics in some parts of teak wood from juvenile age stems showed the potential of raw material for bioactive compounds extraction which are used in commercial applications.

Tab 2: Total phenolic content (mg GAE/g) measurement for n-hexane and methanol soluble extracts of *Tectona grandis*.

No	Stem part	n-hexane	Methanol	Combination
1	6BH	31.72 (7.89)	188.84 (42.82)	220.56 (78.56)
2	6TH	31.04 (10.82)	184.54 (18.14)	215.58 (68.83)
3	6BS	26.27 (8.05)	163.92 (6.98)	190.19 (84.07)
4	6TS	38.66 (2.88)	200.85 (14.84)	239.51 (76.75)
5	6BBa	21.31 (1.04)	189.45 (16.26)	210.76 (81.1)
6	6TBa	10.87 (1.81)	193.33 (5.18)	204.2 (91.23)
7	6BrS	33.99 (4.87)	211.77 (47.21)	245.76 (88.89)
8	6BrBa	21.39 (3.84)	208.46 (9.77)	229.85 (93.54)
9	6TwS	46.75 (1.41)	237.17 (24.59)	283.92 (95.21)
10	6TwBa	25.86 (8.04)	261.38 (47.43)	287.24 (117.76)
11	8BH	28.2 (10.92)	183.54 (21.75)	211.74 (77.67)
12	8TH	44.92 (1.05)	213.62 (8.53)	258.54 (68.6)
13	8BS	12.48 (13.16)	149.68 (50.05)	162.16 (91.65)
14	8TS	11.93 (19.10)	181.37 (29.37)	193.3 (84.35)
15	8BBa	23.93 (2.64)	207.14 (30.89)	231.07 (84.72)
16	8TBa	31.45 (14.07)	208.94 (40.40)	240.39 (88.75)
17	8BrS	47.51 (5.68)	245.73 (35.54)	293.24 (99.11)
18	8BrBa	23.23 (12.58)	254.85 (50.75)	278.08 (115.81)
19	8TwS	45.08 (9.54)	214.99 (12.06)	260.07 (84.96)
20	8TwBa	33.34 (7.90)	261.90 (7.53)	295.24 (114.28)

Remark: B- base stem, T- top stem, Br- branch, Tw- twig, H- heartwood, S- sapwood, Ba- bark, 6- six-year-old, 8- eight-year-old. Mean of three trees with standard deviation in parentheses.

Total soluble polysaccharide

The sugar contents in wood serve as a nutrient that provides energy for metabolic processes, osmoregulation, and is the source of the C-skeleton (Niamke et al. 2018, Kampe and Magel 2013). Meanwhile, the most important reserved carbon compounds are non-structural carbohydrates (NSC), which consist of starch and low molecular weight sugar (soluble sugar) such as glucose, fructose, and sucrose (Hoch et al. 2003). In this study, total soluble polysaccharides (TSP) were calculated from the hot-water soluble extract. The highest value was from the sapwood of twig of 8-year-old trees (423.97 mg GluE/g) and the heartwood of the top stem of 6-year-old gave the lowest value (166.28 mg GluE/g sample) (Fig. 6). Compared to previous studies, these results were lower than the spruce bark (Le-Normand et al. 2012).

Regarding the age, it was shown that the TSP in heartwood at the main stem and bark at the branch of 8-year-old had higher values than 6-year-old samples. These results confirmed the previous studies on *Nothofagus pumilio* (Piper and Fajardo 2011) and *Pinus ponderosa* (Sala and Hoch, 2009). This is due to the difference in trees height which affects the light intensity and causes a low carbohydrate storage capacity from juvenile trees (Niinemets 2010). Furthermore,

the lower TSP of 6-year-old trees was correlated to the harvesting season where the trees were felled in a longer drought period in the same year. During the drought, the teak wood also molts gradually which leads to a decrease in carbon reserves (Lloret et al. 2018).

For vertical direction, the sapwood at the branch and twig had a higher of TSP concentration compared to the main stem. This shows that the location of the twig is adjacent to leaves on which the photosynthesis products are formed and translocated (Rosell et al. 2020). Furthermore, previous results in other species also showed a similar phenomenon (Barbaroux et al. 2003, Sala and Hoch 2009). The high level of TSP in a twig is also correlated to the anatomical change in organs and the cambium aging process which enhances vessel formation (Barbaroux et al. 2003).

A previous study by Niamke et al. (2011, 2018) showed the drastic decrease from sapwood toward heartwood of the teak (5 to 10 years) in NSC content. This trend was observed only from the sapwood to heartwood in 6-year-old samples. Furthermore, the TSP levels increase from the heartwood toward the bark at the main stem and were also observed in previous studies (Rosell et al. 2020, Barbaroux et al. 2003). Moreover, soluble sugars are the dominant constituent in bark (Rosell 2020). The high value of TSP in the bark is related to secondary phloem that translocates photosynthate (Savage et al. 2016) and the hydrolysis process of tannins to generate gallic acids and sugars (Sjöström 1993).

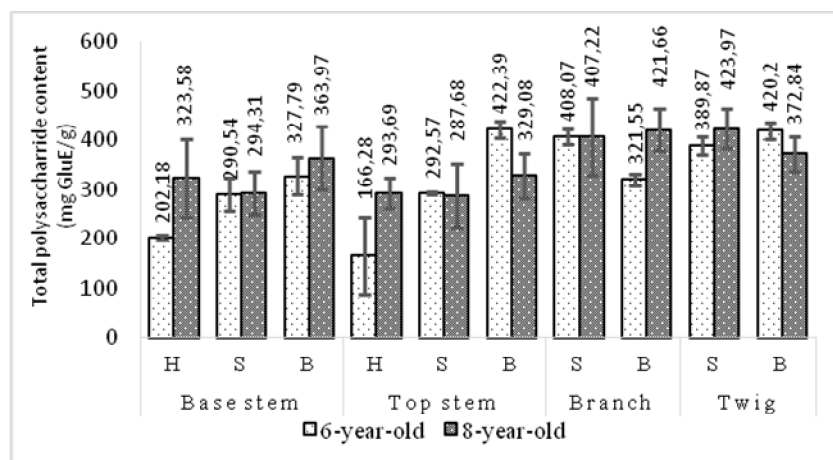


Fig. 6: The total soluble polysaccharide (mg GluE/g sample) from *T. grandis* (means of three trees) with error bar standard deviation. H- heartwood, S- sapwood and B- bark.

CONCLUSION

The evaluation of the extractive content of the main stems, branches, and twigs of the two different ages of juvenile teak wood showed the variation between the wood and bark. These results showed that the 8-year-old trees were higher in methanol extractive content and lower in hot water than the 6-year-old trees. Furthermore, it was also higher in methanol, hot-water, and total extractive contents in the bark than other parts in a radial direction. The branch and twig parts contained more methanol and total extractive content than the main stem. The phenolics content and polysaccharides concentrations were higher in branch and twig parts at the base.

Therefore, this high extractive and phenolics contents in bark parts attracted interest in exploring valuable extracts and compounds.

ACKNOWLEDGEMENT

This research was partially financed by Thesis Recognition Grant 2021 and DPP Grant of Faculty Forestry , Universitas Gadjah Mada.

REFERENCES

1. Aregay, N., Belew, D., Zenebe, A., Haile, M., Gebresamuel, G., Girma, A., 2021: Tree age and harvesting season affected physicochemical and bioactive compounds of elite type of Gunda Gundo orange (*Citrus* Spp) in the Northern Ethiopia. *Fruit Science* 20: 1-14.
2. Arisandi, R., Ashitani, T., Takahashi, K., Marsoem, S.N., Lukmandaru, G., 2019: Lipophilic extractives of the wood and bark from (*Eucalyptus pellita*) F. Muell grown in Merauke, Indonesia. *Wood Chemistry and Technology* 40: 146-154.
3. Ayton, J., Mailer, R.J., Haigh, A., Tronson, D., Conlan, D., 2007: Quality and oxidative stability of Australian olive oil according to harvest and irrigation. *Food Lipids* 14: 138–156.
4. Baptista, I., Miranda I., Quilhó T., Gominho, J., Pereira, H., 2013: Characterisation and fractioning of *Tectona grandis* bark in view of its valorisation as a biorefinery raw-material. *Industrial Crops and Products* 50: 166–175.
5. Barbaroux, C., Bréda, N., Dufrêne, E., 2003: Distribution of above-ground and below-ground carbohydrate reserves in adult trees of two contrasting broad-leaved species (*Quercus petraea*) and (*Fagus sylvatica*). *New Phytologist* 157: 605–615.
6. Caron, A., Clemens, M.A., Barry, G., Michael, C.J., 2013: Distribution of extractives in sitka spruce (*Picea sitchensis*) grown in the northern UK. *Wood Product* 71: 697–704.
7. Drózdź, P., Pyrzynska, K., 2018: Assessment of polyphenol content and antioxidant activity of oak bark extracts. *Wood and Wood Products* 76: 793–795.
8. DuBois, M., Gilles, K.A., Hamilton, J.K., Rebers, P.A., Smith, F., 1956: Colorimetric method for determination of sugars and related substances. *Analytical Chemistry* 28(3): 350-356.
9. Fengel, D., Wegener, G., 1984: *Wood—chemistry, ultrastructure, reactions*. Walter de Gruyter, Berlin and New York.
10. Haupt, M., Leithoff, H., Meier, D., Puls, J., Richter, H.G., Faix, O., 2003: Heartwood extractives and natural durability of plantation-grown teakwood (*Tectona grandis* L.) – a case study. *Holz als Roh- und Werkstoff* 61: 473–474.
11. Hillis, W.E. 1987. *Heartwood and tree exudates*. Springer. New York.
12. Hoch, G., Richter, A., Korner, C., 2003: Non-structural carbon compounds in temperate forest trees. *Plant, Cell and Environment* 26: 1067–1081.
13. Kampe, A., Magel, E., 2013: *New insights into heartwood and heartwood formation: Cellular aspects of wood formation*. Springer. Berlin, 78 pp.

14. Lattanzio, V., Kroon, P.A., Quidheu, S., Treutter, D., 2008: Plant phenolics - secondary metabolites with diverse functions. In: Recent advances in polyphenol Research (ed. Daayf F., Lattanzio V.). Pp 1-35, Blackwell Publishing. Foggia.
15. Le Normand, M., Ulrica, E., Holmbom, B., Monica, E.K., 2012: Hot-water extraction and characterization of spruce bark non-cellulosic polysaccharides. *Nordic Pulp and Paper Research* 27(1): 18–23.
16. Lloret, F., Sapes, G., Rosas, T., Galiano, L., Saura-Mas, S., Sala, A., Martínez-Vilalta, J., 2018: Non-structural carbohydrate dynamics associated with drought-induced die-off in woody species of a shrubland community. *Annals of Botany* 121: 1383–1396.
17. Li, T., Li, G., Lu, Q., Zhou, J., Li, M., Zhang, S., Li, J., 2017: Characterization of *Tectona grandis* extractives by GC-MS and IR and their infusion into rubberwood to modify dimensional stability. *Bioresources* 12(3):4500-4514.
18. Lukmandaru, G., Takahashi, K., 2008: Variation in the natural termite resistance of teak (*Tectona grandis* Linn. fil.) wood as a function of tree age. *Annals of Forest Science* 65: 708.
19. Lukmandaru, G., Takahashi, K., 2009: Radial distribution of quinones in plantation teak (*Tectona grandis* L.f.). *Annals of Forest Science* 66: 605.
20. Masendra., Purba, B.A.V., Lukmandaru, G., 2021: Antioxidant activity of *Swiethenia macrophylla* King bark extract. *Wood Research* 66(1): 57-70
21. Neamatallah, A., Yan, L., Dewar, S.J., Austin, B., 2005: An extract from teak (*Tectona grandis*) bark inhibited *Listeria monocytogenes* and methicillin resistant *Staphylococcus aureus*. *Letters in Applied Microbiology* 41: 94–96.
22. Neiva, D.M., Araujo, S., Gominhoa, J., Carneiro, A.D.C, Pereira, H., 2018: Potential of *Eucalyptus globulus* industrial bark as a biorefinery feedstock: Chemical and fuel characterization. *Industrial Crops and Products* 123: 262–270.
23. Niamke, F.B., Amusant, N., Charpentier, J.P., Chaix., G., Baissac, Y., Boutahar., N., Adima, A.A., Coulibaly, S.K., Allemand, C.J., 2011: Relationship between biochemical attributes (non-structural carbohydrates and phenolic) and natural durability against fungi in dry teak wood (*Tectona grandis* L.f.). *Annals of Forest Science* 68: 201-211.
24. Niamke, F.B., Amusant, N., Stien, D., Chaix., G., Lozano, Y., Kadio, A.A., Lemenager, N., Goh, D., Adima, A.A., Coulibaly, S.K., Allemand, C.J., 2012: 4',5'-Dihydroxy-epiisocatalponol, a new naphthoquinone from *Tectona grandis* L.f. heartwood, and fungicidal activity. *International Biodeterioration & Biodegradation* 74: 93-98.
25. Niamke, B.F, Adima, A.A., Seraphin, K., Amusant, N., Jay-Allemand, C., 2018: Heartwood formation process in teak (*Tectona grandis* L): Fate of non-structural carbohydrates and characterization of forsythoside B. *International Journal of Biological and Chemical Sciences* 12(3): 1102-1112.
26. Niinemets, Ü., 2010: Responses of forest trees to single and multiple environmental stresses from seedlings to mature plants: Past stress history, stress interactions, tolerance and acclimation. *Forest Ecology and Management* 260: 1623–1639.

27. Piper, F.I, Fajardo, A., 2011: No evidence of carbon limitation with tree age and height in *Nothofagus pumilio* under Mediterranean and temperate climate conditions. *Annals of Botany* 108(5): 907–917.
28. Rizanti, D.E., Wayan, D., Beatrice, G., Andre, M., Stephane, D., Hubert, C., Christiane, G., Eric, Gelhaye., Phila, R., Rita, K.S., Syafii, W., Rozi, M., Philippe, G., 2018: Comparison of teak wood properties according to forest management: Short versus long rotation. *Annals of Forest Science* 75: 39.
29. Rosell, J.A., Piper, F.I., Jiménez-Vera, C., Vergílio, P.C.B., Marcati, C.R., Castorena, M., Olson, M.E., 2020: Inner bark as a crucial tissue for non-structural carbohydrate storage across three tropical woody plant communities. *Plant, Cell & Environment* 44: 156–170.
30. Sakai, K., 2001: Chemistry of bark. In: wood and cellulosic chemistry: Second edition, revised and expanded (ed. David N.S.H and Nobuo S). Marcel Decker Inc. New York.
31. Sala, A., Hoch, G., 2009: Height-related growth declines in ponderosa pine are not due to carbon limitation. *Plant, Cell and Environment* 32: 22–30.
32. Savage, J.A., Clearwater, M.J., Haines, D.F., Klein, T., Mencuccini, M., Sevanto, S., Turgeon, R., Zhang, C., 2016: Allocation, stress tolerance and carbon transport in plants: how does phloem physiology affect plant ecology? *Plant, Cell & Environment* 39: 709–725.
33. Singleton, V.L., Orthofer, R., Lamuela-Raventos, R.M., 1999: Analysis of total phenols and other oxidation substrates and antioxidants by means of Folin–Ciocalteu reagent. *Methods in Enzymology* 299: 152–178.
34. Sjöström, E., 1993: Wood Chemistry. Fundamentals and Applications, 2nd edition, Academic Press. San Diego, USA. 113 pp.
35. Thulasidas, P.K, Bhat, K.M., 2007: Chemical extractive compounds determining the brown-rot decay resistance of teak wood. *Holz als Roh- und Werkstoff* 65: 121–124.
36. Villagomez, H.Z., Peterson, D.M., Herrin, L., Young, R.A., 2005: Antioxidant activity of different components of pine species. *Holzforschung* 59: 156–162.
37. Windeisen, E., Klassen, A., Wegener, G., 2003: On the chemical characterisation of plantation teakwood from Panama. *Holz als Roh- und Werkstoff* 61: 416–418.
38. Withouck, H., Boeykens, A., Luyten, W., Lavigne, R., Wagemans, J., Broucke, M.V., 2019: Phenolic composition, antimicrobial and antioxidant properties of Belgian apple wood extracts. *Biologically Active Products from Nature* 9(1): 24–38.
39. Yeh, T.F., Braun, J.L., Goldfarb, B., Chang, H., Kadla, J.F., 2006: Morphological and chemical variations between juvenile wood, mature wood, and compression wood of loblolly pine (*Pinus taeda* L.). *Holzforschung* 60: 1–8.
40. Zobel, B.J., Buijtenen, J.P., 1989: Wood variation – Its causes and control. *International Association of Wood Anatomists* 10: 1–363.

FAIS RAHMAN, GANIS LUKMANDARU*
UNIVERSITAS GADJAH MADA
FACULTY OF FORESTRY
DEPARTMENT OF FOREST PRODUCTS TECHNOLOGY
JL. AGRO NO. 1, BULAKSUMUR 55281
YOGYAKARTA, INDONESIA
*Corresponding author: glukmandaru@ugm.ac.id

RESEARCH ON BAMBOO DEFECT SEGMENTATION AND CLASSIFICATION BASED ON IMPROVED U-NET NETWORK

JUNFENG HU, XI YU, YAFENG ZHAO, KAI WANG, WENLIN LU
NORTHEAST FORESTRY UNIVERSITY
CHINA

(RECEIVED AUGUST 2021)

ABSTRACT

In this paper, computer vision technology is used to quickly and accurately identify and classify the surface defects of processed bamboo, which overcomes the low efficiency of manual identification. The datasets consist of 6360 defective bamboo mat images of four categories taken by the author at the same position, which are split at a ratio of 8:2 for training and testing. In this experiment, we improved the U-net to segment the datasets and use VGG16, GoogLeNet and ResNet50 with attention mechanism for classification and comparison. The experimental results show that the accuracy of this method is 5.65% higher than the commonly used neural network method. The highest accuracy rate is 99.2%.

KEYWORDS: Deep learning, U-net, ResNet, convolutional neural network.

INTRODUCTION

Many methods have been proposed for the detection and classification of images feature defects. A paper studied the machine vision of bamboo online sorting (Xuemin et al. 2010), used IK030M face scan black-and-white industrial camera for bamboo image acquisition and processing, designed the image processing algorithm and color sorting platform of bamboo color recognition, and used the sorting algorithm based on his and gray mean value to realize the color recognition of bamboo. The method based on HOG feature and support vector machine (Mallik et al. 2011) classifier are used to detect whether there are grape leaves in the image, and the sliding window method is used to search leaves (Felzenszwalb et al. 2010). This method has good detection effect for the leaves with positive position, and poor detection accuracy for the leaves with incorrect position and incomplete surface. Gabor transform was used to recognize the homogeneous texture image in Brodatz (Riaz et al. 2013), and the effect is remarkable. However, the Gabor transform method inevitably extracts the feature noise, which affects the efficiency of the algorithm. A simple k-means algorithm is often used as a texture recognition

method, but it is difficult to obtain a better recognition effect because it is easily affected by the initial midpoint to get the local optimal solution (Patgar et al. 2014, Venkateswaran et al. 2013). Lin et al. (2012) proposed an approach to represent and recognize objects with a massive number of local image patches, can directly update the feature weights by defining and calculating feature correlations. This method works well with the task of object detection and localization from images. Differential evolution (DE) algorithm is an evolutionary algorithm based on swarm intelligence, which has been used to solve the optimal cluster center and achieved good results (Kwedlo 2011, Kuo et al. 2013). Dongxu et al. (2014) proposed the recognition of the front and back sides of bamboo based on BP neural network, the accuracy rate reached 97%, but it took a long time and could not identify the defects of bamboo itself. The scope of wood surface defects was determined by 3D image (Sioma. 2015), and the defect area was defined accurately, which enhanced the ability of wood surface defect evaluation. A graph cut method (Rother et al. 2004, Hosang et al. 2016) used Markov random field (MRF) to model the image pixels and their adjacent relations, then minimizes the energy equation through graph cut. This method requires cumbersome human-machine interaction to obtain the target and background. Aimed at the problem of high bit number in Gabor transform (Arivazhagan et al. 2006), the author proposed a method based on the combination of relief and Gabor transform. The relief algorithm is used to select the image twice, and then the optimized k-means algorithm is used to obtain high-precision texture recognition and improve the classification accuracy. To improve the robustness of binary mode to noise, a method was proposed to segment the pixel difference between the center pixel and adjacent pixels of the image object into local ternary mode (Tan et al. 2010). U-net segmentation network was used to detect and mark the infection of COVID-19 CT images with the accuracy was 95% (Saood et al. 2021). Gu et al. (2010) used a tree structured SVM to classify the defective wood board images with the accuracy rate reached 96.5%. Yusof et al. (2013) used a fuzzy logic-based pre-classifier as a means of treating uncertainty to improve the classification accuracy of tropical wood recognition system. The accuracy of wood recognition system is improved by 4%. K-Nearest Neighbor (KNN) classification algorithm has been proposed to classify the wood knot images (Cetiner et al. 2014), knot images are correctly divided into seven different categories with a correct rate of 98% by the authors. Hanbay et al. (2016) proposed that the principal curvature of image has the feature of continuous rotation invariance. The principal curvature of image can not only improve the robustness of classification neural network to image rotation changes, but also obtain the macro structure and micro structure information of target features at the same time, which can improve the effectiveness of classification algorithm. Researchers used a fuzzy pre-classifier to mark the input image as one of four categories based on the pore texture, and used SVM to classify an input image into specific tree species using a set of extracted texture features (Ibrahim et al. 2017). Hong et al. (2021) studied the influence of long-hop connection based on convolutional neural network on bamboo classification. The results show that the network model with long-hop connection has faster convergence speed and will not overfitting, but the classification accuracy is low in the face of large model.

With the development of deep learning and computer vision technology, the main method for solving bamboo defect detection is to use deep learning technology. Convolution neural

network (CNN), as a technical direction of deep learning, has successfully made a great breakthrough in image classification (Krizhevsky et al. 2012), can accurately extract the characteristics of the object in the image, train a large number of extracted object feature data, then it can classify the characteristics of the object quickly and efficiently. One contribution of this paper is proposed an effective deep learning methodology, which is used to identification bamboo slices. The deeper layers of neural network, the higher accuracy of the model achieve in the same datasets (Szegedy et al. 2015, Simonyan et al. 2015). Transfer learning is easy to build a deep layers model and leverage the feature extracting capability of the trained layers (Pan 2013). Fortunately, transfer learning is used in our method, it can classify the bamboo slices effectively. The recognition of bamboo slices made for different varieties and processing technology has strong robustness, which overcomes the shortcomings of traditional methods that need to adjust parameters frequently.

Deep learning

As a new technology in the field of machine learning, the purpose of deep learning is to enable machines to recognize the information of text, sound and image just like human beings. Deep learning has the advantages of strong learning ability, high efficiency, strong adaptability and good portability. However, its disadvantages are obvious, such as large amount of calculation, high cost of hardware and complex model design.

Convolutional neural network (CNN)

Convolutional neural network is composed of convolutions, activations and pooling. Its output is a specific feature space of image. Taking this feature space as input, it outputs a specific category through the fully connected layer, that is to complete the classification task. According to the different functions, the forward and backward connection and intra layer adjustment of each part of CNN are different, and the convolution kernel size, activation function, pooling and weight parameters are also different. At present, the popular convolutional neural networks such as VGG16, GoogLeNet and ResNet50 are all composed of basic convolutional neural networks.

VGG16

VGG16 network was proposed by Oxford University in 2014, which mainly proves that the final performance of the network will be better with the increase of network depth. VGG16 has 16 layers, including 13 convolution layers and 3 fully connected layers. Compared with AlexNet, which won the champion of ImageNet competition in 2012, the biggest improvement of VGG16 is to use continuous 3*3 convolution core instead of 5*5, 7*7 and other larger convolution cores, because there are only 3*3 convolution and 2*2 maximum pooling layers in the network, which can increase the network depth and reduce the amount of parameters. Therefore, the effect of network training is better.

GoogLeNet

GoogLeNet was proposed by Christian Szegedy in 2014. Compared with VGG16. The output layer of GoogLeNet is 1*1 convolution layer, not VGG16 full connection layer. There are

different ways to solve the disadvantages of network deepening. GoogLeNet introduces a parallel network structure, in which there are four different lines in each layer to process the network input, focusing on the "wider" structure rather than the "deeper" structure of VGG16. The core of GoogLeNet lies in the emergence structure block. Its main functions are as follows: firstly, 1*1 convolution is used to increase or decrease the dimension, so that more convolutions can be superimposed to obtain richer image features and reduce the computational complexity. Secondly, convolution and regrouping on multiple dimensions at the same time to obtain more abundant features and more accurate classification (Fig. 1).

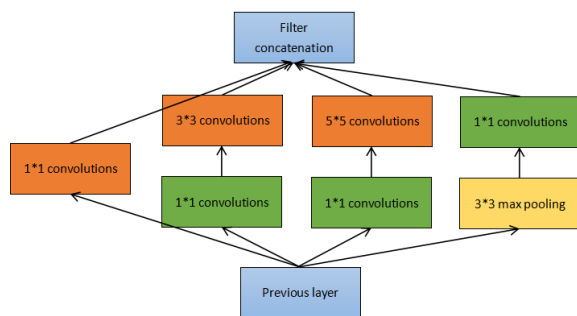


Fig. 1: The inception module of GoogLeNet.

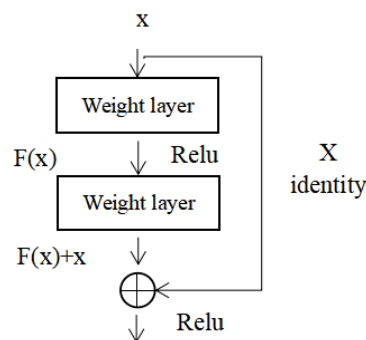


Fig. 2: Basic unit of residual model.

ResNet50

ResNet50 network was proposed by Kaiming et al. (2015). The characteristic of ResNet50 network is that it adds residual structure. By using multiple parameter layers to learn the residual structure of input and output, it not only has faster convergence speed, but also can avoid the gradient disappearing, and has higher classification accuracy. As the main part of ResNet, the residual learning unit is shown in Fig. 2. The residual structure can learn the input of each layer to form a residual function. The residual function of the first layer is defined:

$$F = \omega_2 \sigma(\omega_1 x) \tag{1}$$

where: σ - represents the ReLu function. After shortcut and the second function of ReLu, the output y is:

$$y = F(x, \{\omega_i\}) + x \tag{2}$$

If it is necessary to change the dimension of input and output, that is, to change the number of channels, the linear transformation of x can be performed at the time of shortcut:

$$y = F(x, \{\omega_i\}) + \omega_s x \tag{3}$$

U-net

U-net was proposed in 2015 by Olaf Ronneberger of Fitzburg University. It is a full convolution deep learning network without full connection layers, which is used for semantic

segmentation of images. It adopts the architecture of encoder and decoder, performs four down sampling and four up sampling operations respectively. It can not only increase the robustness to the small disturbance of the input image, but also reduce the overfitting and the amount of computation, get better segmentation results. The structure of U-net network is shown in Fig. 3.

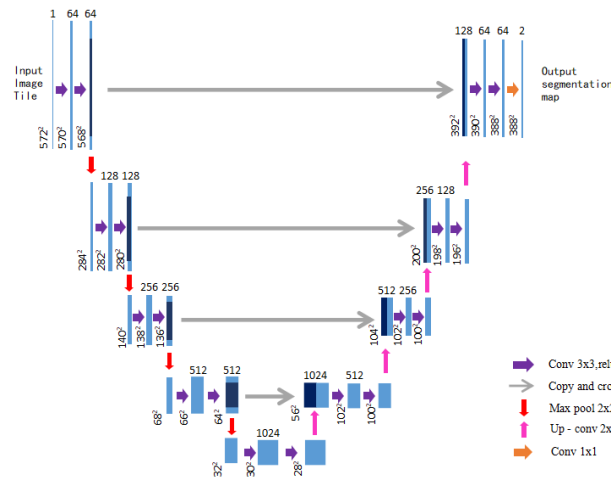


Fig. 3: U-net network structure.

Attention mechanism

Attention mechanism is a kind of resource allocation mechanism, which enables the computer to get the target area that needs attention just like human attention, and allocate more attention to the target area, ignoring the information of irrelevant areas. Attention mechanism includes soft attention mechanism and hard attention mechanism. Soft attention mechanism allocates a weight between $[0,1]$ according to the attention degree of features in the image region, that is, most information is considered, but the degree of consideration is not. Soft attention pays more attention to the channel, which is deterministic attention and differentiable and ensures that soft attention can calculate the size of the gradient through deep learning algorithm, get the weight of attention through forward propagation and backward propagation. Strong attention pays more attention to point, which is a random prediction process and emphasizes dynamic change. At the same time, strong attention is not differentiable, the weight parameters are obtained by reinforcement learning.

Channel attention and spatial attention

Channel attention can be used to automatically obtain the importance of each channel feature through deep learning, and assign different weight parameters to each channel, so as to enhance the important features and weaken the unimportant features.

Spatial attention can transform the spatial information in the original image to another space after using the spatial transfer module, retain the important feature information while transferring, and generate a weight mask for each position. After weighted output, it can enhance the important features and weaken the unimportant features.

Continuous block attention module (CBAM) is a hybrid attention mechanism module which combines space and channel. Compared with the attention mechanism which only focus on channel or space, it can achieve better effect, and can be embedded into deep learning networks

as a plug and play module: (1) The CBAM module based on VGG16 network is added after each build-up layer. (2) The CBAM module based on GoogLeNet, like VGG16, adds this module after each build-up layer. (3) CBAM module based on ResNet50 is added after each residual structure. The relevant illustration are shown in Figs. 4 and 5.

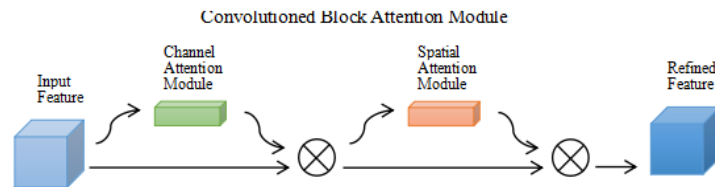


Fig. 4: Convolution layer of attention module.

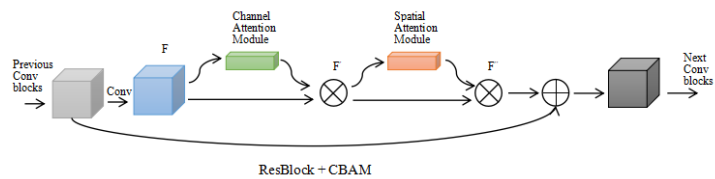


Fig. 5: Residual structure of attention module.

MATERIAL AND METHODS

Datasets

In order to ensure that the image quality will not be affected by the external factors, 6360 images were selected for the experiment after screening out some blurred images on the premise of ensuring that only the bamboo itself is different and other conditions are the same. According to the different types of defects, it can be divided into four categories, type (a) 1713 pictures, type (b) 1727 pictures, type (c) 1718 pictures, and type (d) 1202 pictures. The representative features of the four types are shown in the Fig. 6 and named Banpiancai, Feipiancai, Huapiancai, Lantoucai separately. Each photo is manually cropped to 256*256 pixels, which makes it easier to be processed by deep learning network. Each image in the datasets is uniquely numbered according to its defect category, which ensures that the defect category of the image can be quickly and accurately identified by numbering.

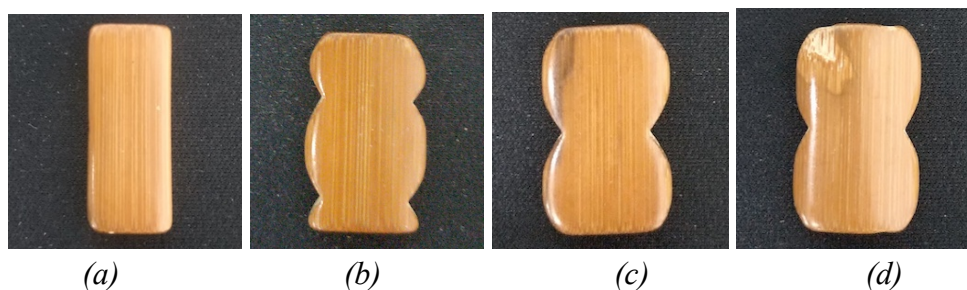


Fig. 6: Datasets image: (a) Banpiancai, (b) Feipiancai, (c) Huapiancai, (d) Lantoucai.

Experimental environment

In this experiment, using PyCharm software, PyTorch1.8.0 framework for bamboo defect segmentation and classification. The experiment adopts windows 10, the CPU is the ninth generation of Intel Core i7-9750H, the RAM is 16GB, the GPU is NVIDIA GeForce GTX 1660Ti, and the CUDA version is 10.2.141.

Research methods

Edge detection

In computer vision, the edge and contour of image objects contain important information. In this experiment, Sobel operator is used to process the original image to obtain the edge contour of bamboo defects. The image obtained is shown in Fig. 7.

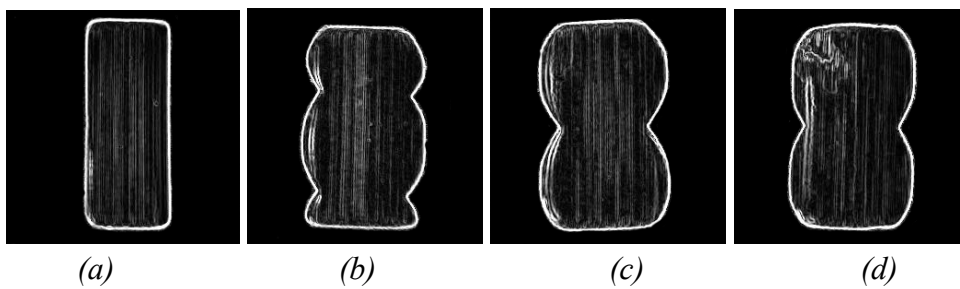


Fig. 7: Edge detection image of datasets after Sobel operator.

Since the obtained image is RGB three channel image, when using U-net network for image segmentation, we need to choose to gray the image and process it into single channel mode. In this experiment, the commonly used weighted average algorithm is used to gray the datasets, that is, the pixel values of R, G and B channels are weighted average according to a certain weight. The calculation formula is shown in Eq. 4:

$$\text{gray} = R * 0.229 + G * 0.587 + B * 0.114 \quad (4)$$

where: R - red channel, G - green channel and B - blue channel.

Improving U-net

In this paper, the improved U-net network adds residual structure to the decoding block, which can not only reduce the loss of image features in the convolution process and suppress the phenomenon of gradient disappearance and gradient explosion in the training process effectively, but also improve the ability of the decoder to recover features.

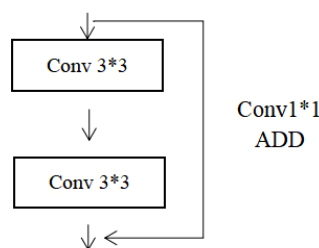


Fig. 8: Residual structure of U-net network.

The residual structure added in U-net is shown in Fig. 8. The residual block connects the output of the shallow network to the deep network and takes it as a part of the convolution input of the deep network. This method can effectively reduce the loss of image features in the convolution process, retain more useful information and improve the utilization of features. When the dimensions of the two images linked by the residual structure are the same, we use the residual structure shown in Fig. 2. When the dimensions are different, it is necessary to convert the dimensions through a one-dimensional convolution layer shown in Fig. 8 and then overlay the images. The improved U-net is shown in Fig. 9 .

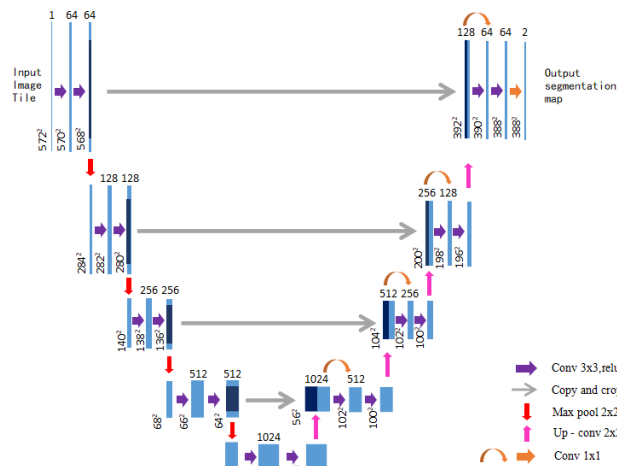


Fig. 9: Improved U-net network structure.

The grayed image is segmented by U-net network (Fig. 10). The image is segmented by the improved U-net network, and the effect is shown in Fig. 11.

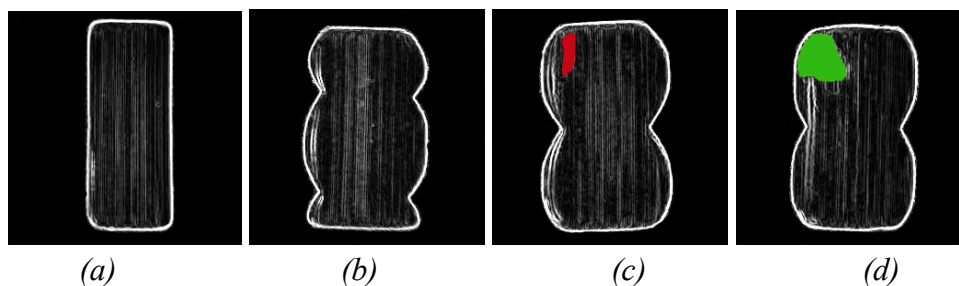


Fig. 10: U-net network segmentation image of datasets.

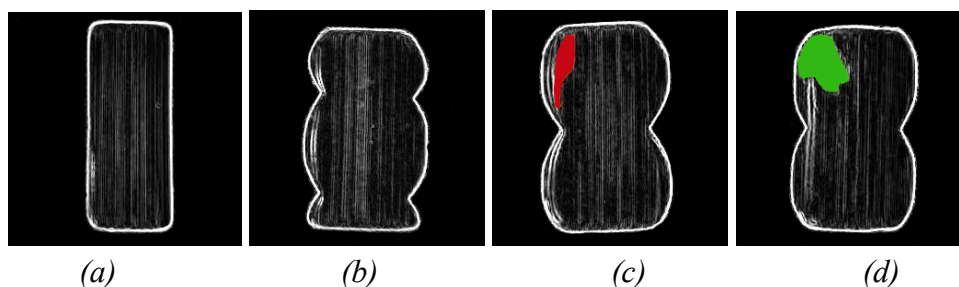


Fig. 11: Image segmentation based on improved U-net network of datasets.

Because the shape of the bamboo pieces with (a) and (b) defects is different from that of the normal mahjong bamboo pieces, the types of the defects can be distinguished by their shapes. Compared with (d) and (c), the color of most (c) defects is darker than the primary color of the bamboo pieces, which is indicated by red (d) The color of the defect is lighter than the primary color, which is indicated by green. It can be seen from the visual comparison chart that the improved U-net network can segment the defects of (c) and (d) bamboo pieces more accurately and the effect is better on the basis of accurately segmenting bamboo pieces.

After the improved U-net segmentation processing, the output of four types of defects are divided by the ratio of training: testing = 8 : 2. By adding three classification networks VGG16, GoogLeNet and ResNet50 of CBAM attention mechanism module to classify defects, the classification accuracy of the three is compared. During the experiment, in order to ensure the reliability and fairness of the experimental results, after using several rounds of tests, the final three kinds of classification network para-meters are as follows: learning rate is 0.0001, optimizer is Adam, batch size is 32, epoch is 60.

RESULTS AND DISCUSSION

The classification accuracy of neural network model based on transfer learning in different segmentation networks and classification network models are shown in Tab. 1. It can be seen that the highest accuracy of the three classification networks is 93.57% of ResNet50 when the segmentation network model is none, but there is little difference compared with the other two networks. When the basic U-net segmentation network is used, the highest accuracy is 97.12% of ResNet50, compared with the accuracy of 93.57% without segmentation network model, the accuracy of ResNet50 is improved by at least 3%, the improvement effect is obvious. Compared with VGG16 and GoogLeNet under the same conditions, the accuracy is improved by 1-2%, and the improvement is obvious. When using the improved U-net segmentation network with residual structure, the accuracy of the three kinds of classification neural networks has been significantly improved compared with the previous ones. The most improved one is GoogLeNet, which has increased by 3.26%, and the highest recognition rate is ResNet50, which has reached 99.22%. Compared with the U-net network before the improvement, the recognition rate has increased by 2.1%.

The experimental results show that the ResNet50 classification network has the highest recognition accuracy under the same condition, whether the segmentation network model is used or not. When the basic segmentation network and the improved segmentation network are used, the recognition accuracy of ResNet50 classification network is significantly improved, and the highest recognition rate reaches 99.22%.

Tab. 1: Accuracy of image recognition of bamboo defects (%).

Segmentation network model	Classification network model		
	VGG16	GoogLeNet	ResNet50
None	93.15	93.56	93.57
U-net	95.81	94.63	97.12
U-net+residual	97.24	97.89	99.22

Fig. 12 shows the broken line graph of bamboo defect recognition accuracy based on VGG16, GoogLeNet and ResNet50 networks respectively. From the graph, we can see the difference in recognition accuracy under different segmentation network models easily and intuitively. The blue line indicates that the segmentation network model is not adopted, the red line indicates that the basic U-net segmentation model is adopted, and the orange line indicates that the improved U-net segmentation model is adopted.

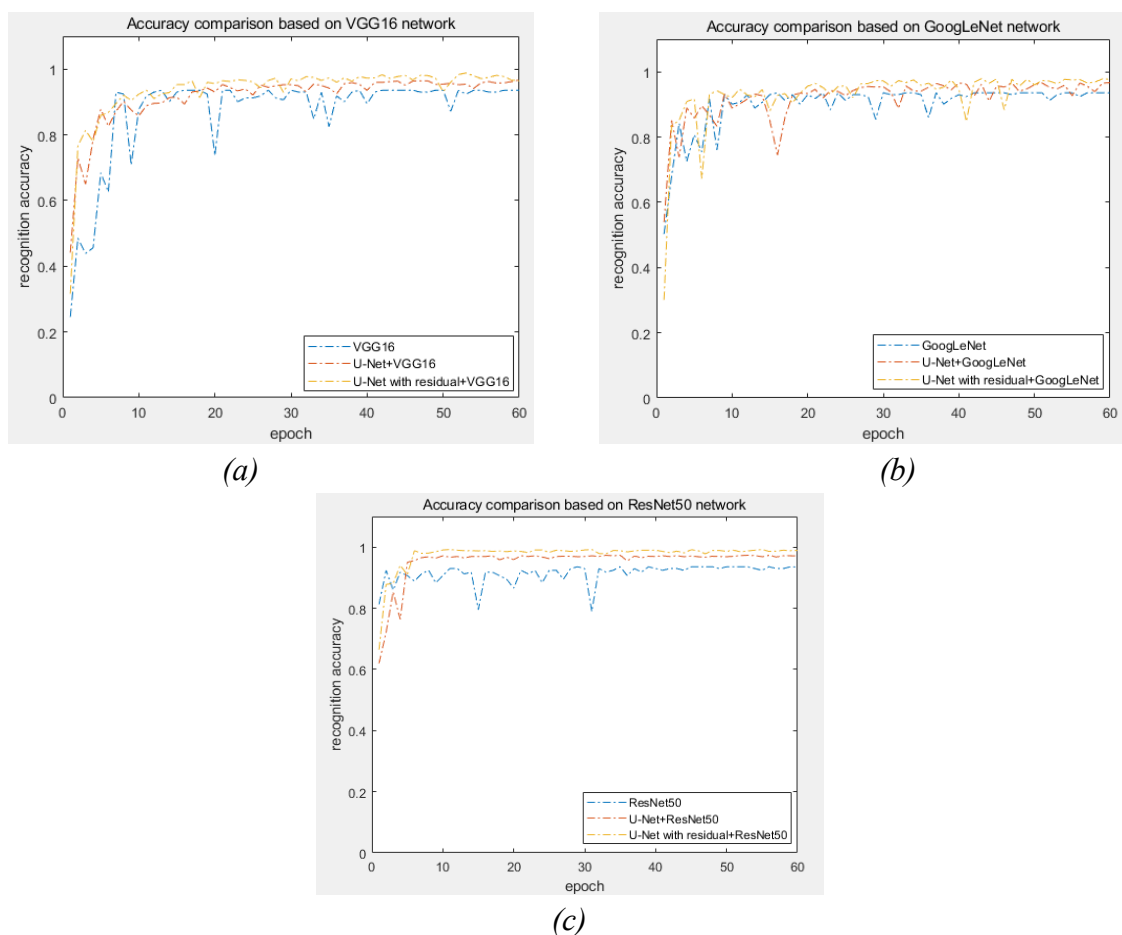


Fig. 12: Comparison of recognition accuracy of different classification networks: (a) comparison of recognition accuracy based on VGG16 network, (b) comparison of recognition accuracy based on GoogLeNet network, (c) comparison of recognition accuracy based on ResNet50 network.

Confusion matrix

Confusion matrix, also known as error matrix, is a visual tool used to evaluate the classification accuracy. The columns of confusion matrix are classification categories, and the total number of each column is the number of network prediction categories. Each row represents the real category of the image, and the total number of each row is the actual number of classified images of the category. In the matrix diagram, the depth of background color represents the accuracy of classification recognition. The deeper the color is, the higher the accuracy of model recognition is.

Because the ratio of training and testing is 8:2, the number of defect images of (a) Banpiancai, (b) Feipiancai, (c) Huapiancai and (d) Lantoucai is 342, 345, 343 and 240, resp. Fig. 13 shows the confusion matrix of different classification networks. It can be seen that the recognition accuracy of (c) is the highest. In 1270 testing photos, 1260 photos are accurately identified, and the recognition accuracy is 99.2%. A small part of the image classification errors may be due to the similar texture between the bamboo defects.

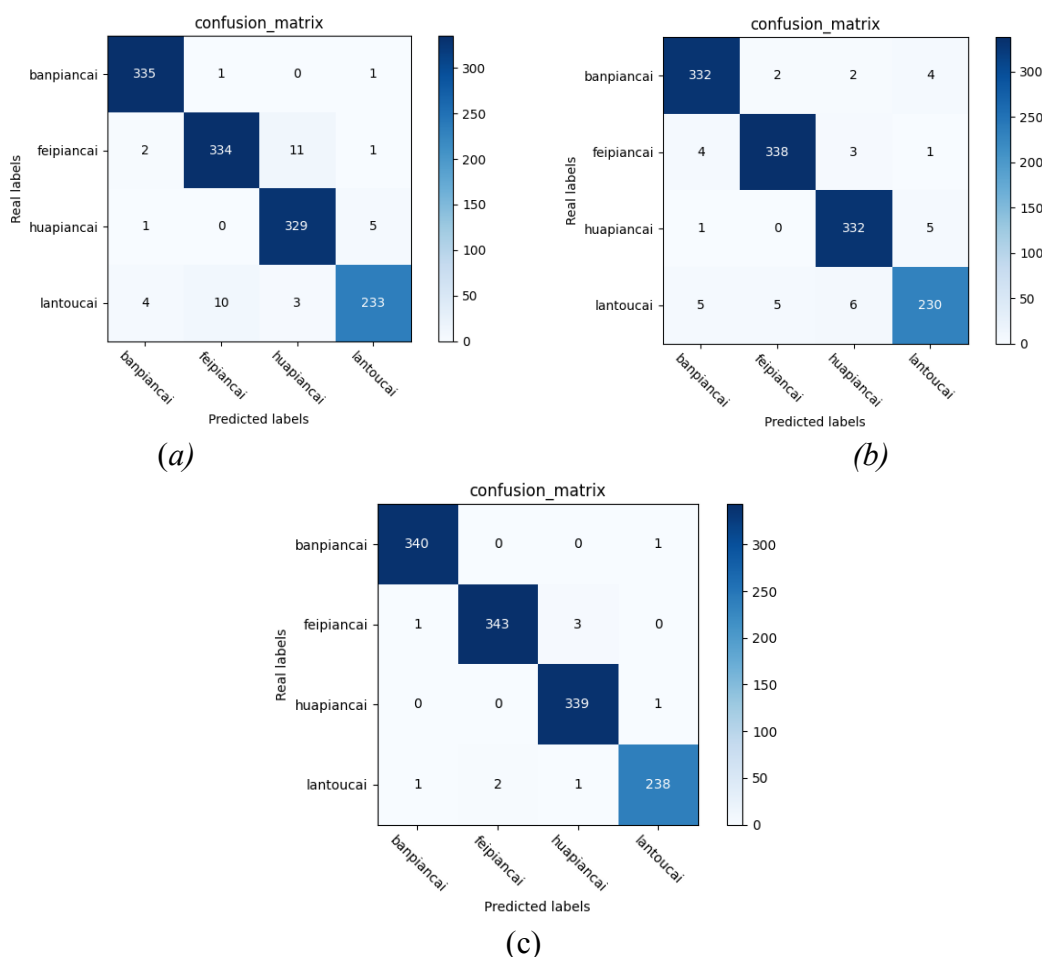


Fig. 13: Confusion matrix of different classification networks: (a) VGG16, (b) GoogLeNet, (c) ResNet50.

CONCLUSION

In order to realize the accurate classification of bamboo defects, we propose a two-stage method for datasets segmentation before classification. In order to achieve better image segmentation, the traditional U-net segmentation network is improved by adding residual blocks to achieve more accurate defect segmentation. The experimental results show that after using the improved segmentation network, the accuracy of the three kinds of classification neural networks has been significantly improved compared with the previous ones. The highest improvement is GoogLeNet, which increases by 3.26%, and the highest recognition accuracy is ResNet50, which reaches 99.22%. Compared with the U-net network before the improvement,

the recognition accuracy increases by 2.1%, It is proved that the improved model can improve the accuracy of defect classification. From the confusion matrix, we can see that there are still some shortcomings in this research. On the one hand, some images in the datasets have similarity in the shape and texture of defects, on the other hand, some images must be divided into a certain category when there are two kinds of defects at the same time, which affects the accuracy of classification. In view of the above problems, the author will carefully select the datasets to ensure that a picture has only one kind of defects. At the same time, the author will continue to learn and choose a new deep learning algorithm for verification.

ACKNOWLEDGEMENTS

This work is supported by the Fundamental Research Funds for the Central Universities (No. 2572019BF09), Heilongjiang Provincial Postdoctoral Science Foundation (No.178157) .

REFERENCES

1. Arivazhagan, S., Ganesan, L., Priyal, SP., 2006: Texture classification using Gabor wavelets based rotation invariant features. *Pattern Recognition Letters* 27(16): 1976-1982.
2. Cetiner, S., Var, AA., Cetiner, H., 2014: Classification of KNOT defect types. *IEEE Signal Processing & Communications Applications Conference*, Pp 1086-1089.
3. Dongxu, W., Shuxiang, X., Pinqun, J., 2014: The algorithm of identifying the front side of bamboo based on BP neural network. *Journal of Guangxi Normal University Natural Science Edition* 32(02): 14-19.
4. Felzenszwalb, P., Girshick, R., McAllester, D., Ramanan, D., 2010: Object detection with discriminatively trained part based models. *IEEE Transactions on Pattern Analysis and Machine Intelligence* 32(9): 1627-1645.
5. Gu, YH., Andersson, H., Vicen, R., 2010: Wood defect classification based on image analysis and support vector machines. *Wood Science and Technology* 44: 693-704.
6. Hanbay, K., Alpaslan, N., Talu, MF., Hanbay, D., 2016: Principal curvatures based rotation invariant algorithms for efficient texture classification. *Neurocomputing* 199: 77-89.
7. Hong, HH., Trinh, HH., 2021: Improvement for convolutional neural networks in image classification using long skip connection. *Applied Sciences* 11: 2092.
8. Hosang, J., Benenson, R., Dollar, P., Schiele, B., 2016: What makes for effective detection proposals? *IEEE Transactions on Pattern Analysis Machine Intelligence* 38(4): 814-830.
9. Ibrahim, I., Khairuddin, ASM., Talip, AMS., Arof, H., Yusof, R., 2017: Tree species recognition system based on macroscopic image analysis. *Wood Science and Technology* 51: 431-444.
10. Krizhevsky, A., Sutskever, I., Hinton, G., 2012: ImageNet classification with deep convolutional neural networks. *Advances in Neural Information Processing Systems* 25(2): 1-9.
11. Kwedlo, W., 2011: A clustering method combining differential evolution with the K-means algorithm. *Pattern Recognition Letters* 32(12): 1613-1621.

12. Kuo, R.J., Suryani, E., Yasid, A., 2013: Automatic clustering combining ng differential evolution algorithm and K means algorithm. *Proceedings of the Institute of Industrial Engineers Asian Conference* 1207-1215.
13. Lin, L., Luo, P., Chen, X., Zeng, K., 2012: Representing and recognizing objects with massive local image patches. *Pattern Recognit* 45(1): 231–240.
14. Mallik, A., Tarrío-Saavedra, J., Francisco-Fernández, M., Naya, S., 2011: Classification of wood micrographs by image segmentation. *Chemometrics and Intelligent Laboratory Systems* 107(2): 351-362.
15. Pan, S.J., 2013: Transfer learning with applications on text, sensors and images. *Machine Learning for Interactive Systems*, Pp 7-7.
16. Patgar, S.V., Sharath, KYH., Vasudev, T., 2014: Detection of fabrication in photocopy document using texture features through K-means clustering. *Signal Image Processing* 5(4): 29-36.
17. Riaz, F., Hassan, A., Rehman, S., Qamar, U., 2013: Texture classification using rotation and scale invariant Gabor texture features. *IEEE Signal Processing Letters* 20(6): 607-610.
18. Rother, C., Kolmogorov, V., Blake, A., 2004: Grabcut: Interactive foreground extraction using iterated graph cuts. *ACM Transactions on Graphics* 23(3): 309-314.
19. Szegedy, C., Liu, W., Jia, Y., Sermanet, P., Reed, S., Anguelov, D., Erhan, D., Vanhoucke, V., Rabinovich, A., 2015: Going deeper with convolutions. *Proceedings of the IEEE Computer society conference on computer vision and pattern recognition*, Pp 1-9.
20. Simonyan, K., Zisserman, K., 2015: Very deep convolutional networks for large-scale image recognition. *International Conference on Learning Representations*, Pp 1-14.
21. Saood, A. , Hatem, I., 2021: COVID-19 lung CT image segmentation using deep learning methods: U-net versus SegNet. *BMC Medical Imaging* 21:19.
22. Sioma, A., 2015: Assessment of wood surface defects based on 3D image analysis. *Wood Research* 60(3): 339-350.
23. Tan, X., Triggs, B., 2010: Enhanced local texture feature sets for face recognition under difficult lighting conditions. *IEEE Transactions on Image Processing* 19(6): 1635-1650.
24. Venkateswaran, K., Kasthuri, N., Balakrishnan, K., 2013: Performance analysis of K-means clustering for remotely sensed Images. *International Journal of Computer Applications* 84(12): 23-27.
25. Xuemin, G., Xiansheng, Q., Feng, H., Qiong, L., Xin, S., 2010: Online defect inspection algorithm of bamboo strip based on computer vision. *IEEE International Conference on Industrial Technology*. Pp 1-5+10.
26. Yusof, R., Khalid, M., Khairuddin, ASM., 2013: Fuzzy logic-based pre-classifier for tropical wood species recognition system. *Machine Vision and Applications* 24: 1589-1604.

JUNFENG HU, XI YU*
MECHANICAL AND ELECTRICAL ENGINEERING
NORTHEAST FORESTRY UNIVERSITY
HARBIN, HEILONGJIANG 150040
CHINA

YAFENG ZHAO*
INFORMATION AND COMPUTER ENGINEERING
NORTHEAST FORESTRY UNIVERSITY
HARBIN, HEILONGJIANG 150040
CHINA

*Corresponding authors: YXyuxi419@163.com and nefuzyf@126.com

KAI WANG, WENLIN LU
MECHANICAL AND ELECTRICAL ENGINEERING
NORTHEAST FORESTRY UNIVERSITY
HARBIN, HEILONGJIANG 150040
CHINA

EFFECTS OF LIQUID NITROGEN IN HARDLY IMPREGNABLE FIR WOOD

SEREF KURT
KASTAMONU UNIVERSITY
TURKEY

(RECEIVED APRIL 2021)

ABSTRACT

The main purpose of this study was to develop new methods to eliminate the problems encountered during the impregnation of wood material, and in this context, to improve the retention of wood material by using liquefied nitrogen. Uludağ Fir (*Abies nordmanniana* subsp. *Bornmulleriana*) was used as wood material impregnated with Tanalith-E, Immersol aqua and borax. The effects of liquid nitrogen and the amount of retention on the mechanical properties were investigated. Application of liquid nitrogen before impregnation has increased the retention in fir wood by an average of 150-200% in all impregnation methods, compared to the groups without liquid nitrogen application. Despite this increase in retention amounts, no significant changes were observed in mechanical properties due to the application of liquid nitrogen.

KEYWORDS: Uludağ fir, Tanalith-E, Immersol aqua, retention, nitrogen.

INTRODUCTION

Wood has played a major role throughout human history and has been used for millennia due to its numerous advantages include being widely distributed, multifunctional, strong, and easy to handle and process, aesthetic, sustainable and renewable (Hill 2006, Rowell 2005, Gecer et al. 2015). However, wood has some disadvantages related to its dimensional instability when wet and degradation occur due to abiotic agents including weathering, fire, erosion and mechanical-related damage and biotic agents including mold, fungi, decay and insects such as termites, beetles and marine borers (Gecer et al. 2015). In the recent years, there is some research about various methods on the preservation of wood (Jensen et al. 2002, Jensen and Schnell 2005, Jensen P. and Jensen J.B. 2006). Generally, these protection methods consist of impregnation, heat treatment, modification, drying and the upper surface treatment.

The impregnation of wood is one of wood preservation methods which is used to improve its material properties by altering its chemical nature in a broader sense. It is also a passive

process, where changes in properties also occur, but without an alteration of the chemistry of the material. Kurt et al. (2012) investigated the effect of liquid nitrogen on dimensional stability of Uludag fir (*Abies bornmülleriana* Mattf) wood after exposing to the steam test (2, 6, 12, 24, 48, and 96 hours). Samples were kept in a container filled with liquid nitrogen for 1, 4 and 10 hours, liquid nitrogen application was carried out in an open area and the liquid nitrogen was constantly filled in case it decreases. As a result, retention amounts were increased while liquid nitrogen and steam time are enhanced. Ors et al. (2006) investigated effects of impregnation with Imersol aqua on the modulus of elasticity in bending of oriental beech, oak, Scotch pine, Uludag fir, oriental spruce, and poplar. They found that the highest modulus of elasticity in bending was obtained in Oriental beech with short-term immersion (10720 Nmm^{-2}) whereas the lowest was in poplar with long-term immersion (4597 Nmm^{-2}). Simsek et al. (2010) studied some mechanical properties such as compression strength parallel to grain, modulus of rupture of wood impregnated with some environmentally-friendly borates (sodium tetra fluor borate, ammonium tetrafluoroborate, and ammonium pentaborate octahydrate and found that the higher concentration levels of borates, the lower mechanical properties of wood resulted. Villasante et al. (2013) determined the effect of preservatives (Vacsol Azure WR 2601 and Tanalith E 3492) on mechanical properties and to establish the relation between the penetration and compression strength for *Pinus sylvestris*. They observed that the treated wood (with either product) presents a statistically significant increase in static bending strength, modulus of elasticity and compression strength parallel to the grain. The purpose of this study was to determine air dry density, mechanical properties, and amount of retention in wood material applied with liquid nitrogen which has the potential to be a new method which can eliminate problems encountered in the impregnation of Uludag fir wood.

MATERIAL AND METHODS

Wood species

Uludag fir (*Abies nordmanniana* subsp. *Bornmulleriana*) was chosen randomly from timber suppliers in Ankara, Turkey. A special emphasis was put on the selection of the wood material. Accordingly, nondeficient, whole, knotless, normally grown (without zone-line, reaction wood, decay, and insect or fungal infection) wood materials were selected.

Impregnation materials

Tanalith E, Immersol aqua, borax (2.5% solution) supplied from Hemel Emp. San. and Tic. A.Ş. were used as impregnation chemicals. Tanalith E as the preservative used for this article is constitute of copper carbonate (CuCO_3), 2-aminoethanol, tebuconazole, boric acid (H_3BO_3) and di-2-ethylhexylphthalate. Tanalith-E impregnating agent was used in the form of a solution at a concentration of 2.36%. Imersol aqua was applied as a solution at 2.5% concentration. Borax was prepared in the laboratory in a way that they were at a concentration of 2.5%, after being completely dissolved.

Liquid nitrogen

Nitrogen is inert to most materials and its fluid is very cold. Due to these features, it is a safe freezer and cooler. Liquid nitrogen is inert, uncolored, odorless, noncorrosive, not support combustion, and extremely cold. Features of nitrogen are given in Tab. 1.

Tab. 1: Features of nitrogen.

Density	0.000808 g cm ⁻³
Freezing point 1 atm	- 210.0°C
Boiling point 1 atm	- 195.79°C

Density determination

Wood materials were kept in the room at $20 \pm 2^\circ\text{C}$ and $65 \pm 3\%$ relative humidity until their weight became stable. The air-dry densities of wood materials were determined according to TS 2472 (2005) before and after the impregnation process. Then, the dimensions of wood materials were measured with a compass of ± 0.001 sensitivity, and their volumes were determined by a stereometric method. The air-dry density (δ_{12}) was calculated using the following Eq. 1:

$$\delta_{12} = M_{12}/V_{12} \text{ (g cm}^3\text{)} \quad (1)$$

where: M_{12} is the perfect air-dry weight (g), and V_{12} is the volume (cm³) of the wood material.

Preparation of experimental samples

Air-dried samples were exposed to liquid nitrogen before impregnation in order to increase the retention amount of the impregnating agent. Samples prepared for each group were kept in liquid nitrogen for 15, 90 and 360 min. Then, the impregnation process was applied to the samples that were air dried, according to ASTM D 1413-76 (1976), TS 344 (1981) and TS 345 (1974) standards.

Before impregnation process, all samples except the control samples were kept under liquid nitrogen environment in the form of 15, 90 and 360 min, resp. Four different impregnation methods were used in each method in which the test samples were treated four different types of impregnation materials. First method, driving method with a brush, the samples were applied impregnation materials with the help of a brush. Second method, using the short term immersion method, the samples were dipped into the impregnation materials for 5 min. Third method, long-term immersion, the samples were dipped into the impregnation materials for 90 min. Fourth method, a pressure vacuuming method, which was equal to 760 mmHg, was applied to the samples. They were then dipped for 60 min in a impregnating tank which filled with impregnation materials to 8–10 atm pressure. The above-mentioned four methods were applied separately for each impregnating agent (Tanalith-E, Imersol aqua, borax 2.5% solution). Before the impregnation process, all samples were weighed in an analytic balance with 0.01 g sensitivity. After the impregnation, the samples were kept until 3-4 days in a sunless environment. After cooling, all dried samples in the desiccator were weighed on the scale. The dry weight of the

samples was determined and recorded. The amount of retention (R , kg m^{-3}) and ratio of retention (R , %) were calculated as follows:

$$R = \frac{G \cdot C}{V} \cdot 10 \quad (\text{kg m}^{-3}) \quad (2)$$

$$R(\%) = \frac{M_{oes} - M_{oeö}}{M_{oeö}} \cdot 100 \quad (\text{kg m}^{-3}) \quad (3)$$

$$G = M_{0es} - M_{0eo} \quad (4)$$

where: R - the weight gain percentage, G - amount of preservative solution absorbed by the sample (kg), C - the concentration of the impregnating material (%), $M_{oeö}$ - the weight of the oven-dried specimens before impregnation (kg), and M_{oes} - the weight of oven-dried after impregnation (kg).

Application of the test

Before testing all samples were climatized until they were stable at $20 \pm 2^\circ\text{C}$ and $65 \pm 3\%$ relative humidity (RH) in climate room. The samples for bending test (MOR) and dynamic bending strength were cut as $2 \times 2 \times 32$ cm according to TS 2474 (1976), TS 2477 (1976) respectively. Modulus of elasticity in bending (MOE) was conducted as compliance with TS EN 310 (1999). Bending strength and modulus of elasticity in bending were determined by using Universal testing machine. Impact strength was determined by using 10 kg m^{-3} pendulum hammer tool. Compression strength in the parallel to the fibers was tested as compliance with TS 2474 (1976), TS 2595 (1976) resp. Specimens were 2 cm in thickness and width and 3 cm in length. Compressive strength in the parallel to the fibers was defined by using the universal testing machine.

Data analyses

By using four impregnation chemicals and one unimpregnated control sample, and four different impregnation methods were prepared using 10 replications for each combination. Multiple analyses of variances were used to determine the effect of liquid nitrogen in impregnation of the prepared samples.

RESULTS AND DISCUSSION

In this study, Uludag fir wood was impregnated by using Tanalith-E, borax and Imersol aqua. All of the samples (not control) before the impregnation process was subjected to liquid nitrogen treatment. The summary results of air dry density, retention rate and mechanical properties for each combination were given in Tabs. 2, 3 and 4.

Tab. 2: Summary of results related to air dry density of Uludag fir wood (g cm^{-3}).

Impregnation materials	Impregnation method	Time of exposure in liquid nitrogen		
		15 min	90 min	360 min
Tanalith-E	Brush	0.428	0.445	0.446
	Short-term immersion	0.426	0.433	0.425
	Long-term immersion	0.430	0.424	0.467
	The pressure-vacuuming	0.415	0.442	0.445
Borax	Brush	0.428	0.438	0.442
	Short-term immersion	0.427	0.437	0.447
	Long-term immersion	0.437	0.428	0.435
	The pressure-vacuuming	0.433	0.435	0.436
Imersol aqua	Brush	0.443	0.442	0.421
	Short-term immersion	0.463	0.463	0.436
	Long-term immersion	0.455	0.456	0.452
	The pressure-vacuuming	0.422	0.427	0.434

The highest air dry density value was determined as 0.467 g cm^{-3} on the samples impregnated with long-term immersion method in Tanalith-E after incubation in liquid nitrogen environment for 360 min and the lowest value was found as 0.415 g cm^{-3} on the samples impregnated with the pressure-vacuuming method in Tanalith-E after waiting in liquid nitrogen environment for 15 min. Ors et al. (2006) determined that the increment with the increase in the impregnation period of air-dry densities of wood species impregnated with Imersol aqua. Air dry density is a measure of the proportion of cell wall material in the wood and is hence dependent on the ratio of cell wall thickness and cell diameter (Lundgren 2004).

Tab. 3 summarizes the mean values of the retention rate in Uludag fir wood. The highest change value of retention rate was 624% with the samples impregnated with the borax, applied by the brush method and exposed to liquid nitrogen for 90 min before impregnation method. In contrast, the lowest change was 18.9% in the samples impregnated with the Imersol aqua, applied by brush method and exposed to liquid nitrogen for 15 min before impregnation.

Tab. 3: The mean values of the retention rate in Uludag fir wood (%).

Impregnation material	Impregnation method	Time of exposure in liquid nitrogen			
		Uludag fir			Control
		15 min	90 min	360 min	
Tanalith-E	Brush	2.026	4.154	3.280	1.289
		0.204*	0.290*	0.136*	0.042*
		57,07**	222.11**	154.34**	
	Short-term immersion	3.348	5.698	4.505	1.602
		0.068*	0.210*	0.138*	0.154*
		108.91**	255.54**	181.07**	
	Long-term immersion	2.488	4.431	4.104	1.647
		0.198*	0.109*	0.163*	0.255*
51.01**		168.94**	149.12**		
The pressure-vacuuming	4.295	5.323	4.343	2.323	
	0.311*	0.376*	0.257*	0.143*	
	84.88**	129.12**	86.92**		
Borax	Brush	4.055	4.994	4.531	0.689
		0.190*	0.191*	0.365*	0.201*

		488.40**	624.60**	557.37**	
	Short-term immersion	4.376 0.214*	4.990 0.289*	3.952 0.324*	1.202 0.102*
	Long-term immersion	4.747 0.298*	6.358 0.421*	3.684 0.216*	1.943 0.142*
	The pressure-vacuuming	6.134 0.258*	8.441 0.462*	5.172 0.260*	1.599 0.125*
Imersol aqua	Brush	1.876 0.112*	2.921 0.241*	5.778 0.433*	1.577 0.213*
	Short-term immersion	4.084 0.310*	5.866 0.392*	5.312 0.319*	2.064 0.162*
	Long-term immersion	4.216 0.295*	6.267 0.059*	8.351 0.378*	2.176 0.217*
	The pressure-vacuuming	5.866 0.417*	6.166 0.459*	5.394 0.318*	1.141 0.112*

* Standard deviation.

** % Change in retention amount according to the samples without pre-impregnation liquid nitrogen application.

Generally, there was an increase in the amount of retention for 15 min and 90 min time of exposed in a nitrogen atmosphere of Uludag fir wood whereas the amount decreased in the time of exposure in nitrogen atmosphere for 360 min. Xu et al. (2015) and Poonia et al. (2016) determined that the retention rate increased by the treatment of the microwave method before the process of impregnation in wood material.

The increase of retention rate is dependent on permeability which increased due to change in cell structure because of high pressure generated by steam within the wood. Under high internal steam pressure, the pit membranes in cell walls, tyloses in vessels, and the weak ray cells rupture to form pathways for easy transportation of liquids and vapours (Vinden et al. 2011). After the treatment of microwave in wood, micro-checks were formed at the intercellular layer of ray cells, and the longitudinal tracheid and pit membranes were damaged (He et al. 2014). The amount of retention rate decreased because of more damage occurred in the cell of wood as a result of a certain period in the liquid nitrogen treatment.

Mechanical properties of Uludag fir wood is given in Tab. 4. The results indicated that the bending strength of samples treated by liquid nitrogen before impregnation process decreased significantly compared to of the corresponding ones in control samples. The minimum bending strength value was 50.23 Nmm⁻² in the samples impregnated with Borax in short-time immersion method and in samples not exposed to liquid nitrogen before impregnation while the maximum bending strength value was 78.41 Nmm⁻² for samples impregnated with Tanalith-E in applied by the brush method and exposed to liquid nitrogen for 90 min before impregnation method. The highest modulus of elasticity in bending value was at 9587.8 Nmm⁻² for samples impregnated with Borax in applied by the vacuum pressure method and held in nitrogen for 360 min whereas the lowest was 7305.9 Nmm⁻².

Tab. 4: Mechanical properties of Uludag fir wood ($N\text{mm}^{-2}$).

Exposure time in liquid nitrogen		Control			15 min			90 min			360 min		
Mechanical properties	Impregnated material / impregnated method	Tanalith-E	Borax	Imersol aqua									
Bending strength	Brush	74.72 (2.95)*	69.62 (5.29)*	53.95 (4.57)*	72.03 (5.55)*	63.66 (4.16)*	59.57 (5.93)*	78.41 (5.17)*	63.34 (5.88)*	77.94 (7.55)*	64.46 (3.93)*	77.73 (5.48)*	75.45 (5.64)*
	Short-term immersion	64.13 (5.85)*	50.23 (1.34)*	60.40 (4.95)*	68.44 (4.88)*	67.05 (4.06)*	70.99 (5.92)*	73.39 (5.76)*	67.89 (3.90)*	70.13 (6.07)*	67.91 (6.17)*	70.94 (5.50)*	64.84 (5.88)*
	Long-term immersion	64.37 (5.94)*	54.69 (4.66)*	65.81 (0.59)*	74.11 (5.75)*	68.48 (5.42)*	67.66 (6.34)*	65.77 (5.14)*	72.93 (2.81)*	73.27 (1.10)*	75.13 (6.24)*	72.88 (5.81)*	75.76 (6.79)*
	The pressure - vacuuming	72.86 (3.49)*	64.44 (6.87)*	72.12 (4.01)*	77.94 (4.41)*	73.01 (4.80)*	71.76 (1.09)*	73.23 (6.36)*	72.29 (5.17)*	58.33 (4.84)*	61.82 (4.51)*	73.29 (2.06)*	64.39 (6.41)*
Modulus of elasticity in bending ($N\text{mm}^{-2}$)	Brush	7772.2 769.14*	7732.3 5.36*	7448.2 255.92*	7495.8 226.49*	8442.4 625.55*	7345.4 627.85*	9432.2 917.45*	7710.6 658,14*	9328.2 681.01*	8311.0 736.83*	9323.8 828.00*	9582.0 908.66*
	Short-term immersion	8007.3 797.22*	7492.6 159.38*	7305.9 89.34*	8435.4 182.34*	8147 644.58*	8504.8 772.36*	8998.8 627.27*	8134 473.41*	8545.2 705.00*	8364.8 804.44*	8455.4 768.46*	7561 670.93*
	Long-term immersion	8152.2 730.72*	7982 56.01*	8818.8 267.36*	8279.4 725.18*	8279.4 725.18*	8289.8 779.93*	8624.2 772.73*	8501.8 273.78*	9026.6 222.06*	8626.8 895.86*	8960.6 808.07*	8942.4 856.05*
	The pressure - vacuuming	8901.6 734,49*	7587.8 534.69*	8097.8 209.23*	9575.2 786.34*	9576.2 864.51*	9435 617.37*	8909.8 722.29*	9852.8 824.69*	7888.8 641.51*	7875.4 844.10*	9587.8 272.67*	7798.4 706,23*
Compression strength parallel to the fibers ($N\text{mm}^{-2}$)	Brush	46.43 (3.28)*	49.18 (3.22)*	49.55 (4.57)*	52.94 (5.37)*	47.21 (6,361)*	47.49 (3.18)*	53.72 (3.06)*	47.50 (3.66)*	53.19 (3.30)*	50.54 (4.79)*	51.28 (4.81)*	50.99 (4.33)*
	Short-term immersion	51.76 (5.35)*	46.03 (1.56)*	48.91 (3.70)*	50.91 (1.61)*	53.32 (4.05)*	52.16 (4.47)*	48.90 (2.93)*	50.77 (2.02)*	48.91 (4.45)*	50.85 (4.26)*	53.17 (5.20)*	50.09 (3.48)*
	Long-term immersion	51.324 (4.37)*	48.32 (1.66)*	49.73 (2.85)*	56.05 (4.21)*	49.24 (5.50)*	54.11 (4.10)*	56.01 (5.42)*	49.69 (4.65)*	48.04 (1.11)*	47.98 (2.11)*	51.91 (4.81)*	50.67 (3.21)*
	The pressure - vacuuming	44.27 (4.01)*	44.27 (3.01)*	51.94 (2.92)*	54.02 (5,29)*	58.25 (5.30)*	52.55 (5.03)*	53.37 (5.23)*	60.22 (2.88)*	51.22 (3.43)*	47.25 (3.57)*	52.90 (4.89)*	50.14 (1.82)*
Impact strength (kNcm^{-2})	Brush	1.4 (0.14)*	2.4 (0.15)*	2.08 (0.08)*	1.44 (0.05)*	1.6 (0.03)*	1.48 (0.02)*	1.40 (0.55)*	1.9 (0.16)*	1.26 (0.05)*	2.04 (0.12)*	1.62 (0.08)*	2.27 (0.03)*
	Short-term immersion	1.28 (0.08)*	1.86 (0.05)*	2 (0.10)*	1.7 (0.02)*	1.78 (0.02)*	1.54 (0.03)*	1.58 (0.02)*	1.76 (0.17)*	1.6 (0.13)*	1.94 (0.07)*	1.4 (0.09)*	1.22 (0.07)*
	Long-term immersion	2,26 (0.11)*	1,48 (0.08)*	2,28 (0.08)*	1,06 (0.01)*	1,96 (0.02)*	1,7 (0.02)*	1,82 (0.02)*	1,78 (0.03)*	1,56 (0.02)*	1,8 (0.06)*	2,02 (0.12)*	1,82 (0.10)*
	The pressure - vacuuming	1.3 (0.10)*	2.06 (0.05)*	0.96 (0.05)*	1.56 (0.05)*	1.64 (0.05)*	1.9 (0.03)*	1.96 (0.15)*	1.16 (0.08)*	1.7 (0.10)*	1.96 (0.05)*	1.72 (0.05)*	1.84 (0.11)*

Ors et al. (2006) reported that a decrease in the impregnation period increased the modulus of elasticity in bending. The highest compression strength parallel to the fibers value was 60.228 Nmm⁻² in the samples impregnated with borax applied by the vacuum pressure method and held in nitrogen for 90 min and the lowest value was 44.274 Nmm⁻² for control samples impregnated with borax applied by the vacuum pressure method. Akhtari et al. (2012) determined some mechanical properties, as bending strength (MOR), the modulus of elasticity in bending (MOE), compression strength parallel to grain of *Paulownia fortunei* wood impregnated with silver, copper and zinc oxide nanoparticles. They concluded that the impregnation treated samples of paulovnia wood with nanoparticles had no negative effect on MOR, MOE and compression strength parallel to grain. The highest impact strength value was 2.4 kNcm⁻² for samples impregnated with borax applied by the brush method and control samples.

The lowest impact strength was 1.3 kNcm⁻² for control samples impregnated with Tanalith-E applied by the vacuum pressure method. The effects of wood preservatives on mechanical properties are directly related to several keys such as preservative chemistry or chemical type, retention rate, post-treatment drying temperature and genus of material (Akhtari and Nicolas 2014).

Tab. 5: ANOVA results on mechanical properties in Uludag fir wood.

Mechanical properties	Variance resources	Sum of squares	Degrees of freedom	Mean square	F value	Significance (P ≤ 0.005)
Bending strength	A: Time of exposure	1752.5	3	584.1	8.2	0.000
	B: Impregnation method	231.4	3	77.1	1.0	0.356
	C: Impregnation material	1932.8	2	644.2	9.053	0.000
	Interaction A*B	1889.3	9	209.9	2.95	0.002
	Interaction A*C	1525.6	6	169.5	2.382	0.013
	Interaction B*C	1059.2	6	117.6	1.654	0.101
	Interaction A*B*C	6019.5	18	222.9	3.133	0.000
	Error	18218.9	256	71.16		
	Total	1594520.1	320			
Modulus of elasticity in bending	A: Time of exposure	3.29E+07	3	1.10E+07	9.155	0.000
	B: Impregnation method	1.47E+07	3	4913585.4	4.105	0.007
	C: Impregnation material	3.52E+07	2	1.17E+07	9.799	0.000
	Interaction A*B	6.13E+07	9	6808080.5	5.688	0.000
	Interaction A*C	3.08E+07	6	3423824.9	2.86	0.003
	Interaction B*C	3.49E+07	6	3874941.5	3.237	0.001
	Interaction A*B*C	7.48E+07	18	2768923.1	2.313	0.000
	Error	3.06E+08	256	1197009.9		
	Total	2.39E+10	320			
Compression strength parallel to the fibers	A: Time of exposure	445.8	3	148.6	6.37	0.000
	B: Impregnation method	293.5	3	97.8	4.194	0.006
	C: Impregnation material	169.1	2	56.3	2.416	0.067
	Interaction A*B	487.6	9	54.1	2.322	0.016
	Interaction A*C	272.7	6	30.3	1.299	0.238
	Interaction B*C	540.8	6	60.0	2.576	0.007
	Interaction A*B*C	784.8	18	29.0	1.246	0.193
	Error	5972.6	256	23.3		
	Total	852675.3	320			
Impact strength	A: Time of exposure	0.72	3	0.242	1.254	0.291

B: Impregnation method	2.1	3	0.7	3.621	0.014
C: Impregnation material	0.54	2	0.181	0.934	0.425
Interaction A*B	2.74	9	0.305	1.576	0.123
Interaction A*C	5.76	6	0.641	3.315	0.001
Interaction B*C	1.39	6	0.155	0.802	0.615
Interaction A*B*C	19.17	18	0.71	3.675	0.000
Error	49.47	256	0.193		
Total	1024.8	320			

According Tab. 5; the effect of time of exposure in liquid nitrogen on all mechanical properties were found significant except the impact strength). The influence of impregnation method did not significantly affect the mechanical properties. The effect of impregnation material in the bending strength and modulus of elasticity in bending were found to be significant while the compression strength parallel to the fibers and impact strength were found to be insignificant.

CONCLUSIONS

Especially, the effect of the increase in retention amounts on the mechanical properties of Uludag fir wood, which is one of the hardly impregnable species, was investigated by liquid nitrogen exposure at different times before impregnation. In the samples where liquid nitrogen was applied before impregnation, according to the control group samples; on average, the retention amount was increased by 150-200% in all impregnating agents used in the study. In the studies conducted by Kurt (2006), Winandy and Rowell (1984), it was determined that the impregnation with water-soluble salts reduced the mechanical properties of wood material by 5-15%. In this study, it can be concluded that the application of liquid nitrogen before impregnation ought not to be seen as a reason for the decrease in mechanical properties, but this decrease may have been caused by impregnating materials and methods. However, a significant decrease is observed in the mechanical properties of wood material with the microwave method which is one of the alternative retentions enhancing methods (Hansson 2007).

The mechanical properties, retention amount and air-dry density of treated wood were determined. Results indicated that the air-dry density increased with longer time of exposure with the application of liquid nitrogen before impregnation of wood treated with Tanalith-E and borax while the impregnation with Imersol aqua decreased. Retention rate amount increased with increasing of the time of exposure at the liquid nitrogen treatment before impregnation process in wood, then decreased. The time of exposure at the liquid nitrogen applied before impregnation of wood influenced the mechanical properties such as bending strength, modulus of elasticity, compression strength from different directions. The bending strength of the samples held in liquid nitrogen decreased. The modulus of elasticity in bending strength values showed significant differences depending on the impregnation method and type of impregnation material. The compression strength parallel to the fibers increased with increases the time of exposure at the liquid nitrogen applied before impregnation of Uludag fir wood. Compared to control samples, impact strength of the samples held in liquid nitrogen is increased early and then decreased.

ACKNOWLEDGMENTS

I thank the staff of the Kastamonu Forest Faculty Laboratory of Kastamonu University for providing the materials.

REFERENCES

1. Akhtari, M., Kokandeh, M.G., Taghiyari, H.R., 2012: Mechanical properties of *Paulownia fortune* wood impregnated with silver, copper and zinc oxide nanoparticles. *Journal of Tropical Forest Science* 24(4): 507–511.
2. Akhtari, M., Nicolas, D., 2014: Effect of profiling and preservative treatments on the weathering characteristics of Southern pine deck boards. *European Journal of Wood and Wood Products* 72(6) : 829-831.
3. ASTM-D 1413-76, 1976: Standard test method of testing wood preservatives by laboratory soil blocks cultures.
4. Gecer, M., Baysal, E., Toker, H., Turkoglu, T., Vargun, E., Yuksel, M., 2015: The effect of boron compounds impregnation on physical and mechanical properties of wood polymer composites. *Wood Research* 60(5): 723-737.
5. Hansson, L., 2007: Microwave treatment of wood. Doctoral thesis. Luleå University of Technology, Sweden, 137 pp.
6. He, S., Lin, L., Fu, F., Zhou, Y., Fan, M., 2014: Microwave treatment for enhancing the liquid permeability of Chinese fir. *BioResources* 2: 1924-1938.
7. Hill, C.A.S., 2006: Wood modification: Chemical, thermal and other processes. John Wiley & Sons, Chichester, England, 470 pp.
8. Jensen, P., Jørgensen, G., Schnell, U., 2002: Dynamic LV-SEM analyses of freeze drying processes for waterlogged wood. In: Proc. 8th ICOM Group on Wet Organic Archaeological Materials Conf. Stockholm 2001. Eds. P. Hoffmann, J.A. Spriggs, T. Grant, C. Cook, A. Recht. Bremerhaven, ICOM: 319-331.
9. Jensen, P., Schnell, U., 2005: The implications of using low molecular weight PEG for impregnation of waterlogged archaeological wood prior to freeze drying. In: Proceedings 9th ICOM Group on Wet Organic Archaeological Materials Conf. Copenhagen 2004. Eds. P. Hoffmann, K. Strætkvern, J.A. Spriggs, D. Gregory. Bremerhaven, ICOM: 279-308.
10. Jensen, P., Jensen, J.B., 2006: Dynamic model for vacuum freeze-drying of waterlogged archaeological wooden artifacts. *Journal of Cultural Heritage* 7: 156-165.
11. Kurt, Ş., Özcan, S., Yapici, F., Likos, E., 2012: Dimensional stability of Uludag fir wood treated with liquid nitrogen after the steam test. *Journal of Forestry Faculty of Kastamonu University* 12(31).
12. Kurt, Ş., 2006: Change of some technological characteristics of impregnated laminated veneer lumbers (LVL). In Sea Water. PhD Thesis, Bülent Ecevit University institute of science. Pp 47-50.
13. Lundgren, C., 2004: Microfibril angle and density patterns of fertilized and irrigated Norway spruce. *Silva Fennica* 38(1): 107-117.

14. Ors, Y., Atar, M., Keskin, H., Güçlü Yavuzcan, H., 2006: Impacts of impregnation with Imersol-aqua on the modulus of elasticity in bending. *Journal of Applied Polymer Science* 99(6): 3210-3217.
15. Poonia, P.K., Hom, S.K. Sihag, K., Tripathi, S., 2016: Effect of microwave treatment on longitudinal air permeability and preservative uptake characteristics of Chir pine wood. *Maderas Ciencia y Tecnología* 18(1): 125 - 132.
16. Rowell, E.R.M., 2005: *Handbook of wood chemistry and wood Composites*. CRC Press, Boca Raton, Florida. Pp 34-70.
17. Simsek, H., Baysal, E., Peker, H., 2010: Some mechanical properties and decay resistance of wood impregnated with environmentally friendly borates. *Construction and Building Materials* 24(11): 2279-2284.
18. TS 2472, 2005: Wood-determination of density for physical and mechanical tests.
19. TS 344, 1981: Basic rules for wood preservation.
20. TS 345, 1974: Testing methods for the effects of wood impregnating substances.
21. TS 2474, 1976: Determination of static bending strength of wood.
22. TS 2477, 1976: Wood-determination of impact bending strength.
23. TS EN 310, 1999: Wood- based panels. Determination of modulus of elasticity in bending and of bending strength.
24. TS 2595, 1976: Wood-determination of ultimate stress in compression parallel to grain.
25. Villasante Plágaro, A.M., Laina, R., Rojas, J.M., Rojas, I.M., Vignote, S., 2013: Mechanical properties of wood from *Pinus sylvestris* L. treated with light organic solvent preservative and with waterborne copper azole. *Forest Systems* 22(3): 416-422.
26. Vinden, P., Torgovnikov, G., Hann, J., 2011: Microwave modification of *Radiata pine* railway sleepers for preservative treatment. *European Journal of Wood and Wood Products* 69: 271-279.
27. Xu, K., Wang, Y., Lv, J., Li, X., Wu, Y., 2015: The effect of microwave pretreatment on the impregnation of poplar wood. *BioResources* 10(1): 282-289.
28. Winandy, J.E., Rowell, R.M., 1984: The chemistry of wood strength. Pp 211-255, *The Chemistry of solid wood*. Chapter 5, Madison.

SEREF KURT*
KASTAMONU UNIVERSITY
FOREST FACULTY
DEPARTMENT OF FOREST INDUSTRY ENGINEERING
37050, TURKEY

*Corresponding author: skurt@kastamonu.edu.tr

**PHYSICAL AND MECHANICAL CHARACTERIZATION OF STRUCTURAL WOOD
USED IN PAKISTAN**

KHAWAJA ADEEL TARIQ
THE UNIVERSITY OF FAISALABAD
PAKISTAN

MUHAMMAD HAROON
BUILDING STANDARDS LIMITED LAHORE
PAKISTAN

ABDULLAH HABIB MUGHAL,
UNIVERSITY OF MISSOURI-KANSAS CITY
UNITED STATES OF AMERICA

SHER ALI
RAJPUT BROTHERS GUJRANWALA
PAKISTAN

(RECEIVED APRIL 2021)

ABSTRACT

Six species of wood (*Vachellia nilotica*, *Eucalyptus camaldulensis*, *Ziziphus mauritiana*, *Albizia lebbeck*, *Melia azedarach*, *Dalbergia sissoo*) were tested in compression and tension parallel to the grain. The specimens were collected from different areas of Pakistan. The compressive strengths, tension parallel to grain and hardness of the wood were determined by testing rectangular shape wooden specimens (ASTM D143 2014, Janka 1906). It was observed that compressive and tensile strength of *Vachellia nilotica* parallel to the grain is higher than other species whereas, *Eucalyptus camaldulensis* hardness behaviour along radial and tangential surface is higher among the wooden samples tested.

KEYWORDS: Wood, compressive strength, tensile strength, hardness, *Vachellia nilotica*, *Eucalyptus camaldulensis*, *Ziziphus mauritiana*, *Albizia lebbeck*, *Melia azedarach*, *Dalbergia sissoo*.

INTRODUCTION

The use of natural wood for structural purpose is increasing worldwide with the passage of time. However, the mechanical properties of structural wood have not been investigated in detail in Pakistan and worldwide. Hence in order to fully utilize the potential of wood, particularly in multi-dimensional structures, every country must have knowledge of the mechanical and physical behavior of the wooden species. The wood products used worldwide comes from both developing (about 60%) and developed countries (about 40%). The uses of wood products are extensive. Wood products ranges from wooden plank floor system, load bearing beams etc (Guo et al. 2017). Laminated woods are also being frequently used worldwide (Yue et al. 2019). The cross laminated products of different species have been investigated by the researchers (He et al. 2020, Ukyo et al. 2021). Layered wood products are more strong in compression and bending as compared with single layered (Akbulut and Ayrilmis 2019, Florisson et al. 2021). Researchers have studied the behaviour of wood panels against cyclic loading. The tests results are promising (Kulman et al. 2019). The use of wood dust is also found beneficial for improving the compressive properties of brick (Arulmani et al. 2017). Woodwork waste has been used for the purpose of thermal treatment (Kajda-Szcześniak and Jaworski 2018). Proper thermal treatment can improve certain properties of the wood (Pulngern et al. 2020). The waste generated from cutting of the wood can be used as a raw material for production of fibreboards (Ihnát et al. 2017). Design manuals are available in developed countries for solid seasoned timber (Han et al. 2019). There must be a balance between plantation of new trees and wood utilization (Puettmann and Wilson 2005, Winjum et al. 1998).

The properties of same species vary with the environmental conditions like temperature, humidity, water and soil. Researchers have observed variation up to 20% in elastic modulus (Moshtaghin et al. 2016). Researchers (Osuji and Nwankwo 2017) have examined physical and mechanical properties of wood like Albizia, Dahoma or Ekhimi, Ekki and Opepe; and have found variation in same species. Strength class system was also developed by researcher for non destructive testing using mechanical properties test results of wood (Zziwa 2012). Tensile and bending characteristics of the wood have been investigated by the researchers using four point bending test on wooden beam (Yusof 2019). Heat treatment also affects the properties of wood. It was observed that *Eucalyptus camaldulensis* compressive strength and surface roughness changes with the heat treatment (Unsal and Ayrilmis 2005). The fibers of the wood are also used for enhancing the tensile properties of material by their use with epoxy composites (Vinod et al. 2020). The use of fibers of wood are also found beneficial in automobile industry. Fibers of *Albizia lebbek* bark can be used as green composites in automobile industries (Manimaran et al. 2019). The variation in some wooden species was observed when they are tested for ultrasonic wave velocity. It was observed that variation of ultrasonic pulse velocity along height of *Melia azedarach* was very small (Duong et al. 2019). Researchers have developed correlation between different species of wood using properties like bending, tensile and modulus of elasticity and rupture (Sun et al. 2019, Sunny et al. 2020).

Pakistan being an under-developed country does not possess the knowledge about mechanical and physical properties of woods. Due to lack of knowledge, the wood being used in

construction based on rough estimation of mechanical properties. In Pakistan, whenever timber structural member is required, either imported glulam or locally available solid seasoned timber found in timber market is used. The guidelines are also not available for appropriate selection of wood structural members, as wood mechanical properties vary from species to species and territory to territory. Locally available timber structural members are abundantly used for retrofitting of old timber buildings, but economy is compromised because of unavailability of any guidelines for timber obtained from local markets. This study herein presents a comprehensive approach for mechanical characterization of natural structural wood commonly available in Pakistan.

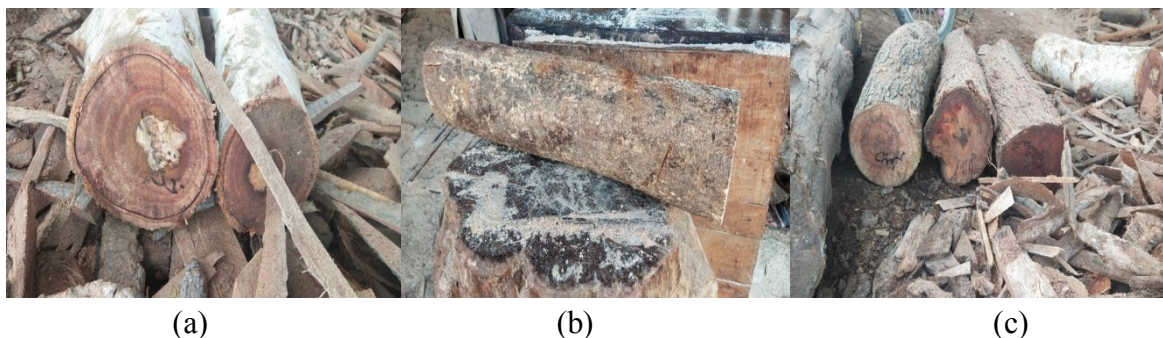
MATERIAL AND METHODS

Sample collection

Random sampling method is used for selection of test specimens. Random sampling provides better estimates of mechanical properties. According to random sampling method, any species of wood can be taken from any region or place. In total, six species of wood were collected from different cities in order to check possibility of difference in the mechanical and physical properties of same species. Seasonal temperature and drought condition can also affect the properties of wood (Hacura et al. 2015). The details of the wood samples collected are mentioned in Tab. 1 and shown in Fig. 1.

Tab. 1: Details of wood species collected.

Scientific name of the specie	Local name (Pakistan)	Cities (Pakistan)	Density (g·cm ⁻³)
<i>Vachellia nilotica</i>	Kikar	Dera Ismail Khan	0.65
		Khushab	0.60
<i>Eucalyptus camaldulensis</i>	Safeda	Sheikupura	0.71
		Khushab	0.70
<i>Ziziphus mauritiana</i>	Bair	Khushab	0.64
		Jhelum	0.59
<i>Albizia lebbek</i>	Shreen	Sarai Alamgeer	0.50
		Gujranwala	0.73
<i>Melia azedarach</i>	Dharaik	Sarai Alamgeer	0.58
		Gujranwala	0.78
<i>Dalbergia sissoo</i>	Tali	Gujranwala	0.69
		Zafarwal	0.75



(a)

(b)

(c)



Fig. 1: Logs of (a) *Eucalyptus camaldulensis* (Safeda), (b) *Albizia lebbbeck* (Shreen), (c) *Ziziphus mauritiana* (Bair), (d) *Vachellia nilotica* (Kikar), (e) *Melia azedarach* (Dharaik), (f) *Dalbergia sissoo* (Tali).

Samples preparation

The logs of wood were cut according to different testing requirements (ASTM D143 2014, Janka 1906). The size of the specimens tested is illustrated in Tab. 2. The logs were cut into straight planks and then these planks were cut down further in the samples of required dimensions. The cutting of logs was done in such a way that the possibility of the sample having a knot is minimum.

Tab. 2: Details of samples.

Mechanical properties	Dimensions (mm)	Number of samples
Compression parallel to grain	50 x 50 x 250	36
Tension parallel to grain	25 x 25 x 450	36
Hardness	50 x 50 x 150	36

Seasoning

Wood drying or wood seasoning diminishes the moisture content of wood before its use. When wood is utilized as a construction material, it is essential to dry it properly as moisture variation can cause shrinkage in wood. The wood samples collected were wet because of the rainfall of winter season. The cut samples were placed under natural sunlight for drying for about 4 weeks. The thermal treatment can affect the behaviour of structural wood (He et al. 2020, Xie et al. 2020). The moisture content variation can also affects the density of wood (Yanming et al. 2018). The moisture content of the tested sample varies from 13 to 18%.

RESULTS AND DISCUSSIONS

Compression and tension test

The displacement controlled uniaxial compression test was performed using Universal testing machine under controlled loading rate of 2 mmmin^{-1} . Tension test was also performed on universal testing machine.

Eucalyptus camaldulensis (Safeda)

Samples from cities of Sheikupura and Khushab were tested for compression and tension. The samples failed in crushing and shear during compression test (Fig. 2). The compressive strength of wooden sample from city of Sheikupura and Khushab was 45 MPa and 33 MPa resp. The compression test performed by the researches on *Eucalyptus camaldulensis* in Thailand had compressive strength from 39 to 48 MPa (Nezu et al. 2020). The tensile strength of wooden sample from city of Sheikupura and Khushab was 17.38 MPa and 14.03 MPa, resp.



Fig. 2: Failure pattern under compression and tension for *Eucalyptus camaldulensis* (Safeda) from city of (a) Sheikupura, (b) Khushab.

Ziziphus mauritiana (Bair)

Samples from cities of Khushab and Jhelum were tested for compression and tension. The samples failed in crushing during compression test (Fig. 3). The compressive strength of wooden sample from city of Khushab and Jhelum was 29 MPa and 40 MPa, resp. The compression test performed by other researches on *Ziziphus mauritiana* had maximum compressive strength of 26 MPa (Damme 2006). The tensile strength of wooden sample from city of Khushab and Jhelum was 18.21 MPa and 12.38 MPa, resp.



Fig. 3: Failure pattern under compression and tension for *Ziziphus mauritiana* (Bair) from city of (a) Khushab, (b) Jhelum.

Albizia lebbeck (shreen)

Samples from city of Sari Aalamgeer and Gujranwala were tested for compression and tension. The samples failed in crushing during compression test (Fig. 4). The compressive

strength of wooden sample from city of Sari Aalamgir and Gujranwala was 28.6 MPa and 29.5 MPa resp. The compression test performed by other researches on *Albizia lebbeck* had maximum compressive strength of 33.5 MPa (Tang et al. 2016). The tensile strength of wooden sample from city of Sari Aalamgeer and Gujranwala was 19.56 MPa and 9.6 MPa, resp.

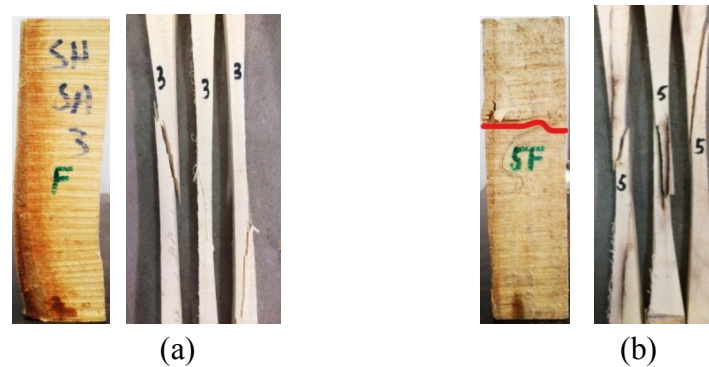


Fig. 4: Failure pattern under compression and tension for *Albizia lebbeck* (Shreen) from city of (a) Sari Alamgir, (b) Gujranwala.

Melia azedarach (Dhariak)

Samples from city of Sari Aalamgeer and Gujranwala were tested for compression. The samples failed in shear and crushing during compression test (Fig. 5). The compressive strength of wooden sample from city of Sari Aalamgeer and Gujranwala was 32 MPa and 24 MPa resp. The compression test performed by other researches on *Melia azedarach* had maximum compressive strength of 27.2 MPa (Tang et al. 2016). The tensile strength of wooden sample from city of Sari Aalamgir and Gujranwala was 20.62 MPa and 7.18 MPa resp.



Fig. 5: Failure pattern under compression for *Melia Azedarach* (Dhariak) from city of (a) Sari Aalamgeer, (b) Gujranwala.

Vachllia nilotica (Kikar)

Samples from city of Dera Ismail Khan and Khushab were tested for compression and tension. The samples failed in shear during compression test (Fig. 6). The compressive strength was 42 MPa and 44 MPa for city of Dera Ismail Khan and Khushab resp. The compression test performed by other researches on *Nilotica* had compressive strength about 32 MPa (Mahmood

et al. 2016). The tensile strength was 34.33 MPa and 32.54 MPa for city of Dera Ismail Khan and Khushab resp.



Fig. 6: Failure pattern under compression for *Vachllia nilotica* (Kikar) from city of (a) Dera Ismail Khan, (b) Khushab.

Dalbergia sissoo (Tali)

Samples from city of Gujranwala and Zafarwal were tested for compression and tension. The samples failed in shear during compression (Fig. 7). The compressive strength was 34 MPa and 36 MPa for city of Gujranwala and Zafarwal resp. The compression test performed by other researches on *Dalbergia sissoo* had compressive strength about 56 MPa (Mahmood et al. 2016). The tensile strength was 12.48 MPa and 21.65 MPa for city of Gujranwala and Zafarwal, resp.



Fig. 7: Failure pattern under compression for *Dalbergia sissoo* (Tali) from city of (a) Gujranwala, (b) Zafarwal.

The load displacement comparison of all species in compression and tension test is shown in Figs. 8 and 9.

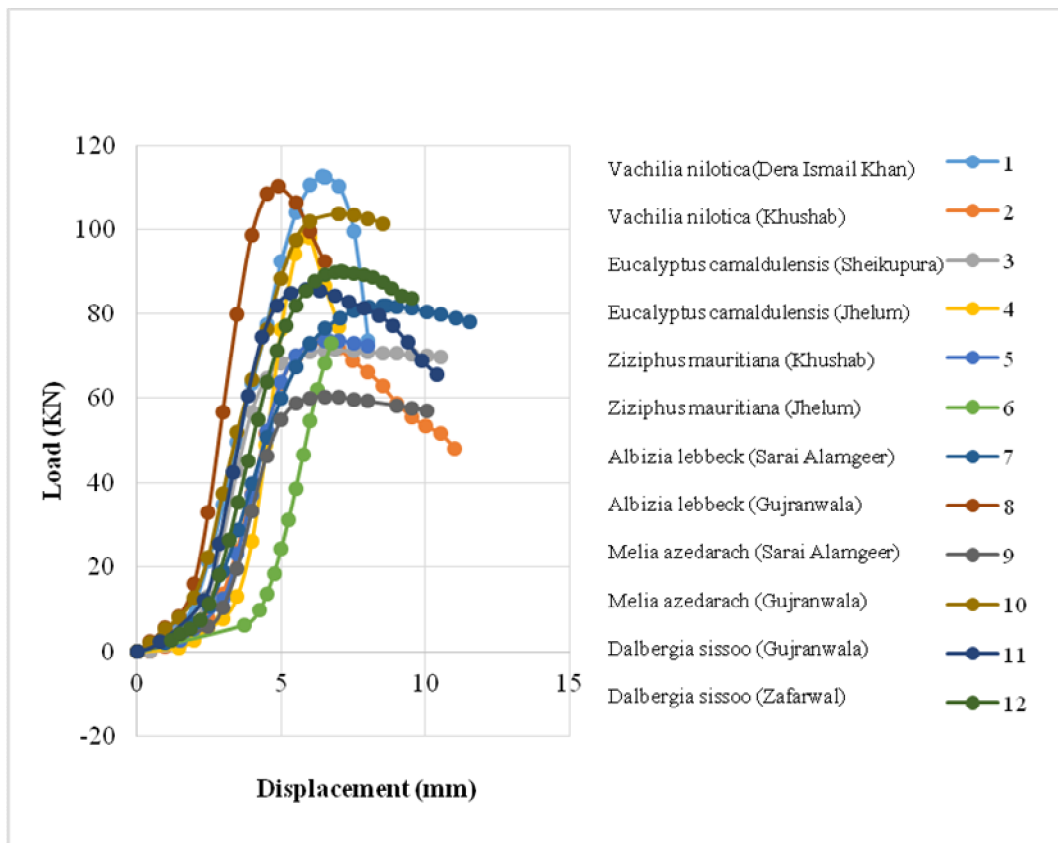


Fig. 8: Comparison of compressive strength of tested wooden samples.

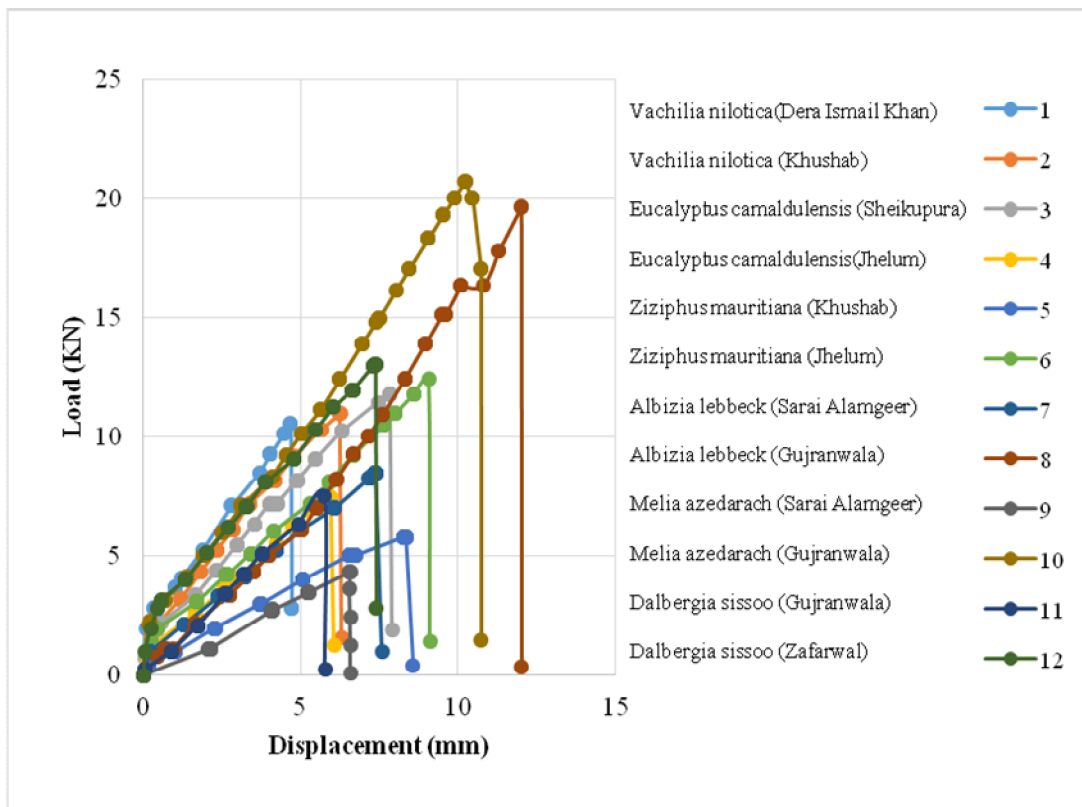


Fig. 9: Comparison of tensile strength of tested wooden samples.

Hardness test

The hardness of wood samples were measured using Gabriel Janka test (Janka 1906). It is a measure of a force which is required for penetration of 11.28 mm steel ball halfway into the tested specimen. Hardness test was also performed on Universal testing machine. The wooden samples were tested along end, tangential and radial surface. The test assembly for UTM and tested specimen is shown in Fig. 10. The results of tested wooden samples are summarized in Tab. 2 and shown in Fig. 11.



Fig. 10: Tested specimens for hardness.

Tab. 2: Details of wood species tested for hardness.

Scientific name of the specie	Cities (Pakistan)	Hardness		
		End surface (kN)	Radial surface (kN)	Tangential surface (kN)
<i>Vachellia nilotica</i>	Dera Ismail Khan	8.90	9.72	7.80
	Khushab	9.24	7.00	10.38
<i>Eucalyptus camaldulensis</i>	Sheikupura	10.44	10.34	11.14
	Khushab	6.44	7.30	5.70
<i>Ziziphus mauritiana</i>	Khushab	7.64	5.58	5.78
	Jhelum	5.56	5.14	4.68
<i>Albizia lebbek</i>	Sarai Alamgeer	8.10	4.24	4.14
	Gujranwala	5.74	5.72	5.72
<i>Melia azedarach</i>	Sarai Alamgeer	6.90	5.00	5.08
	Gujranwala	5.32	5.26	5.46
<i>Dalbergia sissoo</i>	Gujranwala	7.88	6.98	6.70
	Zafarwal	6.28	6.34	5.58

Tiny cracks and bulging pattern was observed when specimens were tested for hardness. When load is applied through a circular ball the grains tend to move inside the timber creating a hole in the surface. When there is moisture in the wood the grains tend to move upward because load is being applied downwards towards the body of wood causing the grains to bulge around the application of load. But, when the moisture content in the wood is less the grains do not move upwards rather they move apart causing tiny cracks around the application of load. Tiny cracks are more often formed rather than bulging failure. The hardness test results obtained are in good agreement with the past published result (Mahmood et al. 2016).

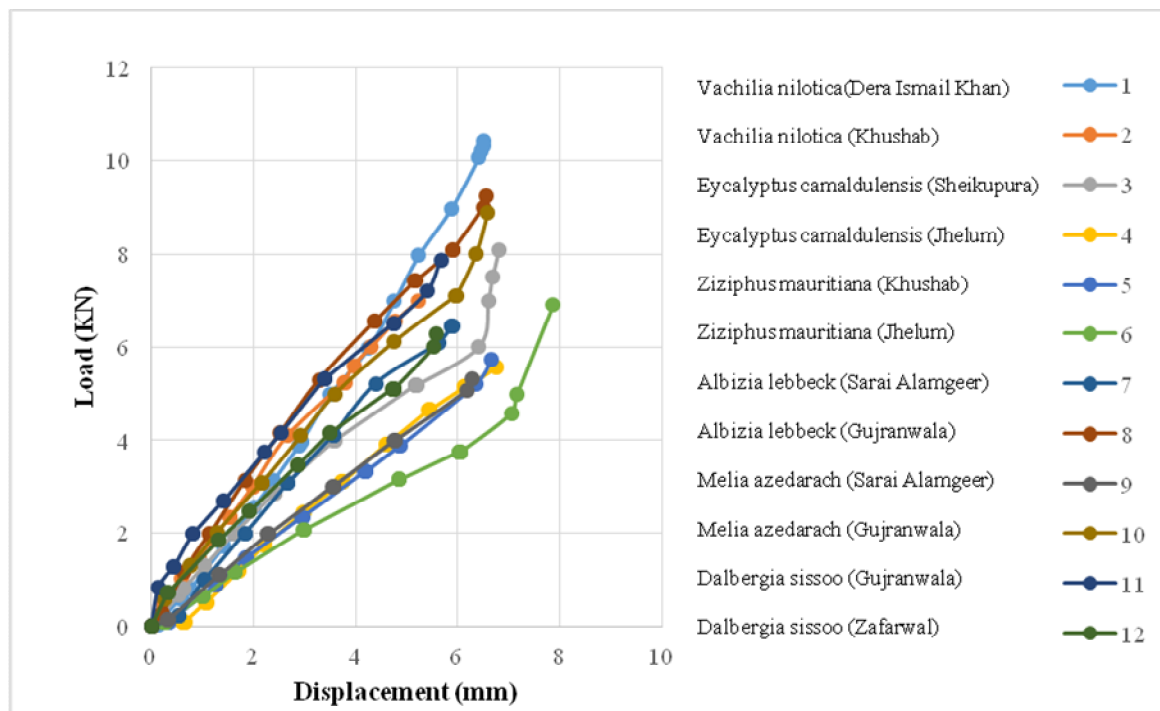


Fig. 11: Comparison of hardness of tested wooden samples.

CONCLUSION

Based on the compression, tension and hardness test on 6 different species of the wood, following conclusion can be drawn for compression parallel to grain: (1) The results show that *Vachellia nilotica* (of city Khushab) having compressive strength of 41.16 MPa is highest among the wooden species tested. (2) *Melia azedarach* (of city Gujranwala) having compressive strength of 21.91 MPa is lowest among the wooden species tested. (3) The most common failure patterns in tested specimens were crushing and shearing. None of them have failure patterns of splitting and end rolling.

For tension parallel to grain: (1) The maximum tensile capacity was 33.59 MPa for *Vachllia nilotica* (of city Dera Ismail Khan). (2) The minimum tensile capacity was 9.95 MPa for *Ziziphus mauritiana* (of city Jhelum). (3) The most common failure pattern in this tested specimens were shearing and splitting.

And for hardness test as well: (1) The maximum hardness was 10.03 kN for *Vachllia nilotica* (of city of Dera Ismail Khan) and the minimum value was 5.25 kN for *Melia azedarach* (of city of Gujranwala). (2) The maximum hardness value at radial and tangential surface was 10.03 kN for *Eucalyptus camaldulensis* (of city of Sheikupura) and the minimum value at tangential and radial surface was 4.5 kN for *Melia azedarach* (of city of Sarai Alamgeer).

During the load application, the failure patterns were either tiny cracks around the circle or bulging occurs around the point of load application was observed.

REFERENCES

1. Akbulut, A., Ayrilmis, N., 2019: Some advantages of three-layer medium-density fibreboard as compared to the traditional single-layer one. *Journal of Wood Science* 65(46): 1-7.
2. Arulmani, A., Sundarraaj, M., Kalaivani, P., 2017: Experimental investigation of green brick using vechellia tree dust. *International Journal for Research in Applied Science and Engineering Technology* 5: 36-39.
3. ASTM D143, 2014: Standard test methods for small clear specimens of timber.
4. Damme, P. V., 2008: Food and nutrition: the role of under-utilised crops in traditional crop improvement and new crop development. Pp 23-35, *International Symposium on New Crops and Uses: Their role in a rapidly changing world*. University of Southampton.
5. Duong, D.V., Hasegawa, M., Matsumura, J., 2018: The relations of fiber length, wood density, and compressive strength to ultrasonic wave velocity within stem of *Melia azedarach*. *Journal of Indian Academy of Wood Science* 16: 1-8.
6. Florisson, S., Muszynski, J, Vessby., 2021: Analysis of hygro-mechanical behaviour of wood in bending. *Wood and Fiber Science* 53(1): 27-47.
7. Guo, X., Wang, H., Chen, Q., Na, B., 2017: The dimensional stability of engineered wood flooring in heating systems. *Wood Research* 62(1): 103-112.
8. Hacura, J., Gryc, V., Vavrčik, H., Hozová, J., Urban, J., 2015: The effect of drought on cell wall thickness and radial dimension of tracheids of *Picea Abies* (L.) karst. *Wood Research* 60(2): 175-188.
9. Han, L., Zhao, X., Zhou, H., Luo, X., 2019: Reliability analysis on compression strength property of Chinese larch visually-graded dimension lumber. *Wood Research* 64(3): 471-482.
10. He, K., Chen, Y., Sun, J., 2020: Axial mechanical properties of small-diameter round timber short columns after exposure to elevated temperatures. *Wood Research* 65(6): 925-936.
11. He, M., Sun, S., Li, Z., Feng, W., 2020: Bending, shear, and compressive properties of three- and five-layer cross-laminated timber fabricated with black spruce. *Journal of Wood Science* 66(38): 1-17.
12. Ihnát, V., Lübke, H., Russ, A., Borůvka, V., 2017: Waste agglomerated wood materials as a secondary raw material for chipboards and fibreboards Part I. Preparation and characterization of wood chips in terms of their reuse. *Wood Research* 62(1): 45-56.
13. Janka, G., 1906: Die Härte des Holzes. *Zentralblatt für das gesamte Forstwesen*, Wien 32(5): 193–202.
14. Janka, G., 1906: Die Härte des Holzes. *Zentralblatt für das gesamte Forstwesen*, Wien 32(6): 241–260.
15. Kajda-Szcześniak, M., Jaworski, T.J., 2018: Characteristics of the combustion process of woodwork waste in the installation of thermal treatment of municipal solid waste (TPOK). *Wood Research* 63(1): 15-24.
16. Kulman, S., Boiko, L., Gurová, D., Sedliačik, J., 2019: Prediction the fatigue life of wood-based panels. *Wood Research* 64(3): 373-388.

17. Mahmood, K., Awan, A. R., Chughtai, M.I., 2016: Anatomical, physical and mechanical properties of salt tolerant tree species grown in Punjab, Pakistan. *Pakistan Journal of Botany* 48(5): 1813-1818.
18. Manimaran, P., Kumar, K.S.S., Prithiviraj, M., 2019: Investigation of physico chemical, mechanical and thermal properties of the *Albizia lebbbeck* bark fibers. *Journal of Natural Fibers*: 1-12.
19. Moshtaghin, A.F., Franke, S., Keller, T., Vassilopoulos, A.P., 2016: Experimental characterization of longitudinal mechanical properties of clear timber: Random spatial variability and size effects. *Construction and Building Materials* 120: 432–441.
20. Nezu, I., Ishiguri, F., Aiso, H., Diloksumpun, S., Ohshima, J., Iizuka, K., Yokota, S., 2020: Repeatability of growth characteristics and wood properties for solid wood production from *Eucalyptus camaldulensis* half-sib families growing in Thailand. *Silvae Genetica* 69: 36-43.
21. Osuji, S.O., Nwankwo, E., 2017: Investigation into the physical and mechanical properties of structural wood commonly used in Nigeria: A case study of Benin City. *Journal of Civil Engineering Research* 7(5): 131–136.
22. Puettmann, M.E., Wilson, J.B., 2005: Life-cycle analysis of wood products: cradle-to-gate LCI of residential wood building materials. *Wood and Fibre Science. Special issue*: 18-29.
23. Pulngern, T., Udtaranakron, T., Chanto, K., 2020: Physical and mechanical behaviors of thermally modified rubberwood glulam beam under sustained and cyclic loading. *Wood and Fibre Science* 52(3): 298-312.
24. Sun, Y., Jiang, Z., Liu, H., Sun, Z., Fang, C., 2019: The bending properties of bamboo strand board I-beams. *Journal of Wood Science* 65(50): 1-10.
25. Sunny, P.P., Dutt, B., Sumthane, Y.Y., Dhiman, B., Panwar, H., 2020: Correlation and regression analysis of wood properties of *Dalbergia sissoo* Roxb. ex DC. procured from local markets of Himachal Pradesh, India. *Journal of Pharmacognosy and Phytochemistry* 9(4): 3414-3417.
26. Tang, A., Chu, P., Leung, M., Chu, L., Liao, W., 2016: Evaluating wood strength properties of subtropical urban trees using fractometer II. *Journal of Tropical Forest Science* 28(3): 249-259.
27. Unsal, O., Ayrimis, N., 2005: Variations in compression strength and surface roughness of heat-treated Turkish river red gum (*Eucalyptus camaldulensis*) wood. *Journal of Wood Science* 51: 405-409.
28. Ukyo, S., Miyatake, A., Shindo, K., Hiramastu, Y., 2021: Shear strength properties of hybrid (Hinoki cypress and Japanese cedar) cross-laminated timber. *Journal of Wood Science* 67(23): 1-18.
29. Vinod, A., Vijay, R., Singaravelu, D.L., Khan, A., Sanjay, M., Siengchin, S., Verport, F., Alamry, K.A., Asiri, A.M., 2020: Effect of alkali treatment on performance characterization of *Ziziphus mauritiana* fiber and its epoxy composites. *Journal of Industrial Textiles*: 1-23.
30. Winjum, J. K., Brown, S., Schlamadinger, B., 1998: Forest harvests and wood products: Sources and sinks of atmospheric carbon dioxide. *Forest Science* 44(2): 272–284.
31. Xie, J., Chen, L., Shao, H., He, L., Jiang, Y., Lu, D., Xiao, H, Chen, Y., Huang, X., Hao, J., Tu, L., Lin, T., Xiao, Y., Chen, G., Qi, J., 2020: Changes in physical-mechanical properties

- and chemical compositions of *Toona sinensis* wood before and after thermal treatment. Wood Research 65(6): 877-884.
32. Yanming, W., Zhongjia, C., Xiangyue, Y., Guosheng, Y., 2018: Influence of die temperature and moisture content on the densification of bamboo powder using die heating method. Wood Research 63(4): 655-668.
33. Yue, K., Wang, L., Xia, J, Zhang, Y., Chen, Z., Liu, W., 2019: Experimental research on mechanical properties of laminated poplar wood veneer/plastic sheet composites. Wood and Fiber Science 51(3): 321-331.
34. Yusof, M.N., Tahir, M.P., Lee, S.H., Khan, M.A., James, R.M.Z., 2019: Mechanical and physical properties of cross-laminated timber made from *Acacia mangium* wood as function of adhesive types. Journal of Wood Science 65(1): 1-11.
35. Zziwa, A., 2012: Strength characterisation of timbers for building construction in Uganda. Second International Conference on Advances in Engineering and Technology. Pp 450–456.

KHAWAJA ADEEL TARIQ*
THE UNIVERSITY OF FAISALABAD
DEPARTMENT OF CIVIL ENGINEERING
FAISALABAD
PAKISTAN

*Corresponding author: khawajaadeel@hotmail.com

MUHAMMAD HAROON
BUILDING STANDARDS LIMITED
LAHORE
PAKISTAN

ABDULLAH HABIB MUGHAL
UNIVERSITY OF MISSOURI-KANSAS CITY
DEPARTMENT OF CIVIL AND MECHANICAL ENGINEERING
UNITED STATES OF AMERICA

SHER ALI
RAJPUT BROTHERS
GUJRANWALA
PAKISTAN

RESEARCH ON WOOD DEFECTS CLASSIFICATION BASED ON DEEP LEARNING

JIAXIN LING, YONGHUA XIE
NORTHEAST FORESTRY UNIVERSITY
P. R. CHINA

(RECEIVED MAY 2021)

ABSTRACT

Whereas the traditional manual detection method of wood defects is problematic due time-consuming, low efficiency and low accuracy, an derived model based on ResNet-v2 was constructed. The new derived model can accurately point out the types of defects such as wormhole, live joint and dead joint on the surface of plate, improve the accuracy of classification, and greatly reduce the labor force. Compared with the traditional convolutional neural network, ResNet-v2 derived model has better recognition effect and stronger generalization ability. The experimental results show that the classification accuracy of ResNet-v2 derived network model based on different number of layers is more than 80%, and the classification accuracy of ResNet-v2 derived model can reach 97.27%.

KEYWORDS: Deep learning, plate defects, ResNet-v2 derivative model, classification recognition.

INTRODUCTION

Wood defects are easy to occur in the period of natural growth, storage after cutting and later wood processing of trees. Wood defects will affect use and service life of plate materials and wood products (Luo and Sun 2019, Fan et al. 2020, Liu et al. 2019). Wood defect detection is one of the important processes of wood processing. The automatic detection of wood defects is the premise of high-quality plate processing, and the recognition of plate defect image is the difficulty of this technology (Cheng et al. 2018, Zhou et al. 2020). There are many kinds of defects in wood, and the surface shape and color of each kind of wood are different, which makes the diagnosis of wood more difficult.

Regarding the problem of plate defect recognition, traditional algorithms were suggested by authors. Qi and Mou (2013) proposed a wood defect detection algorithm based on Hu moment invariants and BP neural network, and completed the wood defect image segmentation. Wang et

al. (2018) proposed a support vector machine method based on texture features and gray histogram to realize the detection and location of wood knot defects. Wu et al. (2010) proposed a wood defect recognition algorithm based on gray level co-occurrence matrix and clustering method. The above three algorithms can effectively recognize the surface defects of wood, but for large sample data, the recognition accuracy is not high.

In recent years, with the improvement of deep learning theory, the pattern recognition algorithms of speech and image have achieved some success. For example, Cheng (2021) proposed the semantic segmentation algorithm of wood defect image based on the platforms OpenCV and Tensorflow. Hu et al. 2019 proposed the wood defect and texture recognition algorithm based on self-learning DBN. Li et al. (2020) proposed the wood automatic defect location model based on MobileNet. Yan and Cheng 2020 proposed a semantic segmentation algorithm of wood defect image based on convolution neural network. Yan et al. (2020) combined deep learning feature extraction method with extreme learning machine (ELM) classification method to establish a deep extreme learning machine model for wood image defect detection. These novel deep learning algorithms have an accuracy rate of more than 80%. Aiming at wood defect classification, this paper attempts to use VGG (Visual Geometry Group) model, GoogLeNet model and ResNet model to detect the types of wood defects, and classify the types of wood defects.

MATERIAL AND METHODS

Sample data acquisition

In this paper, a small sample library was established by selecting the wood sheet materials with three kinds of defects such as wormhole, live joint and dead joint. Because there are only 2630 images in the original sample, it is not suitable for deep learning. So we use the method of data enhancement to deal with the 2630 images by rotation, translation, scale transformation, gray transformation and so on, so as to expand the sample library. After the expansion, there were 10687 images in the sample library, 7480 of which are selected as the training set, 2137 as the validation set, and 1070 as the test set at the ratio of 7:2:1. For illustration some samples of wood defects are shown in Fig. 1.

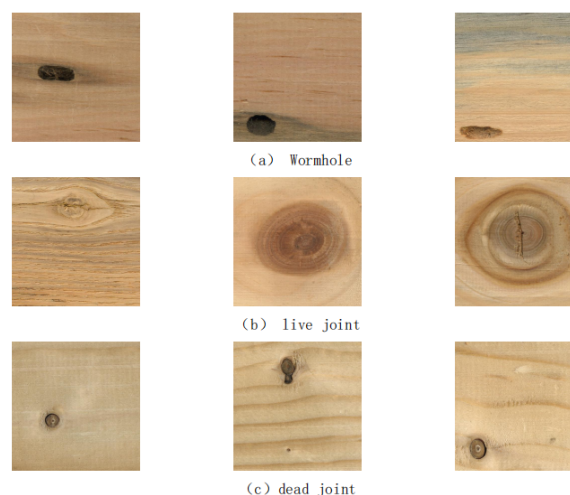


Fig. 1: Samples of wood defects in a sample library.

Visual geometry group model (VGG)

VGG model was proposed by Visual Geometry Group of Oxford University in 2014, so this model algorithm is named Visual Geometry Group, abbreviated as VGG model. It is derived from the AlexNet model. On the basis of the AlexNet model, the LRN layer is removed, and the convolution kernel of 7×7 is removed. The size of convolution kernel and pooled kernel is 3×3 , and the parameters are reduced to get the VGG network model. Among them, VGG-16 network is the network model with the best classification performance (Zhang et al. 2018, Bao et al. 2021). VGG-16 has 16 layers of network structure, which is composed of 13 layers of convolution layer and 3 layers of full connection layer. Firstly, the pixels of the plate defect sample image are converted into $224 \times 224 \times 3$ and input into the network. Firstly, after two layers of convolution layer, the convolution core size is $3 \times 3 \times 64$, and the maximum pooling processing is adopted; secondly, after two layers of convolution layer, the convolution core size is $3 \times 3 \times 128$, and the maximum pooling processing is adopted; thirdly, after three layers of convolution layer, the convolution core size is $3 \times 3 \times 512$, and the maximum pooling processing is adopted. Finally, the data are processed by softmax function for three times, and the classification of plate defect sample images is realized. The experimental results of VGG model are shown in Fig. 4.

GoogLeNet model

The GoogLeNet model was proposed by Christian Szegedy in 2014, which is a 22 layer neural network based on the perception network. A $224 \times 224 \times 3$ sheet defect image is input into GoogLeNet network (Xue et al. 2020, Huang et al. 2020, Peng and Wang 2019). First, it goes through the first layer of convolution layer, convolution core size is $7 \times 7 \times 64$, convolution is followed by ReLU operation, and then through the maximum pooling process of 3×3 , then, it goes through the second layer of convolution layer, convolution core size is $3 \times 3 \times 192$, convolution is followed by ReLU operation, and then through the maximum pooling process of 3×3 , finally, it goes through the third layer of intrusion 3A layer, which is divided into four branches, which are processed by convolution kernels of different scales. The convolution kernels of three convolution processing are resp. $1 \times 1 \times 64$, $1 \times 1 \times 96$, $1 \times 1 \times 16$ and $5 \times 5 \times 32$, and the other branch is 3×3 pooling layer, which connects the results of the four branches. The third dimension of the output results of the four branches is parallel, which is the dimension of the output image; the third layer is perception 3b layer, this layer is divided into four branches, which are processed by convolution kernels of different scales. The convolution kernels of three convolution processing are $1 \times 1 \times 128$, $1 \times 1 \times 128$, $3 \times 3 \times 192$ and $1 \times 1 \times 32$, $5 \times 5 \times 96$ and another branch is 3×3 pooling layer processing and $1 \times 1 \times 64$ convolution processing (Liu et al. 2020). The results of the four branches are connected, and the third dimension of the output results of the four branches is parallel, which is the output of the data dimension: the fourth level of perception (4a-e) and the fifth level of perception (5a,b) are similar to the third level, so we will not repeat them. Finally, the output data is the type label of the plate defect image, so as to achieve the purpose of classification. The algorithm covers convolution layer and pooling layer of different scales, which can effectively alleviate the problem of training gradient dispersion

caused by large amount of data processing. The experimental results of GoogLeNet model are shown in Fig. 5.

ResNet model structure

CNN model will enhance the detection effect with the increase of learning layers. However, there are many problems in deep CNN, such as huge model structure and heavy computation, which affect the speed and accuracy of training. Therefore, this paper uses residual neural network to learn and recognize wood samples. In the ordinary convolution model, the series mechanism is added to form ResNet model. It effectively reduces the training difficulty of network parameters, and will not cause the decline of accuracy (Zhang et al. 2021). The following figure is the schematic diagram of two-layer basic block unit. The three-layer basic block structure is based on the two-layer structure, adding a layer of convolution layer structure on the main branch. Basic block units are connected in series to form res block module, which is the smallest unit of ResNet model (Xie and Dong 2021, Tong and Xu 2021, Jin et al. 2021, Wang and Hi 2019). The schematic diagram of basic block unit is shown in Fig. 2.

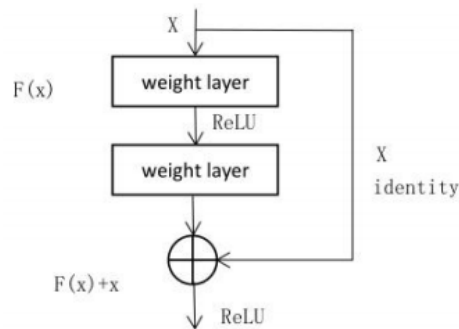


Fig. 2: Schematic diagram of basic block unit.

Due to the different layers of ResNet network, the unit structure of residual block is also slightly different. Therefore, the network structure of ResNet can be roughly divided into two categories: one is based on two-layer structure of basic block, such as ResNet-18 and ResNet-34; the other is based on three-layer structure of basic block, such as ResNet-50, ResNet-101, ResNet-152 and higher-layer ResNet network structure (Zhang and Hu 2019). In ResNet network, the structure sequence of residual block is convolution processing, BN processing, and ReLU activation processing. After processing results are superimposed, ReLU activation processing is performed. The specific network structure configuration is shown in Tab. 1.

Tab. 1: ResNet network configuration table.

Layer	Output size	ResNet-18	ResNet-34	ResNet-50	ResNet-101
Conv1	112×112	7×7×64, stride = 2			
Conv2_x	56×56	3×3max pool, stride = 2			
		$\begin{bmatrix} 3 \times 3 \times 64 \\ 3 \times 3 \times 64 \end{bmatrix} \times 2$	$\begin{bmatrix} 3 \times 3 \times 64 \\ 3 \times 3 \times 64 \end{bmatrix} \times 3$	$\begin{bmatrix} 1 \times 1 \times 64 \\ 3 \times 3 \times 64 \\ 1 \times 1 \times 256 \end{bmatrix} \times 3$	$\begin{bmatrix} 1 \times 1 \times 64 \\ 3 \times 3 \times 64 \\ 1 \times 1 \times 256 \end{bmatrix} \times 3$
Conv3_x	28×28	$\begin{bmatrix} 3 \times 3 \times 128 \\ 3 \times 3 \times 128 \end{bmatrix} \times 2$	$\begin{bmatrix} 3 \times 3 \times 128 \\ 3 \times 3 \times 128 \end{bmatrix} \times 4$	$\begin{bmatrix} 1 \times 1 \times 128 \\ 3 \times 3 \times 128 \\ 1 \times 1 \times 512 \end{bmatrix} \times 4$	$\begin{bmatrix} 1 \times 1 \times 128 \\ 3 \times 3 \times 128 \\ 1 \times 1 \times 512 \end{bmatrix} \times 4$
Conv4_x	14×14	$\begin{bmatrix} 3 \times 3 \times 256 \\ 3 \times 3 \times 256 \end{bmatrix} \times 2$	$\begin{bmatrix} 3 \times 3 \times 256 \\ 3 \times 3 \times 256 \end{bmatrix} \times 6$	$\begin{bmatrix} 1 \times 1 \times 256 \\ 3 \times 3 \times 256 \\ 1 \times 1 \times 1024 \end{bmatrix} \times 6$	$\begin{bmatrix} 1 \times 1 \times 256 \\ 3 \times 3 \times 256 \\ 1 \times 1 \times 1024 \end{bmatrix} \times 23$
Conv5_x	7×7	$\begin{bmatrix} 3 \times 3 \times 512 \\ 3 \times 3 \times 512 \end{bmatrix} \times 2$	$\begin{bmatrix} 3 \times 3 \times 512 \\ 3 \times 3 \times 512 \end{bmatrix} \times 3$	$\begin{bmatrix} 1 \times 1 \times 512 \\ 3 \times 3 \times 512 \\ 1 \times 1 \times 2048 \end{bmatrix} \times 3$	$\begin{bmatrix} 1 \times 1 \times 512 \\ 3 \times 3 \times 512 \\ 1 \times 1 \times 2048 \end{bmatrix} \times 3$
	1×1	Average pool, 1000-d fc, softmax			

ResNet-v2 derived model structure

According to the original residual network unit, some improvements are proposed to form a new residual network unit. In the original ResNet model, the ReLU function is used as the activation function, which requires high learning rate and is prone to “neuron death“. The improved ResNet-v2 derived model uses sigmoid function to put sigmoid activation function into ‘pre-activation’ which is regarded as weight layer instead of traditional “post-activation”. From this point of view, a new residual cell is generated, as shown in Fig. 3 below.

The new algorithm based on ResNet-v2 algorithm is as follows: firstly, convolution processing is performed on the plate defect image, the convolution core is $7 \times 7 \times 64$, the step size is 2, and the convolution result of the previous step is maximized. Analysis of residual in ResNet. According to the parameter configuration in Tab. 1, if the ResNet-v2 network structure is 18 or 34 layers, repeat the above operation twice; if the network structure is 50 or 101 layers, repeat the above operation three operations. The data of the last convolution operation is superimposed with the data just entering BN normalization processing. According to the network layer requirements of ResNet-v2, repeat the PreActBlock. The last layer of ResNet-v2 network system is the same as the ResNet network structure. It adopts average pooling, FC full connection and sigmoid activation function to classify. The cross entropy loss function is used as the loss function, and momentum SGD is used as the optimization method.

The new algorithm based on ResNet-v2 can simplify the optimization process and reduce the loss of information in the process of information transmission. In addition, as a ‘pre-activation’ BN layer plays a role of regularization, which can effectively suppress the over fitting phenomenon. Compared with the original ResNet network structure, the new algorithm

based on ResNet-v2 is easier for deep learning and has stronger generalization ability. The structure comparison diagram of ResNet and the new algorithm derived from ResNet-v2 is shown in Fig. 3.

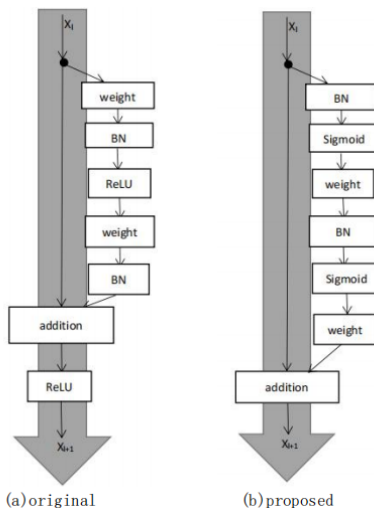


Fig. 3: Network structure of PreActBlock link.

RESULTS AND DISCUSSION

Experimental results

In this paper, we use the method of comparative experiment, put the data set into VGG-16 model, GoogLeNet model, ResNet model and ResNet-v2 model at the same time, and then compare the test accuracy of various models with other irrelevant variables, such as batch size, optimization method, loss function, etc. The experiment was completed based on inter (R) core (TM) i5-6300hq CPU@2.30GHz, memory 8.00GB, hard disk 208GB hardware environment.

VGG-16 model realizes the plate defect classification, and the highest accuracy of test set is 83.301% in the 14th iteration. The training set loss function and test set accuracy of VGG-16 model are shown in Fig. 4a. In the 16th iteration, the highest accuracy of test set is 86.648%. The training set loss function and test set accuracy of GoogLeNet model are shown in Fig. 4b.

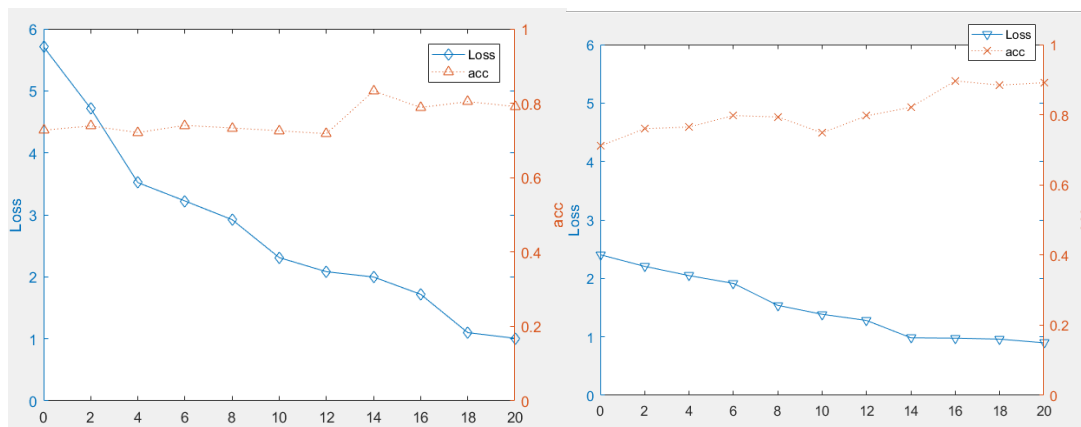


Fig. 4: Loss function and accuracy: a) VGG-16, b) GoogLeNet model.

For the ResNet model of layers 18, 34, 50 and 101, the accuracy of the test set is shown in Fig. 5a. The loss function of training set is shown in Fig. 5b. In the 71st iteration of ResNet-18 network structure, the maximum accuracy is 82.108%. In the 81st iteration of ResNet-34 network structure, the maximum accuracy is 87.745%. The maximum accuracy of ResNet-50 network structure is 98.625% in the 71st iteration. In the 81st iteration of ResNet-101 network structure, the maximum accuracy is 96.814%.

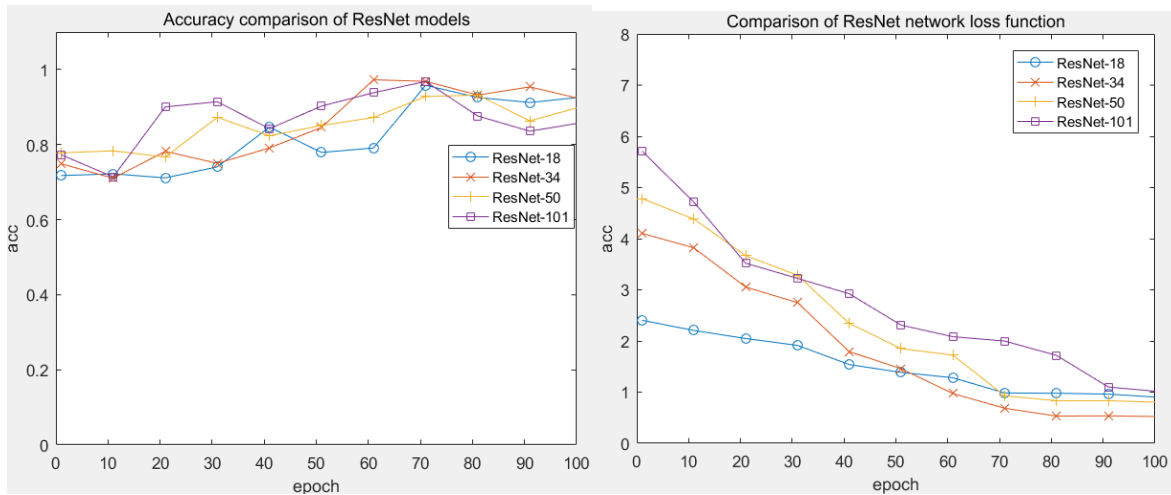


Fig. 5: a) Accuracy comparison of ResNet test set, b) loss function comparison of ResNet training set.

For the ResNet-v2 derived model based on layers 18, 34, 50 and 101, the accuracy of the test set is shown in Fig. 6a. The loss function of training set is shown in Fig. 6b. In the 81st iteration of the 18 layer network structure, the maximum accuracy is 95.801%. In the 71st iteration, the maximum accuracy is 97.266%. In the 81st iteration, the maximum accuracy of 50 layer network structure is 93.203%. In the 71st iteration, the maximum accuracy of 101 layer network is 91.814%.

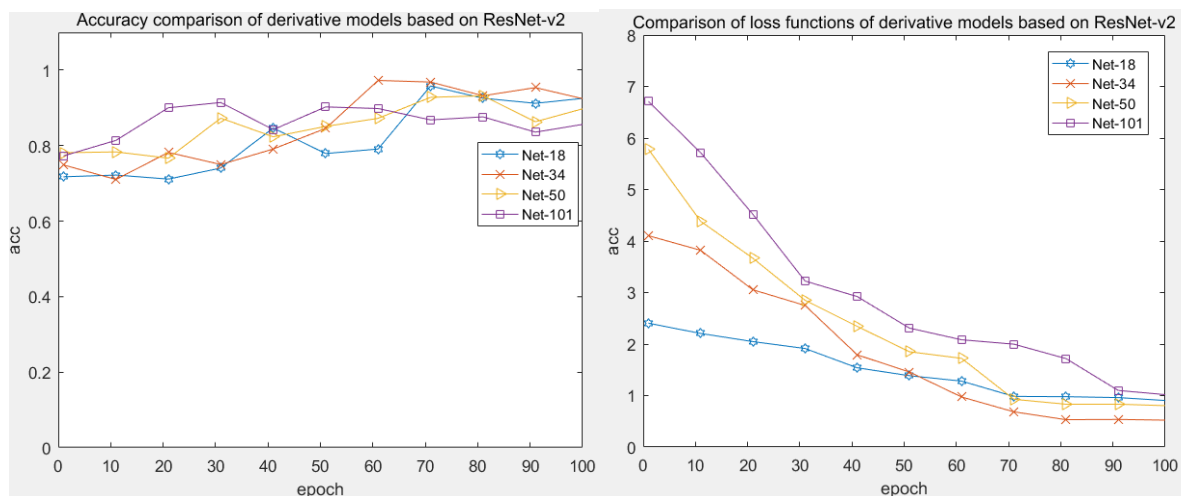


Fig. 6: a) Accuracy comparison of derived model test set based on ResNet-v2, b) comparison of training set loss function based on ResNet-v2 derivative model.

The accuracy of ResNet model and derived model test set based on ResNet-v2 is shown in Tab. 2, and the classification accuracy of three types of defects is shown in Tab. 3.

Tab. 2: Classification accuracy of test set.

	18	34	50	101
ResNet	82.108%	87.745%	98.625%	96.814%
ResNet-v2 derived model	95.801%	97.266%	93.203%	91.422%

Tab. 3: Defect accuracy of ResNet-v2 derived model.

	Wormhole	Dead joint	Live joint
Derived model-18	94.172%	93.834%	98.638%
Derived model-34	92.824%	99.401%	97.343%
Derived model-50	93.900%	95.412%	91.629%
Derived model-101	89.159%	95.928%	90.033%

VGG model, GoogLeNet model, ResNet model and the derived model of ResNet-v2 are compared for the recognition accuracy of plate defects, as shown in Tab. 4.

Tab. 4: Comparison of accuracy of four models.

	VGG	GoogLeNet	ResNet	ResNet-v2 derived model
Accuracy	83.301%	86.648%	98.625%	97.266%

CONCLUSIONS

In this paper, VGG-16 model, GoogLeNet model, ResNet model, and the derived model based on ResNet-v2 are constructed to identify wood defects. The images of wood defects are put into each model for deep learning. By comparing the data results of the four models, it is found that the derived model of ResNet-v2 can well distinguish the types of sample defects, and has high accuracy and good performance. By controlling the learning rate, the speed of data learning can be accelerated, and the phenomenon of gradient explosion and gradient dispersion can be effectively avoided. However, with the increase of convolution layers, the classification accuracy of ResNet-v2 system is not as good as that of ResNet system, which is also the deficiency of this study. It is hoped that further improvement can be made in future research.

ACKNOWLEDGEMENTS

This research is partially supported by the Natural Science Foundation of Heilongjiang Province in China (lh2020c034). The authors have no conflict of interest to declare.

REFERENCES

1. Bao, W.X., Wu, G., Hu, G.S., Zhang, D.Y., Huang, L.S., 2021: Identification of apple leaf diseases based on improved convolution neural network. *Journal of Anhui University (Natural Science Edition)* 45(01): 53-59.
2. Cheng, Y.Z., Gu, Q., Wang, Z.H., 2018: Wood defect image detection method based on deep learning. *Forestry Machinery and Woodworking Equipment* 46(08): 33-36.
3. Cheng, Y.Z., 2021: Wood defect image segmentation teaching software based on OpenCV Python. *Forestry Machinery And Woodworking Equipment* 49(01): 36-39+42.
4. Fan, J.N., Liu, Y., Yang, Y.T., Gou, B.L., 2020: Research progress on application of machine vision in wood defect detection. *World Forestry Research* 33(03): 32-37.
5. Hu, Z.K., Liu, Y., Zhou, X.L., Zhao, Q., Shen, L.X., 2019: Research on defect and texture recognition of solid wood based on depth confidence network. *Computer Application Research* 36(12): 3889-3892.
6. Huang, J.B., Zhu, Y.H., Zhou, J.T., Gao, W.J., 2020: Fine grained image classification of succulent plants based on convolutional neural network. *Journal of Shanghai University (Natural Science Edition)* 26(02): 283-291.
7. Jin, Y., Ye, S., Li, H.L., 2021: Research on intelligent diagnosis model of fruit tree diseases based on resnet-50 deep convolution network. *Journal of Agricultural Library and Information Science* 33(04): 58-67.
8. Li, R.C., Zhu, Y.X., Sun, W.M., Gong, S.Y., Qian, X., Ye, N., 2020: Recognition and location of wood defect image based on deep learning. *Data Acquisition and Processing* 35(03): 494-505.
9. Liu, C.L, Lin, L., Yu, C.C., Wu, J.Z., 2020: Classification of peanut hyperspectral images based on deep learning. *Computer Simulation* 37(03): 189-192 + 283.
10. Liu, Y., Zhou, X.L., Hu, Z.K., Yu, Y.B., Yang, Y.T., Xu, C.Y., 2019: Wood defect detection based on optimized convolution neural network. *Journal of Forestry Engineering* 4(01): 115-120.
11. Luo, W., Sun, L.P., 2019: Support vector machine learning classification of wood defects using fusion features of local binary pattern and directional gradient histogram. *Journal of Northeast Forestry University* 47(06): 70-73.
12. Peng, D.L., Wang, T.X., 2019: Pruning algorithm based on GoogLeNet model. *Control and Decision* 34(06): 1259-1264.
13. Qi, D.W., Mou, H.B., 2013: Wood defect detection based on Hu moment invariants and BP neural network. *Journal of Southeast University (Natural science edition)* 43(S1): 63-66.
14. Tong, Z., Xu, A.J., 2021: Segmentation method of standing tree image based on improved RESNET UNET. *Journal of Central South University of Forestry Science and Technology* 41(01): 132-139.
15. Wang, D.D., He, D.J., 2019: Apple target recognition before fruit thinning by robot based on R-FCN deep convolution neural network. *Journal of Agricultural Engineering* 35(03): 156-163.

16. Wang, Z.R., Fang, Y.M., Feng, H.L., Du, X.C., Xia, K., 2018: Detection and location method of wood knot defects. *Progress of Laser And Optoelectronics* 55(05): 317-324.
17. Wu, D.Y., Ye, N., Su, X.Q., 2010: Wood defect recognition based on gray level co-occurrence matrix and clustering method. *Computer and Digital Engineering* 38(11): 38-41.
18. Xue, Y., Wang, L.Y., Zhang, Y., Shen, Q., 2020: Apple defect detection method based on GoogLeNet deep transfer learning. *Journal of Agricultural Machinery* 51(07): 30-35.
19. Xie, Y.R., Dong, J.N., 2021: Research on Dongba pictograph recognition based on RESNET network. *Computer Age* (01): 6-10.
20. Yan, F., Cheng, Y.Z., 2020: Semantic segmentation of wood defect image based on convolutional neural network. *Forestry and Grassland Machinery* 1(06): 52-56.
21. Yang, Y.T., Zhou, X.L., Liu, Y., Hu, Z.K., Ding, F.L., 2020: Wood defect detection based on depth extreme learning machine. *Applied Sciences* 10(21): 7488.
22. Zhang, J.H., Kong, F.T., Wu, J.Z., Zhai, Z.F., Han, S.Q., Cao, S.S., 2018: Cotton disease identification model based on improved VGG convolutional neural network. *Journal of China Agricultural University* 23(11): 161-171.
23. Zhang, X., Hu, X.J., 2019: Application of deep fusion neural network based on GoogLeNet and RESNET in pulse wave recognition. *Computer System Applications* 28(10): 15-26.
24. Zhang, Y., Zhao, Z.M., Wang, X.C., Feng, H.Q., Lin, J., 2021: Construction of green tea species recognition model based on RESNET convolutional neural network. *Tea Science* 41(02): 261-271.
25. Zhou, Y., Pan, S.H., Liu, W.J., Yu, Y.S., Zhou, Z.K., Liu, J., 2020: Wood defect image detection method based on Zhongzhiji. *Forestry Machinery and Woodworking Equipment* 48(10): 64-68.

JIAXIN LING, YONGHUA XIE*
NORTHEAST FORESTRY UNIVERSITY
COLLEGE OF MECHANICAL AND ELECTRICAL ENGINEERING
HARBIN 150040
P.R. CHINA

*Corresponding author: zdhxyh@163.com

REDUCTION OF EFFECT OF GROWTH STRESS PRESENCE USING ENDLESS SCREW DURING KILN DRYING AND STEAMING AND HEATING TREATMENT IN LOG BEFORE SAWING

RÓGER MOYA, CAROLINA TENORIO
ESCUELA DE INGENIERÍA FORESTAL
COSTA RICA

(RECEIVED JULY 2021)

ABSTRACT

The relaxation of growth stress in trees growing in fast-growth conditions, as plantation in tropical areas, affects lumber quality during of sawing or drying process. It was evaluated two pretreatments (heating and steaming application) before sawing process and endless screw use to maintain the boards pressed during drying of *Dipteryx panamensis* and *Hieronyma alchorneoides* wood with objective to reduce the effects of relaxation of growth stress. The results showed endless screw is used to maintain the boards pressed, the moisture content (MC) or drying rate did not vary. The use of endless screws with daily adjustment during drying produced a reduction of cup, check and split defects in lumber and this treatment is accompanied with a pre-treatment before sawing (heating or steaming treatment) decreased the incidence of drying defects. Then the use of both treatments is an opportunity to reduce the effects of relaxation of growth stress on the quality of the wood of *D. panamensis* and *H. alchorneoides* from fast-growth plantation conditions.

KEYWORDS: Drying defects, tropical wood, log treatment, drying improvement.

INTRODUCTION

One of the main problems of trees from fast-growth plantations is that the logs extracted from those trees show a high manifestation of growth stress (Kojima et al. 2009), which is evidenced during the sawing process, the wood presents a high incidence of warps, checks and splits and they are accentuated during the drying process, producing dried-lumber of low quality (Moya et al. 2013, 2019, Tenorio et al. 2016).

The effect of growth stress on wood processing has been extensively studied (Yang and Waugh 2001, Gril et al. 2017). Growth stress is referred to the mechanical stress permanently

endured by the wood of the living tree during its growth (Gril et al. 2017). The magnitude of these defects depends on the species and can be result in considerable economic losses for the forester and sawler (Gril et al. 2017).

Different treatments on logs and lumber have been implemented in order to increase lumber quality and reduce the effect of growth stress (Ratnasinga et al. 2013). The application of heat and steam are techniques that reduce growth stress during the sawing or drying process (Pelozzi et al. 2014, Rodrigues et al. 2018). Both processes have been applied with a wide variety of purposes, besides of reducing growth stress levels, such as changing color, improving dimensional stability, increasing permeability, improving drying rate, and reducing the initial moisture content and reducing of drying defects (Calonego and Severo 2007, Ratnasinga et al. 2013).

Different techniques have been implemented to reduce drying defects: drying schedule adjusted to relaxed residual growth stress (Kong et al. 2018), drying techniques such as temperature and steaming application (Lenth and Kamke 2001), frequency-vacuum drying systems (Avramidis and Liu 1994), microwave pretreatment (He et al. 2017) and drying schedule with high temperature (Baranski 2018).

Recently, a mechanical system has been tested to reduce drying defects, which consists in the placement of endless screws with plates that traversed the pile of wood from side to side (Fig. 1b). Every 12 hours the nuts on screws are adjusted in order to maintain the pressed boards and to avoid formation of twists in the wood (Berrocal et al. 2017).

On the other hand, several tropical species have acquired importance in commercial reforestation based on the knowledge of their genetics, reproduction, and plantation management in Costa Rica (Murillo 2018). Fast-growing species (with rotation periods of less than 25 years), such as *Dipteryx panamensis* and *Hieronyma alchorneoides* have excellent growth and production in forest plantations (Redondo-Brenes and Montagnini, 2006). Recent research on these species in relation to the quality of wood indicate two types of problems (Moya and Muñoz 2010, Carolina Tenorio et al. 2016, Moya et al. 2019): (i) problems during sawing process and (ii) high incidence of drying defects after drying process.

There are few studies in tropical species where the effect of the application of heat and steam a priori in logs on the quality of wood after sawing processing or during drying process is evaluated for relaxation of growth stress. Thus, the present work aims to evaluate the effect on the quality of dried-lumber after the application of four treatments, two applied on logs (heating and steaming treatments) and two applied during the drying process (steam application and endless screw is used to maintain the boards pressed), of *Dipteryx panamensis* and *Hieronyma alchorneoides* wood from forest plantations trees.

MATERIAL AND METHODS

Site and plantation characteristics

A plantation of *Hieronyma alchorneoides* and a plantation of *Dipteryx panamensis* were sampled for this study. Plantation age were 12 and 16 years old, respectably. A plantation of *H. alchorneoides* had a density of 450 N·ha⁻¹, while the *D. panamensis* plantation had 550 N·ha⁻¹

at sampling time. More details on the conditions of the plantations can be consulted in Moya et al. (2021).

Sampling and sawing of trees

Sampled trees were cut close to the average diameter breaks height (DBH) of each plantation. Logs were sawn using a cutting pattern typical for lumber production in Costa Rica (Serrano and Moya 2011), where a semi-log was obtained and this sawn into 2.5 cm thick boards.

Treatments used for relaxation of growth stress in logs

Two treatments were used on the logs with the objective of relaxation of growth stress: (1) application of a temperature of 115°C for 24 hours ($\text{Log}_{\text{heating}}$) and (2) application of steaming for 24 hours at a pressure of 70 Pa ($\text{Log}_{\text{steaming}}$). As a complement and comparison, logs without heating or stemming were used ($\text{Log}_{\text{un-treated}}$). 4-6 logs were placed inside a horizontal tank in both treatments. Conditions of application and tank description for heating and steaming are extensively detailed in Moya et al. (2021).

Treatments for relaxation of residual growth stress during drying process

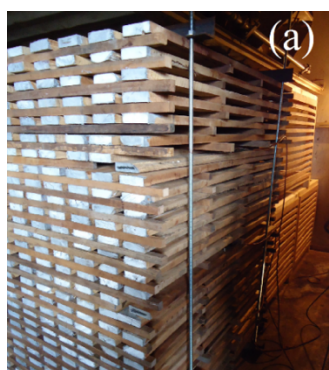
The relaxation of residual growth stress during drying in sawn-lumber were used drying schedules detailed in Tab. 1 for two species studied according to Moya et al. (2019). A conventional kiln with a 2 m³ capacity pilot chamber (NARDI, Italy) was used for drying. Conventional kiln uses an electrical power source to heat the resistance inside the chamber. For maintain the relaxation of residual growth stress was used endless screw in during drying process of both species, which had shown appropriated performance for reducing drying defects ($\text{Drying}_{\text{with-screw}}$). The endless screws consisted in the placement of endless screws with plates that traversed the pile of wood from side to side (Fig. 1a) in three different positions: extremes and middle of length pile. They were two twice adjusted with the aid of the nuts on the screw in order to maintain the boards pressed and thus avoid formation of twists in the wood, according to proposed by Denig et al. (2000). As a complement and comparison, a treatment without endless screw was tested ($\text{Drying}_{\text{without-screw}}$). The treatments used on the logs and during drying to increase wood quality are detailed in Fig. 1b.

Tab. 1: Drying schedule utilized in lumber from steaming and heating treatment log for *D. panamensis* and *H. alchorneoides*.

Species	Stage	DBT (°C)	WBT (°C)	EMC (%)	RH (%)	MC (%)
<i>Dipteryx panamensis</i>	Heating	37	-	-	-	-
		40	37	15.8	82	Green
	Drying	44	38	11.5	68	40
		46	38	9.7	60	30
		48	38	8.4	53	20
		50	38	7.4	47	15
		Equalization	50	42	10	62
	Conditioning	50	46	14	79	-
<i>Hieronyma</i>	Heating	40	-	-	-	-

<i>alchorneoides</i>	Drying	40	37	14.8	82	Green	
		40	35	12.5	72	40	
		45	37	9.7	60	30	
		50	40	7.9	55	25	
		55	42	6.2	47	20	
		55	37	5.0	33	15	
		Equalization	55	47	10	64	-
		Conditioning	55	51	15	81	-

Note: DBT - dry bulb temperature, WBT - wet bulb temperature, EMC - equilibrium moisture content, RH - relative humidity and MC - moisture content.



Log treatment	Dry treatment
Heating (Log _{heating})	With screw (Drying _{with-screw})
	Without screw (Drying _{without-screw})
Steaming (Log _{steaming})	With screw (Drying _{with-screw})
	Without screw (Drying _{without-screw})
Un-treated (Log _{un-treated})	With screw (Drying _{with-screw})
	Without screw (Drying _{without-screw})

Fig. 1: a) Endless screw location in lumber stacked in piles for adjustment during drying (Berrocal et al. 2017), and b) treatments applied to sawn timber of *D. panamensis* and *H. alchorneoides*

Moisture control

Moisture content (MC) was monitored using control or kiln samples and was determined before and after drying. MC before drying, named initial MC (IMC), a cross section of 2.5 cm thick to 20 cm of the end was extracted from kiln samples (Simpson 1991) and was determined according to ASTM-4442-07 standard (ASTM 2007). After kiln samples were placed at different heights in the package in drying chamber according to log and drying treatment. Kiln samples were weighed two twice per day for MC and to establish the change in the schedule (steps) applied (Tab. 1) and MC decreasing during drying process. For final MC (FMC), again, a variation cross section of 2.5 cm thick was extracted from each board after drying. The average values for IMC and FMC for these six samples were used to determine the average drying rate for each charge, which means moisture loss in percentage determined by Eq. 1:

$$\text{Average drying rate (\%/hr)} = (\text{IMC-FMC}) / \text{Total drying time (hours)} \quad (1)$$

where: IMC - initial moisture content in percentage and FMC - final moisture content (%)

Wood color change

Wood color was measured before and after the drying process in the same point in a longitudinal surface. Measures were taken in both heartwood and sapwood. Color was measured using a HunterLab Mini Scan XE Plus spectrophotometer. The CIEL*a*b* system was used to measure the reflectance spectra (from 400 to 700 nm), with an 11 mm opening.

Color change (ΔE^*) ΔE^* was determined by the values L^* , a^* and b^* before and after drying and calculated according to the formula laid down in the standard ASTM D 2244 (ASTM 2005).

Evaluation of drying defects

The defects measured were warp (twist, crook, bow and cup), splits and checks and were determined before and after drying. The methodology detailed in Salas and Moya (2014) and Tenorio et al. (2012), were used to evaluate all the drying defects. The Index of quality after drying (IQ_{after}) was determined. The official Chilean standard Nch993EO72 was used to determine IQ_{after} , which was computed for twist, crook, cup, bow, check and split according to Eq. 2 (Tenorio et al. 2016). The values close to 0 in this index means lower presence of defects and values close to 5 higher presences of defects. This standard sets limit quality values for the different parameters (Tab. 2). For splits and checks the classification was done according to American Softwood Lumber Standard PS20-05 (NIST-National Institute of Standards and Technology 2005) which establishes four different categories (Tab. 2). Finally, dried-lumber index quality was classified using Kauman and Mittak (1966) methodology (Tab. 2).

$$QI_{after} = \frac{(Na \cdot 0 + Nb \cdot 0.5 + Nc \cdot 1.0 + 2.5 \cdot Nd)}{\text{Total boards dried}} \quad (2)$$

where: QI_{after} - quality index after drying; Na - number of pieces without any presence of warp; Nb - number of pieces with a slight presence of warp; Nc - number of pieces with a moderate presence of warp; Nd - number of pieces with a severe presence of warp.

Tab. 2: Limits values for classification of drying defects and classification of drying quality according to drying defects utilized in the *D. panamensis* and *H. alchorneoides* dried-lumber (Kauman and Mittak 1966).

Drying defects	Limits of quality	Drying quality	Limits of dried-lumber quality index
Cup	not present: 0 mm, slight: 1-3 mm, moderate: 3-5 mm severe: > to 5 mm	Excellent	0.0
Bow	not present: 0 mm, slight: 1-3 mm, moderate: 3-6 mm severe: > to 6 mm	Very good	0.1-0.5
Crook	not present: 0 mm, slight: 1-2 mm, moderate: 2-3 mm severe: > to 3 mm	Good	0.51-1.0
Twist	not present: 0 mm, slight: 1-5 mm, moderate: 5-8 mm severe: > to 8 mm	Satisfactory	1.1-1.5
Checks	not present: 0 mm, slight: 1-10 mm, moderate: 10-25 mm,	Regular	1.51-2.0
	severe: > to 25 mm	Defective	2.1-3.0
Splits	not present: 0 mm, slight: 1-25 mm, moderate: 25-42 mm,	Poor	3.1-5.0
	severe: > to 42 mm	Very poor	> 5.0

RESULTS

Initial and final moisture content, drying time and drying rate.

IMC ranged from 28% to 43%, the FMC ranged from 9% to 11%, the drying time was 168 hours for all treatments and the drying rate ranged from 0.13 to 0.20%/hr in *D. panamensis* lumber (Tab. 3). For *H. alchorneoides* lumber, IMC ranged from 64% to 128%, FMC 7.0% to 8.2%, drying time for all six treatments was 164 hours and drying rates were lowest in lumber

from $\text{Log}_{\text{Heating}}$ (about 0.35 %/hour), while the highest value in $\text{Log}_{\text{Steaming}}$ with 0.73 %/hour (Tab. 3).

Tab. 3: Drying variables for *D. panamensis* and *H. alchorneoides* lumber with and without endless screw use during drying process.

Species	Log treatment	Screw use in drying	IMC (%)	FMC (%)	Drying time (hours)	Drying rate (%/hours)
<i>D. panamensis</i>	$\text{Log}_{\text{heating}}$	Drying _{with-screw}	29.98	7.01	168	0.14
		Drying _{without-screw}	38.05	7.20	168	0.18
	$\text{Log}_{\text{steaming}}$	Drying _{with-screw}	41.99	8.27	168	0.20
		Drying _{without-screw}	28.07	7.05	168	0.13
	$\text{Log}_{\text{un-treated}}$	Drying _{with-screw}	35.80	9.01	168	0.16
		Drying _{without-screw}	42.74	11.27	168	0.19
<i>H. alchorneoides</i>	$\text{Log}_{\text{heating}}$	Drying _{with-screw}	64.08	7.88	164	0.35
		Drying _{without-screw}	66.36	7.00	164	0.36
	$\text{Log}_{\text{steaming}}$	Drying _{with-screw}	127.85	8.20	164	0.73
		Drying _{without-screw}	74.85	8.17	164	0.41
	$\text{Log}_{\text{un-treated}}$	Drying _{with-screw}	107.91	7.24	164	0.61
		Drying _{without-screw}	90.84	7.78	164	0.51

Note: IMC - initial moisture content, FMC - final moisture content.

Variation of moisture content and drying rate in relation drying time

The variation of MC with time of *D. panamensis* and *H. alchorneoides* lumber showed a homogeneous behavior of decreasing MC with time in all treatments (Fig. 3). It was observed that there were no differences in the behavior of MC variation between Drying_{with-screw} and Drying_{without-screw} (Fig. 3a,b). The variation of drying rate showed homogeneous behavior time in all treatment of *D. panamensis* (Fig. 3c), there were more differences in the lumber from $\text{Log}_{\text{Steaming}}$ and Drying_{without-screw} in *H. alchorneoides* lumber, which presented a higher value of drying rate during the first two days (Fig. 3d), due to its high IMC (Tab. 3).

Drying defects

The quality classification of dried-lumber considering IQ_{after} cup of *D. panamensis* showed that lumber was classified as excellent in the different treatments (Tab. 4). The use of endless screw increased IQ_{after} of bow in lumber from $\text{Log}_{\text{heating}}$ and $\text{Log}_{\text{un-treated}}$, thus there was a decreasing the quality in Drying_{with-screw}. IQ_{after} of crook increased in Drying_{with-screw} in lumber from $\text{Log}_{\text{heating}}$. The IQ_{after} of twist increased in lumber from three different log treatments. For IQ_{after} of checks, only dried-lumber from $\text{Log}_{\text{un-treated}}$ increased, while IQ_{after} of split increased in lumber from $\text{Log}_{\text{heating}}$ and $\text{Log}_{\text{steaming}}$ (Tab. 4).

For the *H. alchorneoides* lumber, the IQ_{after} of bow increased only in lumber from $\text{Log}_{\text{heating}}$ and $\text{Log}_{\text{steaming}}$, but IQ_{after} of crook did not increase lumber-dried quality (Tab. 4). For twist and check, the IQ_{after} increased in lumber from $\text{Log}_{\text{steaming}}$ and $\text{Log}_{\text{un-treated}}$ in Drying_{with-screw} (Tab. 4). In the case of cup defects, the IQ_{after} increased the quality of the lumber when steaming treatment is applied during drying. For split defects, the use of endless screw decreased wood quality in all log treatment (Tab. 4).

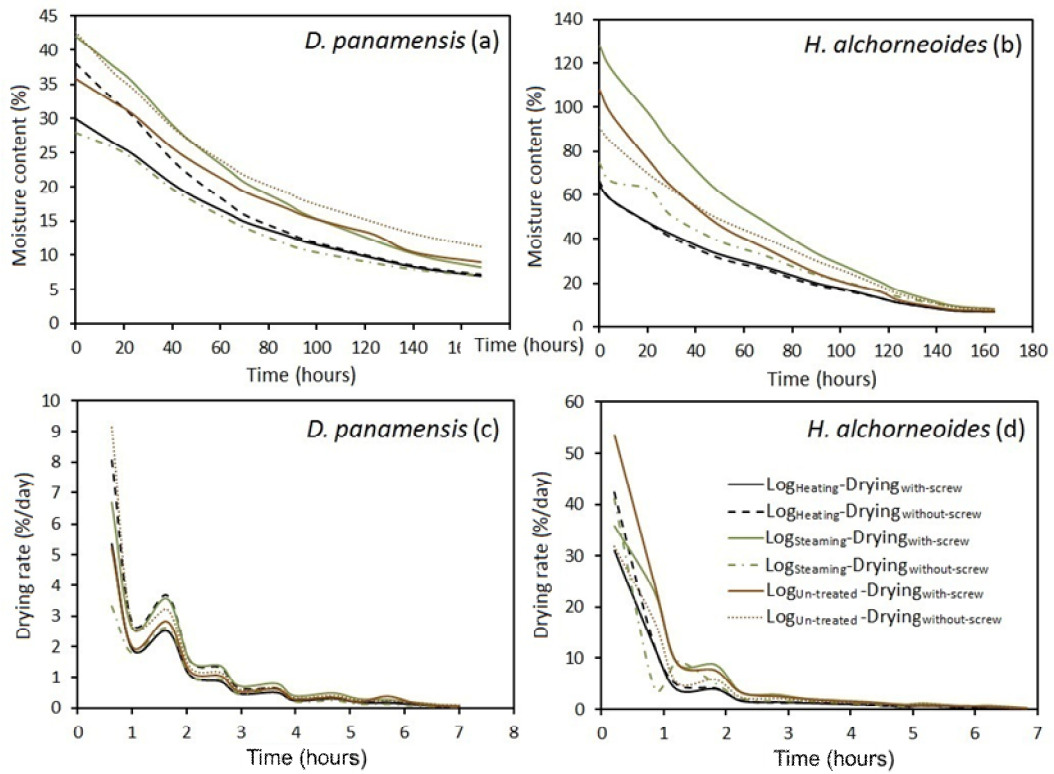


Fig. 3: Variation of moisture content and drying rate in relation to time for *D. panamensis* (a and c) and *H. alchorneoides* (b and d) lumber with endless screw use.

Tab. 4: Quality index after drying (IQ_{after}) and classification of dried-lumber obtained for log treatment and used or not of endless screw for increasing lumber quality of *D. panamensis* and *H. alchorneoides*.

Species	Log treatment	Screw use in drying	Cup	Bow	Crook	Twist	Check	Split
<i>D. panamensis</i>	Log _{heating}	Drying _{with-screw}	0.00 (Excellent)	1.39 (Satisfactory)	1.32 (Satisfactory)	0.03 (Excellent)	1.87 (Regular)	1.82 (Regular)
		Drying _{without-screw}	0.00 (Excellent)	2.05 (Regular)	1.71 (Regular)	0.74 (Good)	0.79 (Good)	2.24 (Defective)
	Log _{steaming}	Drying _{with-screw}	0.00 (Excellent)	2.18 (Defective)	2.25 (Defective)	0.41 (Very good)	1.11 (Satisfactory)	1.68 (Regular)
		Drying _{without-screw}	0.00 (Excellent)	1.57 (Regular)	2.11 (Defective)	1.14 (Satisfactory)	1.07 (Good)	2.32 (Defective)
	Log _{un-treated}	Drying _{with-screw}	0.00 (Excellent)	1.59 (Regular)	1.93 (Regular)	0.02 (Excellent)	1.02 (Good)	0.57 (Good)
		Drying _{without-screw}	0.00 (Excellent)	2.29 (Defective)	1.84 (Regular)	0.58 (Good)	1.58 (Regular)	1.05 (Good)
<i>H. alchorneoides</i>	Log _{heating}	Drying _{with-screw}	0.33 (Very good)	1.88 (Regular)	2.50 (Defective)	0.83 (Good)	1.77 (Regular)	1.90 (Regular)
		Drying _{without-screw}	0.25 (Very good)	2.22 (Defective)	2.28 (Defective)	1.06 (Good)	1.72 (Regular)	1.50 (Satisfactory)
	Log _{steaming}	Drying _{with-screw}	0.50 (Very good)	1.96 (Regular)	2.48 (Defective)	0.63 (Good)	1.20 (Satisfactory)	1.69 (Regular)
		Drying _{without-screw}	0.57 (Good)	2.27 (Defective)	2.33 (Defective)	1.17 (Satisfactory)	1.50 (Satisfactory)	1.17 (Satisfactory)
	Log _{un-treated}	Drying _{with-screw}	0.17 (Very good)	2.17 (Defective)	2.50 (Defective)	0.31 (Very good)	0.83 (Good)	1.55 (Regular)
		Drying _{without-screw}	0.36 (Very good)	2.14 (Defective)	2.32 (Defective)	0.89 (Good)	1.18 (Satisfactory)	1.21 (Satisfactory)

Color change

Color change (ΔE^*) was similar between in dried-lumber of heartwood and of sapwood in the 3 log treatments of *D. panamensis* (Tab. 5). In addition, it was observed that the ΔE^* , both of sapwood and heartwood, was higher in the lumber from Log_{heating} and Log_{steaming} than the lumber from de Log_{un-treated} (Tab. 5). For *H. alchorneoides*, lumber from Log_{heating} and Log_{steaming}, the ΔE^* was lower in heartwood than sapwood in both de Drying_{with-screw} and Drying_{without-screw}. But contrary result was presented in lumber from Log_{un-treated}, where heartwood presented the highest ΔE^* value compared to sapwood (Tab. 5). Likewise, no effect of endless screw during drying was observed in ΔE^* value in all treatments (Tab. 5). An important aspect to note is that ΔE^* of two species studied was categorized as very evident, this because the ΔE^* values are in the range of 6 to 2 (Cui et al. 2004).

Tab. 5: Color change in *D. panamensis* and *H. alchorneoides* lumber from different log treatments and with / without steam application during drying.

Species	Log treatment	Endless screw used	Color change ΔE^*	
			Sapwood	Heartwood
<i>D. panamensis</i>	Log _{heating}	Drying _{with-screw}	11.8	10.9
		Drying _{without-screw}	10.8	11.3
	Log _{steaming}	Drying _{with-screw}	10.4	10.0
		Drying _{without-screw}	10.5	10.7
	Log _{un-treated}	Drying _{with-screw}	8.6	7.8
		Drying _{without-screw}	7.8	8.8
<i>H. alchorneoides</i>	Log _{heating}	Drying _{with-screw}	13.3	9.2
		Drying _{without-screw}	16.5	8.8
	Log _{steaming}	Drying _{with-screw}	15.8	14.0
		Drying _{without-screw}	17.9	13.1
	Log _{un-treated}	Drying _{with-screw}	9.8	12.8
		Drying _{without-screw}	9.8	12.9

DISCUSSION

Although the IMC was not related with endless screw use during drying, the influence of the log treatment (heating or steaming) on this parameter was observed. IMC of lumber of Log_{steaming} and Log_{heating} treatments were lower than Log_{un-treated} (Tab. 3). This decreasing of IMC in lumber is attributed to the fact that during the application of steaming or temperature, there is an expansion of the water inside the wood, resulting in the wood coming out at the ends and also because when the wood cools down, there is a greater loss of moisture due to evaporation of this moisture (Zhang and Cai 2008).

In relation to the average drying rate, no effect of the use of screws during drying (Drying_{with-screw} treatment) was observed (Tab. 3). Berrocal et al. (2017) agreed those results in *Tectona grandis* wood, who found that drying rate was not affected the use of screws during drying.

The variation of the MC and drying rate with time of the *D. panamensis* and *H. alchorneoides* lumber in all treatments showed a homogeneous decreasing of MC with time (Figs. 3a-c). This situation is to be expected, since the use of endless screw has the objective of keeping the boards fixed within the pile (Denig et al. 2000, Berrocal et al. 2017). Therefore, the drying rate and MC will not be affected over time, as occurred in the two species studied (Figs. 3a-c).

The presence of warps, split and check before drying of these two species (Tab. 4) is attributed to the fact that the trees used come from fast-growth trees condition with a high percentage of juvenile wood (Zobel and Sprague 1998) and high levels of growth stresses (Gril et al. 2017). Stemming and heating treatment applied as pre-treatments before sawing logs aims to relax the residual longitudinal stress of the wood and increase its permeability (Gril et al. 2017). In addition, with the increase in permeability, moisture gradients decrease and thus there is improving the quality of the wood in relation to the presence of warps, check and split (Lenth and Kamke 2001, Gril et al. 2017, Rodrigues et al. 2018). However, in the case of the two

species studied, the effect was not congruent with the different types of drying defects present in dried-lumber (Tabs. 4).

Log_{steaming} and Log_{heating} treatment were not presented effects in the incidence or magnitude of warping, splitting or checking, although a slight reduction in the incidence of these quality parameters was observed in Log_{steaming} (Tabs. 4). This difference was attributed to the fact that steam treatment creates better conditions for the relaxation of the different polymers in the wood (Kong et al. 2017, Moya et al. 2021). Among them, the higher temperature reached with the Log_{steaming} in the internal part of the log or sawn timber than with the Log_{heating}. High temperature reached in Log_{steaming} treatment is probably making the entire cross section of the log reach the glass transition temperature of the wood, allowing greater relaxation (Kong et al. 2017) and as well, the steaming reduces the crystalline zones of cellulose, therefore the amorphous zones increase (Kong et al. 2017).

Endless screw has objective to reduce check and split defects due to the application of temperature during drying and variations in the moisture content in the cross-section of a piece of wood during drying (Berrocal et al. 2017). The use of this system (Fig. 1b) allows the wood pile to be held in place to prevent movement and to have a positive influence when applied to wood above the FSP in combination with high temperatures (Vansteenkiste et al. 1997). In this case, the improvement of wood quality using endless screw to maintain wood quality was irregular and each defect behaves differently; the values obtained for incidence and magnitude of the defect increased or decreased according to the defect (Tab. 4). However, the effect of the use of the endless screw was reflected in the value of IQ_{after}, this value decreased, therefore, there was an increase in the quality of dried-lumber (Tab. 4). The reduction of these defects by endless screws used is due to the fact that this forces for maintaining pile working in the direction of the tangent of the growth rings could reduce the development of internal checking. Besides, this force can be viewed as a counteracting force for stresses developed during drying or as a restraining force to internal stresses in the wood that give it a great tendency to accumulate drying defects (Denig et al. 2000).

Likewise, the use of endless screws for daily adjustment during drying produced a lower percentage of dried-lumber classified as "low drying stress", in relation to the lack of screws in the wood pile (Tab. 4). This result, together with good pretreatment before sawing (heat or steam treatment) reduced the incidence of warping, checking and cracking (Tabs. 4).

In relation to color change (ΔE^*), the sapwood and heartwood show different behaviors of both *D. panamensis* and *H. alchornoides* wood (Tab. 5). Heartwood has a higher amount of extractives than sapwood (Hillis 1987), which produce a chemical change when temperature is applied (Tolvaj et al. 2012, Berrocal et al. 2016). During steaming, the polyphenolic compounds in the heartwood that give it its dark color can migrate into the sapwood and darken it (Tolvaj et al. 2012), as was evident in heartwood of both *D. panamensis* and *H. alchornoides* of present study. The highest color change was obtained when log received steaming before sawing. Tolvaj et al. (Tolvaj et al. 2012) based on studies of *Robinia pseudoacacia* indicated that the color changes are attributed to the fact that parameter L* decreased and the parameters a* and b* increased with temperature and steaming.

Endless screw use during drying does not change the chemical structure of the wood and the chemical composition of wood (Tolvaj et al. 2012, Berrocal et al. 2016), then no effects on the change in color or ΔE^* was not evidenced (Tab. 5). Therefore, the changes observed in the color of lumber whose drying process included endless screw treatment are related to the pretreatments ($\text{Log}_{\text{steaming}}$ and $\text{Log}_{\text{heating}}$) of the logs prior to sawing.

CONCLUSIONS

The use of endless screw during drying, being a treatment that does not change the chemical structure of the wood but are external supports to maintain the shape of the board, has no effect on color change, drying time or drying rate, but its main benefits are related to the improvement of the magnitude, incidence and quality category of cup, check and split defects. In addition, this decreasing of defects is favored again when the use of endless screw in the wood piles was accompanied with a pre-treatment of the logs such as steaming and heating before sawing.

ACKNOWLEDGEMENTS

The authors wish to thank the Vicerrectoría de Investigación y Extensión, Instituto Tecnológico de Costa Rica (ITCR, Cartago, Costa Rica) for the financial support of the project. We would also like to thank the company Cinco Ceibas Rainforest Reserve and Adventure Park for providing material and financial support for this research.

REFERENCES

1. ASTM, 2005: Standard practice for calculation of color tolerances and color differences from instrumentally measured color coordinates.
2. ASTM, 2007: Standard test methods for direct moisture content measurement of wood and wood-base materials.
3. Avramidis, S., Liu, F., 1994: Drying characteristics of thick lumber in a laboratory radio-frequeocy/vacuum dryer. *Drying Technology*: 12 1963–1981.
4. Baranski, J., 2018: Moisture content during and after high- and normal-temperature drying processes of wood. *Drying Technology* 36: 751–761.
5. Berrocal, A., Moya, R., Rodríguez-Solis, A.M., Muñoz, F., 2017: Drying of plantation-grown *Tectona Grandis* wood with daily-controlled drying rate schedules. *Journal of Tropical Forest Science* 29: 69–79.
6. Berrocal, A., Moya, R., Rodríguez-Solis, M., Starbird, R., Muñoz, F., 2016: Surface chemical and color characterization of juvenile *Tectona grandis* wood subjected to steam-drying treatments. *Surface Review and Letters* 23: 1-14.
7. Calonego, F.W., Severo, E.T.D., 2007: Influence of boards diametrical position and steaming on the drying defects of *Eucalyptus grandis*. *Cerne* 13: 10–18.
8. Cui, W., Kamdem, D.P., Rypstra, T., 2004: Diffuse reflectance infrared Fourier transform spectroscopy (DRIFT) and color changes of artificial weathered wood. *Wood and Fiber Science* 36: 291–301.

9. Denig, J., Wengert, E.M., Simpson, W.T., 2000: Drying hardwood lumber. General technical report FPL-GTR-118. Forest Product Laboratory, Madison, USA, 144 pp.
10. Gril, J., Jullien, D., Bardet, S., Yamamoto, H., 2017: Tree growth stress and related problems. *Journal of Wood Science* 63: 411–432.
11. He, X., Xiong, X., Xie, J., Li, Y., Wei, Y., Quan, P., Mou, Q., Li, X., 2017: Effect of microwave pretreatment on permeability and drying properties of wood. *BioResources* 12: 3850–3863.
12. Hillis, W.E., 1987: Heartwood and tree exudates. Springer Series in Wood Science. Springer Berlin Heidelberg, Berlin, Heidelberg, 208 pp.
13. Kauman, W., Mittak, G., 1966: Drying test of coigüe (*Nothofagus dombeyi*). Informe Técnico 5. INFOR, Santiago, Chile, 20 pp.
14. Kojima, M., Yamamoto, H., Okumura, K., Ojio, Y., Yoshida, M., Okuyama, T., Ona, T., Matsune, K., Nakamura, K., Ide, Y., Marsoem, S.N., Sahri, M.H., Hadi, Y.S., 2009: Effect of the lateral growth rate on wood properties in fast-growing hardwood species. *Journal of Wood Science* 55: 417–424.
15. Kong, L., Zhao, Z., He, Z., Yi, S., 2018: Development of schedule to steaming prior to drying and its effects on *Eucalyptus grandis* × *E. urophylla* wood. *European Journal of Wood and Wood Products* 76: 591–600.
16. Kong, L., Zhao, Z., He, Z., Yi, S., 2017: Effects of steaming treatment on crystallinity and glass transition temperature of *Eucalyptus grandis* × *E. urophylla*. *Results in Physics* 7: 914–919.
17. Lenth, Ch.A., Kamke, F.A., 2001: Moisture dependent softening behavior of wood. *Wood and Fiber Science* 33: 492–507.
18. Moya, R., Muñoz, F., 2010: Physical and mechanical properties of eight fast-growing plantation species in Costa Rica. *Journal of Tropical Forest Science* 22: 317–328.
19. Moya, R., Tenorio, C., Conde-Torres, J.D., 2021: Steaming and heating treatments in logs of *Dipteryx panamensis* from fast-growth plantations: Effect on reducing growth stresses and lumber quality. *Forest Products Journal* 71(1): 3-10.
20. Moya, R., Tenorio, C., Salas, J., Berrocal, A., Muñoz, F., 2019: Tecnología de la madera de plantaciones forestales (Technology of wood from forest plantation). Editorial Tecnológica de Costa Rica, 1ra ed. Editorial Tecnológica de Costa Rica- Editorial Universidad de Costa Rica, Cartago, Costa Rica, 480 pp.
21. Moya, R., Urueña, E., Salas, C., Muñoz, F., Espinoza, O., 2013: Kiln drying behavior of lumber from ten fast-growth plantation species in Costa Rica. *Wood Material Science and Engineering* 8: 37–45.
22. Murillo, O., 2018: Cuáles especies forestales nativas debemos priorizar en el país? (Which native forest species should we prioritize in the country?). *Ambientico* 267: 4–9.
23. NIST, 2005: Softwood lumber standard: Voluntary Product Standard.
24. Pelozzi, M.M.A., Severo, E.T.D., Rodrigues, P.L.M., Calonego, F.W., 2014: Temperature charts of *Hevea brasiliensis* during log steaming and its effect on the board cracks. *European Journal of Wood and Wood Products* 72: 123–128.
25. Ratnasinga, J., Abdullah, A.M., Ramasamy, G., Seng, C.Y., 2013: A Review of different

- sawing and drying techniques used in processing small-diameter logs. *Journal of Applied Sciences* 13: 341–347.
26. Redondo-Brenes, A., Montagnini, F., 2006: Growth, productivity, aboveground biomass, and carbon sequestration of pure and mixed native tree plantations in the Caribbean lowlands of Costa Rica. *Forest Ecology and Management* 232: 168–178.
 27. Rodrigues, P.L.M., Severo, E.T.D., Calonego, F.W., Pelozzi, M.M.A., 2018: Drying behavior and decay resistance of rubberwood from steamed log and presteamed lumber. *Drying Technology* 36: 1243–1249.
 28. Salas, C., Moya, R., 2014: Kiln-, solar-, and sir-drying behavior of lumber of *Tectona grandis* and *Gmelina arborea* from fast-grown plantations: moisture content, wood color, and drying defects. *Drying Technology* 32: 32(3) 301-310.
 29. Serrano, R., Moya, R., 2011: Procesamiento, uso y mercado de la madera en Costa Rica: aspectos históricos y análisis crítico (Timber processing, uses and marketing of wood in Costa Rica: historical aspects and analysis). *Revista Forestal Mesoamericana Kurú* 8: 1–12.
 30. Simpson, W., 1991: Dry kiln operator's manual. United States Department of Agriculture. Madison, WI. USA, 256 pp.
 31. Tenorio, C., Moya, R., Quesada-Pineda, H.J., 2012: Kiln drying of *Acacia mangium* wood: colour, shrinkage, warp, split and check in dried lumber. *Journal of Tropical Forest Science* 24: 125-139.
 32. Tenorio, Carolina, Moya, R., Salas, C., Berrocal, A., 2016: Evaluation of wood properties from six native species of forest plantations in Costa Rica. *Bosque (Valdivia)* 37: 71–84.
 33. Tenorio, C., Salas, C., Moya, R., 2016: Kiln drying behavior utilizing drying rate of lumber from six fast-growth plantation species in Costa Rica. *Drying Technology* 34(4): 443-453.
 34. Tolvaj, L., Papp, G., Varga, D., Lang, E., 2012: Effect of steaming on the colour change of softwoods. *BioResources* 7: 2799–2808.
 35. Vansteenkiste, D., Stevens, M., Van Acker, J., 1997: High temperature drying of fresh sawn poplar wood in an experimental convective dryer. *Holz Als Roh - Und Werkstoff* 55: 307–314.
 36. Yang, J.L., Waugh, G., 2001: Growth stress, its measurement and effects. *Australian Forestry* 64: 127–135.
 37. Zhang, Y., Cai, L., 2008: Impact of heating speed on permeability of sub-alpine fir. *Wood Science and Technology* 42: 241–250.
 38. Zobel, B.J., Sprague, J.R., 1998: Changing juvenile wood in juvenile wood in forest trees. *Springer Series in Wood Science Springer Berlin, Heidelberg*. Pp 141–172.

RÓGER MOYA*, CAROLINA TENORIO
ESCUELA DE INGENIERÍA FORESTAL
INSTITUTO TECNOLÓGICO DE COSTA RICA
P.O.BOX: 159-7050 CARTAGO
COSTA RICA

*Corresponding author: rmoya@itcr.ac.cr

*Short notes***THE LOW-VELOCITY IMPACT RESPONSE OF BIO-COMPOSITES**

MAHARSHI J. DAVE, TEJAS S. PANDYA, SUMAN BABU UKYAM
UNIVERSITY OF MISSISSIPPI
USA

JASON STREET
MISSISSIPPI STATE UNIVESITY
USA

(RECEIVED SEPTEMBER 2021)

ABSTRACT

In this paper, an experimental investigation on the low-velocity impact response of wood-based bio-composites is presented. This study is to map the suitability of plant-based materials instead of petroleum-based plastic as a constituent raw material in composites. Wood-based composites panels were made from southern yellow pine (SYP), corn starch (CS), and methylene diphenyl diisocyanate (MDI) using a Diefenbacher hot press. The impact performance of the specimens was evaluated in terms of energy absorption capacity. Five types of bio-composites were prepared with varying compositions with SYP: 4% MDI; 2% CS and 2% MDI; 2% CS and 4% MDI; 4% CS and 4% MDI. These samples were prepared at two different manufacturing pressures. The bio-composite produced with higher manufacturing pressure had the highest absorbed energy among five different types of bio-composites, this shows that material behavior at impact loading is strongly dependent on the manufacturing pressure during fabrication.

KEYWORDS: Corn starch, impact loading, southern yellow pine, wood-based bio-composites.

INTRODUCTION

Bio-composites are composites made from natural and biocompatible material. The increase in awareness of the damage caused by synthetic petroleum-based materials on the environment has led to the development of eco-friendly materials. Interest in natural composites is growing for

many reasons including their potential to replace synthetic petroleum-based composites at lower cost with improved sustainability.

Wood-based composites have been frequently used for automobiles (Koronis et al. 2013), vibration damping and noise reduction applications (Mohanty and Fatima 2015), and the packaging of nuclear waste (Bragov and Lomunov 1997). Bio-composites have a wide range of structural and nonstructural applications (Riedel and Nickel 1999) due to their, high energy absorption capabilities (Dave et al. 2018), renewability, biodegradability, low cost, thermal conductivity, high strength-to-weight ratio, and excellent thermal and sound insulation properties (Dave et al. 2018, 2019, Li et al. 2018, Kang et al. 2012, Pandey et al. 2010). Hence, bio-composites are a valid alternative to replace man-made petroleum-based composites.

When bio-composites are used for mechanical applications, they may be exposed to various impacts during their service life. It is generally accepted that low-velocity impacts occur at velocities below 10 ms^{-1} (Richardson et al. 1996), and can reduce the strength of the whole structure under quasi-static and dynamic loads due to the localized internal damage inside the composite structure (Sutherland 2018). Therefore, it is extremely important to study the low-velocity impact behavior of materials to select a potential bio-composite for a particular application.

Experimental results have indicated that the damage tolerance of a structure can be improved by using bio-composites, including wood-based materials (Ramakrishnan et al. 2017, Mahesh et al. 2019, Abdalslam 2013, Demircioğlu et al. 2018). Despite extensive investigations of the impact behavior and damage tolerance using wood based-materials, no studies have focused on bio-composites reinforced with corn starch (CS) under low velocity impact testing.

Motivated by the current trends towards natural-based composites, the Mechanical Engineering department at the University of Mississippi and the Department of Sustainable Bioproducts at Mississippi State University focused on the development of new wood-based bio-composite made from agricultural and plant-based material. By employing cornstarch (CS) with southern yellow pine (SYP), this study aimed to improve the low velocity impact response of this type of bio-composite. These materials were impacted at energy level of 85 kJ using a drop weight test, and comparisons were made concerning the force and energy displacement response, and the condition of the damaged specimens. The outcome of this research may provide some useful information on how effectively plant-based materials can be used as a substitute material for plastic designed for structural and non-structural applications.

MATERIAL AND METHODS

Bio-composite samples created for the analysis of the high strain rate test were made from southern yellow pine (SYP), corn starch (CS) and methylene diphenyl diisocyanate (MDI) resin with different mass fractions (Tab. 1). MDI is an aromatic diisocyanate and is an efficient binder that has been used in the production of composite wood products for over 30 years. Corn starch (CS) is the starch derived from the corn (maize) grain or wheat. SYP was first run through chipper and then through a hammer mill to produce particles up to required size of 2 mm to 3 mm. SYP particles were mixed with corn starch and MDI in exact mass fraction ratios to form

the composite mass for creating panels. The amount of mass used to create the bio-composite panels was approximately 2.95 kg except for the Material 2 panel manufactured at a mat pressure of 10.5 MPa (with ram pressure of 27.58 MPa) where twice the amount of mass (5.9 kg) was used. The temperature used to form the panels was approximately 185°C. A Diefenbacher 915 × 915 mm hot press system located at the Sustainable Bioproducts Laboratory at Mississippi State University was used to create the bio-composite panels used in this study. This hot press with steam injection capability was coupled with the Alberta Research Council's Pressman operations and monitoring software. The Diefenbacher hot press was used to create all composite panels of equal thickness (6.35 mm) by compressing different materials at varying pressures as shown in Tab. 1. The various pressures required to form the panel to the appropriate thickness were based on the ability of the composite material in the mat to be compressed to the appropriate thickness.

Tab. 1: Types of bio-composites.

Designation of bio-composites	Mass fraction (%) of raw material constituents			Approx. pressure (MPa)	Curing time (s)	Density kg·m ⁻³
	SYP	CS	MDI			
Material 1	96	-	4	8.9	140	826
Material 2	96	-	4	10.5	140	1389
Material 3	96	2	2	8.7	140	855
Material 4	92	2	4	8.7	140	850
Material 5	92	4	4	8.4	140	946

Experimental technique

The low-velocity impact response of the bio-composites was studied using DYNATUP 8250 drop weight system (Fig. 1) according to the ASTM D3763 standard at the structure and Dynamics Laboratory at the University of Mississippi.

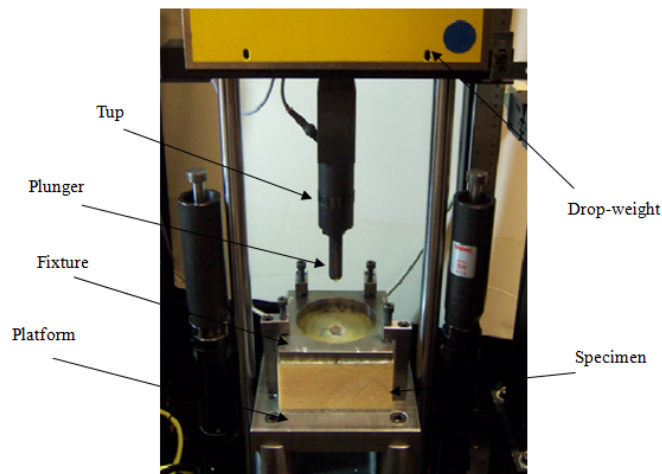


Fig. 1: Experimental setup of low velocity impact (Brahmananda and Mantena 2009).

The impact energy ranged from 84 J to 108 J and velocity ranged from 2.2 m·s⁻¹ to 2.5 m·s⁻¹. The impactor assembly consisted of a hemispherical end with a diameter of 12.70 mm and a steel rod measuring 50.8 mm which impacted the center of each specimen. The pneumatically assisted specimen clamp assembly consisted of parallel rigid plates with a 76.2 mm diameter hole in the center of each. The low-velocity impact test using Dynatup 8250 was conducted as follows.

The bio-composite specimen dimensions were $101.6 \times 101.6 \times 6.35$ mm, and the specimen was sandwiched between parallel rigid plates of the clamp. The impact drop height (0.25 m) and weight (23 kg) were determined such that velocity slowdown was less than 20% during the impact event. The applied impact energy was at least three times the energy absorbed by the specimen at peak load (ASTM D3763). The impact response of the specimens including velocity, displacement, load and absorbed energy were recorded and stored by a computer using the Dynatup impulse TM data acquisition system. The configuration provided 85 J of impact energy and 2.23 m s^{-1} of impact velocity for bio-composite Material 1 and Materials 3-5, and 108 J of impact energy and 2.5 m s^{-1} of impact velocity for bio-composite Material 2. Five specimens were tested for each bio-composite configuration and average data average values were considered for analysis.

RESULTS AND DISCUSSIONS

A load–displacement curve is the signature of a composite material’s response to impact loading (Cesim and Dahsin 2008). Fig. 2 shows the force-displacement curves of five different types of bio-composites impacted in the range of 85 J to 108 J.

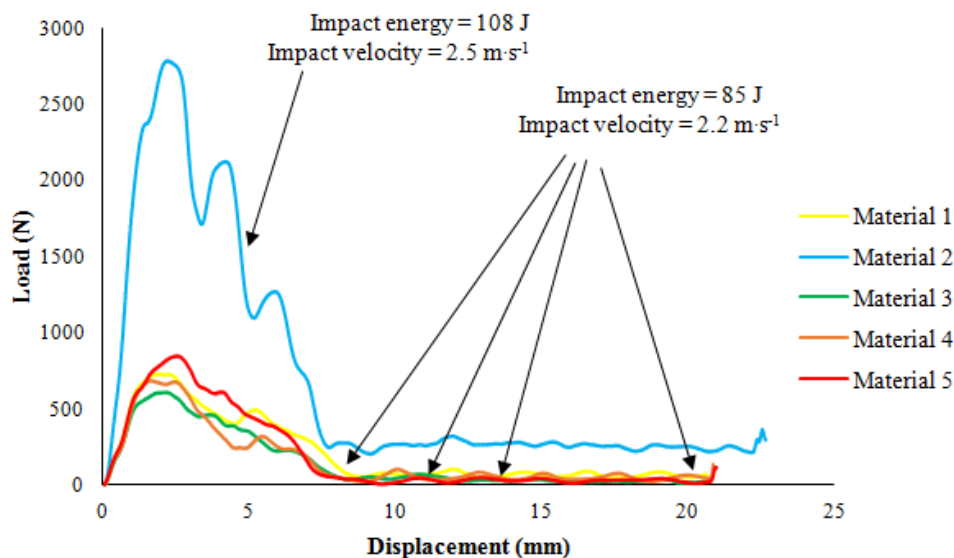


Fig. 2: Load-displacement curves of bio-composites.

A load–displacement curve consists of an ascending section of loading and a descending section combining loading and unloading. The ascending section of load–displacement may also be called the stiffening section as it represents the bending stiffness history of the composite material under impact loading (Cesim and Dahsin 2008). Depending on the level of impact energy, the descending section may have three different possibilities. This descending section may be a pure rebounding curve representing the rebounding of the impactor from the specimen. This descending section could also contain partial softening of the specimen and partial rebounding of the impactor. The descending section may even be a complete softening curve of the specimen. If the descending section is completely a softening curve, the load–displacement

curve should be an open curve in that the impactor penetrates into the specimen or even perforates the specimen.

Fig. 2 shows that the bio-composite specimen material 2 had the highest peak load of 2800 N at impact energy of 108 J. This increment in damage resistance could be attributed to higher dynamic strength and density of the material. Moreover, analyzing the samples on the basis of similar manufacturing conditions, similar pressure and curing times, the specimen material 5 had the highest peak load and material 3 had the lowest peak among tested specimens at impact energy of 85 J. This increment in load bearing capacity of bio-composite sample material 5 could be attributed to the higher mass fraction of CS contained in this specimen.

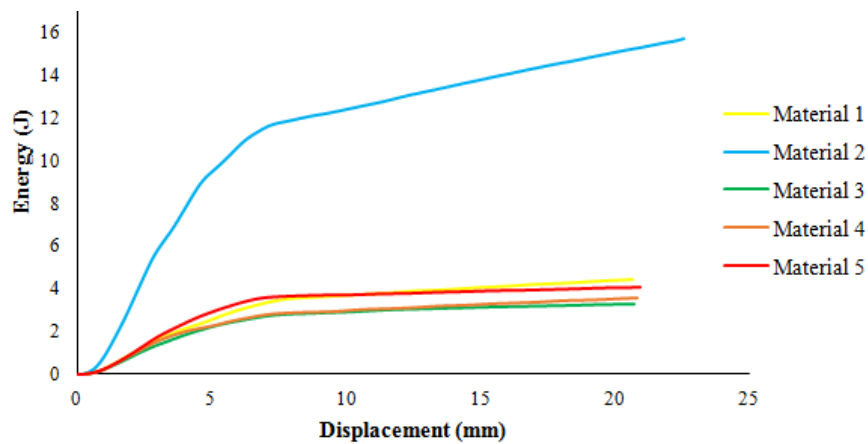


Fig. 3: Energy-displacement curves of bio-composites.

Fig. 3 represents energy-displacement diagrams of different bio-composites impacted in the range of 85 J to 108 J. It is evident that maximum energy is absorbed at peak load for all bio-composite specimens tested. A similar trend was observed during investigations of the low-velocity impact response of composites containing wood-based material (Demircioğlu et al. 2018, Mohammadabadi et al. 2018).

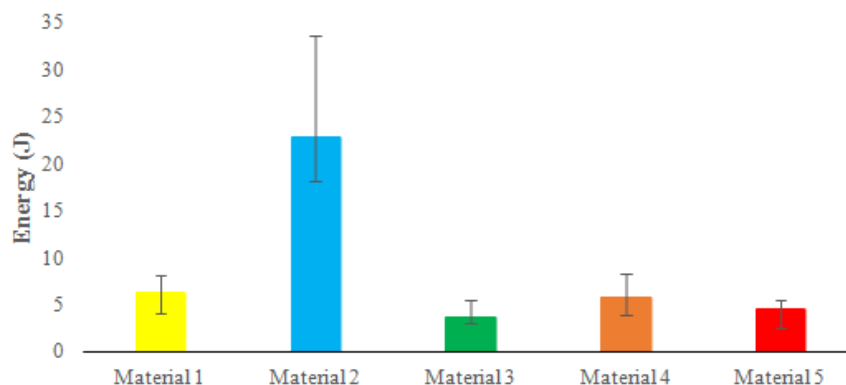


Fig. 4: Total absorbed energy during low velocity impact test of different bio-composites.

Fig. 4 reports the total energy absorption of different bio-composites under low velocity impact testing. The bio-composite specimen material 2 had the highest energy absorption and

material 3 had lowest energy absorption among tested specimens. The CS adversely affected the energy absorption capacity of bio-composites among all bio-composites tested.

Fig. 5 shows the damage views of impacted specimens. All bio-composite specimens were penetrated during the impact event. Furthermore, it depicts that the radial growth of damage is least in specimen material 3, whereas more in the material 2.



Fig. 5: Damage views of the impacted bio-composites.

CONCLUSIONS

Low-velocity impact responses of novel bio-composites were examined using a drop weight impact testing machine. From the impact response data and damage study, the following conclusions can be made. The composite created at the highest pressure (material 2) had the greatest stiffness among all the samples. This shows that improved damage resistance and energy absorption characteristics can be achieved when material is compressed at a higher pressure during the fabrication process. The applications of these bio-composites can be various including packaging and decking material.

REFERENCES

1. Abdalslam, S., 2013: Impact damage analysis of balsa wood sandwich composite materials. PhD diss. Detroit, Michigan: Wayne State University, Mechanical Engineering Department, Pp 74-75.
2. ASTM D3763-18, 2018: Standard test method for high speed puncture properties of plastics using load and displacement sensors.
3. Atas, C., Sevim, C., 2010: On the impact response of sandwich composites with cores of balsa wood and PVC foam. *Composite Structures* 93(1): 40-48.
4. Bragov, A., Lomunov, A., 1997: Dynamic properties of some wood species. *Journal de*

- Physique IV 07(C3): 487–492.
5. Cesim, A. Dahsin L., 2008: Impact response of woven composites with small weaving angles. *International Journal of Impact Engineering* 35(2): 80-97.
 6. Crupi, V., Epasto, G., Guglielmino, E., 2016: Internal damage investigation of composites subjected to low-velocity impact. *Experimental Techniques* 40: 555-568.
 7. Dave, M.J., Pandya, T.S., Stoddard, D., Street, J., 2018: Dynamic characterization of biocomposites under high strain rate compression loading with split Hopkinson pressure bar and digital image correlation technique. *International Wood Products Journal* 9(3): 115-121.
 8. Dave, M.J., Pandya, T.S., Stoddard, D., Street, J., Blake, C., Ly, P., 2018: Dynamic and damping properties of novel bio-composites using the hammer excitation vibration technique *Wood Research* 63(2): 215-226.
 9. Demircioğlu, T.K., Balıkoğlu, F., İnal, O., Arslan, N., Aya, İ., Ataş A., 2018: Experimental investigation on low-velocity impact response of wood skinned sandwich composites with different core configurations. *Materials Today Communications* 17: 31-39.
 10. Kang, C., Oh, S., Lee, T., Kang, W., Matsumura, J., 2012: Sound absorption capability and mechanical properties of a composite rice hull and sawdust board. *Journal of Wood Science* 58: 273-278.
 11. Koronis, G., Silva, A., Fontul, M., 2013: Green composites: A review of adequate materials for automotive applications. *Composites Part B: Engineering* 44(1): 120–127.
 12. Li, T., Song, J., Xinpeng Zhao, X., Yang, Z., Pastel, G., Xu, S., Jia, C., Dai, J., Chen, C., Gong, A., Jiang, F., Yao, Y., Fan, T., Yang, B., Wågberg, L., Yang, R., Hu, L., 2018: Anisotropic, lightweight, strong, and super thermally insulating nanowood with naturally aligned nanocellulose. *Science Advances* 4(3).
 13. Mahesh, V., Joladarashi, S., Satyabodh M., Kulkarni, S.M., 2019: An experimental investigation on low-velocity impact response of novel jute/rubber flexible bio-composite. *Composite Structures* 225: 111190.
 14. Mohammadabadi, M., Yadama V, Yao, L., Bhattacharyya, D., 2018: Low-velocity impact response of wood-strand sandwich panels and their components. *Holzforschung* 72(8): 681 -689.
 15. Mohanty, A., Fatima, S., 2015: Noise control using green materials. *Sound and Vibration* 49(2): 13-15.
 16. Pramanik, B., Mantena, P.R., 2009: Punch-shear characteristics of nanoclay and graphite platelet reinforced vinyl ester plates, laminated face sheets and sandwich composites under low velocity impact. *ASME Early Career Technical Journal* 1.1-1.9.
 17. Pandey, J.K., Ahn, S.H., Lee, C.S., Mohanty, A.K., Misra, M., 2010: Recent advances in the application of natural fiber-based composites. *Macromolecular Materials and Engineering* 295: 975–989.
 18. Pandya, T.S., Dave, M.J., Street, J. Blake, C., Mitchell, B., 2019: High strain rate response of bio-composites using Split Hopkinson pressure bar and digital image correlation technique. *International Wood Products Journal* 9(3): 115-121.
 19. Ramakrishnan, K.R., Corn, S., Moigne, N.L., Slangen, P., 2017: Low velocity impact damage assessment in natural Fibre biocomposites. ICCM21 - 21st International Conference

- on Composite Materials, Xi'an, China.
20. Richardson, M.O.W., Wisheart, M.J., 1996: Review of low-velocity impact properties of composite materials. *Composites Part A: Applied Science and Manufacturing* 27(12): 1123-1131.
 21. Riedel, U., Nickel, J., 1999: Natural fibre-reinforced biopolymers as construction materials. *Die Angewandte Makromolekulare Chemie* 272: 34-40.
 22. Sutherland, L., 2018: A review of impact testing on marine composite materials. Part III-damage tolerance and durability. *Composite Structures* 188: 512-518.

MAHARSHI J. DAVE*, TEJAS S. PANDYA, SUMAN BABU UKYAM
MECHANICAL ENGINEERING DEPARTMENT
THE UNIVERSITY OF MISSISSIPPI
OXFORD, MS 38677
USA

*Corresponding author: mjdave@go.olemiss.edu

JASON STREET
DEPARTMENT OF SUSTAINABLE BIOPRODUCTS
MISSISSIPPI STATE UNIVERSITY
MISSISSIPPI STATE, MS 39762-9820
USA